Solidification Behaviour of Magnesium Alloys

A thesis submitted for the degree of

Doctor of Philosophy

by

Bo Jiang

BCAST

Brunel University

Uxbridge, UB8 3PH

United Kingdom

August 2013

Supervision : Professor Zhongyun Fan

Abstract

Magnesium alloys have been extensively used for structural and functional applications due to their low densities. In order to improve the mechanical properties, grain refinement of the microstructures of magnesium alloys has been studied for many years. However, an effective and efficient grain refiner or refinement technique hasn’t been achieved yet, especially for those with aluminium contained. In this study, solution for this problem has been discovered through further understanding of the solidification process, including the potency and the efficiency of nucleation particles, the role of solute, and the role of casting conditions. First of all, the study suggested that MgO particles can act as nuclei in magnesium alloys by measuring and analyzing the differences in cooling curves with various amount of endogenous MgO particles. The differences indicated that the number density of MgO particles has a huge influence on the microstructure. This idea has been fatherly proved by the inoculation of MgO particles in magnesium alloys because the microstructures have been significantly refined after the inoculation. A new kind of refiner (AZ91D-5wt%MgO) has been developed based on such understandings. Secondly, the study discovered that the role of solute has much smaller effect on the grain size than it was suggested in traditional understandings. The inverse-proportional relationship between the grain size and the solute is highly suspected and the major role of solute is to cause columnar- equiaxed transition. The role of casting conditions has also been studied in order to provide experimental evidence for the existence of melt quenching effect in magnesium alloys. It is shown that various casting conditions, such as pouring temperatures and mould temperatures, have large influence on the critical heat balance temperature after rapid pouring. In this study, a theoretical model based on the analysis of cooling curves is presented for grain size prediction. An analytical model of the advance of equiaxed solidification front is developed based on the understanding of the role of casting conditions. Eventually, all these understandings have been applied to magnesium direct-chill (DC) casting. The refined microstructure of DC cast ingots can further assist in understanding the mechanism of advanced shearing achieved by MCAST unit. The comparison of the ingots with and without melt shearing indicated that the advance shearing device can disperse MgO film into individual particles.

Acknowledgements

I would like to sincerely thank Prof. Zhongyun Fan who provided me with the opportunity to pursue my PhD who has extensively and continuously encouraged me during the four years of study in Brunel University. Without his support and guidance throughout my research, not even the slightest improvement would ever have been achieved. He is not only my Supervisor but also the dearest friend who not only guides me on realms of research but also mentors my value of life. I am extremely fortunate to have the opportunity to work with him who is so dedicated and diligent in his work. My full appreciation is indescribable.

I wish to thank my colleagues who have supported me especially: Dr. Y. Zuo, Dr. M. Xia, Dr. H-T. Li, Dr. S. Ji, and Mr. F. Yan for their help with processing and their technical knowledge, Dr. Y. Wang and Dr. W. Yang for their help with advance electron microscopy, Prof. Shu-Zu Lu and Prof. John Hunt for their assistance in theoretical study, and Mr. Stephen Cook, Mr. Carmelo Nunez, and Mr. Peter Lloyd, for their technical assistance. I want to specially thank Dr. Y. Zuo and Dr. M. Xia, who have been working with and encouraging me throughout the whole program, and Prof. Shu-Zu Lu, who has been working endlessly to revise my thesis writing. Without their support and help, this thesis would never have been made possible.

I would like to show my gratitude to Drs. Y. Huang, Drs. Jayesh Patel, Dr. H. Zhang, Dr. Y. Zhang, Drs. B. McKay, Drs. Hari Babu Nadendla, Mrs Pam Eade, Mrs Carla Cummins, Mrs Nikki Elliott, Mr. Phil Enright, Dr. S. Liang, Mr. Ritwik Ritwik, Mr. Simon Jones, Mr. Zen Cassinath, and Dr. Kawther Al-Helal, for their support in conducting the research work, preparing this thesis, and for many inspiring discussions.

Eventually, I offer my best wishes to my best friend Mr. Chi Chen, who has been encouraging me during the program. I owe my deepest gratitude to my mother and father, who provide me with their love and support unconditionally. Their decency and wisdom will guide me throughout my life.

Publication List

1. Men, H., Jiang, B., Fan, Z. (2010) Mechanisms of grain refinement by intensive shearing of AZ91 alloy melt. Acta Materialia, 58: 6526-6534.

2. Zuo, Y., Jiang, B., Zhang, Y., and Fan, Z. (2011) Grain refinement of DC cast magnesium alloys with intensive melt shearing. Proc. of ICASP3, Aachen, June 2011.

3. Fan. Z., Zuo, Y., and Jiang, B. (2011) A new technology for treating liquid metals with intensive melt shearing. Proc. of ICASP3, Aachen, June 2011.

4. Zuo, Y., Jiang, B., and Fan, Z. (2011) Microstructures of DC cast light alloys under the influence of intensive melt shearing. Proc. of 5th Light Metal Technology Conf. Germany July 2011.

5. Zuo, Y., Jiang, B., Enright, P., Scamans, G.M. and Fan, Z. (2011) Degassing of LM24 Al-alloy by intensive melt shearing. Jnl of Cast Metals Research, 2011.

6. Zuo, Y.B., Jiang, B., Zhang, Y.J., and Fan, Z. (2012) Degassing LM25 aluminium alloy by novel degassing technology with intensive melt shearing. International Journal of Cast Metals Research 26 (1): 16- 21.

7. Zuo, Y.B., Jiang, B., Zhang, Y. and Fan, Z. (2012) Melt conditioned DC (MC-DC) casting of magnesium alloys. Magnesium Technology, 155- 160.

8. Ji, S., Jiang, B., Yang, W. and Fan, Z. (2013) Melt Quenched High Pressure Die Casting (MQ-HPDC) of an A356 Alloy. Materials Science Forum 765: 195-199.

9. Patel, J.B., Prasada Rao, A.K., Jiang, B., Zuo, Y.B., and Fan, Z. (2012) Melt conditioned direct chill casting (MC-DC) process for production of high quality Mg-Alloy billets. Mg2012, 9th International Conference of Magnesium Alloys and their Applications, 2012, 713-736.

10. Ji, S., Yang, W., Jiang, B., Patel, J.B., and Fan, Z. (2013) Weibull statistical analysis of the effect of melt conditioning on the mechanical properties of AM60 alloy. Materials Science & Engineering A 566: 119-125.

11. Zuo, Y., Li, H., Xia, M., Jiang, B., Scamans, G.M., and Fan, Z. (2011) Refining grain structure and porosity of an aluminium alloy with intensive melt shearing. Scripta Materialia 64: 209-212.

Nomenclature

A list of symbols is given with a brief description and units used.

Symbol	Definition and Units
A	constant
a, a_0, a_1	constant
a_S	atomic spacing of nucleated phase
a_{Sub}	atomic spacing of nucleation substrate
b	constant
C	composition (wt%; at%)
C_0	composition of alloy (wt%; at%)
C_L, C_S	interfacial solute content in liquid and solid (wt%; at%)
C_{p1}, C_{p2}	enthalpy per unit volume of the metal and container (J m^{-3} K^{-1})
C_V	heat capacity of the melt (J m^{-3} K^{-1})
D	diffusion coefficient (m s^{-2})
$\overline{D}$	predicted mean grain size (m)
d	diameter of nucleation substrate (m)
f	calculated lattice disregistry, or solid fraction
f_0	vibration frequency of the atoms
f_I	solid fraction when impingement occurs
f_L, f_s	liquid and solid volume fraction
f_p	volume fraction of the particles (m^{-3})
G	temperature gradient (K m^{-1})
ΔG_r	change in the Gibbs free energy to form a small solid sphere with radius r (J mol^{-1}; J m^{-3})
ΔG_V	Gibbs free energy difference per unit volume

	between solid and liquid phases at the same temperature (J mol^{-1}; J m^{-3})
ΔG^*	maximum excess free energy
ΔG^*_{hec}	critical energy barrier for heterogeneous nucleation (J mol^{-1}; J m^{-3})
ΔG^*_{hom}	critical energy barrier for homogeneous nucleation (J mol^{-1}; J m^{-3})
Δh_f	latent heat of fusion per unit volume (J m^{-3})
k	equilibrium solute distribution coefficient
k_B	Boltzmann's constant
L_V	latent heat of fusion (J mol^{-1}; J m^{-3})
$\bar{l}$	measured linear intercept length (m)
m	slope of the liquidus line (K wt%$^{-1}$)
N_0	total number of particles
N_e	number density of effective nucleation substrates (m^{-3})
$N(d)$	number of particles of with diameter d
N_g	number density of grains (m^{-3})
N_{hom}	homogeneous nucleation rate
P	constitutional-supercooling parameter (K)
$P(T)$	distribution function of numbers of nucleation particles against temperature per unit volume (m^{-3})
Q	growth restriction factor (K)
R	radius of grains (m)
r	nucleus radius (m)
r^*	critical nucleus radius (m)
r_p	radius of the particles (m)
$S(\theta)$	a factor in terms of the wetting angle
ΔS_v	entropy of fusion (J mol^{-1}K^{-1}; J m^{-3}K^{-1})

T	temperature (K)
T_e	equilibrium temperature (K)
T_I	temperature for impingement (K)
T_L, T_S	liquidus and solidus temperature (K)
ΔT	undercooling (K)
ΔT_C	columnar growth front temperature (K)
ΔT_c	critical undercooling in epitaxial nucleation model (K)
ΔT_I	undercooling for impingement (K)
ΔT_N	heterogeneous nucleation undercooling (K)
ΔT_r	undercooling caused by the curvature of the dendrite tips (K)
ΔT_{fg}	free growth undercooling (K)
T_F	minimum temperature before recalescence (K)
T_{hb}	critical heat balance temperature (K)
T_m	equilibrium melting temperature (K)
T_N	starting temperature of the growth of nucleation substrates (K)
T_R	recalescence temperature (K)
V	growth velocity of grains (m s^{-1})
V_{o1}, V_{o2}	volume of the metal and container (m^{-3})
V_m	volume of the melt (m^{-3})
v	interface velocity (m s^{-1})
v_g	growth velocity of grains (m s^{-1})
v_e	advance velocity of equiaxed solidification front (m s^{-1})
x	distance from the interface (m)
$\varepsilon, \xi, \Theta, \eta, \delta, s$	constant
Γ	Gibbs-Thomson parameter (K m^{-1})

Υ_{ML}	mould-liquid interfacial energy (J m^{-2})
Υ_{SL}	solid-liquid interfacial energy (J m^{-2})
Υ_{SM}	solid-mould interfacial energy (J m^{-2})
ϕ_E	extended volume fraction
θ	wetting angle
φ_0	atoms per unit volume (m^{-3})

Abbreviation	**Description**
CNT	classical nucleation theory
ESF	equiaxed solidification front
GRF	growth restriction factor
MCAST	melt conditioning casting
NS	non-sheared
SH	sheared
PS	pseudomorphic solid

Table of Contents

Chapter 1. Introduction

1.1. Background

Magnesium and magnesium alloys have superior specific strength and stiffness comparing with other engineering materials, due to their low density [1-5]. They also offer a number of attractive properties such as dimensional stability, good machinability, recyclability, good heat dissipation, good damping, and good electro-magnetic shield [1, 4]. Therefore, they meet the need for weight reduction and energy saving in modern industries, especially in power equipment, computer and communication products, and the automotive industry [2, 3]. In recent years, research studies and applications on magnesium alloys have greatly expanded around the world [5]. The increased use of magnesium and magnesium alloys requires further understanding of solidification behaviour in order to develop advanced casting technologies for magnesium alloy castings with fine grain size, minimum porosity or cracks and further improved metallurgical quality.

One major problem for magnesium alloy castings is that the microstructures of these castings tend to be coarse, which lead to poor mechanical properties and possible microporosity [6-7]. Based on the Hall-Petch equation, magnesium alloys exhibit strong influence of grain size on strength because the hexagonal close packed structure of magnesium provides fewer independent slip systems and larger Taylor factor comparing to those metals with cubic structures [8]. Large grain sizes also cause shrinkage and hot tearing, low thermal conductivity, and large volumetric shrinkage in most magnesium alloys [9-11]. Therefore, a high efficient and applicable grain refinement technology brings about an urgent need for magnesium alloys.

The two main stages in solidification are nucleation and grain growth. Thus, in order to achieve refinement of microstructures, we can either enhance nucleation or restrict grain growth. In the previous research studies [12-18], a number of grain refinement technologies have been developed and applied to magnesium alloy castings.

Grain refiner addition, i.e., inoculation, is the most common way to refine grains. The mechanism of this method is to enhance heterogeneous nucleation by introducing a large number of effective nucleation substrates in the melt. For aluminium free magnesium alloys, zirconium is usually added as the refiner since the crystal structures of magnesium and zirconium are the same and the misfit between the two are relatively small [12]. So most aluminium free magnesium alloys are usually alloyed with or inoculated with zirconium addition, such as ZE41, ZK60, WE43, AM-SC1, and ML10 alloy systems. However, as it is known, zirconium is an expensive grain refiner, and the cost of refinement using zirconium will certainly limit the application to magnesium alloys. Thus, a cheaper replacement for zirconium is a main challenge that needs to be addressed. For aluminium bearing magnesium alloys, such as AM50, AM60, AZ31, and AZ91 alloy systems, the grain refining effect of zirconium vanishes because aluminium reacts with zirconium first in the melt and form Al_3Zr compound. Some researchers [13-17] suggest that carbon, C_2Cl_2, C_6Cl_6, Al_4C_3, SiC, CaC_2, ZnO, or $MgCO_3$ can be used as refiners for this group of alloys. However, all of these potential refiners may have some problems. Either it is difficult to mix the refiner consistently into molten magnesium with no excess inoculants left in the melt to cause corrosion, or it requires a large quantity of inoculants and cause porosity and cracks [18]. In today's industry, there is no commercially available grain refiner, which is both reliable and easy to apply, for aluminium bearing magnesium alloys [18].

Another solution for grain refinement is to restrict grain growth. Some researchers [18] suggest that solutes should play an important role in restriction of grain growth. A possible way to achieve fine grains, as suggested by Easton and StJohn [18], is to alloy with some solutes which have high growth restriction factor (GRF). However, some studies done in this work, which will be discussed in detail in a later chapter, is somehow in conflict with the conclusion on the growth restriction factor study, so the effect of solute in grain refinement is arguable and needs further study.

Since grain refinement is important for improvement of mechanical properties and there has been no suitable solution found for magnesium alloys, a thorough understanding of solidification behaviour is necessary to achieve a better grain refinement and to improve the quality of magnesium castings. Such understandings include, but are not limited to, the potency and efficiency of nucleation particles in magnesium alloys, the role of undercooling during solidification, the effect of solute on grain refinement, and the effect of various solidification conditions.

1.2. Research Objectives

The major objectives of this study are:

- To discover the mechanism of grain refinement of magnesium alloys with MgO inoculation, including the role of potency and efficiency of MgO inoculant in magnesium alloys, and to develop an applicable grain refiner for magnesium alloys.
- To discover mechanisms of the effects of solute and alloy composition on the grain refinement of magnesium alloys.
- To investigate the effect of casting conditions and melt quenching on solidification behaviour and grain structures of magnesium alloys.
- To discover the mechanism of grain refinement achieved by intensive melt shearing treatment of magnesium alloys.
- To improve and optimize magnesium alloy direct chill casting by applying the intensive melt shearing device, and study the mechanism of the grain refinement achieved by intensive melt shearing in magnesium alloy direct chill casting.

1.3. Outline of Thesis

After a sincere acknowledgement and an introduction of the research background, previous literatures are reviewed in Chapter 2 beginning with a brief introduction followed by a detailed overview of previous theoretical studies in solidification behaviour. The studies include the classical nucleation theories, the studies on potency of nucleation particles, the studies of efficiency of nucleation particles, the effect of solute and alloy composition, columnar equiaxed transformation model, and modelling for nucleation and growth for equiaxed grains. Also in Chapter 2, the solidification behaviour in magnesium alloys from previous studies are summarized. Finally, the technologies developed for magnesium alloy melt treatments are reviewed. Chapter 3 describes the experimental procedures and technologies in details. In Chapter 4 the results of the experiments are provided, including the cooling curve measurement of AZ91D alloy with and without melt shearing, TP-1 casting for Mg-Al and Mg-Zn binary alloys with and without melt shearing, TP-1 casting and cooling curve measurement for Mg-Al with MgO inoculation, cooling curve measurement of AZ91D with various casting conditions, and AZ31 and AZ91D direct chill casting with and without melt shearing. Chapter 5 offers discussions on the solidification behaviour of magnesium alloys including the potency and efficiency of nucleation particles, the effect of solute and composition, the application of MgO as a grain refiner, the effect of the casting process, and the application in magnesium direct chill casting. Also in Chapter 5, there are two modelling studies, one is a model showing the relationship between undercooling and the number of nucleation particles, and the other is to predict the advancement of solidification front for fully equiaxed grain growth. The main conclusions of the study and suggestions for further work are presented in Chapter 6 and Chapter 7, respectively.

Chapter 2. Literature Review

2.1. Theoretical Studies in Solidification Behaviour

In this section, previous theoretical studies on solidification behaviour have been reviewed, starting with the well-known classical nucleation theory in section 2.1.1. Research on the potency of nucleation substrate is inspected in section 2.1.2 to provide an understanding on the crystallographic conditions for potential qualified substrates. Efficiency of nucleation substrates is reviewed in section 2.1.3, working towards a better understanding on the mechanism of invoking nucleation substrate based on thermal analysis. In section 2.1.4, research studies on the role of solute are revisited to provide a general understanding of the grain restriction factor. The columnar-equiaxed transition is inspected in section 2.1.5. Finally the modelling on fully equiaxed growth is reviewed in 2.1.6 to achieve a general understanding on equiaxed solidification with various conditions.

2.1.1. Classical Nucleation Theory

The classical nucleation theory (CNT) is the first approach on the nucleation theory [19]. The formulation of CNT relies on equilibrium thermodynamics and the use of macroscopically determined properties [20]. To form a small solid sphere with radius r in a supercooled liquid, the change in the Gibbs free energy can be expressed as [21]

$$\Delta G_r = \left\{-\frac{4}{3}\pi r^3 \Delta G_V + 4\pi r^2 \Upsilon_{SL}\right\} S(\theta) \tag{2.1}$$

where Υ_{SL} is the solid-liquid interfacial energy, ΔG_V is the Gibbs free energy difference per unit volume between solid and liquid phases at the same temperature, and $S(\theta)$ is the factor in terms of the wetting angle θ, given by [21]

$$S(\theta) = (2 + \cos\theta)(1 - \cos\theta)^2/4 \qquad (2.2)$$

The two main types of nucleation are homogeneous nucleation, where the new phase is formed in a uniform substance, and heterogeneous nucleation, where nucleation occurs on a pre-existing substrate. For homogeneous nucleation, since there is no nucleation substrate, the wetting angle can be simply considered as 2π. The energetical description of the classical nucleation theories both for homogeneous nucleation and heterogeneous nucleation will be discussed in more detail in the following sections.

2.1.1.1. Homogeneous Nucleation

Homogeneous nucleation considers a given volume of liquid at a temperature below the liquidus of the metal [22]. The free energy barrier, therefore, is caused by the difference between changes in volume free energy and the interfacial energy when the transformation takes place [21], as it is illustrated in **Figure 2.1**.

For homogeneous nucleation, since there is no wetting angle factor, therefore $S(\theta) = 1$, and equation 2.1 becomes

$$\Delta G_r = -\frac{4}{3}\pi r^3 \Delta G_V + 4\pi r^2 \Upsilon_{SL} \qquad (2.3)$$

Since the Gibbs free energy difference per unit volume ΔG_V can be approximated as

$$\Delta G_V \cong L_V \frac{\Delta T}{T_m} \qquad (2.4)$$

where L_V is the latent heat of fusion per unit volume at the equilibrium melting temperature, ΔT is the undercooling, and T_m is the equilibrium melting temperature [21]. The critical nucleus radius [21-22] is obtained from the equation 2.3,

$$r^* = \frac{2\Upsilon_{SL}}{\Delta G_V} \cong \frac{2\Upsilon_{SL}}{L_V}\frac{T_m}{\Delta T} \tag{2.5}$$

and the critical energy barrier for nucleation is [21]

$$\Delta G^*_{hom} = \frac{2\Upsilon_{SL}}{\Delta G_V} \cong \frac{16\pi {\Upsilon_{SL}}^3 {T_m}^2}{3{L_V}^3}\left(\frac{1}{\Delta T}\right)^2 \tag{2.6}$$

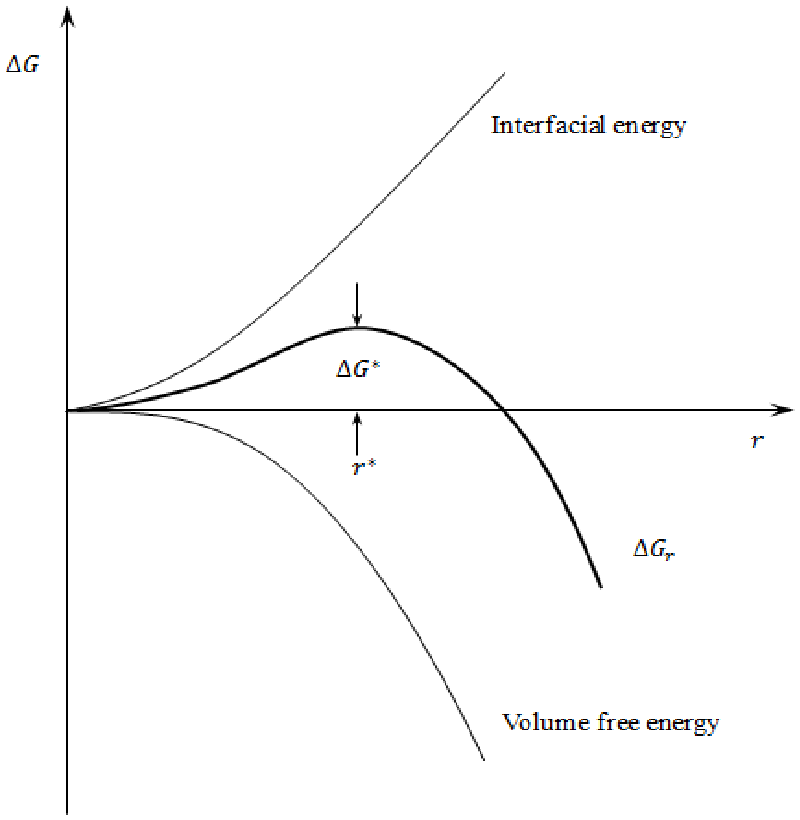

Figure 2.1 Schematic representation of the free energy change associated with homogeneous nucleation of a sphere of radius r, where r^* is the critical nucleus size, and ΔG^* is the maximum excess free energy [21].

For a given undercooling, there exists a critical radius, which is associated with the maximum free energy or nucleation barrier [23]. From equations 2.5 and 2.6, it is easy to see that for atomic clusters with radius smaller than the critical radius, the system can lower its free energy by dissolution of the solid and when atomic clusters have larger radius than the critical radius, the free energy of the system decreases if the solid grows. If the atomic clusters have the radius r^*, the solid clusters can be in equilibrium but unstable with their surrounding liquid [24]. This relationship between the cluster radius and the critical radius is useful in helping to explain the results from tentative homogeneous nucleation experiments with small metal droplets.

The homogeneous nucleation rate, based on the previous understanding [21], is given by

$$N_{hom} = f_0 \varphi_0 \exp\left(-\frac{\Delta G^*_{hom}}{k_B T}\right) \tag{2.7}$$

where φ_0 is the atoms per unit volume contained in the liquid, k_B is Boltzmann's constant, and f_0 is a complex function that depends on the vibration frequency of the atoms, the activation energy for diffusion in the liquid, and the surface area of the critical nuclei. Its exact nature is not important here and it is sufficient to consider it a constant.

2.1.1.2. Heterogeneous Nucleation

In classical nucleation theory, heterogeneous nucleation comprises the thermodynamics and the kinetics of the formation of the nuclei of a new phase on the surface of a foreign substrate [21] as illustrated in **Figure 2.2**. The thermodynamic theory to explain the diminishing of the energetic barrier of formation of a critical nucleus considers the interfacial energy between the substrate and the solid [25]. The energetical expression of heterogeneous nucleation is shown in equation 2.1 and 2.2, and the description in section 2.1.1 also stands for heterogeneous nucleation except for the wetting angle factor, $S(\theta)$. The relationship between the nucleation barrier of homogeneous nucleation and heterogeneous nucleation is given by

$$\Delta G^*_{hec} = S(\theta) \Delta G^*_{hom} \tag{2.8}$$

The energy barrier for heterogeneous nucleation can be much smaller than for homogeneous nucleation considering relatively small wetting angle, for example, a 30 °wetting angle results in 0.02 for $S(\theta)$ [21]. Based on such an understanding, the wetting angle of the solid on substrates is considerably important for enhancing heterogeneous nucleation. Hypothetically, if the wetting angle becomes 0, there should be no energy barrier for heterogeneous nucleation [21]. This is useful in helping to understand grain refinement effect and producing a better grain refiner.

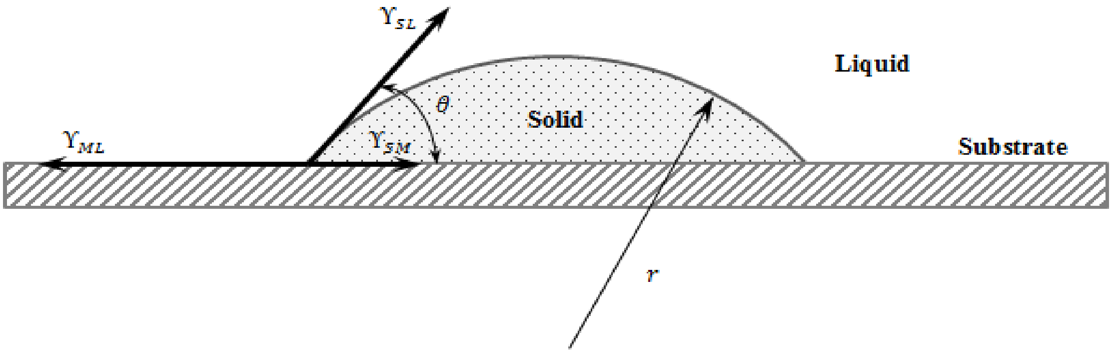

Figure 2.2 Schematic illustration of heterogeneous nucleation of a spherical cap on a flat mould wall, where θ is the wetting angle of the solid on the mould, Υ_{SL}, Υ_{ML}, and Υ_{SM} are the interfacial energies of liquid/solid, mould/liquid, and solid/mould interfaces, respectively [21].

2.1.2. Potency of Nucleation Substrates

The potency of nucleation substrates is the ability for potential substrates to nucleate [26]. According to CNT, the potency of a particle or inoculant should depend on the wetting angle, θ, and the interfacial energies [21]. However, experimentally it is relatively hard to measure the wetting angle during the solidification of an alloy. Also, a simple description of the interfacial energy is not possible [27, 28] because the interfacial energy is composed of several contributory factors [26], including but limited to the chemical nature of the substrate [29], the topographic features of the substrate surface [30], the electrostatic potential between the substrate and the nucleated solid [31], and the lattice strain or disregistry between the two phases at the interface [27]. Therefore, it is relatively hard to use CNT to determine whether a certain type of particle can be the effective nuclei for the given alloy system. In order to solve this problem, the lattice misfit between the particle and the alloy has been used to determine the potency of the particles. This is based on the basic understanding that low values of wetting angle usually lead to low-energy interface between the particle and the solid nucleus, γ_{SM}, which should in turn be favoured by good lattice matching between the particle and solid [21]. Therefore, the lattice misfit can be used as a critical value to determine the potency of potential nucleation substrates.

According to Turnbull and Vonnegut [27], the crystallographic disregistry between the substrate and the melt is the leading influential factor on whether a substrate can enhance heterogeneous nucleation. The theoretically calculated lattice disregistry, or misfit [27, 33], is defined as

$$f = \frac{|a_S - a_{Sub}|}{a_S} \times 100\% \tag{2.9}$$

where a_S and a_{Sub} are the atomic spacing along a specific direction on the matching planes of the nucleated phase and the nucleation substrate respectively. The numerator of the right hand-side in equation 2.8, therefore, is the difference between the atomic spacing of the nucleated phase and the nucleation substrate, as shown in **Figure 2.3**. The interface region can be explained by a simple dislocation model that compensates for the lattice strain in the nucleated phase for a nucleation misfit up to 0.20 [26]. This critical value is used to resolve the qualification of a potential nucleation substrate for a certain alloy system.

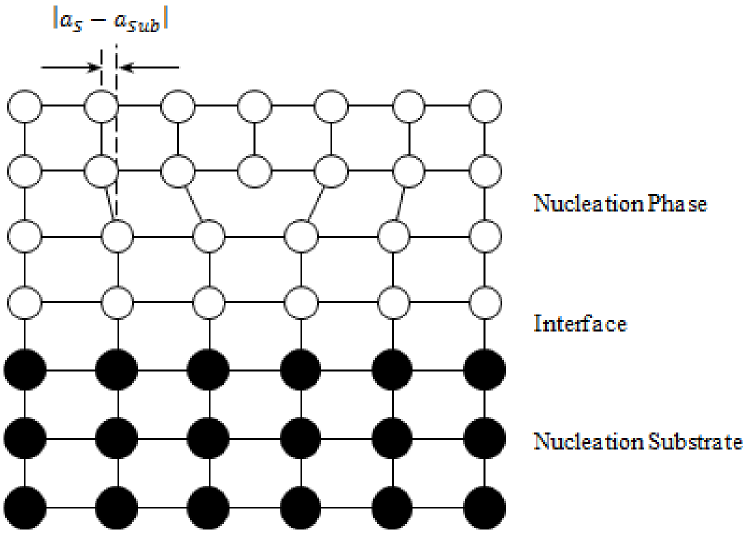

Figure 2.3 Schematic Illustration of nucleation phase, substrate, interface, and the difference between the atomic spacing of the nucleated phase and the nucleation substrate [21].

Further study by Bramfitt [26] pointed out the inherent limitation of the Turnbull-Vonnegut equation. The calculation might potentially neglect an extremely large misfit from other directions which doesn't parallel to the calculated one, especially when dealing with the nucleation phase and substrate with various crystallographic structure, for example, the interface between (110) of a *b.c.c.* substrate and the (0001) of a *h.c.p.* phase shown in **Figure 2.4** [26].

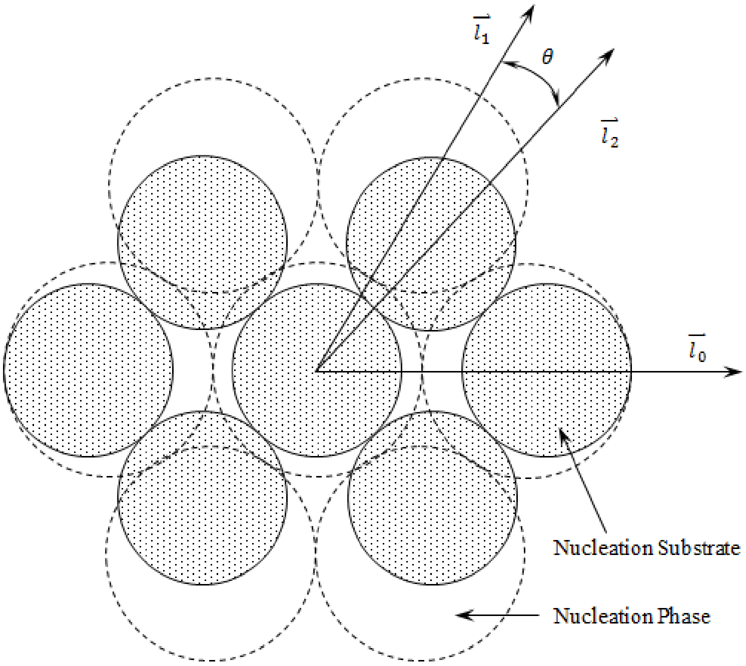

Figure 2.4 The crystallographic illustration at the interface between the (110) of a *b.c.c.* nucleation substrate and the (0001) of a *h.c.p.* nucleation phase [26].

Based on the understanding of Bramfitt, the arithmetic mean of three pairs of different directions from the substrate and the nucleation phase were suggested and the angles between each pair should also be taken into consideration [26, 32].

Further study of an epitaxial nucleation model developed by Fan [33] describes the atomistic mechanisms of heterogeneous nucleation on a potent substrate. The model considered heterogeneous nucleation on a potent substrate takes place by epitaxial growth of a pseudomorphic layer on the surface of the substrate, beyond a critical undercooling [33]. The solid phase is formed by creating misfit dislocations at the PS/N interface, where PS refers to the pseudomorphic solid [33-36], to transform the pseudomorphic layer into the solid phase and the initially coherent PS/N interface to a semicoherent S/N interface [33], as shown in **Figure 2.5**.

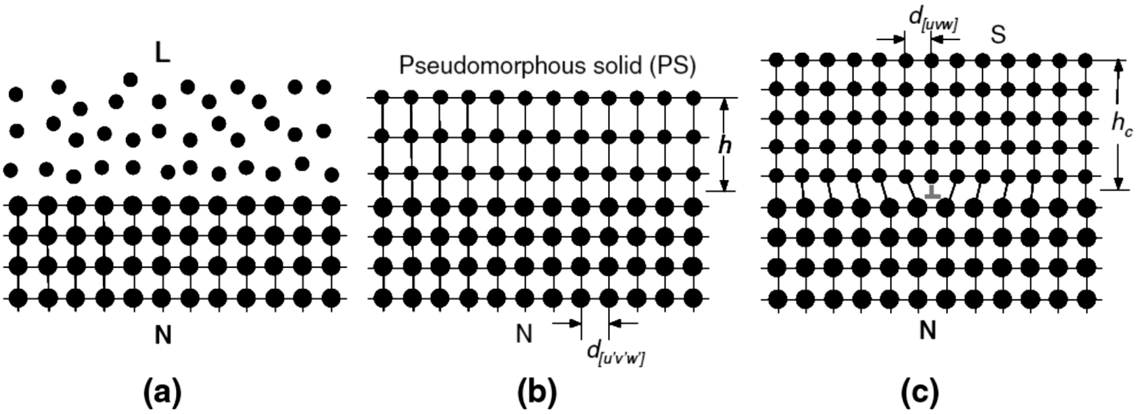

Figure 2.5 Schematic illustration of the epitaxial model for heterogeneous nucleation of a solid phase (S) on a potent nucleating substrate (N) from a liquid phase (L) under $\Delta T > \Delta T_c$: (a) liquid and substrate interface before the growth of the PS layer, (b) the formation of the PS layer, and (c) completion of the epitaxial nucleation at a critical thickness (h_c) by creation of misfit dislocations at the S/N interface to change the PS layer into the solid and to convert the coherent PS/N interface to a semicoherent S/N interface [33].

In all these theories, the lattice misfit has been used to determine the potency of nucleation substrate. Due to the difficulty in achieving wetting angle and interfacial energy by experiment, the lattice misfit is much more applicable. Therefore, the lattice misfit can be used to determine whether a certain type of particle can be the nucleation substrate for an alloy system.

2.1.3. Efficiency of Nucleation Substrates

The efficiency of nucleation substrates is the number density of effective nucleation substrates per unit volume in heterogeneous nucleation, which is the key factor that determines the final grain structure [33, 36]. Therefore, quantitative prediction of nucleation events during solidification of metallic liquids is not a trivial task [37-39]. In CNT, the description of efficiency normally uses the calculation of nucleation rate [21]. However, such calculation has certain shortcomings. The most important shortcoming is that the prediction of number density of viable nuclei in CNT is equal to the number of potential sites [21]. This implies that the number density of grains in the final casting should be identical for all cooling conditions [21]. However, the number density of grains increases significantly at higher cooling rates. Therefore, it is relatively difficult to provide an accurate quantitative prediction of phase nucleation rate in modelling microstructural development during solidification based on CNT [38].

In Turnbull's mercury droplets experiments [40], the size distribution of the nucleant patches has been derived by fitting the data on solidified fraction of undercooled mercury droplets, as it is shown in **Figure 2.6**. Turnbull's study suggested that higher undercooling might potentially increase the nucleation rate during solidification [40]. The study implied that nucleation might not occur simultaneously.

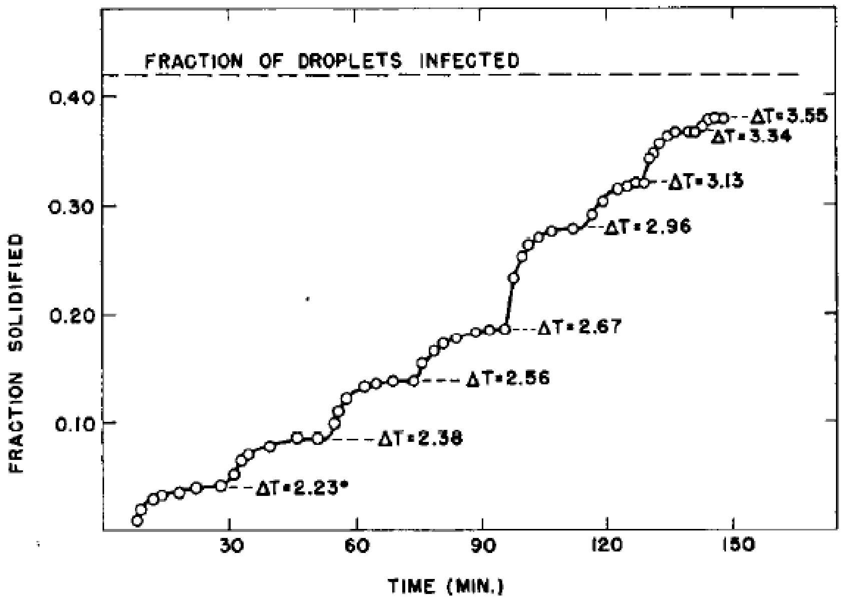

Figure 2.6 Fraction of mercury droplets solidified with increasing supercooling. 42 per cent of the droplets are infected with nucleant patches [40].

Further understanding achieved by Maxwell and Hellawell [41] suggested that the final grain size is the result of competition between heterogeneous nucleation and growth in the melt, in which the nucleation rate will become negligible when the temperature rises due to the latent heat evolved by the growth of the nucleated crystals when recalescence appears, or when the nucleation sites are exhausted. Even though this model only applied single sized nucleation particles, it pointed out the finishing conditions of nucleation as shown in **Figure 2.7**.

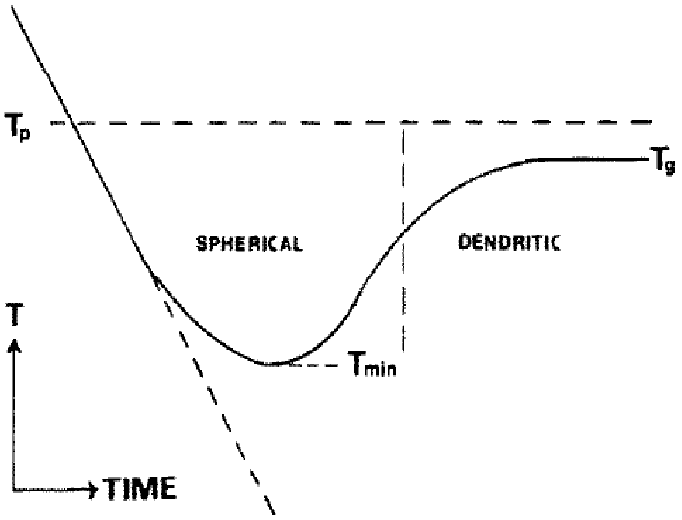

Figure 2.7 Schematic Illustration of cooling curve; the initial slope is the cooling rate, with the equilibrium transformation temperature T_p, the minimum temperature before recalescence T_{min}, and the growth temperature after recalescence T_g [41].

Based on previous understandings, Greer et al. [36, 42, 43] developed a free growth model, which suggested that a new crystalline phase should start free growth with no delay on a given particle at a required undercooling inversely proportional to the diameter of the particle. The main progress achieved by this model is that the grain initiation in this model is not time-dependent and not stochastic, compared to the previous models, and the nucleation substrates are with multiple sizes rather than a single size as described by Maxwell and Hellawell [42]. This model revealed that the largest particles in the melts start to grow first as soon as the required undercooling is reached, followed by the smaller ones as the undercooling is increased [36, 42]. The grain sizes are limited by the recalescence that causes temperature rise, and there will be no further initiation of free growth occurring afterwards. The required undercooling, ΔT_{fg}, for the free growth on a given particle is simply related to the diameter of the substrates. The calculation of undercooling is given by

$$\Delta T_{fg} = \frac{4\Upsilon_{SL}}{d\Delta S_v} \tag{2.10}$$

where Υ_{SL} is the solid-liquid interfacial energy, ΔS_v is the entropy of fusion per unit volume, and d is the diameter of nucleation substrate [42]. In this model, the size distribution of nucleation substrates is important, and has been well fitted by Quested and Greer [36] using a log-normal function,

$$N(d) = \frac{N_0}{\sigma d\sqrt{2\pi}} \exp - \left(\frac{\ln d - \ln d_0}{2\sigma^2}\right)^2 \tag{2.11}$$

where d is the particle diameter, d_0 is the geometric mean diameter, σ is the geometric standard deviation, N_0 is the total number of particles, and $N(d)$ is the number of particles of diameter between d and $d + \Delta d$. The fitted and measured size distribution of nucleant $\mathrm{T_iB_2}$ in the free growth model is shown in **Figure 2.8** [43].

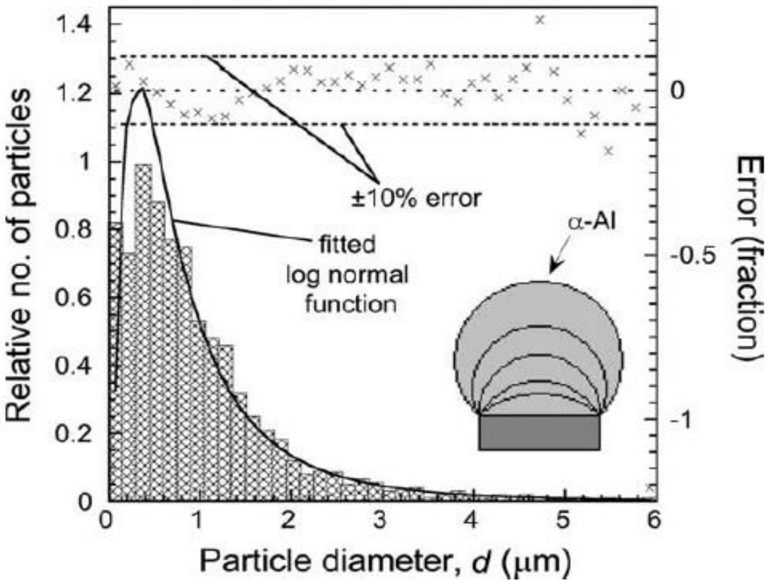

Figure 2.8 Measured size distribution of nucleant TiB2 particles in a commercial Al–5Ti–1B refiner (shaded bars) shown with log-normal fit (solid line). The error in the integrated population of particles greater than a given size (×) is found to be <10% over most of the range [43].

According to Turnbull's study, higher undercooling might potentially increase the nucleation rate. Therefore, the nucleation process might not occur simultaneously. Based on this idea, Maxwell and Hellawell applied the CNT to calculate the number of heterogeneous nucleation events in an isothermal melt with a single particle size [38, 41]. The model suggested that no further heterogeneous nucleation would occur when the temperature rises due to recalescence or when the nucleation substrates are exhausted [38, 41]. Based on their model, Greer et al. developed the free growth model. This model is basically considering grain initiation on potent nucleating substrates [38, 42]. The model suggested that a new crystalline phase could start free growth on the potent particles at an undercooling inversely proportional to the diameter of the nucleating substrate [38, 42]. The difference between the free growth model and the Maxwell-Hellawell model is that the grain initiation in the free growth model is neither time dependent nor stochastic [38, 42]. Also, the free growth model applied a distribution of particle sizes. The most important conclusion from the free growth model is that the largest particles require the smallest undercooling, and start to grow first, followed by smaller particles as the undercooling increases [38, 42]. When the recalescence occurs, no further particles can start to grow freely. Based on this model, the critical diameter of nucleation particles is determined by the maximum undercooling before recalescence occurs. Therefore, the efficiency of nucleation substrates can be achieved using the size distribution of nucleation particles.

In sections 2.1.1, 2.1.2, and 2.1.3, the basic theories of nucleation have been summarized. Applying the present understanding, the basic question for nucleation is what the actual nucleation particles are in a particular alloy system. In order to answer this question, both potency and efficiency of the nucleation substrates need to be examined. In practice, homogeneous nucleation described in CNT is never encountered in solidification [21]. The potency of nucleation substrates for heterogeneous nucleation is explained with interfacial energies and wetting angle in the CNT. However, due to the difficulty in measuring the wetting angle or the interfacial energies, later studies usually applied the lattice misfit to represent the potency of nucleation substrates. Due to the shortcomings in calculation of the nucleation rate, the free growth model is developed to understand the relationship between the size and the efficiency of nucleation substrates.

2.1.4. The Role of Solute in Solidification

Empirically, the segregating power of the solute is critical in determining the final microstructures [18]. When the temperature falls below liquidus, the first thing is nucleation and then growth. The growth is a diffusion controlled process, so the solute distribution during solidification is important to determine the final structure. **Figure 2.9** is a portion of a principle binary alloy phase diagram. As shown, the liquidus line and solidus line of the phase diagram are illustrated, where the composition of the considered alloy is C_0. The volume fraction of solid phase can be expressed as

$$f_s = \frac{C_L - C_0}{C_L - C_S} \tag{2.12}$$

meanwhile, the liquid is solute concentrated with a composition of C_L.

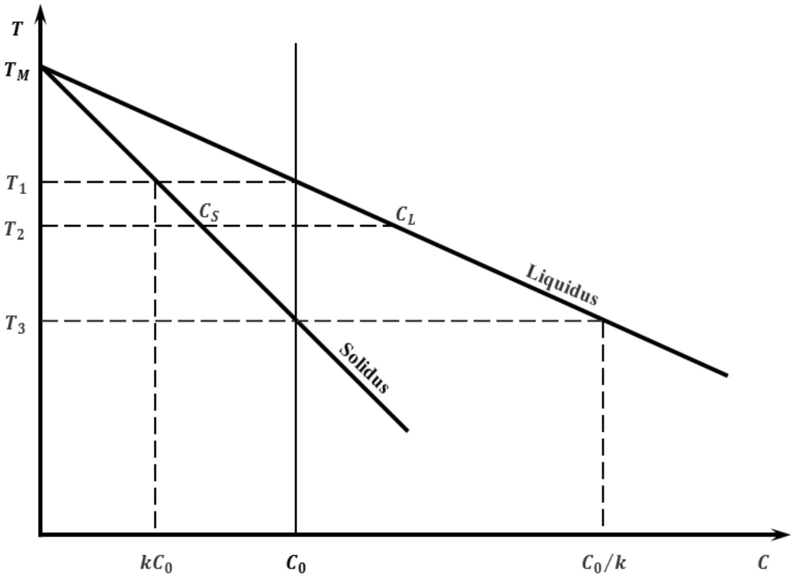

Figure 2.9 Schematic illustration of a portion of hypothetical binary phase diagram.

As the solidification process continues, the interface undercooling at a dendrite tip contains two parts if the thermal undercooling is neglected,

$$\Delta T = \Delta T_c + \Delta T_r \tag{2.13}$$

where ΔT_c is the undercooling caused by solute concentration due to the solute piled up at the growth front, and ΔT_r is the undercooling caused by the curvature of the dendrite tips [44]. The solute rejection at the tip of a dendrite is shown in **Figure 2.10**.

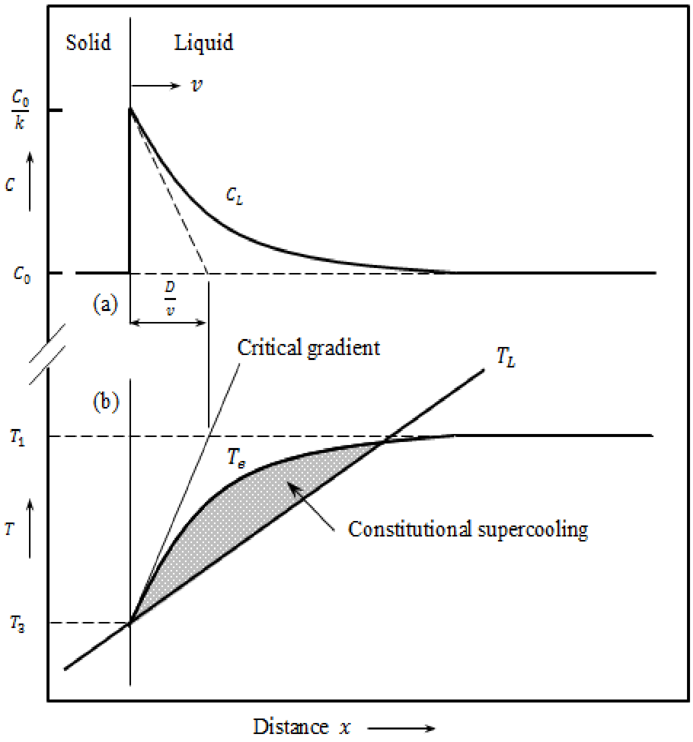

Figure 2.10 Schematic illustration of the origin of constitutional supercooling ahead of a planar solidification front [21].

The profile of concentration for steady-state diffusion in the coordinate system moving with the interface at a velocity v [45,46] is given by the well-known Fick's second law,

$$D\frac{\mathrm{d}^2C}{\mathrm{d}x^2}+v\frac{\mathrm{d}C}{\mathrm{d}x}=0 \tag{2.14}$$

where C is the composition in the liquid, D is the diffusion coefficient, and x is the distance from the interface. The concentration distribution, which is the solution for equation 2.14 [45], is

$$C=C_0+C_0\left(\frac{1}{k}-1\right)\exp\left(-\frac{x}{D/v}\right) \tag{2.15}$$

where C_0 is the bulk concentration of the liquid, and k is the equilibrium solute distribution coefficient. As shown in **Figure 2.10**, the temperature of the liquid ahead of the solidification front follows line T_L, the equilibrium liquidus temperature for the liquid adjacent to the interface varies as T_e, and the constitutional supercooling is the difference between T_L and T_e. It arises when T_L lies under the critical gradient [21].

The constitutional supercooling, in early work [47], is considered as the restriction force of the growth of equiaxed grains. The degree of growth restriction for a particular solute was described by the constitutional-supercooling parameter P given by

$$P = \frac{m(k-1)C_0}{k} \tag{2.16}$$

where m is the slope of the liquidus line, C_0 is the composition of the alloy, and k is the partition coefficient. The P value for a multicomponent alloy can be estimated by the summation of the P values for each element considering no interaction between the elements [48]. Spittle and Sadli [49] found a universal curve relating grain size to P after examining a wide range of solute types and amounts. It appears that the grain size decreases sharply at first as P increases, then levels off at a certain stage [49].

Maxwell and Hellawell [41] considered growth of spherical crystals restricted by the partitioning of a single solute and brought out the growth restriction factor (GRF) Q, which is $1/X$ in their study. Q is often used as a measure of the solute effect on grain refinement during solidification in the absence of solute interactions given by [13, 14, 18, 42],

$$Q = mC_0(k-1) \tag{2.17}$$

Empirically, as the composition of the alloy increases, the grain size will normally decrease with a positive $m(k-1)$. Desnain et al. [50] discovered that for multicomponent alloys, the Q is again the sum of the Q values for the individual solutes. Based on experimental results of aluminium and magnesium binary alloys, Easton and StJohn [52] developed a model which indicated that grain size can be described as a linear function of $1/Q$. The relationship between $1/Q$ and the experimental results of the grain sizes of binary magnesium alloys with Al, Zr, Zn, Ca, and Si is shown in **Figure 2.11** [18]. In Easton and StJohn's model [18, 52, 53], the relationship between grain size, d, and the growth restriction factor Q is described as,

$$d = a + b/Q \tag{2.18}$$

where b is a constant which is related to the potency of the nucleant particles and a is a constant which corresponds to the number of particles that actually nucleate grains at infinite values of Q as shown in **Figure 2.12**. A steeper slope, b, corresponds to a lower potency. The model also suggested that changing the potency or the efficiency of nucleant particles should affect the final grain size by changing the intercept or the slope of the line but should not affect the linearity of relationship between grain sizes and $1/Q$ [53].

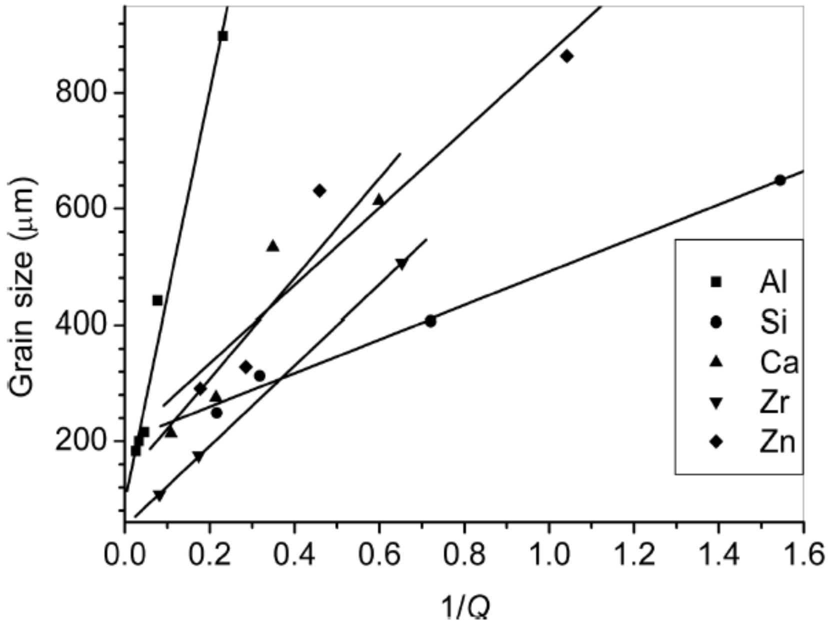

Figure 2.11 The grain size of binary magnesium alloys with Al, Zr, Zn, Ca, and Si plotted against the growth restriction factor 1/Q [18].

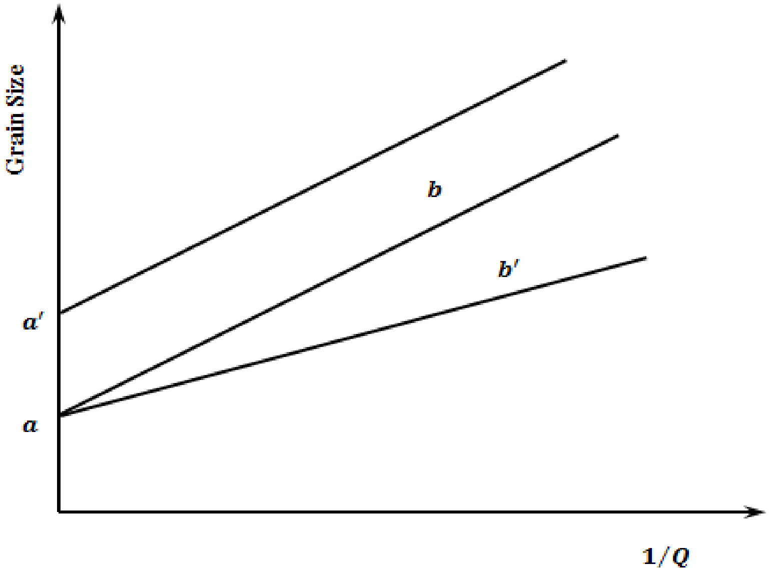

Figure 2.12 Schematic illustration of the relationship between $1/Q$ and grain sizes based on Easton and StJohn's model [18].

As these studies suggested, the growth restriction factor, Q, is often used as a measure of the solute effect on grain refinement during solidification. In the model [18] a linear relationship between $1/Q$ and grain sizes has also been discovered. However, these theories are questionable because the castings with very low alloying elements may contain columnar grains in microstructure and the measurement of the 'grain size' might not actually be the true grain sizes. Therefore, the role of solute will be further examined based on experiments in the present study.

2.1.5. Columnar Equiaxed Transition

In an ingot or casting, two types of growth behaviour can generally be distinguished, which are the equiaxed growth and the columnar growth. As it is known, pure materials usually freeze with a columnar structure. When sufficient amounts of alloying additions are present, equiaxed growth often occurs. The prediction of columnar to equiaxed transition (CET) is of great interest for the evaluation and design of the mechanical properties of solidified products [54]. A number of analytical models for the CET have been proposed over the last half century that have tried to provide analyses on the conditions that govern~~s~~ the transition [54-63].

Tiller's pioneering model [56] considered the unidirectional freezing of a semi-infinite liquid from one end. The model calculated the solute and temperature distributions in the liquid with time assuming that the solid/liquid interface advances at a rate proportional to square time. The assumption of the advancing rate has also been applied in simulation models of Lipton et al. [57], and Fredriksson and Olsson [58]. The pioneering model [56] assumed that nucleation of equiaxed grains occurred in the constitutionally supercooled region ahead of the interface and that this was directly responsible for the CET. The transition from columnar to equiaxed growth was assumed to occur at a critical nucleation frequency corresponding to a critical maximum undercooling value for a particular alloy [54].

Witzke et al. [59] considered the thermal and chemical fields ahead of the tips of dendrites growing as a vertical columnar front ahead of which liquid is flowing under conditions of thermal laminar flow. This model as the previous one, also accounts for the fact that development of the equiaxed zone is favored by low superheat, strong undercooling at the dendrite tips, high values of thermal to chemical diffusivity ratio and mould height [54].

One major progress in this subject has been achieved by Hunt [55], who introduced the blocking mechanism into the picture as it is shown in **Figure 2.13**. In his model, the CET might occur when the volume fraction of equiaxed grains ahead of the columnar primary dendrite tip front exceeds a critical value of 0.49 [55].

Based on such an assumption, he successfully established the relationship between columnar primary dendrite tip growth velocity and the local temperature gradient at the moment when CET occurs [55]. These are described as, for fully equiaxed growth:

$$G < 0.617 {N_0}^{1/3} \left\{ 1 - \frac{(\Delta T_N)^3}{(\Delta T_C)^3} \right\} \Delta T_C \tag{2.19}$$

and for fully columnar growth:

$$G > 0.617(100N_0)^{1/3}\left\{1 - \frac{(\Delta T_N)^3}{(\Delta T_C)^3}\right\}\Delta T_C \tag{2.20}$$

where G is the temperature gradient, N_0 is the number density of nucleation sites, ΔT_N is the undercooling for heterogeneous nucleation, and ΔT_C is the columnar growth front temperature.

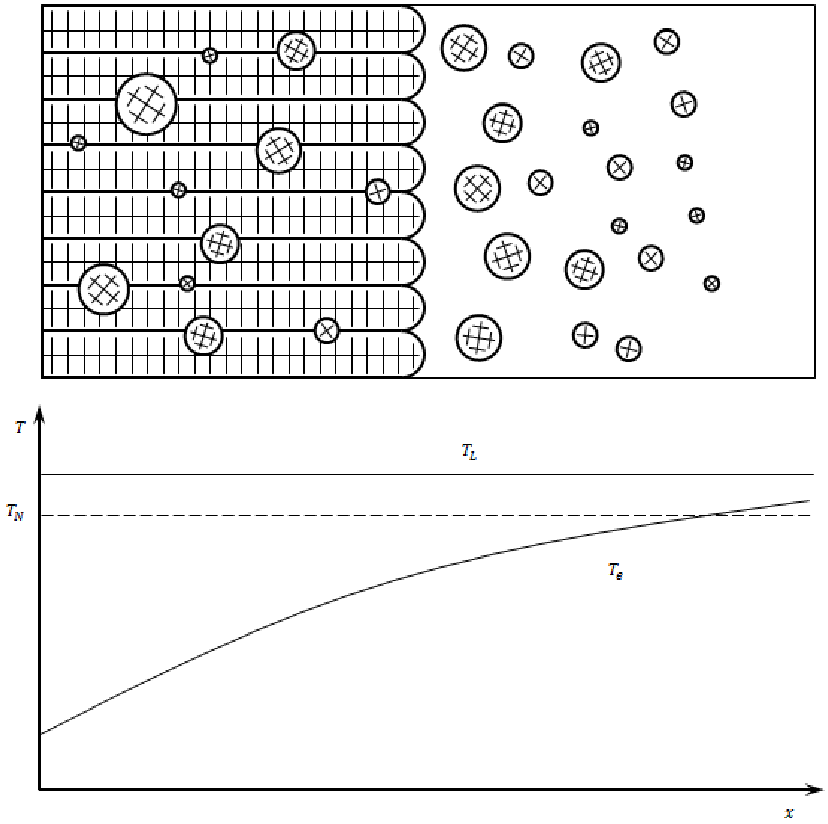

Figure 2.13 Schematic illustration of columnar front with grains nucleating and growing ahead of the front (Top) actual temperature in relation to the liquidus $\mathrm{T_L}$ (Lower) [60].

Figure 2.14 is the plot of the growth velocity against temperature gradient for Al-3wt%Cu showing columnar and equiaxed regions [55]. Equations 2.20 and 2.21 provide the limitation for fully equiaxed growth and fully columnar growth, respectively. The columnar growth front temperature ΔT_c is the tip undercooling for a columnar grain which depends on growth velocity V, temperature gradient *G* and alloy composition, given by,

$$\Delta T = \frac{GD}{V} + A(C_0V)^{1/2} \tag{2.21}$$

with the constant A

$$A = \frac{D}{8m(1-k)\Gamma} \tag{2.22}$$

where D is the liquid diffusion coefficient, m is the liquidus slope, k is the distribution coefficient and Γ is the Gibbs-Thomson parameter. Under the assumption of steady state growth, the growth velocity of the dendrite tip can be given as

$$V = \frac{A\Delta T^2}{C_0} \tag{2.23}$$

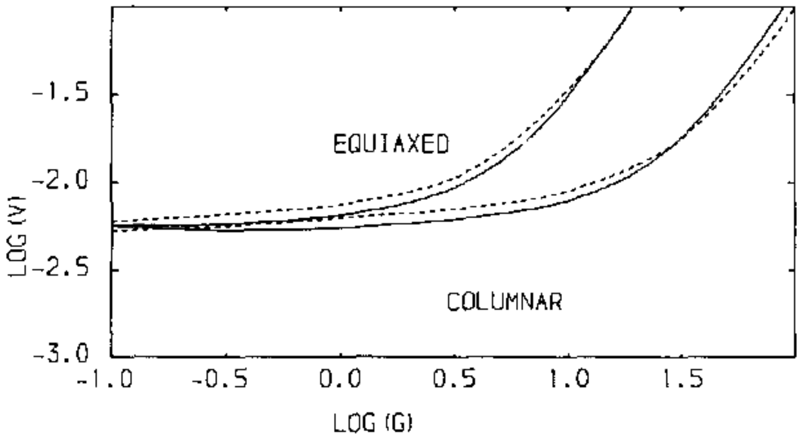

Figure 2.14 Plot of growth velocity against temperature gradient for Al-3wt%Cu showing columnar and equiaxed regions calculated using approximate analysis and more accurate analysis of Hunt's CET model [55].

This CET map was later confirmed and justified experimentally [61, 62] and further improved by including nucleation effects, more precise growth kinetics and by incorporation of a multi-field system taking hard-blocking and soft-blocking mechanisms into account [63- 68]. According to the model, number density of effective nucleation particles, nucleation undercooling, and the composition of the alloy system are the major factors to determine the CET map. In this study, the map will be used to examine the role of solute in magnesium alloy, and the blocking mechanism will be used to develop a model for equiaxed solidification.

2.1.6. Modelling for Nucleation and Equiaxed Grain Growth

There has been a long history and a number of modelling in studying nucleation and equiaxed grain growth. A recent modelling by Hunt and Fan [60] suggested that casting conditions such as pouring temperature and mould temperature have an extremely large influence on the final grain size. In their model, once the melt is poured into a mould, the strong convection of the melt heats up the mould and reaches a critical heat balance temperature with the mould. The critical heat balance temperature may potentially result in two different conditions, either it is higher than the liquidus temperature of the melt, or it is slightly lower than the liquidus. For the situation when critical heat balance temperature is above liquidus, the heat will be absorbed by the mould and released to the environment continuously and form a temperature gradient which eventually causes nucleation to take place gradually and continuously from edge to centre. For the later situation when critical heat balance temperature drops below liquidus, nucleation in the melt takes place simultaneously since the melt is nearly isothermal [60].

According to this model, the pouring temperature, the mould temperature, and the casting procedure are considerably important. When the melt is cast rapidly with high pouring temperature and high mould temperature, the critical heat balance temperature of the melt caused by the strong convection should be above liquidus. When the melt is cast rapidly with low pouring temperature and/or low mould temperature, the critical heat balance temperature of the melt should be lower than liquidus. The critical heat balance temperature caused by the strong convection in the melt is considered as a quench effect [60]. When the melt is poured into the mould slowly, there will be no quench effect since the low convection will not heat up the melt rapidly. Based on such understanding, there should be a critical relationship between the pouring temperature and mould temperature which makes the critical heat balance temperature equal to liquidus. This model may explain the mechanism of the effect of mould and pouring temperature on the final grain structure, however, no experimental evidence has been reported yet to support the model and the present study shall provide verification with a series of experiments.

2.2. Solidification Behaviour in Magnesium Alloys

In this section, firstly the magnesium and magnesium alloys will be reviewed, including the basic physical parameter of magnesium and magnesium alloys, processing of magnesium alloys, and applications of magnesium alloys. In section 2.2.2 and 2.2.3, previous research studies on nucleation and grain refinement in magnesium alloys will be reviewed. Finally, new technology innovations in magnesium alloy casting will be discussed in section 2.2.4.

2.2.1. Magnesium and Magnesium Alloys Castings

2.2.1.1. Magnesium and Magnesium Alloys

Magnesium is a light-weight metal with a density around two thirds of aluminium, and a quarter of iron. It has a hexagonal close-packed (*h.c.p.*) crystal structure as shown in **Figure 2.15**. This structure is essentially different from most commercial metals.

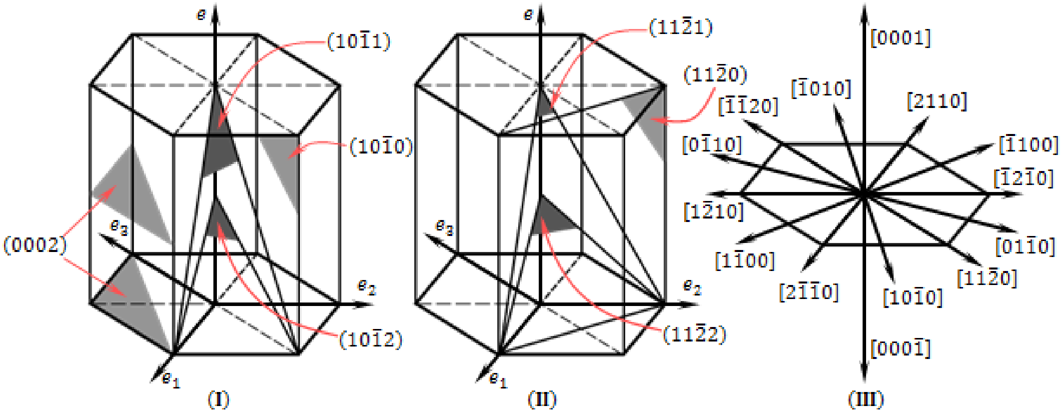

Figure 2.15 Principle planes and directions in the magnesium hexagonal unit cell [6].

The lattice parameters of magnesium are $a = 0.3203\ \text{nm}$ and $c = 0.5211\ \text{nm}$ at 25 ℃ [69], and $a = 0.3266\ \text{nm}$ and $c = 0.5307\ \text{nm}$ at 597 ℃ [70]. In order to study the nucleation and growth of magnesium during typical casting procedures, the latter parameters are preferable since they take thermal expansion into account. Solute concentration can also affect lattice parameters of magnesium [71]. As shown in **Figure 2.16**, the lattice parameter a of magnesium varies as the atom percentage of solute increases. Therefore, the actual lattice parameters of magnesium close to the melting temperature need to be justified by both thermal expansion and solute concentration [71].

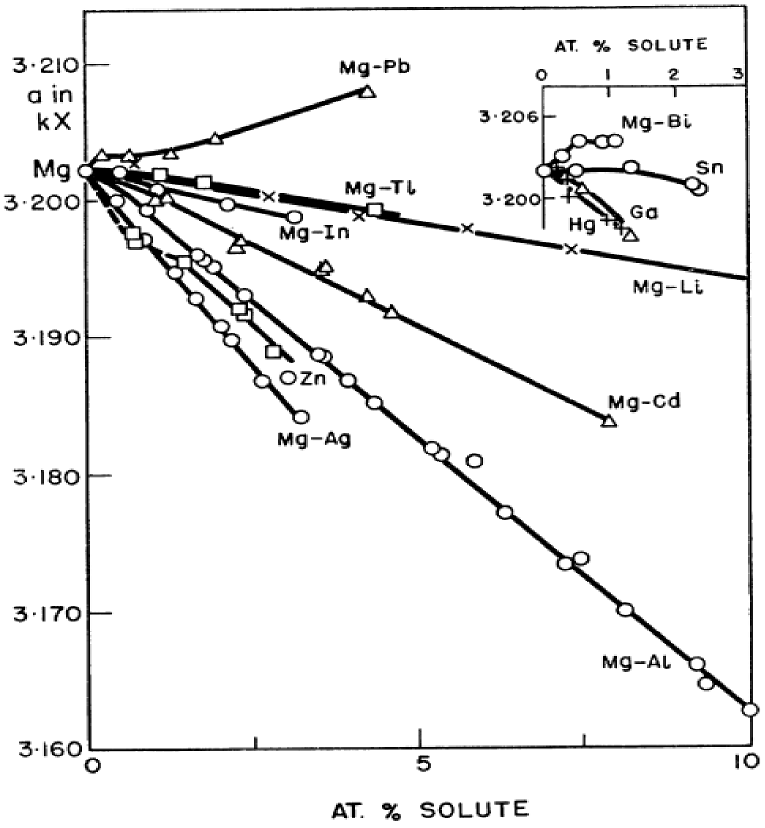

Figure 2.16 Lattice parameter a of magnesium $(1\,\mathrm{kX} = 1.00202\,\text{Å} = 0.100202\,\mathrm{nm})$ as a function of solute concentration (AT. %) [71].

In industrial practice and engineering applications, magnesium is usually alloyed with other metals to improve the alloy properties [72]. The major factors that govern the extensive solid solutions are types of crystal structures, equivalent valencies, and electrochemical factors. Several important elements such as Al, Zn, Mn, Y, etc. have relatively high solid solubility in magnesium and the solubility always decreases with increasing temperature [73].

Until now, the most commonly used magnesium alloys can be classified into several systems, such as Mg-Al system, Mg-Mn system, Mg-Zn system, Mg-RE system (rare earth), and Mg-Th system [6]. The first alloying elements to be used commercially were aluminium, zinc, and manganese and the Mg-Al-Zn system is still the one most widely used for castings [6]. Most alloys in AZ series of Mg-Al system contain 3~9wt% aluminium with small amount of zinc, which gives some increase in tensile properties, and manganese, which improves corrosion resistance [2]. The AM series of Mg-alloys with reduced aluminium content have improved mechanical properties due to the reduction of the amount of $Mg_{17}A1_{12}$ compound around grain boundaries [74]. In present study, the major alloys used in experiments are Mg-Al binary alloy, Mg-Zn binary alloys, AZ31 commercial alloy, and AZ91D commercial alloy, and the phase diagrams for Mg-Al binary system, Mg-Zn binary system, and Mg-Al-Zn ternary system are shown in **Figure 2.17**, **2.18**, **2.19**, respectively.

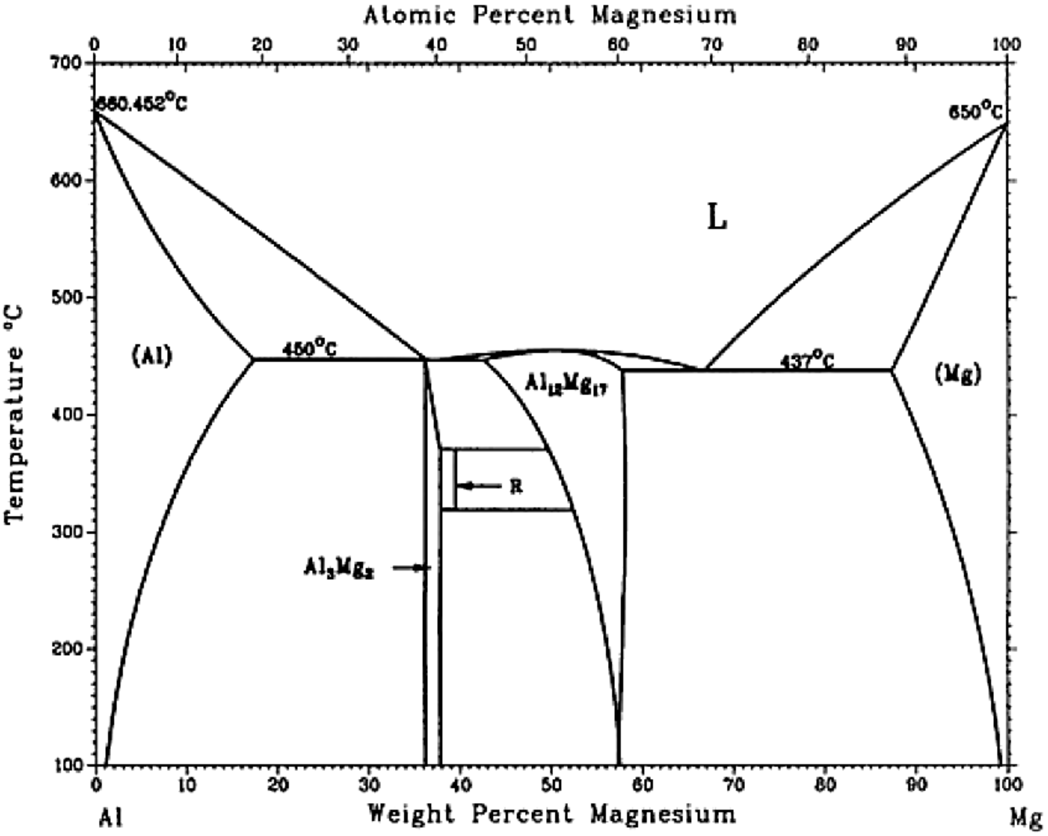

Figure 2.17 Mg-Al Phase Diagram [75].

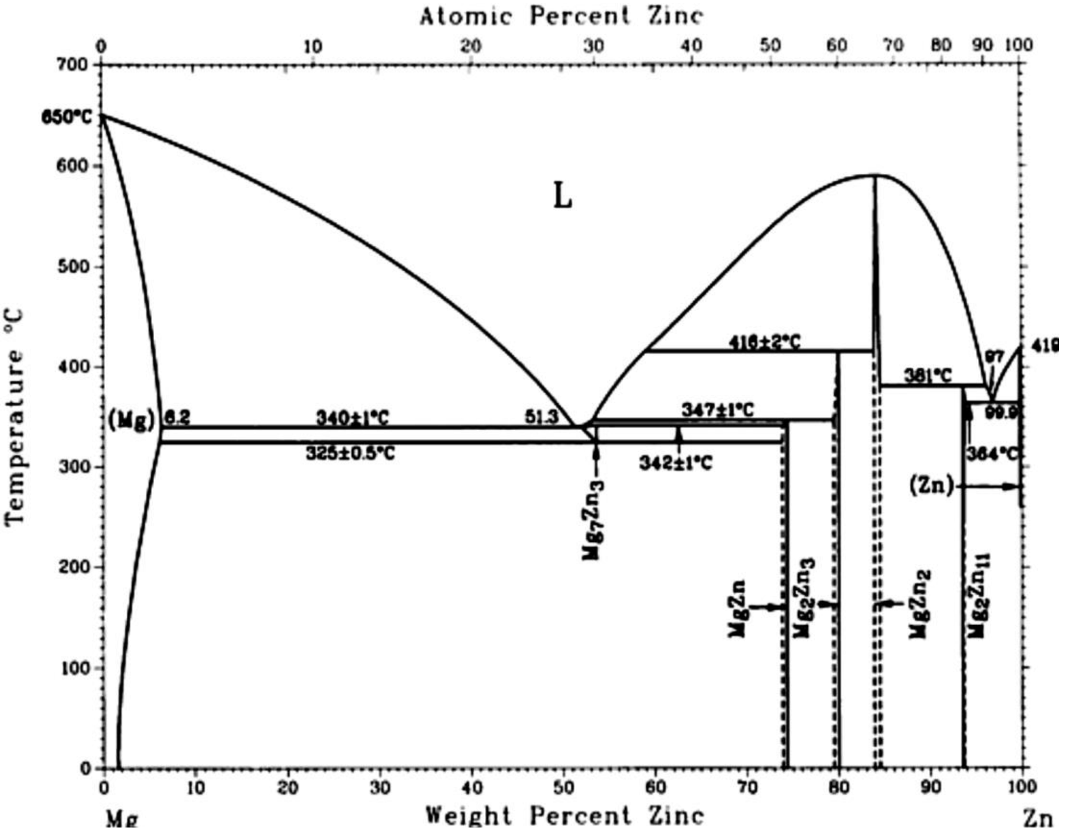

Figure 2.18 Mg-Zn Phase Diagram [75].

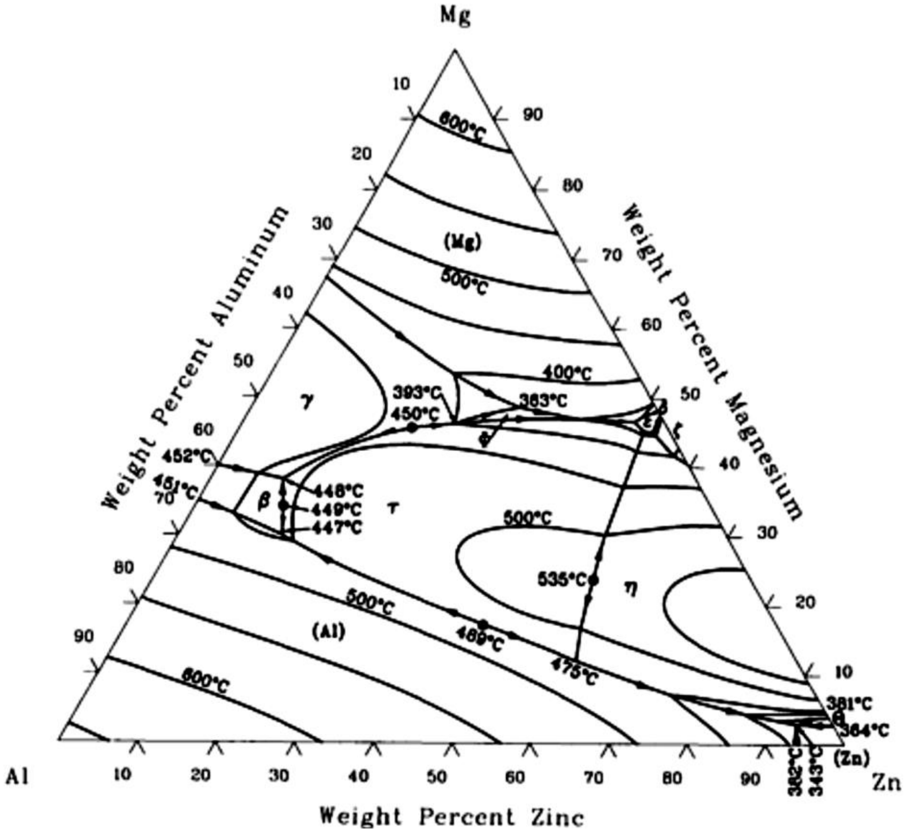

Figure 2.19 Mg-Al-Zn Liquidus Projection [76].

2.2.1.2. Processing of Magnesium Alloys

Melt processing of magnesium alloys

Magnesium alloys are used to produce light-weight structural components due to the lowest density among metallic materials in practical application. However, the widespread usage is limited due to poor oxidation resistance [77-79]. When molten magnesium alloys are exposed to air, the oxide layers formed on the surface of the melt will provide a certain level of protection. However, unlike aluminium and aluminium alloys, magnesium alloys usually suffer from severe oxidation or even burning. There are several reasons for the low oxidation resistance. First of all, the MgO scales cannot cover the whole surface due to its Pilling-Bedworth ratio (P-B ratio) as 0.81 [77, 80]. For any metals with P-B ratio less than 1, the oxide coating layers will be too thin so that they will likely be broken and provide no protective effect to the melt [80]. Secondly, the vapor pressure of magnesium keeps increasing as the temperature increases [78]. Thirdly, the oxidation of magnesium is an exothermic reaction [78, 79] Therefore, heat will be released during the oxidation process causing further oxidation.

Due to the nature of the oxidation during melt processing of magnesium alloys, suitable fluxes or atmospheres must be applied [2]. Suitable fluxes mostly applied in magnesium processing usually contain $MgCl_2$, KCl, $BaC1_2$, CaF_2 and MgO [2, 77-81], which might potentially decrease the corrosion resistance of the magnesium alloys because of the retention of the flux [2]. Therefore, the fluxless method is proved to be more acceptable [2]. The fluxless method usually comprises of either a single gas or a mixture of a diluting gas and an active gas. SO_2 or Ar can be used as protection gas during melt processing of magnesium alloys [2]. SF_6 mixed with CO_2, N_2 or air has also been applied in order to protect the magnesium alloy melt and has been found as the most efficient protection method [82]. However, there are certain limitations for these options either due to health and safety issues or because of environmental issues [2]. For example, SF_6 can potentially harm the environment. Therefore, several attempts have been reported to replace the use of SF_6 [83-85].

Casting of magnesium alloys

Magnesium alloy products can be produced by nearly all the conventional casting methods that have been applied in steel casting and aluminium casting [2]. These methods contain but not limited to sand casting, permanent mould casting, twin-roll casting, direct chill casting, and high pressure and low pressure die-casting [2]. The key factors that determine which casting method should be selected are the application, the properties required, the total number of castings, and the cost [86-88].

Sand casting is one of the most versatile processes, providing tremendous freedom of design in terms of size, shape, and product quality [89]. Magnesium alloy sand castings generally weigh from a few grams up to as much as 1400kg [88-89] and are used in aerospace applications considering their weight advantage over other materials [86]. Although the magnesium alloy sand casting is generally easy to practice, it is limited in certain respects [88]. The sand casting components do not provide high complexity and it is not capable of producing castings that satisfy the level of dimensional accuracy [90].

The most commonly used technology for magnesium alloy casting is high pressure die-casting (HPDC) due to the economic benefit and high productivity [91].The weight of HPDC products can vary from a few grams to more than 15kg [92]. The mould of HPDC is clamped together by hydraulic force, and during the processing of die-casting, is filled rapidly (mostly 5 to 100m/s) by forcing the molten metal through a narrow gate [72]. The melt solidifies under high-pressure with a relatively high cooling rate (mostly 100 to 1000 ℃/s) [72]. Therefore, the HPDC products usually result in fine structural materials. The HPDC process has two different types, which are cold chamber HPDC (**Figure 2.20a**) and hot chamber HPDC (**Figure 2.20b**) [6]. In hot-chamber machines, the supplying container is immersed in the metal melt. During the procedure, the piston forced the melt into the die. Therefore, the metal chamber is heated at a certain temperature. In cold-chamber machines, neither the metal chamber nor the plunger is heated. Normally, the cold-chamber machines are used to make large castings because of the higher injection pressure and faster piston movement [92].

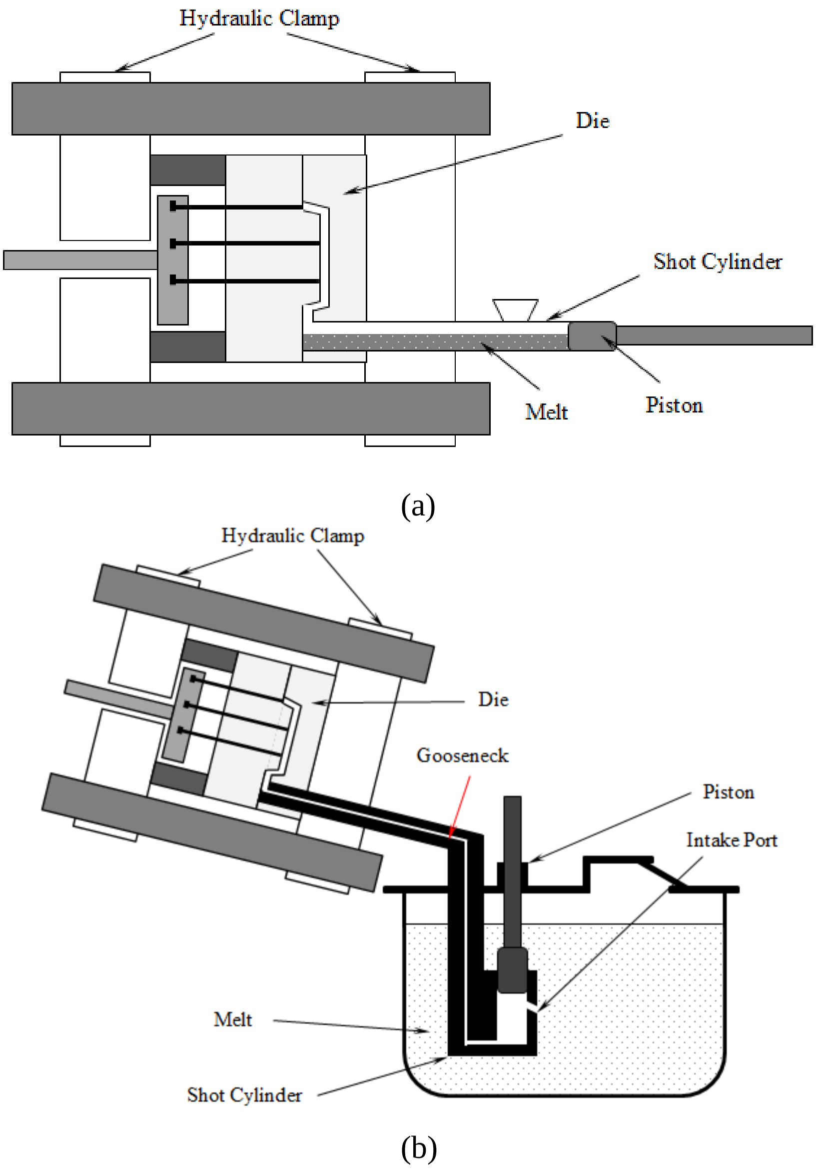

Figure 2.20 Schematic illustrations of cold chamber HPDC (a), and hot chamber HPDC (b) machines [6].

Direct chill (DC) casting of billets, shown schematically in **Figure 2.21** [93], is the main process to produce primary materials for nonferrous magnesium wrought products as well as the remelt stock for magnesium cast products [94-97]. During DC casting, the liquid metal is initially poured onto a dummy block located inside a water cooled mould [93]. Once the metal reaches a predetermined height inside the mould, the dummy block is lowered into a pit at a controlled speed. When the dummy block is lower than the mould, cooling water is sprayed on the cast surface. Steady-state casting conditions are then achieved considering the sump profile ceases to evolve with time relatively [96, 97]. The sump profile includes liquid metal, solidified billet, and the mushy zone in between. The casting process stops when the desired cast length is obtained or the bottom of the pit is reached [96, 97]. This process is similar to the DC casting process used to produce aluminum alloys [93]. Although magnesium alloy DC casting has been used in industrial practice for approximately 50 years [94-97], solidification defects, hot tearing, cold cracks and dimensional control remain as serious issues [98].

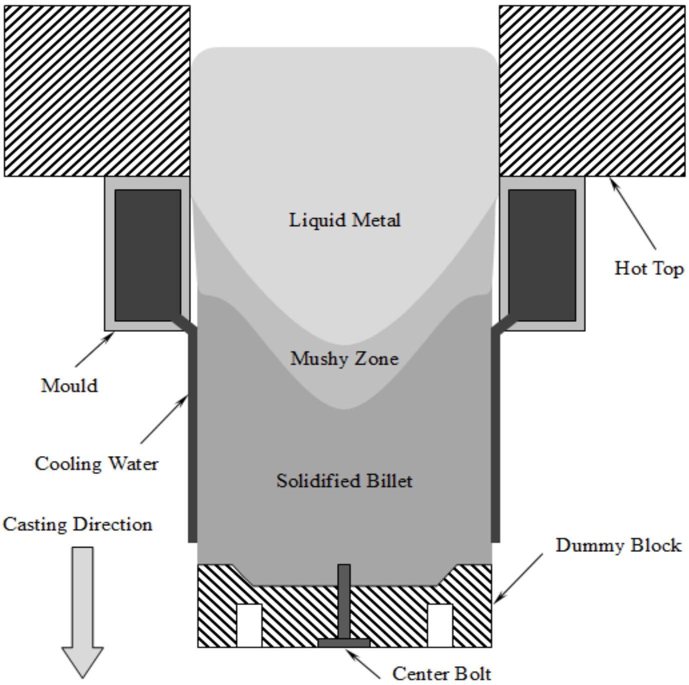

Figure 2.21 Schematic DC casting process used for magnesium billet casting [93].

2.2.1.3. Applications of Magnesium Alloys

The renewed interest in magnesium and magnesium alloys has been triggered by the requirement to reduce the weight of vehicle components since the slump of the military application back in World War II [99]. In 1998, the consumption of magnesium reached 360,000 ton, and the growth rate reached 7% per annum [2]. Currently, magnesium alloys have been used in the European automobile industry encompassing parts such as steering wheels, steering column parts, instrument panels, seats, gear boxes, air intake systems, stretcher, gearbox housings, tank covers, etc. [99]. The main driving force of magnesium alloy applications can be summarized in four aspects, the environment and fuel economy, the cost of materials, mechanical properties, and the advanced technological research and development.

Due to the increasing concern of environment conservation issues, particularly CO_2 emissions, vehicle weight and fuel economy are becoming extremely important in the automobile industry [100]. Global trends force the automotive industry to manufacture lighter, more environmentally friendly cars [101]. The relationship between automotive weight and the fuel economy can be seen in **Figure 2.22** [102]. Weight reduction of 100 kilograms represents a fuel saving of about 0.5 liters per 100 kg for a vehicle [103]. It has been estimated that each 10% saving in the weight of a motor vehicle corresponds to an increase in fuel economy of 5.5% [103].

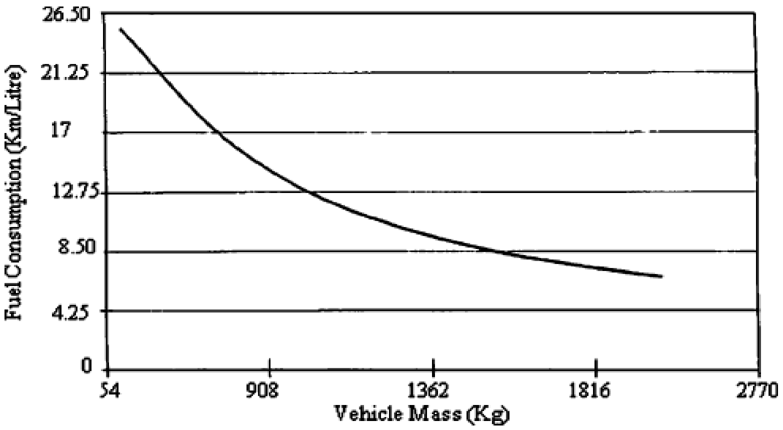

Figure 2.22 The relation between vehicle mass and fuel consumption [102].

Weight reduction not only saves energy, but reduces greenhouse gas emissions as well. It is the most cost effective option for significantly decreasing fuel consumption and CO_2 emissions [104]. The European and North American car producers committed themselves to reduce fuel consumption by 25% and thereby to achieve 30% CO_2 emissions reduction by the year 2010 [104]. In 2007, the European Union adopted a strategy to reduce carbon dioxide emissions from new cars and vans sold in the European Union [105]. The strategy would enable the EU to reach its long-established objective of limiting average CO_2 emissions from new cars to 140 g/km by 2012 and 120 g/km by 2014, which means a 25% reduction from current levels ensuring the EU meets its greenhouse gas emission targets under the Kyoto Protocol [106]. All these examples show that the ecological and economic requirements of vehicles have to be met by components and, consequently lightweight design is always a significant requirement.

The cost of magnesium is another reason for the increasing interest. In recent years, the price of magnesium has been decreasing. The current prices for magnesium and aluminium are \$1.25/LB and \$0.80/LB respectively [107]. Therefore, the Mg/Al price ratio is 1.56/1. In the automotive industry it is estimated that if the price ratio between magnesium and aluminium is less than 1.7/1, then magnesium components will replace the aluminium ones on a one-to-one basis [6]. If the ratio falls below 1.4/1, then magnesium usage will increase exponentially [6].

As the lightest of all structural metals, magnesium has superior strength/weight ratios, low inertia, and low density [2-6]. As it is known, it also has excellent electromagnetic shielding and damping capabilities, good castability, and recycling ability, which make magnesium a very attractive structural material compared with not only metal alloys, but also plastics and composites [2-6]. Therefore, mechanical properties can be another reason for the increasing interest in magnesium.

Finally, advanced technological research and development in magnesium alloys also have encouraged the growth of the magnesium industry in China, Israel, Canada and Australia [108]. The constructional uses of Mg-alloys are successfully practiced in a wide variety of applications with the advanced technological development [109].

2.2.2. Nucleation Substrates in Magnesium Alloys

In order to understand the solidification behaviour in magnesium alloys, the first step is to figure out what the nucleation substrates are in the alloys. For aluminium free magnesium alloys, zirconium is usually added in order to provide nucleation substrates. The melting point of zirconium is 1855 ℃, and below 865 ℃, β-Zr will transit to α-Zr [71], which has a hexagonal close-packed (*h.c.p.*) crystal structure with lattice parameters of $a = 0.3213\mathrm{nm}$ and $c = 0.5148\mathrm{nm}$ [71]. For general magnesium alloy casting, the melting temperature is usually below 750 ℃. Therefore, α-Zr particles in aluminium free magnesium alloys can be acted as potential nucleation substrates during solidification. The calculated misfit between α-Mg and α-Zr for $< 11\bar{2}0 > \{0001\}_{\alpha-\mathrm{Mg}}$ and $< 11\bar{2}0 > \{0001\}_{\alpha-\mathrm{Zr}}$ is about 0.35%, and that for $< 0001 > \{10\bar{1}0\}_{\alpha-\mathrm{Mg}}$ and $< 0001 > \{10\bar{1}0\}_{\alpha-\mathrm{Zr}}$ is about 0.98%. Both calculations suggest that the interfacial energy for α-Mg / α-Zr interface is relatively small. Therefore the energy barrier for magnesium to nucleate on zirconium particles is small, and zirconium can act as an effective nucleation substrate for aluminium free magnesium alloys, such as ZE41, ZK60, WE43, AM-SC1, and ML10 [11, 13, 18]. For aluminium bearing magnesium alloys, such as AM50, AM60, AZ31, and AZ91, adding zirconium into the alloy will cause a reaction between zirconium and aluminium and the formation of Al_3Zr, which has a much larger misfit against α-Mg [18]. Some research studies suggest that Al_8Mn_5 can act as the nucleation substrates for magnesium alloys. However, there has been considerable debate as to whether Al_8Mn_5 particles can act as potent nucleation sites for α-Mg during the solidification of aluminium bearing magnesium alloys.

In the studies of Tamura et al. [110], Al-Mn-(Fe) particles were reported to be frequently observed in molten AZ91E magnesium alloy by rapid solidification. Therefore, they suggested that these Al-Mn-(Fe) particles observed could act as the potential nucleation substrates for an α-Mg phase. Similar conclusion has also been drawn by Byun et al. [111] during their investigations of the slurry formation process of AZ91 alloy containing different Mn concentrations ranging from 0.23wt% to 0.45wt%. They observed $Al_8(Mn, Fe)_5$ particles in the centre of the α-Mg grains and thus believed that these $Al_8(Mn, Fe)_5$ particles acted as effective nucleation sites during solidification. Further research on this issue was carried on by Kim et al. [112], who studied the effect of carbon addition on the grain refinement of AZ91D alloy. In their studies, they suggested that $Al_8(Mn, Fe)_5$ served as nucleation sites for α-Mg through a duplex nucleation mechanism, in which aluminium carbides enhance the nucleation of $Al_8(Mn, Fe)_5$ particles, and $Al_8(Mn, Fe)_5$ particles in turn promote nucleation of the α-Mg phase. However, the research studies of Cao et al. [113] suggest otherwise. In their experiment, they added an Al-60wt%Mn master alloy (containing mainly Al_8Mn_5) into the AZ31 molten alloy and the grain size of as-cast ingots decreased for a short holding time, but increased for a long holding time. Therefore, they suggested that the high-temperature ε-AlMn phase, rather than Al_8Mn_5, was the effective grain refiner. Further studies on the crystallographic match between the rhombohedral Al_8Mn_5 phase and the α-Mg has been carried out by Zhang et al. [114] using the edge-to-edge matching technique. Their results indicated a poor crystallographic match between the two crystalline phases. Fan et. al. [115] studied the Al_8Mn_5 / α-Mg interface using HRTEM, and failed to find any well-defined OR between these two phases. Their work concluded that it is very unlikely that Al_8Mn_5 particles can act as potent nucleation sites for the α-Mg phase during solidification of aluminium bearing magnesium alloys.

MgO particles have also been studied as the potential nucleation substrates. Kooi et al. [116] studied the MgO/α-Mg interface in oxidized Mg nano-particles prepared by gas-phase synthesis. In their studies, potential orientation relationships between MgO/α-Mg were suggested although there is a lack of convincing experimental evidence. According to research studies of Fan et. al. [115], MgO is suggested as the nucleation substrates for α-Mg because they found that increasing the number density of individual MgO particles could refine grain structures of AZ91 alloy. In their experiment, large MgO films have been dispersed into small individual MgO particles (usually 200 nm~1 μm) by applying a twin-screw unit. Shown in **Figure 2.23** [115] is SEM micrograph showing that the old oxide film aggregates collected at 650 ℃ from the intensively sheared AZ91D alloy melt by the pressurised filtration. Their result from HRTEM is shown in **Figure 2.24** [115], indicating that there is fine orientation relationship between the α-Mg and MgO phases along the closely packed directions $< 1\bar{2}10 > \{0001\}_{\alpha-\mathrm{Mg}}$ and $< 01\bar{1} > \{111\}_{\mathrm{MgO}}$, and the misfit between them is only 5.46% [115]. Therefore, they believed that MgO particles could act as effective nucleation substrates in aluminium bearing magnesium alloys.

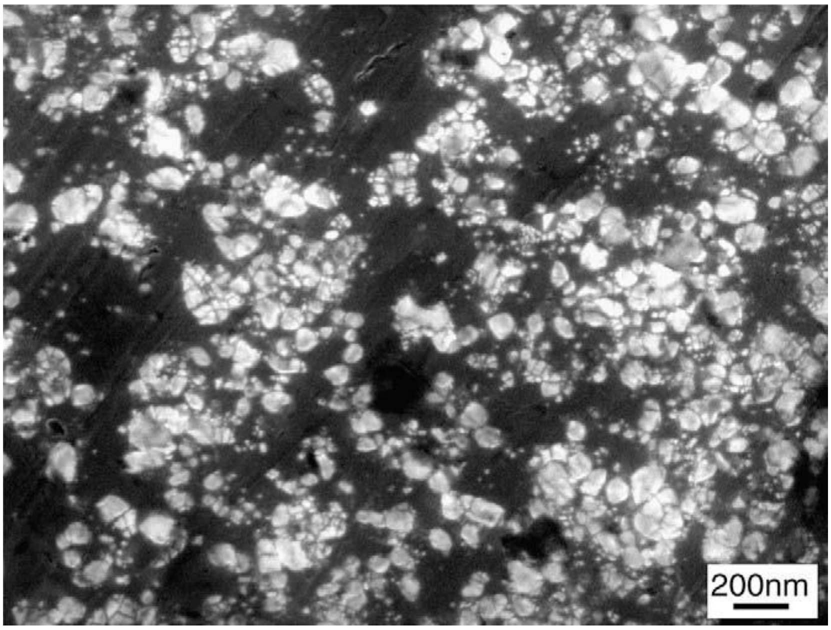

Figure 2.23 SEM micrograph showing that the MgO oxide aggregates collected at 650 ℃ from the intensively sheared AZ91D alloy melt by the pressurised filtration. The alloy melt was sheared at 650 ℃ and 800 rpm for 45 s before filtration [115].

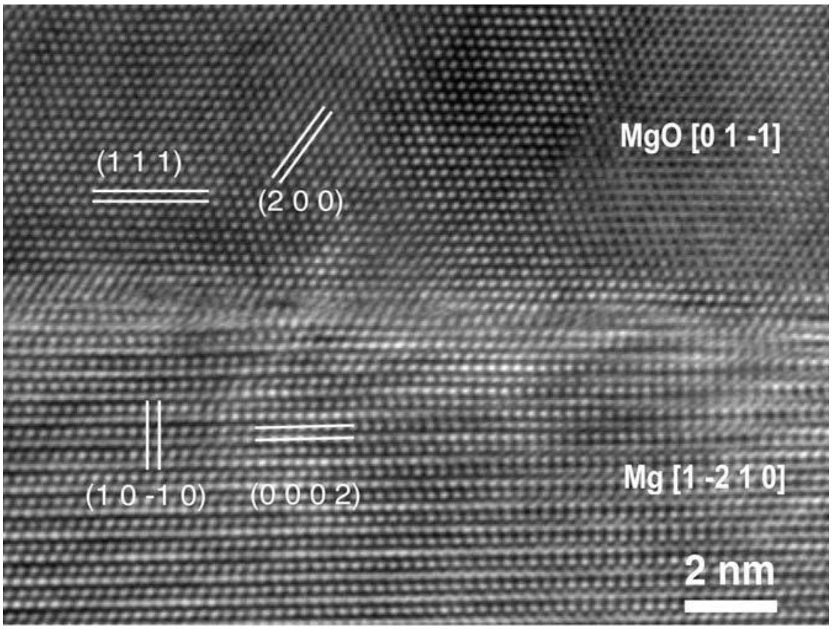

Figure 2.24 High-resolution TEM micrograph of the interface between MgO and a-Mg matrix, where the α-Mg matrix (bottom part) is viewed along $[1\bar{2}10]$ direction and the MgO (top part) is along $[01\bar{1}]$ direction [115].

2.2.3. Grain Refinement Technologies for Magnesium Alloys

In order to achieve better microstructures in the final casting of magnesium alloys, inoculants are usually added as the nucleation substrates in the alloys. Grain refinement technologies for magnesium alloys, based upon whether they are alloyed with aluminium, can be generally classified into two major groups, aluminium free and aluminium bearing. Zirconium is a very effective grain refiner for magnesium alloys that contain no or little aluminium, manganese, silicon, and iron [18, 117]. These elements can form stable compounds with zirconium and potentially decrease the effect of grain refinement of zirconium on magnesium alloys. When zirconium is added in aluminium free magnesium alloys, it can not only reduce the average grain size of the alloys from several millimeters to about 50μm at normal cooling rate [18], but also lead to formation of nodular grains, which enhance the structural uniformity of the final alloy [117]. This ability leads to further development of several commercial magnesium alloys, such as ZE41, ZK60, WE43, AM-SC1, and ML10. Therefore, zirconium can be an acceptable grain refiner for aluminium free magnesium alloys. However, the price of zirconium is relatively high, and the increased cost of grain refinement might also increase the cost of applications of these alloys in related industries, and a replacement of zirconium with a much cheaper refiner is desirable. For aluminium bearing magnesium alloys, no universal grain refinement technology has been found until now [18]. However, there are several methods that can reduce the grain size of these alloys. These methods include superheating, carbon inoculation, the Elfinal process, native grain refinement by control of impurity level, and other additives [18].

Although most of the metals and alloys should not be heated far above their liquidus due to oxidation, gas absorption, and grain coarsening [118], aluminium bearing magnesium alloys is an exception, because they can be grain refined by superheating treatment [18]. These alloys show finer grain structure and smaller grain size when they are heated up to between 180 ℃ to 300 ℃ above their liquidus, held for a short time, then rapidly cooled to, and shortly held at their pouring temperatures [18]. This treatment was first found and described back to 1931 in a British granted patent [119], however, due to certain limitations, it hasn’t been widely used in commercial practice. Since the rapid cooling procedure is relatively hard to achieve, this method is almost impossible for large castings [118]. Also, the life of the mould for the alloys during this practice will be greatly shortened [18].

Another approach for the grain refinement of aluminium bearing magnesium alloys is carbon inoculation [18], which basically introduces carbon into molten alloys by adding carbonic compounds or carbonaceous gases. These compounds or gases include, but are not limited to, graphite, paraffin wax, lampblack, organic compounds such as hexachloroethane (C_2Cl_6) and hexachlorobenzene (C_6Cl_6), carbides such as Al_4C_3, SiC, CaC_2, and gases such as CO, CO_2, CH_4 [12, 18]. The grain refinement achieved by this method is comparable to that achieved by superheating [18]. Therefore, it has been considered as an effective approach for the grain refinement of aluminium bearing magnesium alloys. That said, there are certain limitations for this approach. Some carbonic compounds or carbonaceous gases used in the process causes environmental problems or can be potentially interfered with elements, such as Be, Zr, Ti, and rare earth elements (RE), that are contained in the alloys [12, 18]. Also the amount of carbon added in the melt could potentially harm the purity of the alloys and cause further problems [18].

The Elfinal process was invented in 1942 by Farbenindustrie based on the idea that iron particles could act as nucleation sites for magnesium grains [18, 120]. The patent claimed that Mg-Al-Zn alloys (Al: 4~8.5wt%, Zn: 0.5~3wt%) could be grain refined by additions of 0.4~1.0wt% of anhydrous $FeCl_3$ at temperatures between 740 ℃ to 780 ℃ [18, 120]. The microstructure of the sample that implemented this approach shows significant grain refinement [18, 120], although the mechanism proposed by the patent is debatable according to other metallurgists [12]. Some researchers believed that the hydrolysis of $FeCl_3$ added in the melt increase the amount of hydrogen chloride (HCl) fumes, which attack steel crucibles and liberate carbon into the melt [12]. Some other researchers believed that Al-Fe-Mn phase formed in the melt by adding $FeCl_3$ acted as nucleation substrates for the alloys [12, 18]. Although the Elfinal process leads to fine grain structures of the aluminium bearing magnesium alloys, there are certain limitations. First of all, some elements, such as Zr and Be, could potentially inhibit the effect of grain refinement because they can remove iron from the melt [12, 18]. Secondly, iron, as it is well-known, harms the corrosion resistance of magnesium alloys, which means the process is sacrificing the life and some mechanical properties of the alloys [12, 18]. Finally, the release of Cl_2 or HCl can potentially cause environmental problems.

Nelson [121] examined the grain structures of high purity level Mg-Al alloys and discovered that they have native fine grain structures. Studies by Tamura et al. [122, 123] also claimed that the purity level of aluminium bearing magnesium alloys could influence the microstructure. In their experiments, the high purity Mg-9wt%Al alloys were prepared using distilled pure magnesium (99.99%) and high-purity aluminium (99.99%). In the alloys, 20 ppm carbon was discovered, which is claimed to form the potential nucleation substrates of Al_4C_3 or Al-C-O compounds [122]. Although the grain structures are fine, the mechanism of the purity level remains unclear, and the role of carbon remains unknown since it is relatively difficult to determine the amount of carbon in the magnesium alloys.

Apart from the approaches summarized above, many other additives have been tried, including but not limited to Sr, RE, Th, Si, Ca, B, AlN, MgO, TiB_2, TiC, and ZnO [124, 125, 126]. Sr was found to be effective only for pure magnesium or magnesium alloys that contained less than 1wt% aluminium [126]. The effect of grain refinement of TiB2 and TiC particles on aluminium bearing magnesium alloys were discovered by Boily and Blouin [124], but no convincing evidence has been provided. ZnO has been studied by Fu et al.[15], and they claimed that ZnO has significant effect of grain refinement on aluminium bearing magnesium alloys. However, the amount of ZnO powder used in the experiments is more than 1wt%.

Since none of the approaches discussed can be applied commercially, there hasn’t been a suitable grain refiner for aluminium bearing magnesium alloys. In order to solve the grain refinement problem, there are two possible directions, either find a new additive that will perform the task or to significantly improve the efficiency of an existing process. For aluminium free magnesium alloys, although the grain refinement technologies are well established both scientifically and commercially, the high cost of zirconium is still a driven force to find a replacement. Therefore, in summary, a suitable grain refiner that can be applied universally for magnesium alloys is still very necessary.

2.2.4. New Technological Development for Magnesium Alloys

In order to provide fine and uniform grain structure of magnesium alloys, a new technology of melt treatment, MCAST (melt conditioning by advanced shear technology), has been developed and applied to magnesium alloys by Fan and his co-workers [127-130]. The MCAST process is a novel technology for conditioning liquid metal prior to solidification processing [129-130]. During the MCAST process, liquid metal is fed into a shearing device, which creates high turbulence, and subjected to high intensity of turbulence and intensive shearing under high shear rate [129-130]. The conditioned liquid metal is then fed to different casting processes for final casting including but not limited to sand casting, permanent mould casting, HPDC, DC, twin-roll casting [129-130].

Significant improvement has been found in microstructural and compositional uniformity for magnesium alloys by applying the MCAST process because the intensive shearing imposed to the liquid metal changes nucleation behaviour during solidification [130, 131]. The grain sizes of magnesium alloys can be reduced from several millimeters to 100μm by applying the MCAST process at normal cooling rate [115, 131]. Although grain refinement has been achieved by applying MCAST in magnesium alloy casting, the mechanism of melt shearing remains unclear and still requires experimental evidence. Currently, two types of MCAST devices have been developed, which are the twin screw device, and the high shearing mixer [130, 131]. Both devices provide intensive melt shearing in the liquid metal prior to the final casting process [130, 131]. In the following sub-sections, overviews of both high shear devices will be provided.

2.2.4.1. Twin Screw Device

Historically, the twin screw device was applied for rubber polymerization in the 1920s, and further applied in polymer, food and pharmaceutical industries since then [132]. The main advantages of the twin screw device are the excellent dispersive mixing of highly viscous materials, continuous processing, plug flow behaviour, and multistaging capability [133]. Traditionally, twin screw devices have hardly been applied to liquid metals due to the high temperature and the chemical reaction between the liquid metal and the barrel and screws [133]. In 2000, a new twin screw device for liquid metal conditioning was developed by Fan and his co-workers and has been applied to various liquid metals, such as zinc, aluminium, and magnesium alloys [127, 133, 134]. This newly developed twin screw device includes five main parts, the driving motor to make the screws rotate, the feeder, a barrel with heating elements and thermocouple, a pair of co-rotating and fully intermeshing screws [129], and a control valve, as shown in **Figure 2.25**. During the MCAST process of the twin screw device, liquid metal is fed into the twin screw device through the feeder. The melt is then held in the heated barrel with an accurate temperature control [129, 130]. After the device starts to work, the screws will rotate in the barrel with speed control from 0~1000 rpm. The liquid metal will then be subjected to intensive shearing and a high intensity of turbulence [129]. **Figure 2.26** is the schematic illustration of the melt flow within the barrel of the co-rotating twin screw device [133].

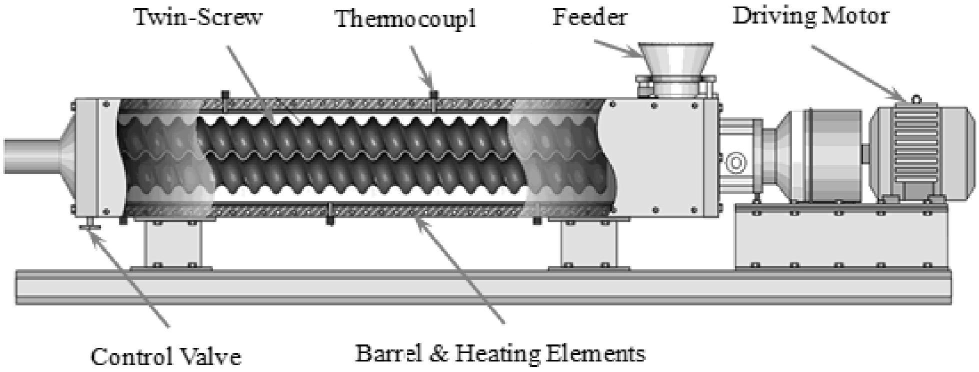

Figure 2.25 Schematic illustration of the twin screw unit providing intensive melt shearing [133].

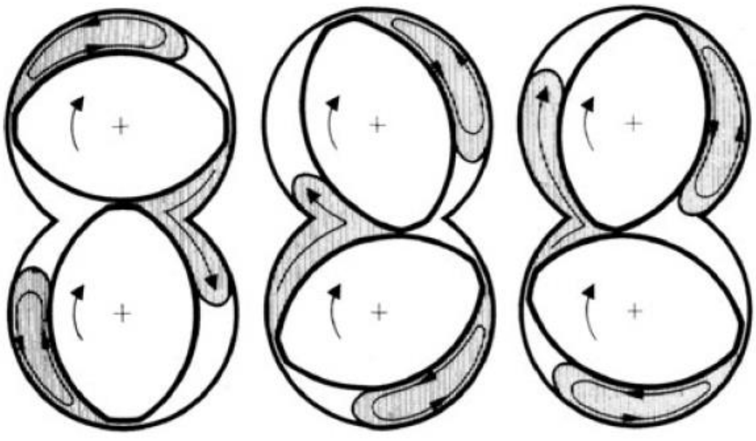

Figure 2.26 Schematic illustrations of flow pattern within the twin screw device [135].

The twin screw unit can be operated at temperatures either above the magnesium alloy liquidus to provide conditioned liquid metal, or below the alloy liquidus to provide semisolid slurry [38, 136-138]. In the latter case, the magnesium alloy semisolid slurry contains a well-controlled solid fraction of primary solid particles with a fine size and a spherical morphology [137]. In the former case, the conditioned magnesium alloy melt produced by the twin screw device has an extremely uniform temperature, uniform composition and well dispersed inclusion particles [38, 115]. These individual particles will have a fine and narrow size distribution, and more importantly, they are believed to be completely wetted by the liquid metal under the intensive forced convection [38, 115,138]. The experimental research [38, 115] also confirmed that the MCAST processing of the twin screw device has significant effect on grain refinement and composition uniformity of magnesium alloys.

In addition, the MCAST process of the twin screw device works either in a batch manner or in a continuous manner depending on the specific requirement of the subsequent casting processes, as shown in **Figure 2.27** [136, 139, 140]. For example, it can be applied to high-pressure die casting (HPDC) to produce shape castings [136], and continuous casting or semi continuous casting to produce feedstock materials for subsequent thermo-mechanical processing [139, 140].

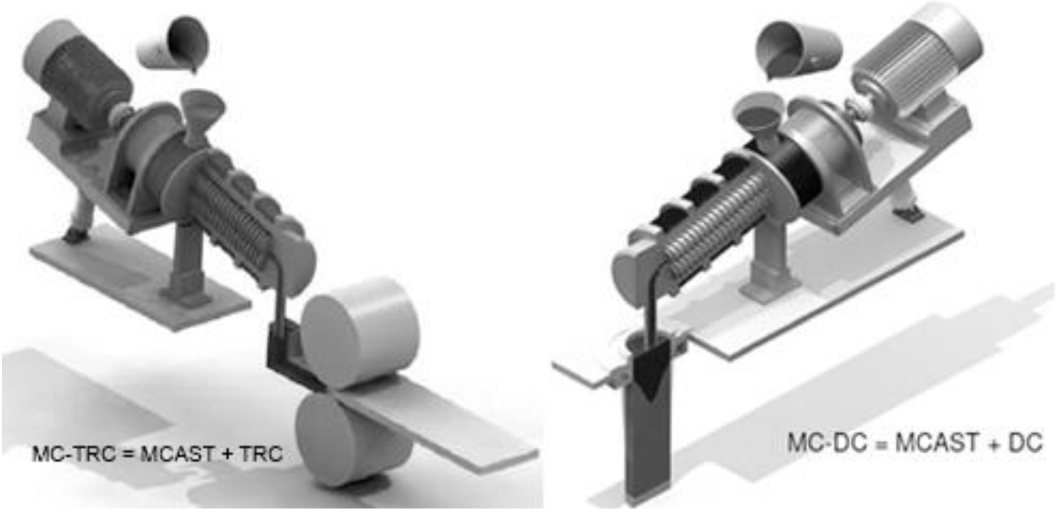

Figure 2.27 Schematic illustrations of the applications of the twin screw device in various casting procedures: (a) twin roll casting (TRC), (b) direct-chill casting (DC) [140, 141].

2.2.4.2. High Shear Mixer

High shear mixers have been widely used in adhesives, chemical, cosmetic, food, pharmaceutical, and plastics industries for dispersion of the ingredient, emulsification, homogenization, and particle size reduction [142]. A normal high shear mixer contains a rotor or impellor, together with a stator for stationary [142]. Due to the high temperature of liquid metals, a normal high shear mixer can hardly be applied in liquid metal treatment. In 2011, Fan and his co-workers [128] developed a new MCAST process of a high shear mixer that provides intensive melt shearing and high intensity turbulence to liquid magnesium alloys treatment prior to solidification. This newly developed MCAST process of high shear mixer has multi functions including but not limited to dispersion and distribution of particles; reduction of particle size, homogenization of microstructure, chemical composition and temperature field; improved wettability and nucleation and enhanced kinetic conditions for chemical reactions and phase transformation [128]. As shown in **Figure 2.28**, the high shear mixer comprises of a stator with multi openings in the wall, and a rotor which rotates inside the stator [128].

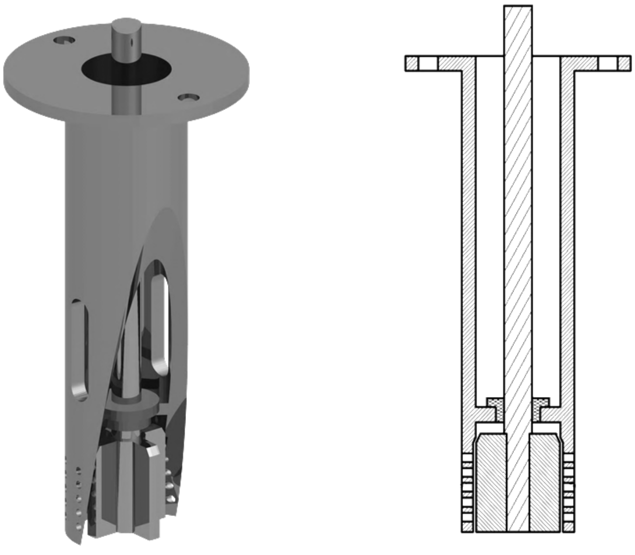
(a) (b)

Figure 2.28 Schematic drawing of the high shear mixer device [128, 131].

The MCAST process of the high shear mixer can work either in a batch manner or in a continuous manner. In either way, the high shear mixer device must be put inside the melt to a certain depth so that at least all the openings are covered. Once the mixer is switched on, the rotor, which is driven by a motor through the shaft, rotates at a controlled speed [128]. The liquid metal in the stator is then pushed out of the stator chamber through the openings by the centrifugal force created by the rotor blades and a negative pressure is created inside the shearing chamber [128]. The negative pressure sucks the liquid metal into the shear chamber through the bottom of the stator [128]. Therefore, macro melt flows are created in the liquid metal outside the mixer, as shown in **Figure 2.29**. The high shear mixer device creates three different shearing forces during its operation. First of all, intensive shearing will be provided in the gap between the stator wall and the surface of the rotor blades. Secondly, since the melt in the shearing chamber is pushed through the small openings, the shearing force will be created in those openings. Eventually, the macro melt flows also provide intensive melt shearing in the liquid metal.

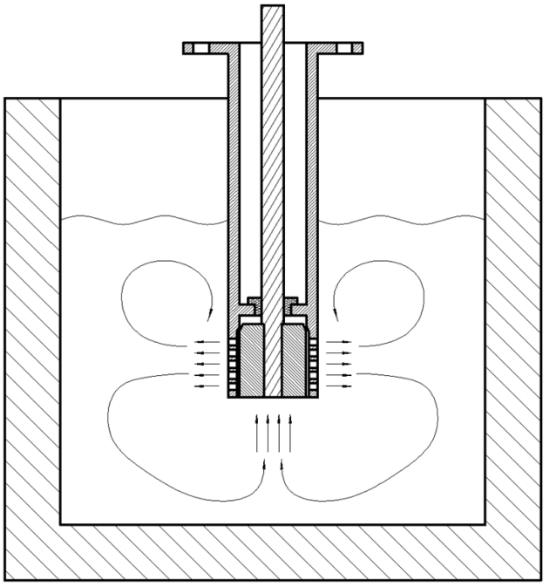

Figure 2.29 Schematic illustration of the macro flow created by the high shear mixer [128].

Considering that the MCAST process of the high shear mixer is relatively easy to operate, it can be applied to various types of magnesium alloy castings, such as sand casting, permanent mould casting, twin-roll casting, direct chill casting, and high pressure and low pressure die-casting. The experimental results confirmed that MCAST process of the high shear mixer has a significant effect on grain refinement and composition uniformity of magnesium alloys, however, further research is required to understand the mechanism of shearing [128, 131, 143-148].

2.3. Summary

In this chapter, previous research studies on solidification behaviour in magnesium alloys have been reviewed both theoretically in section 2.1 and experimentally in section 2.2. In order to understand solidification behaviour in magnesium alloys, both the nucleation and the growth of magnesium alloys are required.

The basic question for nucleation is what has acted as the nucleation substrates in a particular alloy system. For example, zirconium has been considered as the nuclei in aluminium free magnesium alloys because the grain sizes of the alloys with and without zirconium addition can differ greatly. Such differences have never been achieved by any other elements or particles with the same amount of addition. A reasonable conclusion from this example is that the potency of the particle~~s~~ is one of the key factors to determine whether they can nucleate the alloy. The amount of zirconium addition can also influence the final grain structure of the aluminium free magnesium alloys. The grain sizes of Mg-0.5wt%Ca-0.1wt%Zr, Mg-0.5wt%Ca-0.4wt%Zr, and Mg-0.5wt%Ca-1.0wt%Zr have shown significant differences [147]. An additional amount of zirconium led to a much smaller grain size. A reasonable conclusion from this example is that the efficiency of the particles also plays an important role in nucleation behaviour. Therefore, both the potency and the efficiency of the potential nuclei need to be examined in order to determine whether a certain type of particle can nucleate the alloy or not.

Classical nucleation theory (CNT) is the very first nucleation theory that attempted to find out what have acted as nucleation substrates, and how nucleation occurs during the solidification process. However, it can hardly be applied to practical problems due to certain limitations. First of all, many of the assumptions made by CNT are unjustified [150, 151]. Also, the interaction of particles around the nuclei hasn’t been considered by CNT [150, 151]. Despite these two limitations, solidification is almost always nucleated heterogeneously according to Cantor [149], since it is impossible to remove all the impurities from the parent liquid. Therefore, the classical homogeneous nucleation theory is almost impossible in reality. For the classical heterogeneous nucleation theory, there are considerable problems when the contact angle θ and the factor $S(\theta)$ are relatively small [149]. Based on Cantor's analysis [149], when θ is less than $\sim 10°$, the nucleus falls below one monolayer, and when θ is less than $\sim 20°$, the nucleus is only a few atoms thick. This means the spherical cap-shaped nucleus is highly impossible in such situations. These limitations of CNT make it hard to apply CNT in a practical problem such as the solidification behaviour in magnesium alloys.

One possible solution to determine whether a certain type of particle can nucleate the alloy or not, is to consider the potency and the efficiency of the particles separately. Misfit or lattice disregistry between the nucleation phase and potential nucleation substrates has been considered to be a good measurement of the potency, since it is one of the most important factors that can influence the interfacial energy [26]. In previous literatures, the misfit has been calculated in several different ways. Turnbull and Vonnegut [27] used the lattice parameters of both phases. Bramfitt [26] used three random directions of the two faces, and he calculated the arithmetic mean value of the three pairs of different directions and taken the angles between each pair under consideration. Fan [33] considered only the close packed faces rather than random faces of the nucleated phase and potential nucleation substrates which seemed to be more reasonable. Present study will use the close packed faces and calculate the misfit using the arithmetic mean of three different directions when analyzing the potency of potential nucleation substrates for magnesium alloys.

The efficiency of nucleation substrates has been studied by many researchers [36-43]. The most recent improvement on this issue is the free growth model developed by Greer et al [36, 42, 43], based on previous understanding. However, the free growth model started with a given distribution of particle sizes, and used the distribution and the number density of particles to determine the maximum undercooling of the alloy. It is theoretically reasonable, but practically, very difficult to find the actual distribution or the number density of particles. On the other hand, it is relatively easy to achieve the cooling curve from experimentation. In this study, an analytical model for cooling curve analysis will be provided. In the model, an analysis will be carried out from measured temperature data of the cooling curve to calculate the total number density of nucleation particles and the distribution of the nucleation particle sizes. The basic assumptions in the model will follow those given in the free growth model, and the model will eventually be tested by experimental results.

The role of solute in the alloy is an important issue to understand the growth during solidification. In previous literatures, many researchers tried to find out the relationship between final grain structure and the composition [18, 47-49, 52, 53]. Some researchers even achieved a linear relationship between grain sizes and the reciprocal of the growth restriction factor Q [18, 52, 53]. However, such a relationship is debatable since columnar equiaxed transition has never been taken into consideration. In this study, the relationship between grain sizes and growth restriction factors will be re-examined in magnesium binary alloys.

In modelling for nucleation and equiaxed grain growth by Hunt and Fan [60], casting conditions have been considered during solidification. In their modelling, some casting conditions might cause quench effect when the critical heat balance temperature after pouring is below liquidus. In this study, some experimental results will be provided to verify the quench effect in magnesium alloys. Also, when the critical heat balance temperature after pouring is above liquidus, a temperature gradient will form in the melt, and the solidification will occur from the edge to the centre. In this study, an analytical model for the advancing of equiaxed solidification front will be provided. The assumptions of the model are basically from the blocking mechanism proposed by Hunt's CET model.

For aluminium free magnesium alloys, zirconium has been used as an efficient grain refiner. However, due to the high cost of zirconium and the lack of grain refiner for aluminium bearing magnesium alloys, an applicable grain refiner or an applicable grain refinement technology is still desirable. In this study, a new type of grain refiner will be suggested based on theoretical studies of solidification behaviour in magnesium alloys. The new technology of MCAST will also be applied to magnesium alloys DC casting to confirm the effect of grain refinement on magnesium alloys achieved by the melt conditioning process. The mechanism of the MCAST process will also be discussed based on the theoretical understanding of nucleation and growth in magnesium alloys.

Chapter 3. Experimental Procedure

3.1. Alloy Compositions and Metallographic Procedures

3.1.1. Alloy Compositions

The magnesium alloys investigated in the present study were AZ91D commercial alloy, AZ31 commercial alloy, Mg-Al binary alloys, and Mg-Zn binary alloys. The compositions of the commercial alloys are shown in **Table 3.1**. The compositions of pure metals which were used to make the binary alloys are shown in **Table 3.2**.

Table 3.1 Compositions of Commercial Alloys AZ31 and AZ91D (in wt%).

	Mg	**Al**	**Zn**	**Mn**	**Other**
AZ31	96.14	2.81	0.73	0.31	~0.01
AZ91D	90.31	8.76	0.67	0.25	~0.01

Table 3.2 Compositions of Pure Mg, Al, and Zn (in wt%).

	Mg	**Al**	**Zn**
Purity	99.9	99.6	99.9

Composition measurements of the alloys were obtained with a ‘Worldwide Analytical Systems AG, Foundry Master’, shown in **Figure 3.1**. The ‘WAS Foundry Master’ is an ‘Arc-spark Optical Emission Spectrometer’ for routine analysis of metal alloys [152]. The system comprises of a solid-state spark source, a vacuum system, an optical system, and an output system [152]. A sample of minimum surface size 100mm^2 was taken from the alloy ingots, surface ground using a SiC 1200 paper to produce a flat surface and washed with methanol for composition testing [152].

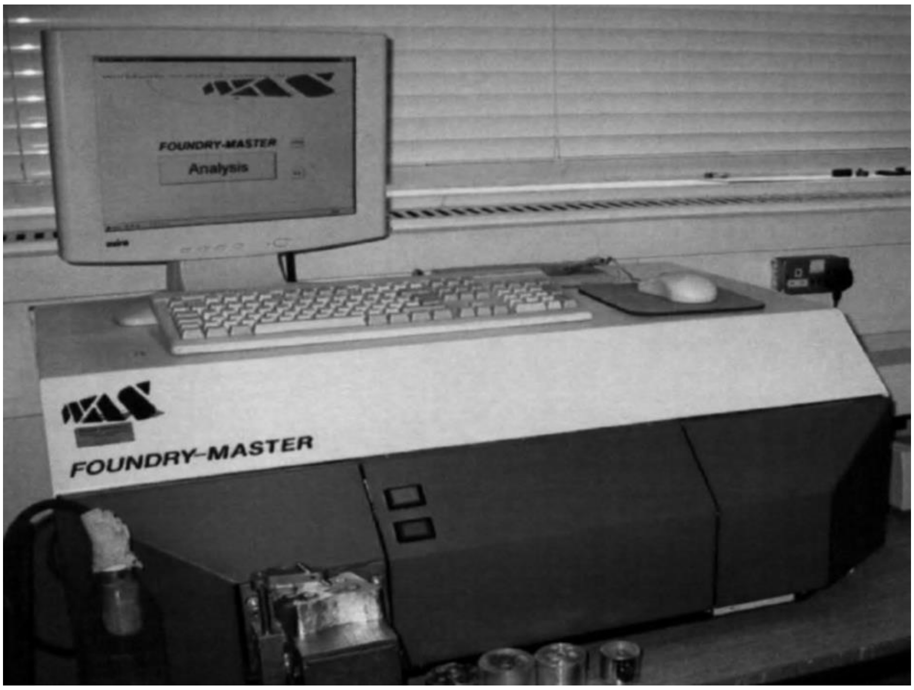

Figure 3.1 The Worldwide Analytical Systems AG Foundry Master.

3.1.2. Metallographic Procedures

For microstructural investigation, magnesium castings were prepared under conventional procedures for metallographic examination of magnesium alloys. The surface that needed to be examined was ground by 120, 240, 400, 800, 1200, and 4000 mash SiC abrasive paper, one after another. After that, the surface was further polished with Al_2O_3 suspension solution, etched with relevant solution, and cleaned with methanol. The colour etching of magnesium alloys was normally conducted with a mixture of picric acid, acetic acid, diluted with water and ethanol.

A Zeiss Optical Microscope (OM) was utilized for microstructural observations and quantitative metallography [152]. The images were taken with an AxioCam MRC digital camera, as shown in **Figure 3.2** [152]. Metallographic sections for optical microscopy and scanning electron microscopy (SEM) were prepared using standard metallographic procedures. The SEM examination was carried out using a Zeiss Supera 35 FEG microscope as shown in **Figure 3.3**. This is equipped with an energy dispersive spectroscopy (EDS) facility, operated at an accelerating voltage of 5–15 kV [152].

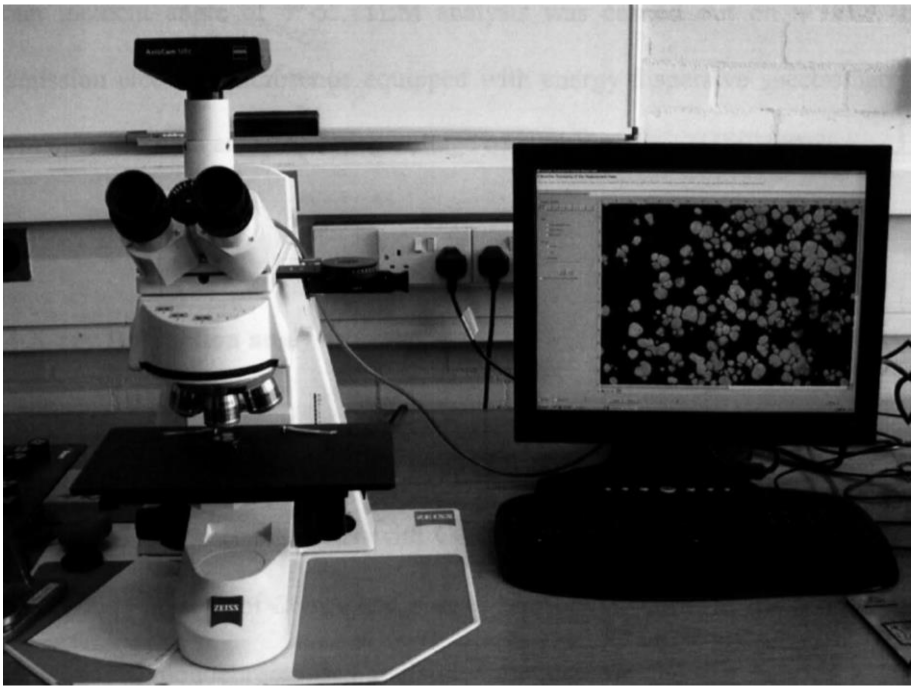

Figure 3.2 The Zeiss Optical Microscope (OM) with an AxioCam MRC digital camera.

Figure 3.3 A Zeiss Supera 35 FEG scanning electron microscope (SEM) with an energy dispersive spectroscopy (EDS) facility [153].

3.2. Overview of the Experiments and their Objectives

In this study, series of experiments have been done to investigate in multiple issues. In order to get a clear image of the whole study, an overview of all the experiments along with the objectives of these experiments is discussed briefly in this section.

In section 3.3, AZ91D alloys with and without melt shearing were cast into a cylinder mould with various thicknesses of thermal insulations. The major objective of this set of experiments is to discover what the nuclei are in magnesium alloys without zirconium addition. Since MgO has been suspected to be the nuclei in AZ91D alloy, the objective can in other word draw as to accept or reject such suspicion and investigate the potency of the endogenous MgO particles. It may also provide clues of the mechanism of melt shearing. The reason why various thicknesses were used to cover the cylinder mould is to reconfirm the universality and consistency of the experimental results. The experiments in this section were listed in **Table 3.3**.

Table 3.3. Experiments in section 3.3.

Experiment	**Alloys**	**Casting Conditions**		**Mould**
		Casting Superheat	Melt Treatment	
1-3	AZ91D	50K	with melt shearing	cylinder (with 6, 13, 25mm insulation)
4-6			without melt shearing	cylinder (with 6, 13, 25mm insulation)

In section 3.4, Mg-Al and Mg-Zn binary alloys with various amounts of solute were cast into TP-1 moulds. The alloys were cast at 10K, 30K, and 50K superheat without melt shearing. For those ingots cast at 10K superheat, a comparison ingot with melt shearing was also cast at 10K superheat. The experiments in this section were listed in **Table 3.4**. The most important objective for this set of experiments is to discover the influence of solute for microstructures. In order to minimize the influence from other factors rather than solute, two types of binary alloys were used, one with aluminium and one without. Various superheating temperatures provide us the consistency and universality of the experiments. The reason melt shearing device was applied to these alloys is because we wanted to see whether there is a significant influence of the efficiency of the nucleation particles, which can only be MgO in this case.

Table 3.4. Experiments in section 3.4.

Experiment	**Alloys**	**Casting Conditions**		**Mould**
		Casting Superheat	Melt Treatment	
1-5	Mg-Al (0.1, 0.3, 1, 3, 9 wt%)	10K	with melt shearing	TP-1
6-10			without melt shearing	
11-15		30K		
16-20		50K		
21-25	Mg-Zn (0.1, 0.3, 1, 3, 9 wt%)	10K	with melt shearing	
26-30			without melt shearing	
31-35		30K		
36-40		50K		

In section 3.5, the experiments are related to the inoculation of MgO nano particles. There are three subsections in section 3.5. In subsection 3.5.1, Mg-Al binary alloys with various amounts of Al and 0.1wt% MgO nano particles were cast into TP-1 mould at 50K superheat. The aim of this set of experiments is to discover whether the MgO inoculants can refine the microstructure of aluminium bearing magnesium alloys. In subsection 3.5.2, the MgO inoculants were applied to AZ91D alloy. In this set of experiments, the AZ91D alloy with and without various amounts of MgO inoculants were cast into TP-1 mould. The cooling curves of AZ91D with and without 0.1wt% MgO inoculants were also measured to reconfirm the role of MgO inoculants. In subsection 3.5.2, an AZ91D-5wt%MgO master alloy was produced using the same MgO used for inoculation. The effect of the master alloy was then tested in AZ91D alloy to see whether it is applicable for grain refinement of aluminium bearing magnesium alloys. The experiments in this section were listed in **Table 3.5**.

Table 3.5. Experiments in section 3.5.

Experiment	**Alloys**	**Casting Conditions**		**Mould**
		Casting Superheat	Melt Treatment	
1-5	Mg-Al (0.1, 0.3, 1, 3, 9wt%)	50K	with 0.1wt%MgO	TP-1
6	Mg-9wt%Al		with 0.1wt%MgO	filtration
7	AZ91D		without MgO	TP-1
8			with 100ppm MgO	
9			with 0.1wt% MgO	
10			with 1wt% MgO	
11			without MgO	cylinder (with 13mm insulation)
12			with 0.1wt% MgO	
13			with 0.1wt% MgO	filtration
14			with 1ppt MA*	TP-1
15			with 2ppt MA	
16			with 5ppt MA	
17			with 1wt% MA	

* MA represents AZ91D-5wt%MgO master alloy.

Experiments in section 3.6 is to discover the influence of casting conditions, such as pouring temperature and mould temperature, on the microstructures. In this section, AZ91D was cast into a cylinder mould rapidly at different temperatures in order to investigate the mechanism of melt quenching effect by measuring the cooling curves of these castings with various superheats. The thermal field within the mould has also been measured in the experiments with 4 thermocouples cast at 10K and 100K superheat. The experiments in section 3.6 are shown in **Table 3.6**.

Table 3.6. Experiments in section 3.6.

Experiment	**Alloys**	**Casting Conditions**		**Mould**
		Casting Superheat	Melt Treatment	
1-5	AZ91D	10K, 30K, 50K, 70K, and 100K	poured rapidly	cylinder (1TC*)
6-7		10K and 100K		cylinder (4TC)

* TC represents thermocouple.

Experiments in section 3.7 are mainly related to DC casting of magnesium alloys, such as AZ91D and AZ31. The castings are either with or without melt shearing. The main objective in this section is to discover whether melt shearing treatment can be applied to magnesium alloy DC casting and influence the microstructure. Thermal fields in the DC casting with and without shearing have been investigated to understand the mechanism of melt shearing treatment. The experiments in section 3.7 are shown in **Table 3.7**.

Table 3.7. Experiments in section 3.7.

Experiment	**Alloys**	**Casting Conditions**		**Mould**
		Casting Superheat	Melt Treatment	
1	AZ91D	650 ℃	without melt shearing	DC
2			with melt shearing	
3			without melt shearing	DC (1 thermocouple)
4			with melt shearing	
5			without melt shearing	DC (4 thermocouple)
6			with melt shearing	
7	AZ31	680 ℃	without melt shearing	DC
8			with melt shearing	

3.3. Cooling Curves of AZ91D with and without Melt Shearing

The AZ91 alloy ingot was melted at 680 ℃ and held for at least 1 hour to keep the temperature stable under the protection of a gas mixture containing 99.6vol% N2 and 0.4vol% SF6. Once the melt temperature was stabilized, 1kg alloy melt was transferred to the twin screw machine (MCAST unit) and subjected to intensive melt shearing at 650 ℃ and 800 rpm for 45s. The melt with and without shearing was then poured into the inner cylindrical crucible shown in **Figure 3.4** which had been preheated to 650 ℃. A Ø0.5mm K-type thermocouple supported by a Ø3.0mm steel tube was fixed on the lid of the cylindrical crucible in order to measure temperature from the same location in the inner crucible. The tip of the thermocouple was 45mm below the bottom of the lid, 35mm above the removable bottom of the inner crucible, right in the middle of the melt. Before each experiment, the thermocouple was first calibrated using pure aluminium in order to prevent systematic error from using the thermocouple. The data of melt temperatures were then recorded through a data logger with a frequency of 20Hz. The schematic drawing of the whole measuring equipment is shown in **Figure 3.4**.

For each experiment, the melt in the inner crucible was controlled by weight and the surface of the melt was 10 mm lower than the top of the inner crucible. The inner crucible was put on a refractory brick in the outer crucible and was covered by thermal insulation with various thicknesses (6mm, 13mm, and 25mm) to set up different cooling conditions. In order to prevent further oxidation though burning of the magnesium alloy, a thin layer of salt flux was used to cover the surface of the melt, and a lid, which was also covered by thermal insulation, was then put on top of the inner crucible.

The samples for microstructural analysis were taken from the central position of the solidified ingot. The preparation of the samples followed standard metallographic procedures and colour etched using a solution mixed by picric acid and acetic acid, diluted with water and ethanol. The grain sizes of the samples were then measured by applying the line intercept method on the section, which gave the mean intercept length.

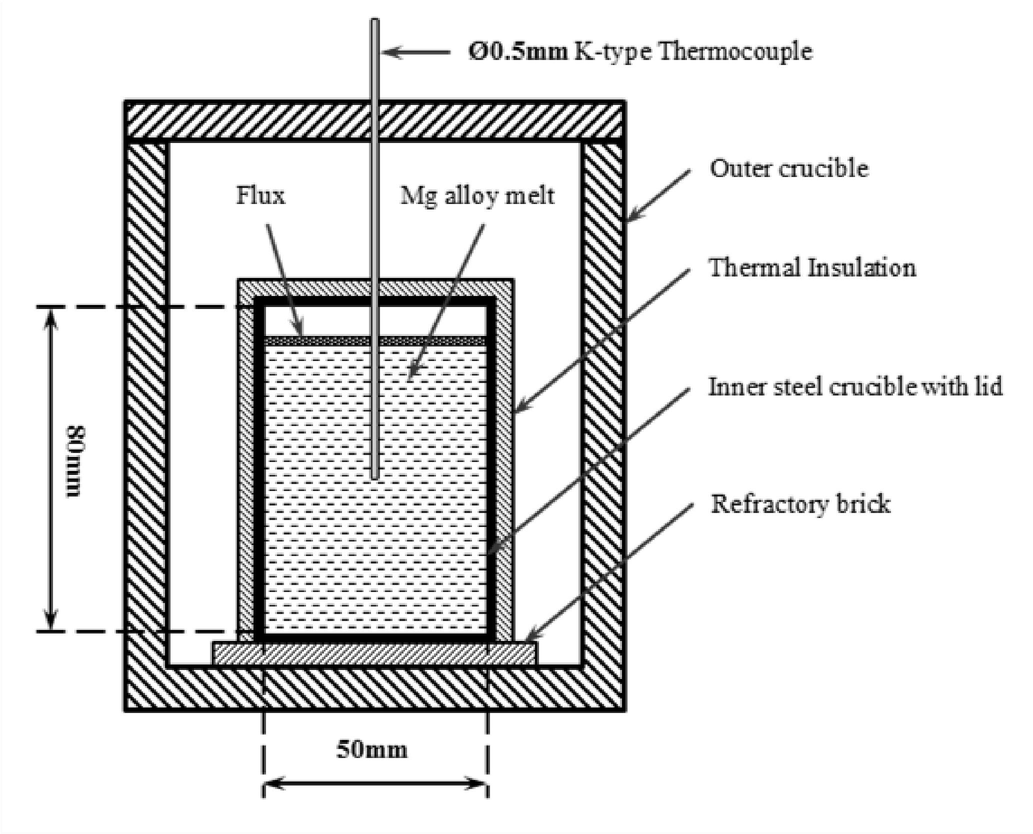

Figure 3.4 Schematic illustrations of the experimental set-up for measuring the cooling curves of alloy melt with and without prior intensive melt shearing.

3.4. TP-1 Casting for Mg-Al and Mg-Zn Binary Alloys

The pure magnesium ingots were melted at 720 ℃. Once the pure magnesium became fully liquid, various weights of pure aluminium (or pure zinc) ingots were mixed in the magnesium melt to make 0.1, 0.3, 1, 3, and 9wt% of Mg-Al (or Mg-Zn) binary alloys. The alloys were then held for at least 1 hour to keep the temperature stable at 60 ℃ above the liquidus for the respective alloys. During the whole process, the alloys were under the protection of a gas mixture containing 99.6 vol% N_2 and 0.4vol% SF_6. The alloys were then cast at 10, 30, and 50 ℃ above the liquidus of the respective alloys in TP-1 moulds preheated to 350 ℃. The alloys were also transferred to the MCAST unit and were subjected to intensive melt shearing at 10 ℃ above the liquidus of the alloys and at 800 rpm for 45s. The alloys with intensive melt shearing treatment were cast at 10 ℃ above the liquidus of the alloys in TP-1 moulds preheated to 350 ℃. The TP-1 mould was put in the round hole of the holding board and cooled with water, as shown in **Figure 3.5**. The cooling water came from a water tank to keep the flow stable at 3.8 liter/min. The samples for microstructural analysis were taken from 38mm above the bottom of the cast ingots for both cross sections and longitude sections, as it is shown in **Figure 3.6**.

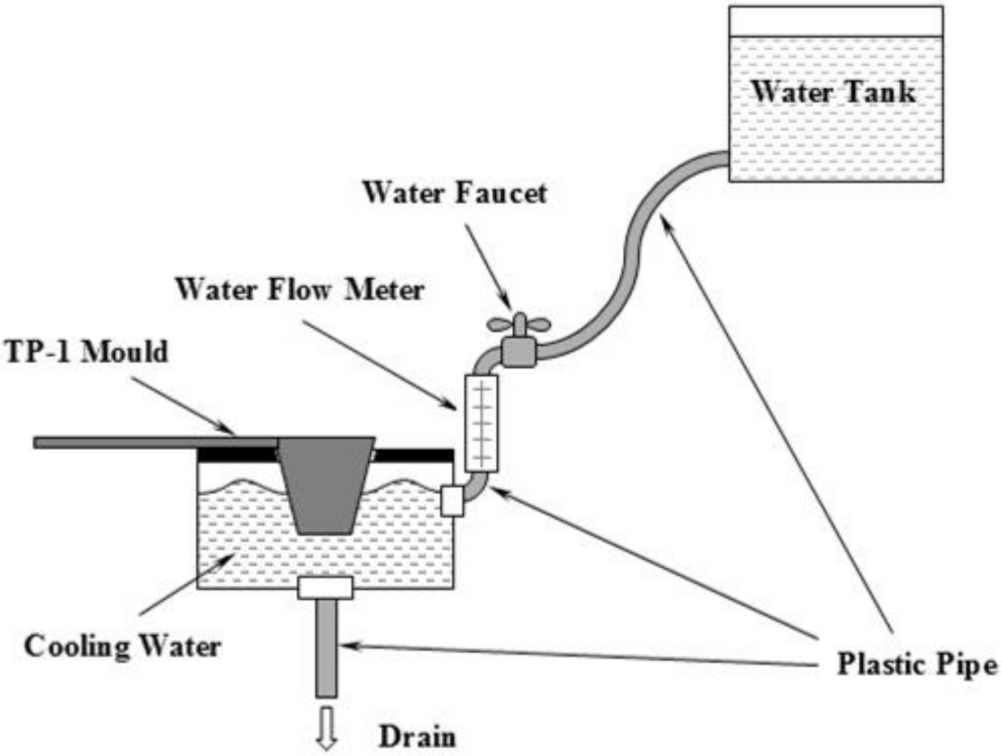

Figure 3.5 Schematic illustration of TP-1 casting.

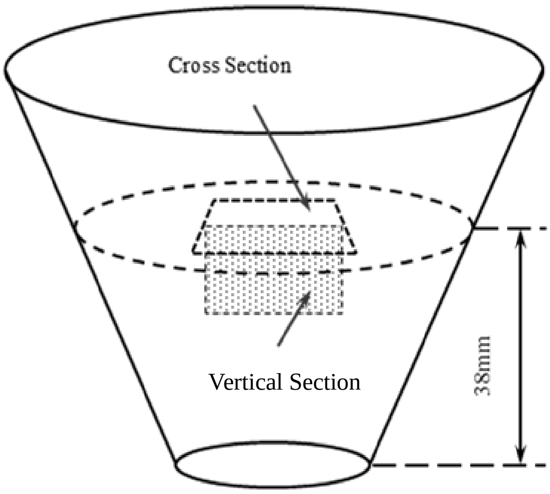

Figure 3.6 Schematic drawing of TP-1 casting samples.

3.5. Magnesium Alloys Grain Refined by MgO Inoculation

3.5.1. Mg-Al Binary Alloy Grain Refined by MgO Inoculation

The pure magnesium ingots were melted in 5 steel crucibles in one furnace at 720 ℃. Once the pure magnesium became fully liquid, various weights of pure aluminium ingots were mixed in the magnesium melt to make 0.1, 0.3, 1, 3, and 9wt% of Mg-Al binary alloys separately. The alloys were then held for at least 0.5 hours in 5 difference furnaces to keep the temperatures stable at 60 ℃ above liquidus of the respective alloys. 0.1wt% of MgO powder preheated to 500 ℃ was added into the alloy using a motor driven steel propeller. The process of inoculation was shown in **Figure 3.7**. The propeller was coated with boron nitride to avoid direct contact with the alloys. For each alloy, the propeller stirred for 45 seconds in order to provide intensive mixing of the MgO powder. During the whole process, the alloys were under the protection of a gas mixture containing 99.6vol% N_2 and 0.4vol% SF_6. The alloys were then held for at least 0.5 hours to allow the temperature of the melt to return to 60 ℃ above liquidus. The alloys were cast at 50 ℃ above the liquidus of the respective alloys in TP-1 moulds preheated to 350 ℃. The compositions of the cast ingots were examined by the 'WAS Foundry Master'. The samples for microstructural analysis were taken from 38mm above the bottom of the cast ingots and were prepared following standard metallographic procedures and colour etched. The grain sizes of the samples were then measured by applying the line intercept method on the section.

In order to investigate the mechanism of grain refinement using MgO, a pressurized melt filtration technique shown in **Figure 3.8** was used to collect the MgO particles added as inoculant in the melt. In this process, the melt is forced to flow through a micro-porous filter and inclusions and intermetallic particles are collected on the top surface of the filter. The Mg-9wt%Al melt (1.5 kg), either with or without MgO inoculation, was transferred to the pre-heated crucible of the filtration unit. Argon was then introduced to the pressure chamber to force the liquid metal to flow through the filter attached at the bottom of the crucible. Solid particles were then collected above the filter in the crucible together with the remaining melt, which was allowed to solidify in the crucible outside the pressure chamber under the same protective atmosphere. The solidified metal adjacent to the filter with a high concentration of inclusion particles was sectioned and prepared for detailed metallographic examination.

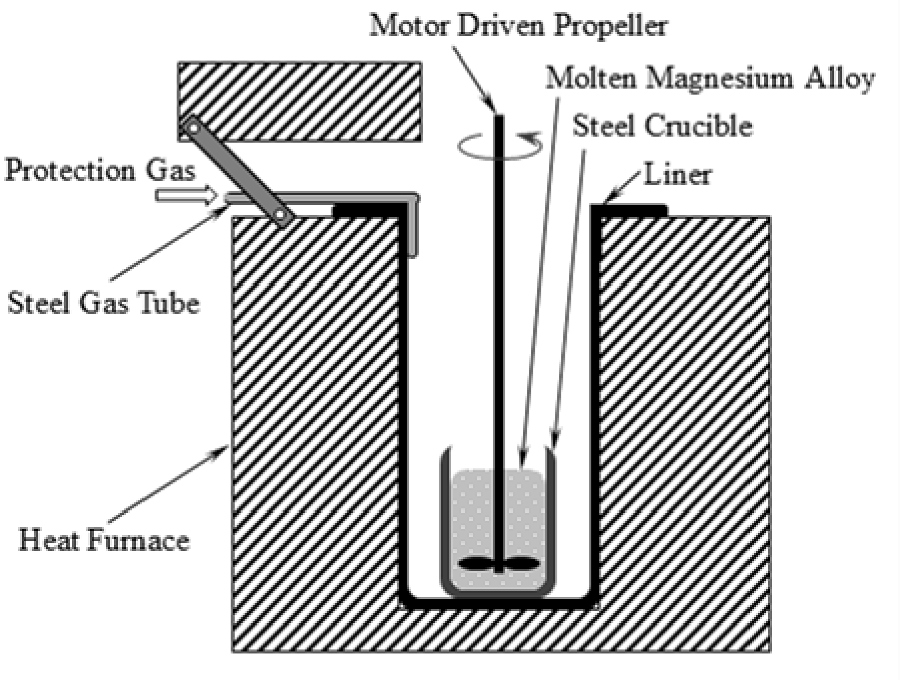

Figure 3.7 Schematic illustration of inoculating MgO in magnesium alloys.

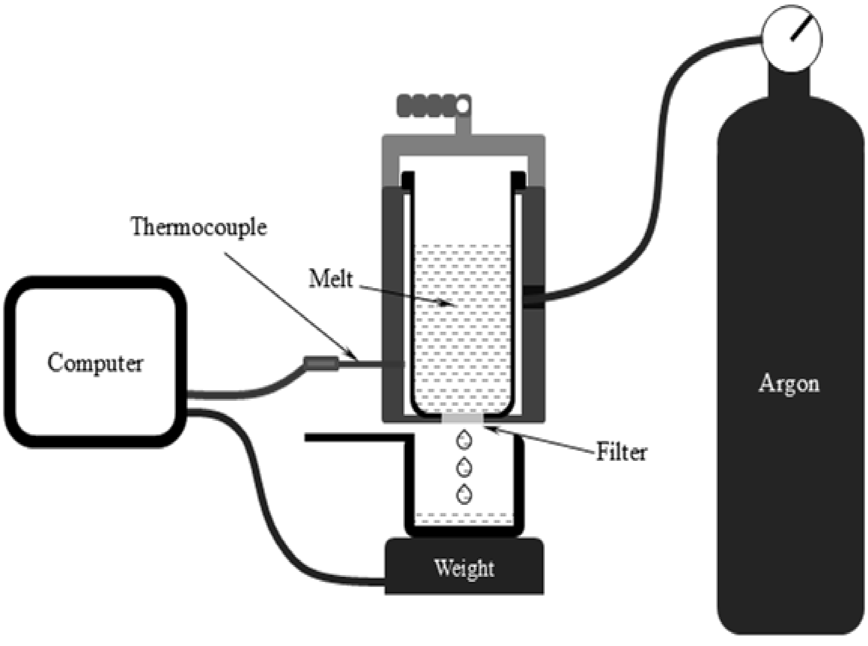

Figure 3.8 Schematic illustration of the pressurized filtration device.

3.5.2. AZ91D Grain Refined by MgO Inoculation

The AZ91D alloy ingots were melted in four steel crucibles in a furnace at 660 ℃ under the protection of a gas mixture containing 99.6vol% N_2 and 0.4vol% SF_6. Once the alloy was fully melted, 0.01wt%, 0.1wt%, and 1wt% of MgO powder was added as inoculants in the melts in three of the four respective crucibles using the motor driven steel propeller coated with boron nitride shown in **Figure 3.7**. After 45 seconds of stirring, the melts were held in the furnace for a further 30 minutes to ensure the melt temperature reached 660 ℃. The melts were cast at 650 ℃ into TP-1 moulds preheated to 350 ℃. The melt without MgO and the melt with 1ppt of MgO inoculation were also poured into the cooling cure curve measurement equipment in **Figure 3.2** at 650 ℃. The temperature data was recorded through a data logger with a frequency of 20Hz. The samples for microstructural analysis were taken from 38mm above the bottom of the TP-1 cast ingots and were prepared following standard metallographic procedures and colour etched. The grain sizes of the samples were then measured by applying the line intercept method on the section.

3.5.3. AZ91D Grain Refined by AZ91D-MgO Master Alloy

The AZ91D alloy ingot of 950 g was melted in a steel crucible at 680 ℃. 50 g MgO powder was added into the melt to produce AZ91D-5wt%MgO master alloy using the propeller shown in **Figure 3.7**. After 10 minutes stirring, the melt was cast in a detachable steel mould. During the melting and stirring process, the alloy was under the protection of a gas mixture containing 99.6 vol% N_2 and 0.4vol% SF_6. Another five AZ91D alloy ingots were melted in steel crucibles in a furnace at 660 ℃. 500ppm, 1ppt, 2ppt, 5ppt, and 1wt% of the AZ91D-5wt%MgO master alloy were mixed in the melts respectively. The melts were held for another 30 minutes and cast at 650 ℃ in TP-1 moulds preheated to 350 ℃. The samples for microstructural analysis were taken from 38mm above the bottom of the TP-1 cast ingots and were prepared following standard metallographic procedures and colour etched. The grain sizes of the samples were then measured by applying the line intercept method on the section.

3.6. Cooling Curves of AZ91D with Various Casting Conditions

The AZ91 alloy ingot was melted at 720 ℃ and held for at least 1 hour to keep the temperature stable under the protection of a gas mixture containing 99.6 vol% N_2 and 0.4 vol% SF_6. A steel mould (Ø60mm×H100mm) with a ceramic base was preheated to around 350 ℃. In the ceramic base, a Ø0.5mm K-type exposed wire thermocouple was supported by a 3mm ceramic tube through a 3mm hole within the base. The height of the base was 10mm, the length of the tube was 50mm, and the exposed part of the wire thermocouple was 2mm, so the thermocouple tip was about 42mm above the upper side of the base. When the melt temperature was stabilized, 540g of AZ91D alloy melt was transferred into a steel crucible and the melt temperature was measured using a 3mm thermocouple. The melt was cast at 10K, 30K, 50K, 70K, and 100K above liquidus. Once the temperature was 5 ℃ higher than the pouring temperature, the mould and the base were taken out of the preheating furnace, and placed on refractory bricks. The melt was then poured into the mould rapidly. The melt temperature was measured by the exposed wire thermocouple and the data was recorded through a data logger with a frequency of 100Hz. A schematic drawing of the equipment is shown in **Figure 3.9**.

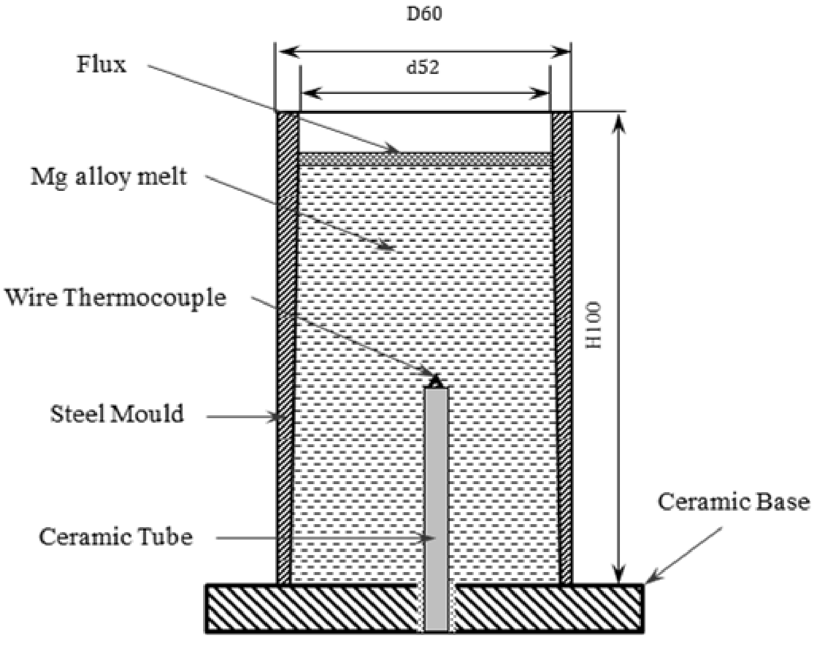

Figure 3.9 Schematic illustration of cooling curve measurement equipment.

The four channel equipment schematically shown in **Figure 3.10** is used for measuring thermal field at various locations in the mould after pouring. The melt was cast at 10K and 100K above liquidus. As it is shown, the wire thermocouple T1 is right in the centre of the mould, both horizontally and vertically. T2 is in the centre of the mould horizontally and 1 cm above T1 vertically. T3 and T4 are in the centre of the mould vertically. Horizontally T3 is 1cm away from the centre, and T4 is 2cm away from the centre. Since the wire thermocouple T2 have a relatively long part exposed to the melt, a thin layer of boron nitride is coated onto T2 to prevent interference of the melt.

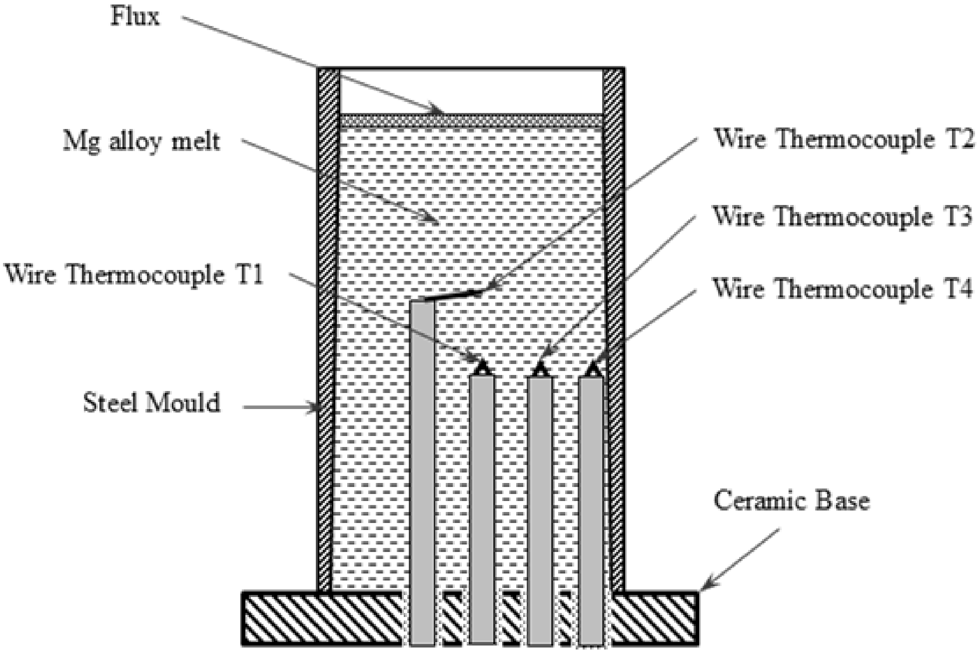

Figure 3.10 Schematic illustration of cooling curve measurement equipment.

The samples for microstructural analysis were taken from the central position of the solidified ingot, exactly where the tips of the thermocouple once were located during the solidification process. The preparation of the samples followed standard metallographic procedures and colour etched using a solution mixed by picric acid and acetic acid, diluted with water and ethanol. The grain sizes of the samples were then measured by applying the line intercept method on the section.

3.7. Magnesium Alloys DC Casting with Intensive Melt Shearing

Commercial AZ31 and AZ91D Mg-alloys were used in this study. The alloys were melted under standard process under the protection of a gas mixture containing 99.6vol% N_2 and 0.4 vol% SF_6 and then the ingots were made using the DC casting process with intensive melt shearing. Samples were cut from the centre of DC cast ingots and then examined by optical microscopy according to the standard metallographic procedures. Intensive melt shearing is achieved by the application of a high shear mixer unit. During the casting process, the motor of the high shear mixer transfer the power to the rotor by the shaft and drives the rotor to rotate and shear the liquid metals in the gap between the rotor and the stator and also in the openings of the stator. The melt is conditioned by intensive shearing in the DC mould as shown schematically in **Figure 3.11**. Also shown in the illustration are the locations in the melt for temperature measurement: T1, centre, 10mm below the bottom of the high shear unit; T2, edge, 10mm below the bottom of the high shear unit; T3, near to the centre, 30mm above the bottom of the high shear unit; T4, near to the centre, 90mm above the bottom of the high shear unit.

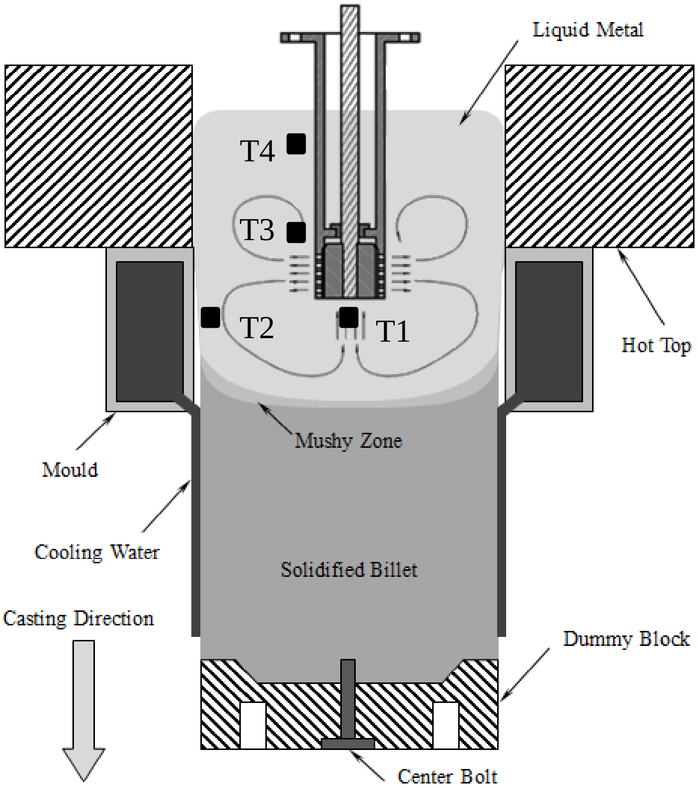

Figure 3.11 Schematic diagram of MC-DC casting process with four thermocouples.

Chapter 4. Results

4.1. Measurement of Undercoolings during Solidification for AZ91D with and without Melt Shearing

There are three major objectives for this experiment. The first one is to investigate the mechanism of melt shearing, by measuring the cooling curve of AZ91D with and without melt shearing. The second one is to provide further understanding of the relationship between undercooling and grain structures. Finally, it helps to find out the nucleation substrates in AZ91D alloy. In section 4.1.1, the results of cooling curve measurement of AZ91D with and without melt shearing is provided. Microstructures of grain structures of the cast ingots corresponding to the cooling curve measurements are shown in section 4.1.2. The morphology and the size distribution of MgO films or particles in AZ91D are given in section 4.1.3.

4.1.1. Cooling curve measurement for AZ91D with and without melt shearing

One of the most important issues for cooling curve measurement is the repeatability of the measured curves. A measurement is considered as valid only if it can be reproduced under the same conditions. In order to prove the reliability of the results in this experiment, two cooling curves under the same conditions have been measured, i.e., the same alloy, type of thermocouple, crucible and positioning. As shown in **Figure 4.1.1**, the curves are almost overlapped. Both curves in the figure are measured cooling curves for the AZ91D alloy melt without prior melt shearing cast at 650℃ into a cylindrical crucible covered with 13mm heat insulation. The correlation coefficient for these two curves is 0.99845, which represents a good correlation between these two curves. It can be seen that cooling curves measured in this experiment are reliable and repeatable, and can be used for further discussion and analysis.

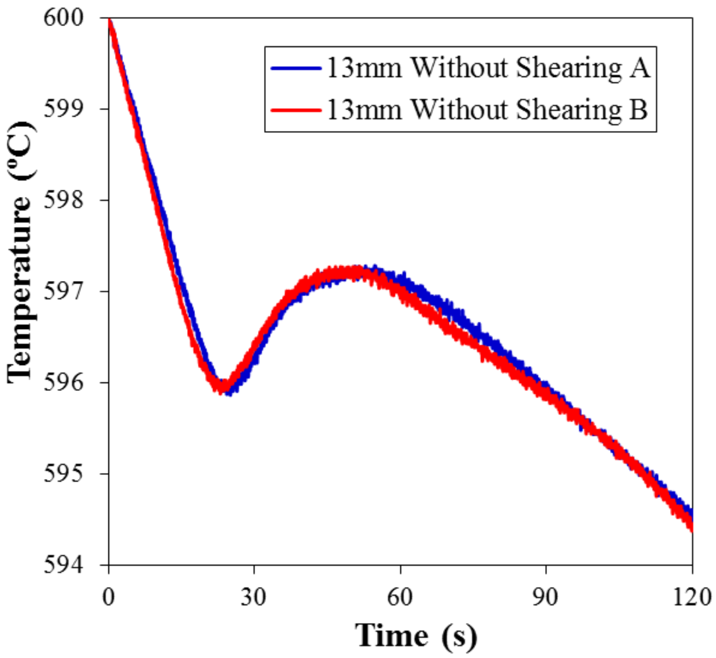

Figure 4.1.1 Measured cooling curves for AZ91D alloy melt without prior melt shearing. The melts were cast at 650 ℃ into a cylindrical crucible covered with 13mm thermal insulation.

As shown in **Figure 4.1.2**, the cooling curves of AZ91D alloy melt have been measured in order to compare the differences between alloy melts with and without melt shearing. For both curves, the melts were cast at 650 ℃ into a cylindrical crucible covered with 13mm thermal insulation. In order to study the difference in undercoolings of the curves, portions of the measured curves have been enlarged in **Figure 4.1.3**.

Prior to solidification, the cooling rates of the curves **in Figure 4.1.3** were almost the same, both around 0.2K/s. The recalescence temperatures, which can be considered as the subtraction of a relatively small growth undercooling from the liquidus of the alloy, are both around 597.23 ℃. Since the growth undercooling is relatively small and usually can be ignored during analysis, the recalescence temperatures can be approximately considered as the liquidus. Therefore, the undercooling can be considered as the difference between the recalescence temperature and the minimum temperature before the recalescence occurs. For the curves with and without shearing, the undercooling is 0.7K and 1.3K, respectively.

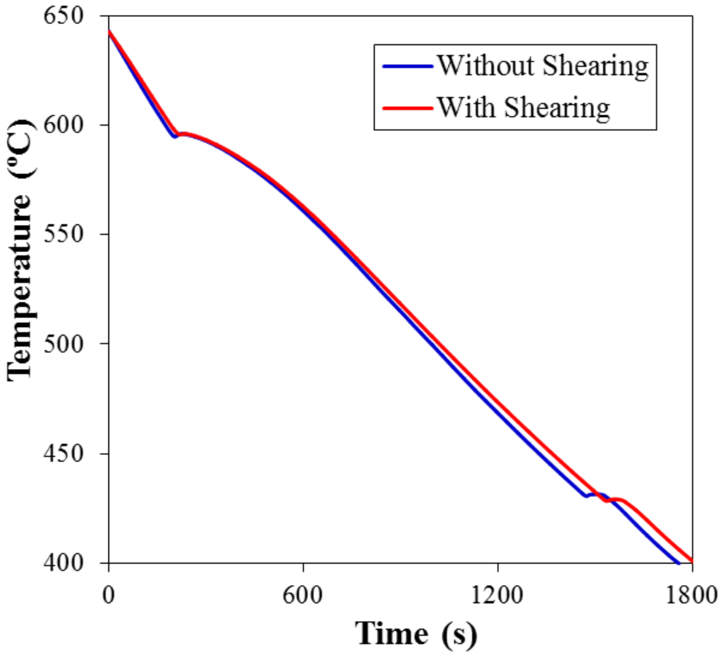

Figure 4.1.2 Measured cooling curves for the AZ91D alloy melt with and without prior melt shearing. The melts were cast at 650 ℃ into a cylindrical crucible covered with 13mm thermal insulation.

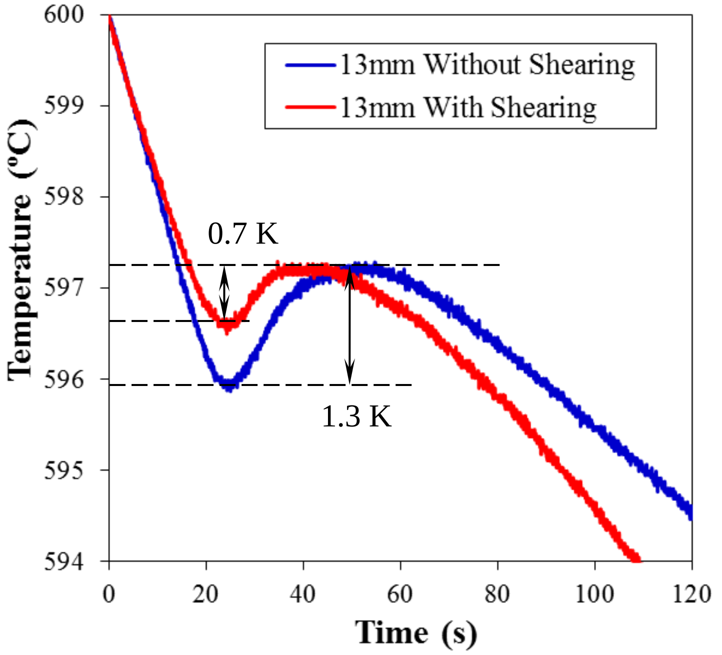

Figure 4.1.3 Portions of measured cooling curves for the AZ91D alloy melt with and without prior melt shearing. The melts were cast at 650 ℃ into a cylindrical crucible covered with 13mm thermal insulation.

In order to understand the relationship between the number density of nucleation particles and the undercooling, a schematic illustration of a typical cooling curve with pronounced recalescence is provided in **Figure 4.1.4**. In the figure, T_L is the liquidus temperature of the alloy, T_N is the starting temperature for nucleation, T_F is the minimum temperature before recalescence, and T_R is the recalescence temperature. The difference between T_L and T_R is the growth undercooling, which is relatively small and usually ignored during analysis. The difference between T_R and T_F is the undercooling from a typical cooling curve.

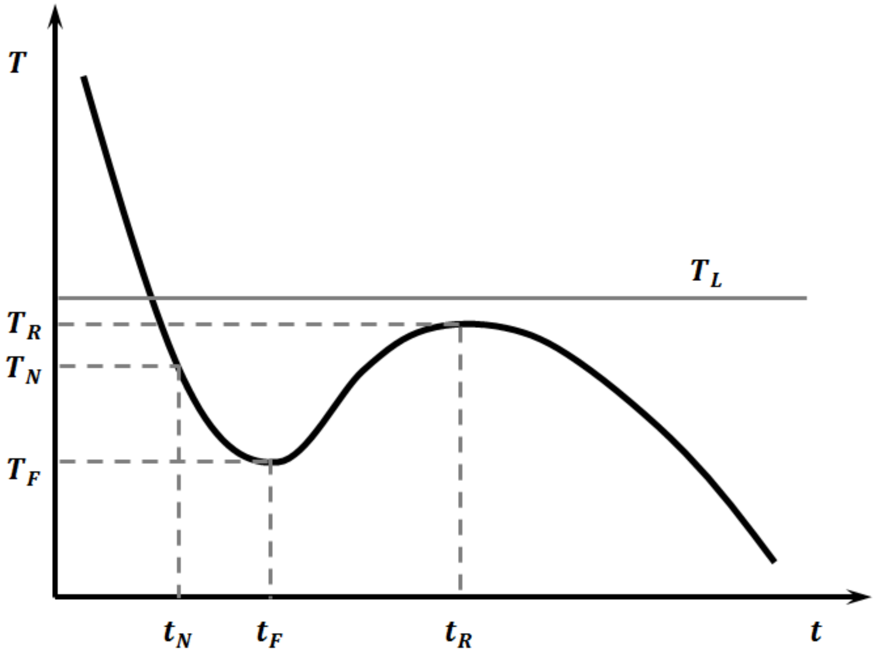

Figure 4.1.4 Schematic drawing of a typical cooling curve with pronounced recalescence.

Before T_N, the cooling rate can be considered as a constant which represent the ability of heat released from the melt into the environment. At this stage, the heat released from the melt is only due to the temperature drop of the melt. When the temperature drops between T_N and T_F, the heat released from the melt is caused by the temperature change of the melt and the phase transformation of the growing crystal. When the temperature drops between T_F and T_R, the heat released by phase transformation of the growing crystal is larger than the ability of heat released from the melt to the environment. Therefore, on the curve, the temperature is increasing at this stage. Finally, after T_R, again, the heat released from the melt is caused by the temperature change of the melt and the phase transformation of the growing crystal.

The most important stage that determines the final grain size is when the temperature drops between T_N and T_F. At this stage, the cooling curve starts to deflect because nuclei start to grow. Further growth leads to more latent heat and more deflection of the curve. Based on the free growth model [36, 42, 43], nucleations on substrates with various diameters starts to grow freely at different temperatures. The larger the substrate diameters are, the smaller the undercooling required. Therefore, the number of growing grains from T_N to T_F is increasing. Once the temperature reaches T_F, no further potential nucleation substrates can produce more grains freely, and the number of growing grains will be determined. Based on empirical studies of solidification behaviour [60, 154], the undercooling is the driving force and key factor for the liquid-solid transformation in a given alloy system. Smaller undercooling implies that less driving force is required, which, in turn, means more effective nucleation substrates are available in the melt.

In **Figure 4.1.3**, the cooling rates for both curves are approximately the same. However, the undercooling for the curve with melt shearing is smaller than the one without. Therefore, it is suggested that there are more growing grains in the one with melt shearing. As it is known, the number of growing grains can potentially determine the final grain size. Therefore, the grain size for the alloy with melt shearing should be smaller than the one without.

The difference in undercoolings between the alloy with and without melt shearing has been further confirmed by cooling curves of AZ91D alloy with different cooling rates in **Figure 4.1.5**, which shows the measured cooling curves for the AZ91 alloy melt with and without prior melt shearing. The melts were cast at 650 ℃ with various thermal insulations (6mm, 13mm, and 25mm in thickness). The cooling rates for the alloys with and without melt shearing with the same thickness of thermal insulation are approximately the same. The undercooling of the alloy with melt shearing is always smaller than that of the one without shearing in all three pairs. Therefore, a reasonable explanation for this phenomenon is that the melt shearing process introduces more effective nucleation substrates. Another finding from **Figure 4.1.5** is that higher cooling rates always lead to increased undercoolings for the ones without shearing. However, for those with shearing, the undercoolings are approximately the same. A summary of the cooling rates and the undercoolings of the measured cooling curves is provided in **Table 4.1**.

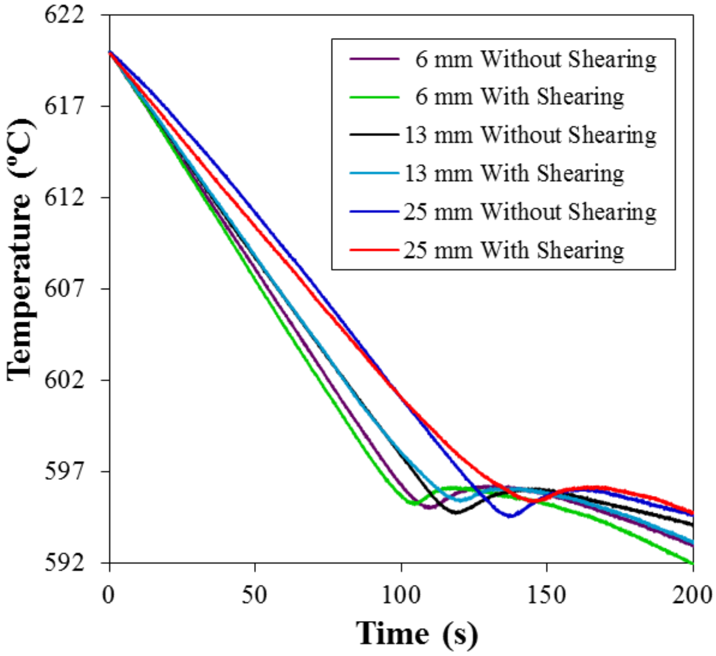

Figure 4.1.5 Portions of measured cooling curves for the AZ91D alloy melt with and without prior melt shearing. The melts were cast at 650 ℃ with various thermal insulations (6mm, 13mm, and 25mm in thicknesses).

Table 4.1 A comparison of cooling rates and undercoolings between AZ91D alloy with and without melt shearing in different conditions

Insulation	Condition	Cooling rate (K/s)	Undercooling (K)
6mm thick	Sheared	0.25	0.7
	None-Sheared	0.25	1.1
13mm thick	Sheared	0.22	0.7
	None-Sheared	0.22	1.3
25mm thick	Sheared	0.18	0.7
	None-Sheared	0.18	1.5

4.1.2. Grain structures for AZ91D with and without melt shearing

A reasonable prediction has been made in 4.1.1 based on the understanding of the relationship between undercooling and the number density of nucleation substrates, which is that the grain size for the alloy with melt shearing should be smaller than the one without. In order to check such a prediction, further experimental evidence is required. The most direct evidence comes from the measured grain sizes of the cast ingots used for cooling curve measurement, as shown in **Figures 4.1.6**, **4.1.7**, and **4.1.8**.

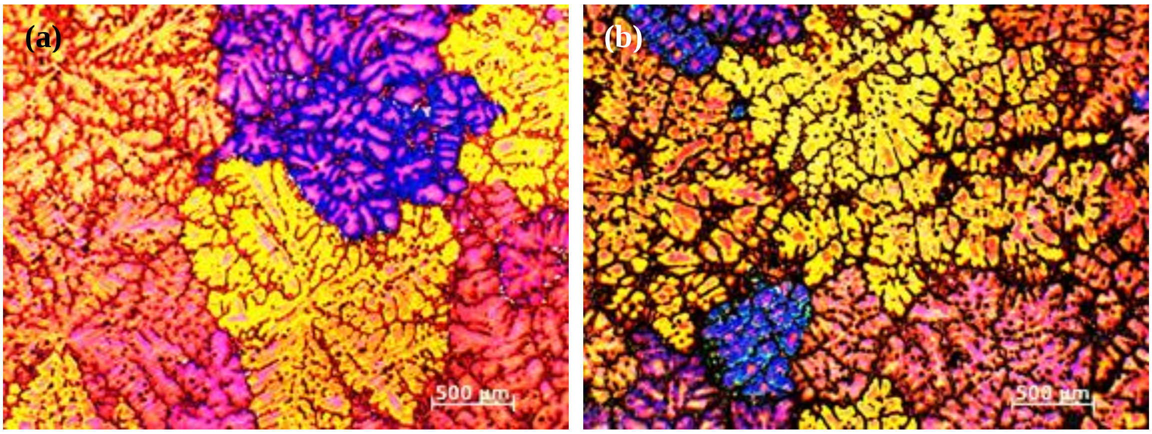

Figure 4.1.6 Optical micrographs showing microstructures in samples of AZ91D alloy samples (a) without and (b) with shearing. The melts were cast at 650 ℃ into a crucible covered with 6mm insulation.

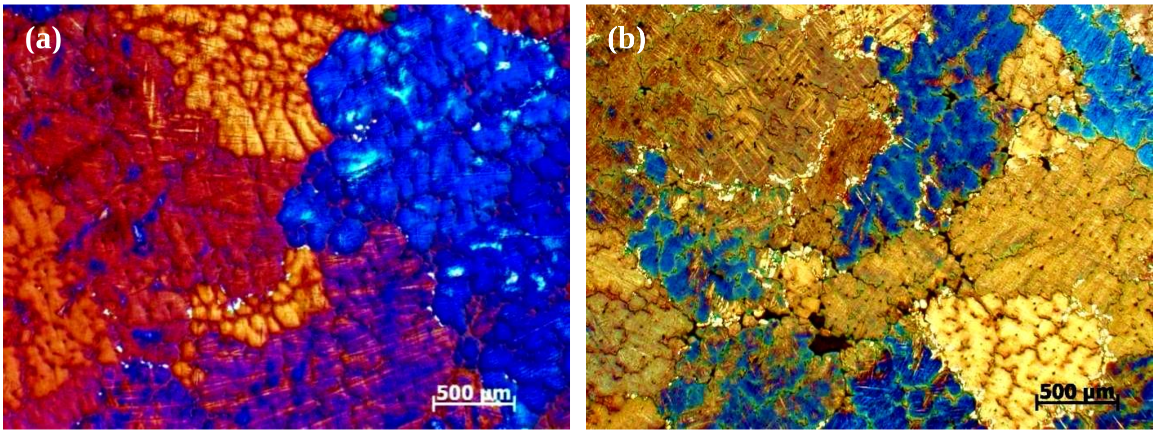

Figure 4.1.7 Optical micrographs showing microstructures in samples of AZ91D alloy samples (a) without and (b) with shearing. The melts were cast at 650 ℃ into a crucible covered with 13mm insulation.

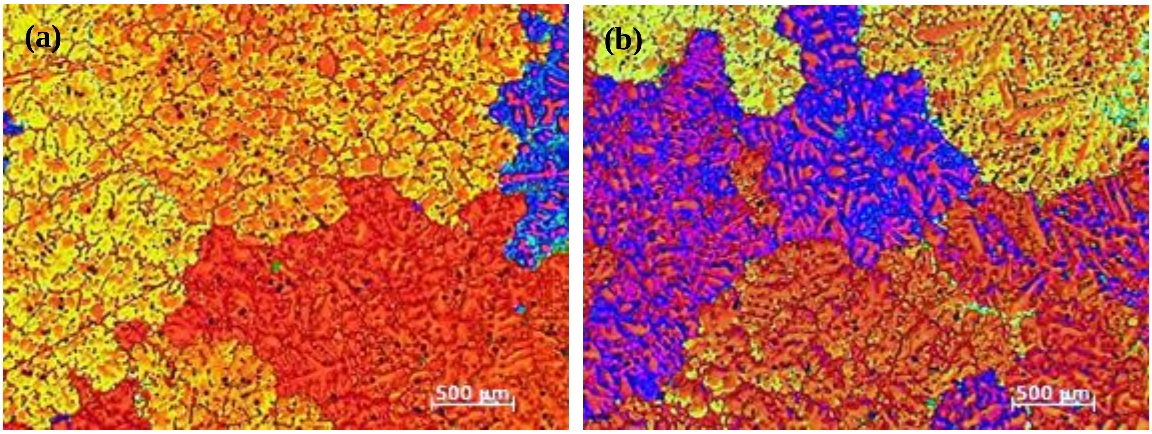

Figure 4.1.8 Optical micrographs showing microstructures in samples of AZ91D alloy samples (a) without and (b) with shearing. The melts were cast at 650 ℃ into a crucible covered with 25mm insulation.

As shown in **Table 4.2**, the grain sizes of the alloys with melt shearing are considerably smaller than those without intensive melt shearing. The maximum difference of the grain sizes of the cast ingots without melt shearing can be as much as 818μm. However, the maximum difference of the grain sizes of the cast ingots with melt shearing is only 164μm. From the data, a reasonable conclusion is that the melt shearing process enhances nucleation by introducing more effective nucleation substrates.

Table 4.2 A comparison of cooling rates, undercoolings, and grain sizes between AZ91D alloy with and without melt shearing under different conditions.

Insulation	Condition	Cooling rate (K/s)	Grain Size (μm)
6mm thick	Sheared	0.25	1178
	None-Sheared	0.25	1643
13mm thick	Sheared	0.22	1210
	None-Sheared	0.22	2005
25mm thick	Sheared	0.18	1342
	None-Sheared	0.18	2461

4.1.3. Results of MgO particles in AZ91D with and without melt shearing

According to the results in section 4.1.1 and 4.1.2, the melt shearing process can enhance nucleation by introducing more effective nucleation substrates. However, the mechanism of melt shearing for grain refinement is still unclear. In order to find out how melt shearing introduces more nucleation substrates, optical micrograph and SEM micrographs are provided. In section 2.2.2, Fan and his co-workers [115] suggested that MgO particles have acted as the nucleation substrates in magnesium alloys without zirconium addition because a fine orientation relationship has been discovered at the interface of α-Mg / MgO. Therefore, if MgO particles are the nucleation substrates in this experiment, it is highly possible to find more MgO particles in the alloy with melt shearing than those in the alloy without melt shearing. **Figure 4.1.9** is an optical micrograph showing the MgO films found in the sample collected at 650 ℃ by the pressurized filtration of AZ91D melts without intensive melt shearing. **Figure 4.1.10** is a SEM micrograph showing the typical morphology of the MgO films found in the sample.

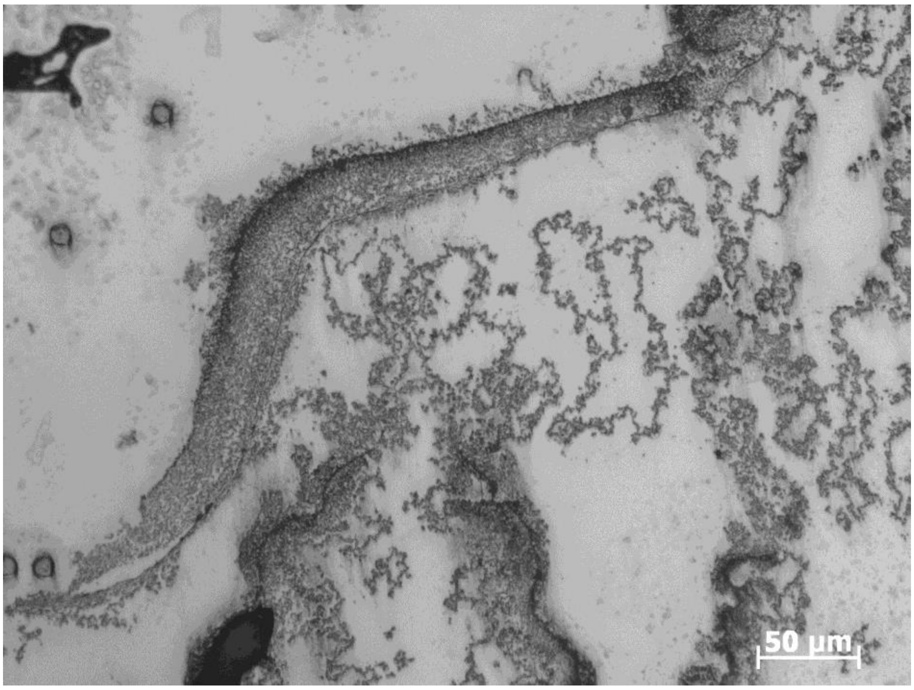

Figure 4.1.9 Optical micrograph showing the MgO films found in the sample collected at 650 ℃ by the pressurized filtration of AZ91D sample without intensive melt shearing.

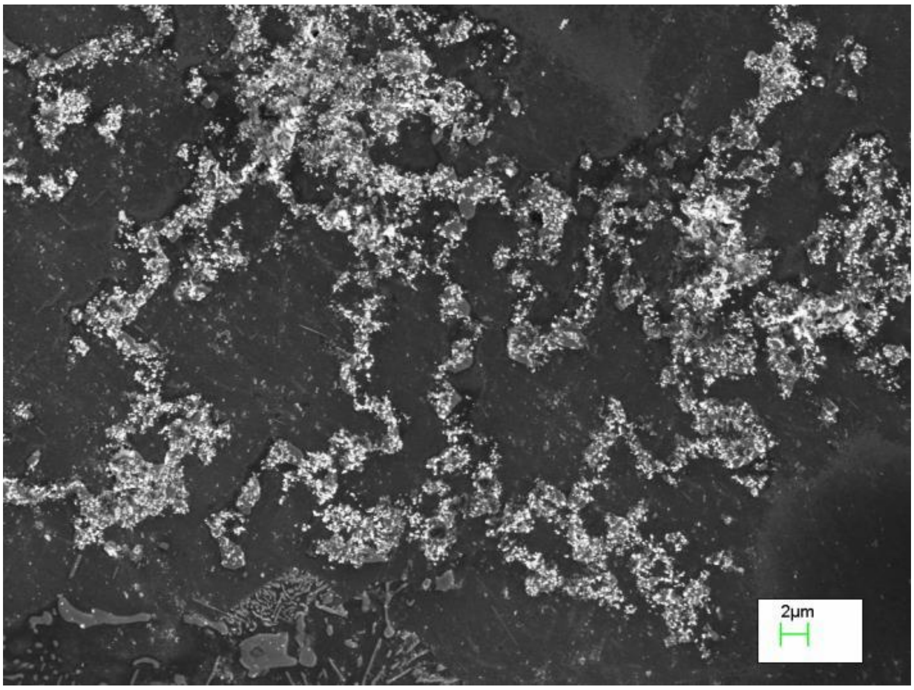

Figure 4.1.10 SEM micrograph showing the MgO films found in the sample collected at 650 ℃ by the pressurized filtration of AZ91D sample without intensive melt shearing.

As shown in both figures, for the sample without intensive melt shearing, the MgO appears as films composed of many individual particles. These films are usually more than ten microns in length. If one of the particles in the film becomes a nucleation substrate and starts to grow, latent heat will begin to release due to the growth and the film will be locally heated up at the moment, so that no further particles in this film can become effective nucleation substrates. This means that there will be only one effective nucleation substrate in each MgO film. **Figure 4.1.11** is a SEM micrograph showing the morphology of the MgO particles collected at 650 ℃ by the pressurized filtration of the AZ91D sample with intensive melt shearing at 650 ℃ before filtration. Compared with the sample without shearing, the one with intensive melt shearing only contains individual MgO particles. No MgO film has been found in the sample with melt shearing. This means that the MgO films in the melt are dispersed into individual particles after intensive melt shearing considering the strength among the particles which form the films are relatively weak. Therefore, it is suggested that the melt shearing process can enhance nucleation by dispersing MgO films into individual MgO particles and distributing the particles in the melt homogeneously.

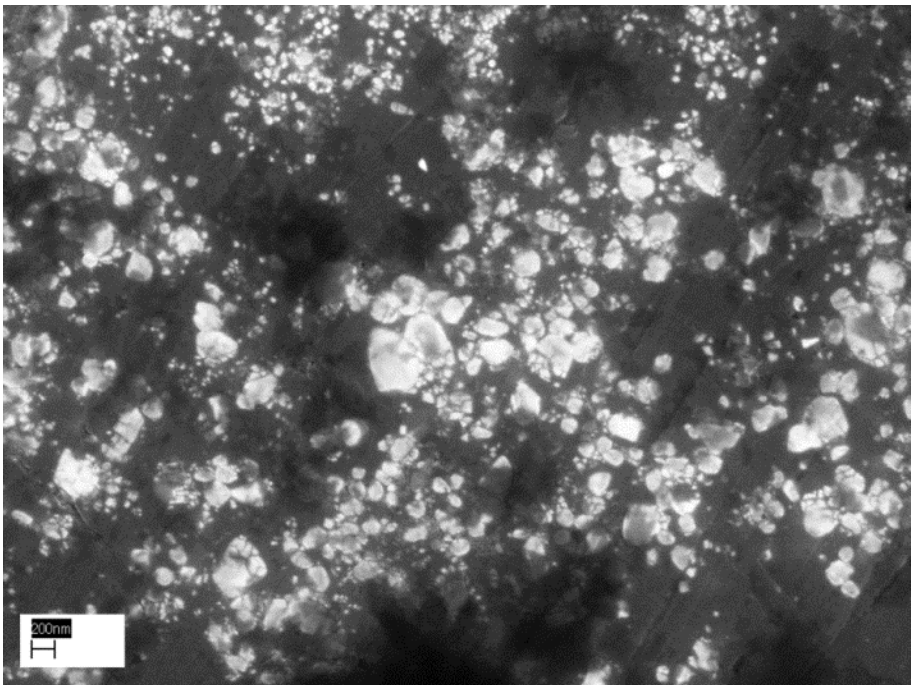

Figure 4.1.11 SEM micrograph showing the morphology of the MgO particles collected at 650 ℃ by the pressurized filtration of the sheared AZ91D alloy melt. The alloy melt was sheared at 650 ℃ and 800rpm for 45 seconds before filtration.

For further analysis, the number density of potential nucleation substrates is required. **Figure 4.1.12** shows the measured size distribution of nucleant MgO particles in the sheared AZ91D alloy melt by the pressurized filtration. The number of total measured particles is 1828, which is large enough to provide the tendency of the size distribution. As shown in the figure, the measurement exhibits a tendency of log-normal distribution. The measurement of particle size distribution has also been fitted by a general log-normal function given by

$$N(d) = \frac{N_0}{\sigma d\sqrt{2\pi}} \exp - \left(\frac{\ln d - \ln d_0}{2\sigma^2}\right)^2 \tag{4. 1}$$

where d is the particle diameter, d_0 is the geometric mean diameter, σ is the geometric standard deviation, N_0 is the total number of particles, and $N(d)$ is the number of particles of diameter between d and $d + \Delta d$. In the fitting, the geometric mean diameter d_0 is 0.07 µm, the geometric standard deviation σ is 0.45, and the total number of particles N_0 is 2000.

The measured data and the fitting in **Figure 4.1.12** is identical to the previous measurement in the publications [36, 42, 43], which suggest a log-normal distribution of effective nucleation particles.

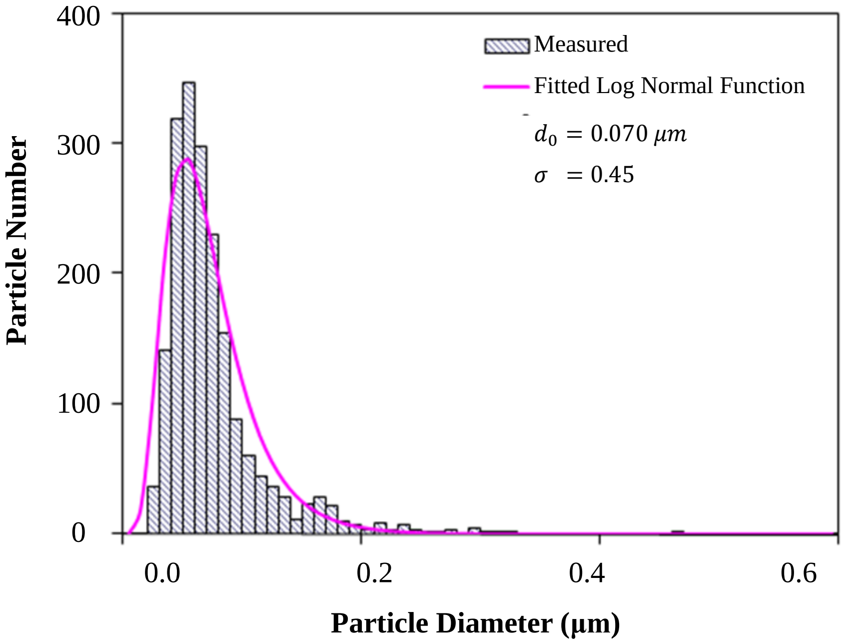

Figure 4.1.12 Measured size distribution of MgO particles in the sheared AZ91D alloy melt by the pressurized filtration.

4.1.4. Summary

This experiment is mainly a comparison of AZ91D alloy with and without intensive melt shearing by the twin screw device, and the most important objective of this experiment is to explain the mechanism of intensive melt shearing. Based on the experimental results, it is suggested that the melt shearing process can enhance nucleation by dispersing MgO films into individual MgO particles and distributing the particles in the melt homogeneously. The second objective of this experiment is to investigate the relationship between undercooling and the grain size and the results show that smaller undercoolings most likely lead to smaller grain sizes. Finally, the experiment also indicates that MgO particles have acted as the nucleation substrates in magnesium alloys without zirconium addition.

4.2. The Effect of Solute on Grain Refinement

The objective of this experiment is to investigate the role of solute on the grain structures of magnesium alloys. In previous literatures, solute has been considered as one of the key factors in columnar-equiaxed transition [55]. In the previous model [18, 52, 53], solute has been used to calculate the growth restriction factor, Q, and $1/Q$ has a linear relationship with grain sizes. In this experiment, the microstructures of TP-1 samples of Mg-Al and Mg-Zn binary alloys with various compositions have been studied, in order to study the effect of solute on grain structures of magnesium alloys.

4.2.1. TP-1 Casting for Mg-Al Binary Alloys

Pure magnesium and Mg-Al binary alloys with various concentrations of aluminium (0.1, 0.3, 1, 3, 9wt%) have been cast following typical TP-1 test procedures with 10 K superheat and melt shearing, and at 10K, 30K, and 50K superheat without melt shearing. **Figure 4.2.1** shows the microstructures of the cross sections of pure magnesium and Mg-Al binary alloys with 10 K superheat. In this figure, the only difference between the samples is the composition of aluminium. As it is shown, the weight percentages of aluminium contained in the alloys have significant influence on the final grain structures. The linear intercept method has been applied to measure grain sizes with these images. The results show a significant decrease in grain size with the increased concentration of aluminium. The measured linear intercept length of Mg-Al binary alloy on cross sections have been plotted against composition of aluminium and $1/Q$ in **Figure 4.2.2** and **4.2.3**, respectively. As shown in these two figures, the measured data has an inverse relationship against composition and a linear relationship against $1/Q$. Therefore, it appears that the quantity of aluminium does have a certain influence on grain sizes of magnesium alloys, as it has been stated in Easton and StJohn's model [18, 52, 53]. There is one thing that needs to be noted, which is that all thedata is measured from the intercept lengths of the cross sections.

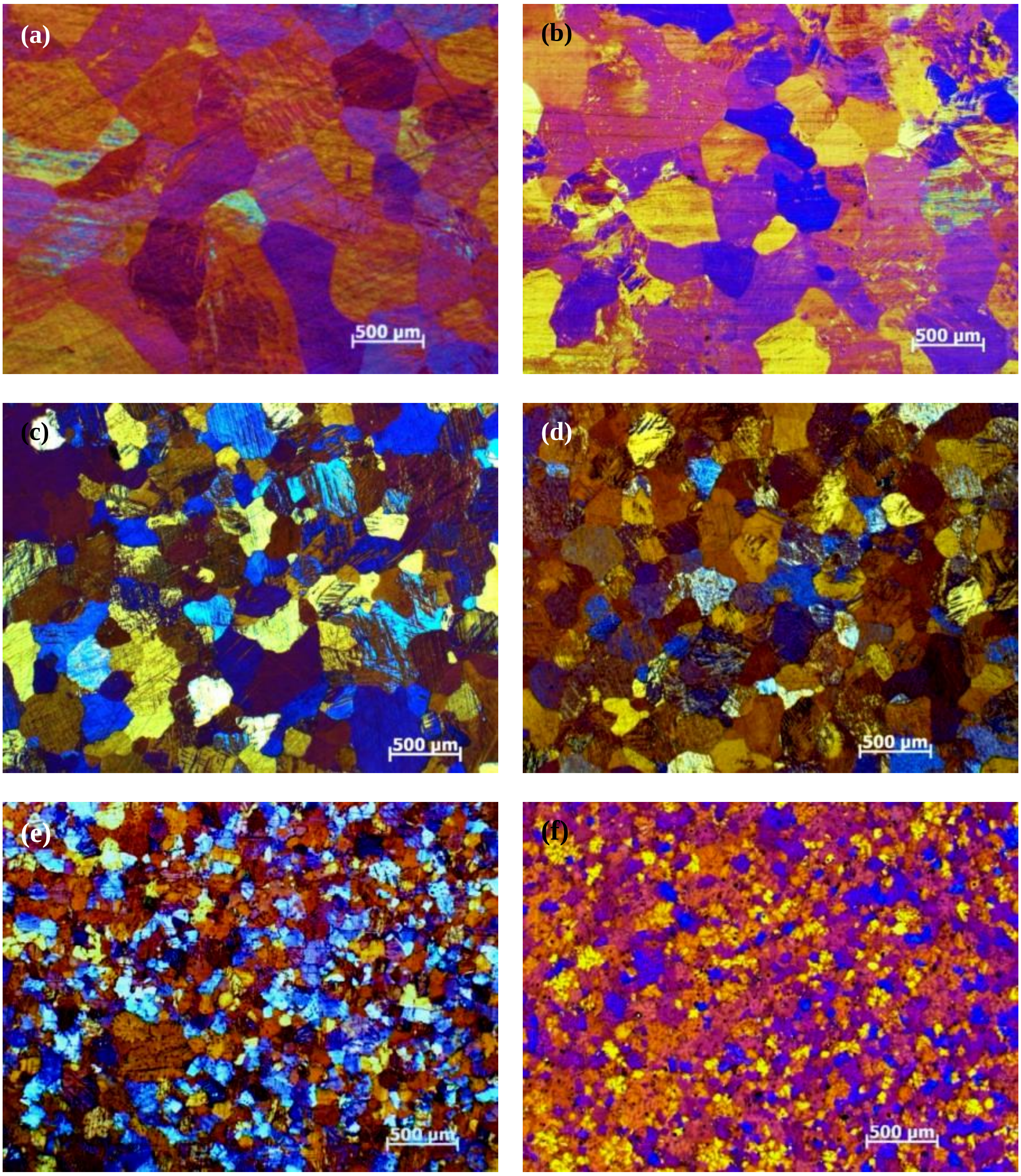

Figure 4.2.1 Microstructures of cross sections of Mg-Al binary alloys without shearing showing the effect of Al contents on grain structure: (a) pure magnesium cast at 660 ℃; (b) Mg-0.1wt%Al cast at 659 ℃; (c) Mg-0.3wt%Al cast at 659 ℃; (d) Mg-1wt%Al cast at 658 ℃; (e) Mg-3wt%Al cast at 645 ℃; (f) Mg-9wt%Al cast at 611 ℃. For each alloy, the pouring temperature is 10 K above the liquidus of the alloy.

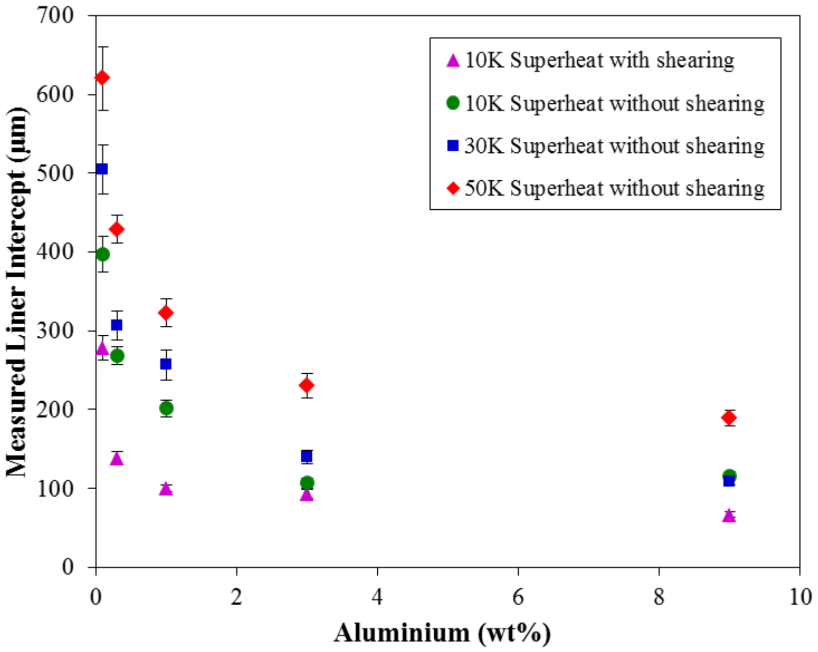

Figure 4.2.2 Measured linear intercept lengths of Mg-Al binary alloys on cross sections as a function of composition of aluminium, showing the effects of aluminium content, superheat, and intensive shearing on grain size.

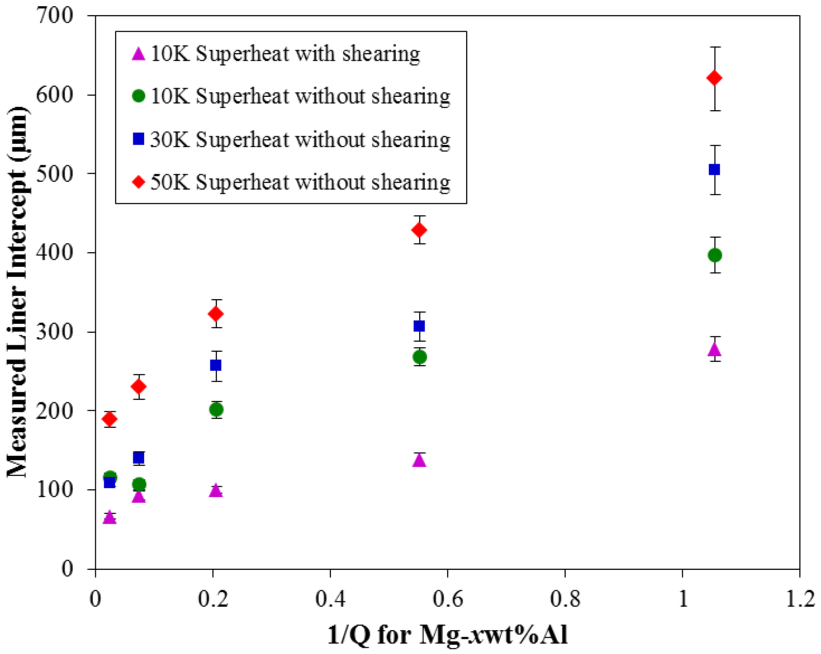

Figure 4.2.3 Measured linear intercept lengths of Mg-Al binary alloys on cross sections as a function of $1/Q$, showing the effects of aluminium content, superheat, and intensive shearing on grain size.

There seems to be no reason to doubt that these measured linear intercept lengths are the actural grain sizes. However, when the microstructures of the vertical sections are shown, the linear relationship between $1/Q$ and the so-called ‘grain sizes’ might be questionable. As shown in **Figure 4.2.4**, on the cross section, all the grains seem to be equiaxed grains. However, in the vertical sections, it is easy to see that they are actually columnar grains. Therefore, in order to determine whether the measured linear intercept lengths are grain sizes, both cross sections and vertical sections need to be examined. The measured linear intercept lengths can be considered as grain size only when the microstructures are equiaxed grains in both cross section and vertical section.

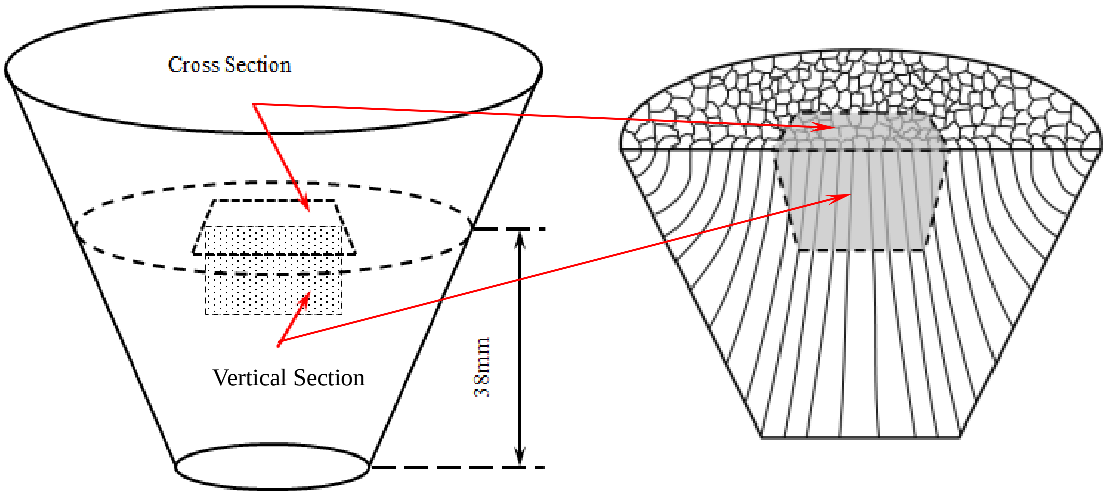

Figure 4.2.4 Schematic illustrations of TP-1 casting sample and the microstructure of the sample.

A good example is shown in **Figure 4.2.5**. This figure is a comparison of the microstructures of Mg-1wt%Al binary alloy vertical sections cast at 10 K superheat with and without shearing. It is easy to find that the sample in **Figure 4.2.5(a)** contains columnar grains, while the one in **Figure 4.2.5(b)** contains only equiaxed grains. Therefore, the measured linear intercept length of the cross section of the sample in **Figure 4.2.5(a)** can’t be simply considered as grain size. In fact, it is not even the columnar width but a value with no clear physical significance. A comparison between such values is completely meaningless. It is then proposed that for TP-1 samples, both the cross section and vertical section of these samples need to be examined before any measurement has been made.

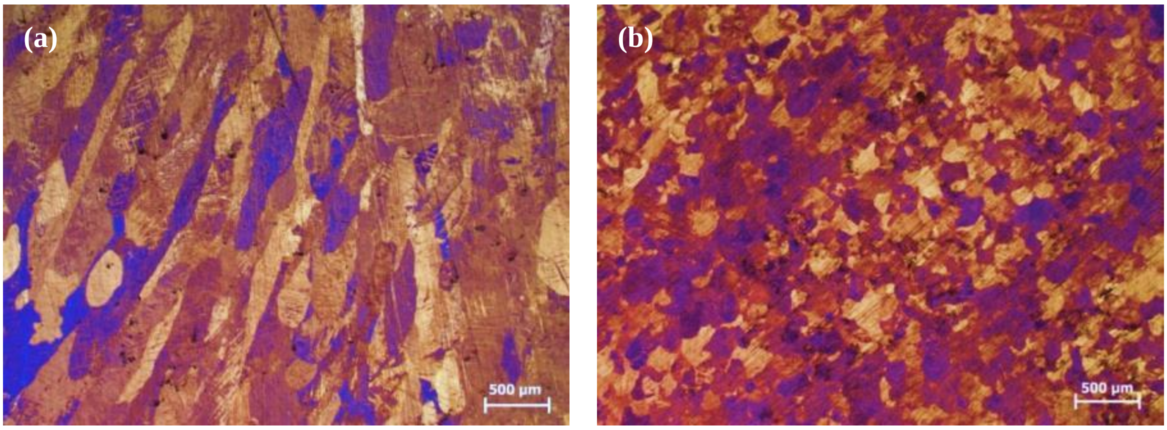

Figure 4.2.5 Microstructures of Mg-1wt%Al binary alloys vertical sections cast at 658 ℃ (10K superheat): (a) without shearing, and (b) with shearing.

Figure 4.2.5 (a) is not the only case. Most data with low aluminium content (less than 1 wt%) fits in such a situation. Therefore, the data can only be regarded as incorrect data rather than grain sizes. As shown in **Figure 4.2.6** and **4.2.7**, only the data outside the dashed box are actual grain sizes.

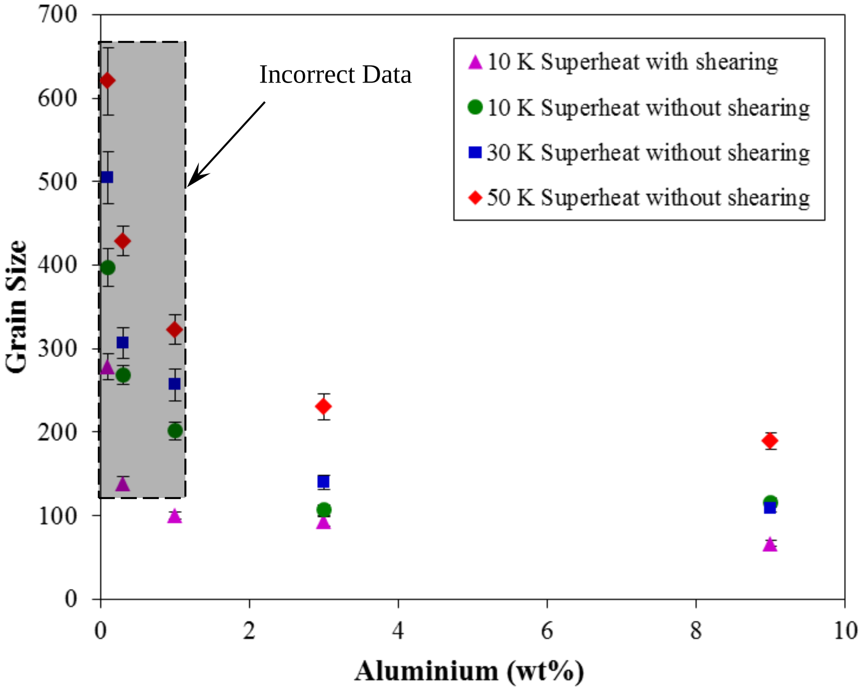

Figure 4.2.6 Grain sizes of Mg-Al binary alloys as a function of composition of aluminium, showing the effects of aluminium content, superheat, and intensive shearing on grain size.

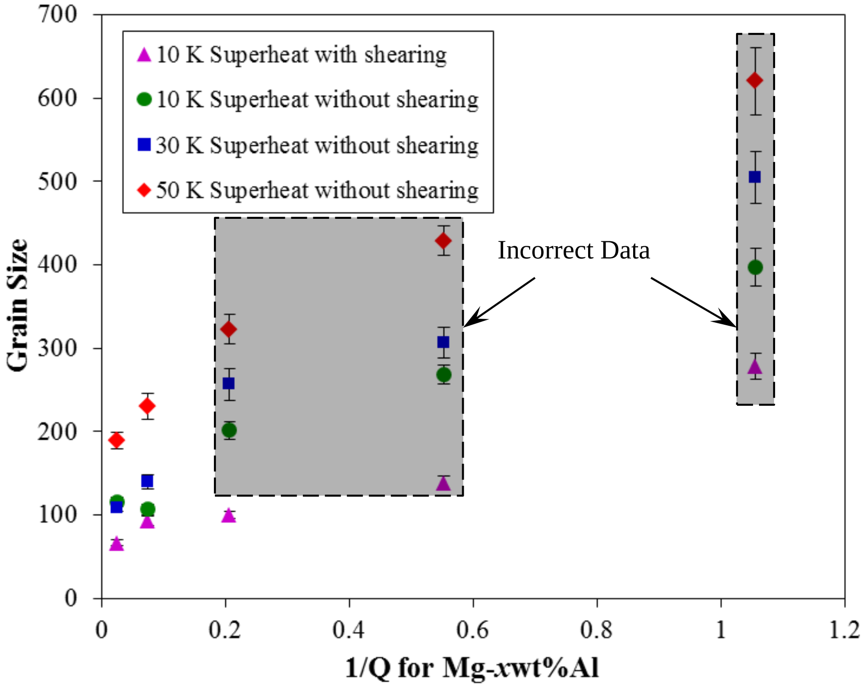

Figure 4.2.7 Grain sizes of Mg-Al binary alloys as a function of $1/Q$, showing the effects of aluminium content, superheat, and intensive shearing on grain size.

In **Figure 4.2.6** and **4.2.7**, the data in the dashed boxes are not actual grain sizes. Therefore, the inverse relationship between grain size and composition is debatable and the linear relationship between grain size and $1/Q$ doesn't seem to exist for Mg-Al binary alloy. **Table 4.3** shows the grain sizes for Mg-3wt%Al and Mg-9wt%Al under various casting conditions. The differences between grain sizes under the same condition are believed to be caused by composition. Since such differences are relatively small, it is suggested that the major function of solute is to cause columnar to equiaxed transition (CET), after CET, solute has little effect on grain size.

Table 4.3 Grain size for Mg-3wt%Al and Mg-9wt%Al with various casting conditions.

Al (wt%)	**10K Superheat**		**30K Superheat**	**50K Superheat**
	With Shearing	Without Shearing	Without Shearing	Without Shearing
3	93.13968	106.8601	139.6719	230.3492
9	66.83963	115.7882	108.9663	189.3461

4.2.2. TP-1 Casting for Mg-Zn Binary Alloys

The experimental results of Mg-Al binary alloys show that the microstructure of Mg-Al binary alloy with low aluminium content contains columnar grains. Therefore, the measured linear intercept lengths cannot simply be considered as grain sizes. In order to find out whether this is general in magnesium alloys with other elements, Mg-Zn binary alloys with various concentrations of zinc (0.1, 0.3, 1, 3, 9wt%) have been cast following typical TP-1 test procedures at 10K superheat with shearing, and at 10K, 30K, and 50K superheat without shearing. As shown in **Figure 4.2.8**, even when the microstructures of the cross sections of Mg-0.3wt%Zn and Mg-1wt%Zn seem to contain fully equiaxed grains only, the vertical section still shows that the microstructures of the sample contain columnar grains.

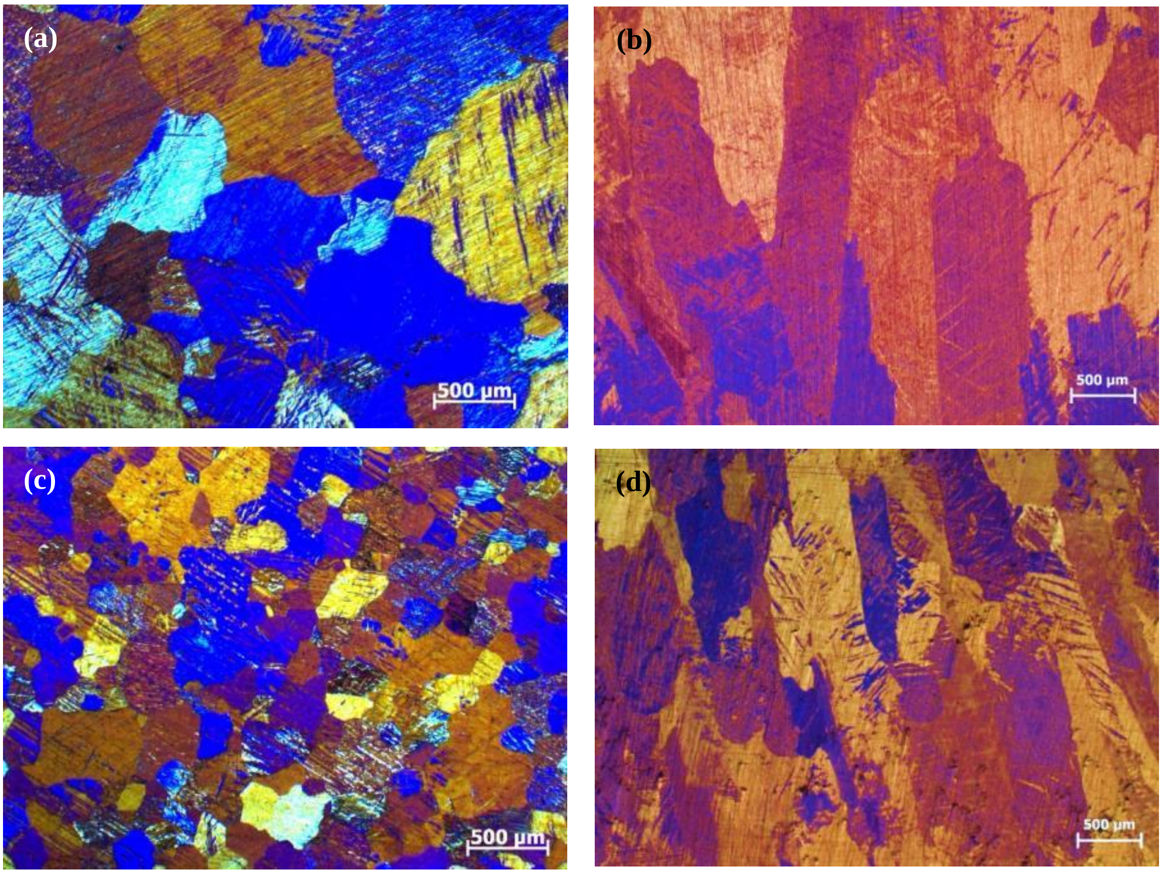

Figure 4.2.8 Microstructures of Mg-0.3wt%Zn binary alloy cross (a) and vertical (b) sections cast at 679 ℃ (30K superheat) and Mg-1wt%Zn binary alloy cross (c) and vertical (d) sections cast at 678 ℃ (30K superheat) without shearing. All samples are without shearing.

The microstructures of Mg-3wt%Zn binary alloy cast at 30 K superheat without shearing, as shown in **Figure 4.2.9**, show fully equiaxed grains (even though some of the grains are elongated) in both cross and vertical sections.

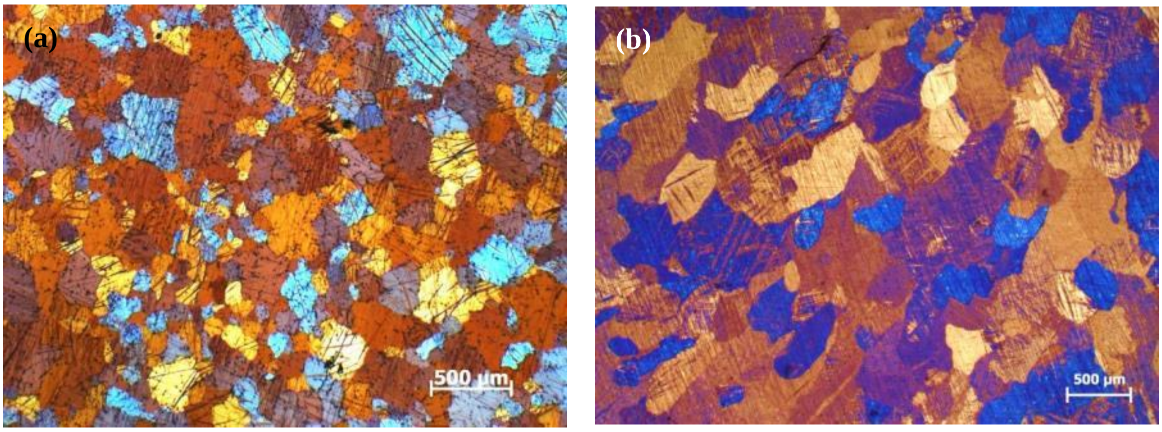

Figure 4.2.9 Microstructures of Mg-3wt%Zn binary alloy cross (a) and vertical (b) sections cast at 665 ℃ (30K superheat) without shearing.

Based on the results in **Figure 4.2.8** and **4.2.9**, it can be seen that Mg-Zn binary alloy share the similar phenomenon as the Mg-Al binary alloy. For low concentration Mg-Zn binary alloys, the microstructures are fully columnar and the measured linear intercept lengths from the cross sections of the samples cannot be simply considered as grain sizes.

The relationship between grain sizes and composition of zinc is shown in **Figure 4.2.10** and the relationship between grain sizes and $1/Q$ is shown in **Figure 4.2.11**. In both figures, the measured data in the dashed boxes are not actual grain sizes, but values with no clear physical significance. Therefore, again, the linear relationship between grain sizes and $1/Q$ is debatable. The difference between grain sizes of Mg-3wt%Zn and Mg-9wt%Zn under the same casting conditions is less than 50μm. Therefore, it is recognized that composition doesn't have as much influence as suggested in various publications [18]. On the other hand, as Hunt [50] suggested, composition is only one of the key factors for columnar equiaxed transition. The present experimental results support the suggestion.

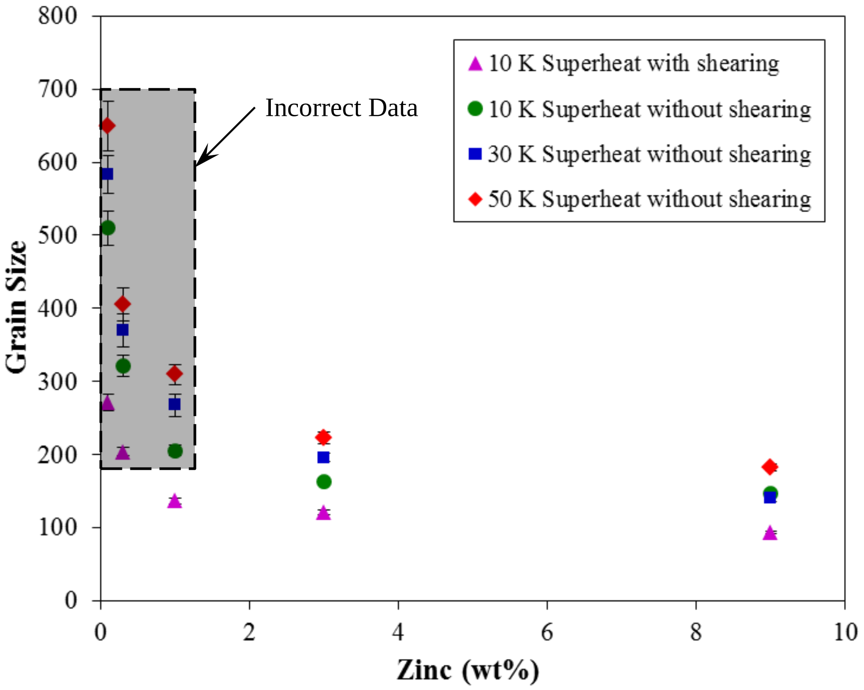

Figure 4.2.10 Grain size of Mg-Zn binary alloys as a function of composition of zinc, showing the effects of zinc content, superheat, and intensive shearing on grain size.

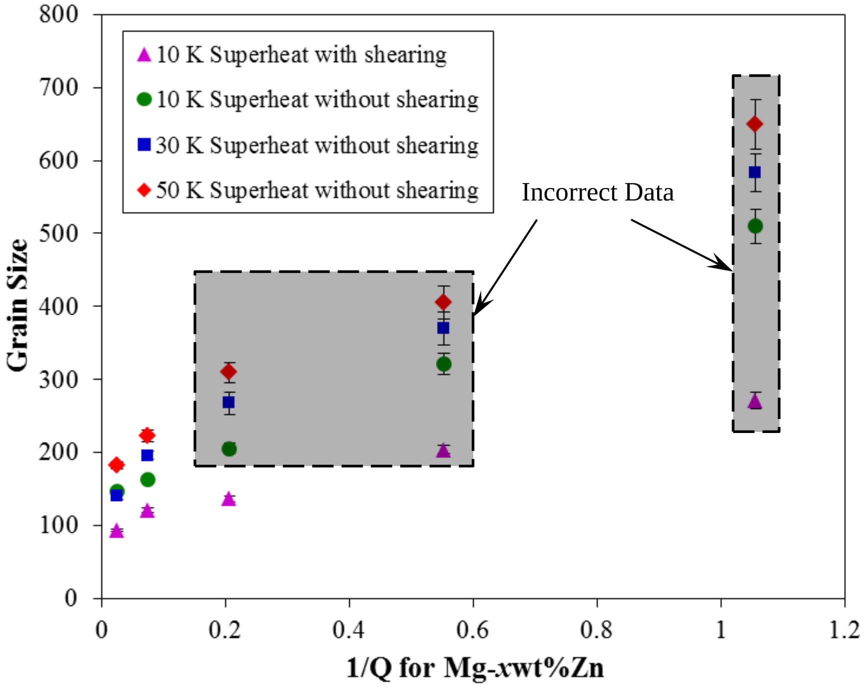

Figure 4.2.11 Grain size of Mg-Zn binary alloys as a function of $1/Q$, showing the effects of zinc content, superheat, and intensive shearing on grain size.

4.2.3. Summary

The aim of this experiment is to find out the role of solute in grain refinement during solidification. In the present experiment, the microstructures of Mg-Al and Mg-Zn binary alloys with various concerntration of aluminium or zinc have been examined. Some researchers [18, 52, 53] suggested a linear relationship between grain sizes and $1/Q$, and even worked out an empirical formula for that relationship. However, based on the present experimental results, such a suggestion is debatable. There appears to be a linear relationship between measured linear intercept lengths and $1/Q$. It is, however, recognized that not all measured linear intercept lengths can be considered as grain sizes, because the microstructures of the magnesium alloys with low solute concentration may contain columnar grains and this may cause an incorrect measurement for grain sizes. Therefore, these measurements may not have a clear physical significance. According to empirical understanding, solute may potentially have two effects on microstructure, causing columnar to equiaxed transition (CET), and decreasing grain sizes. Based on the results in this experiment, for magnesium alloys with low solute content, solute is only one of the key factors for columnar to equiaxed transition. The effect of solute on grain sizes may only be effective after a critical composition when the grains in the microstructure of the casting are fully equiaxed.

4.3. Magnesium Alloys Grain Refined by MgO Inoculation

The primary objective of this set of experiments is to develop a new grain refiner for magnesium alloys, especially the aluminium bearing magnesium alloys. A series of selected materials has been tested with various inoculation additions and, among them, MgO nano particles showed the best refinement effect on the grain structures of the aluminium bearing magnesium alloys. In section 4.3.1, MgO nano particles have been examined in detail with SEM. The effect of grain refinement on Mg-Al binary alloys by MgO nano particle inoculation is shown in section 4.3.2. In section 4.3.3, MgO nano particles were applied to commercial alloy AZ91D. MgO nano particles have also been added in AZ91D alloy to make an AZ91D-5wt%MgO master alloy. The effect of grain refinement achieved by this master alloy on AZ91D is shown in section 4.3.4.

4.3.1. MgO Powder

The morphology of MgO nano particles used in this experiment is shown in **Figure 4.3.1(a)**. As shown in the photograph, most of the MgO nano particles are typically faceted, cubic with sharp interfaces. This is different from the endogenous MgO particles shown in **Figure 4.3.1(b)**.

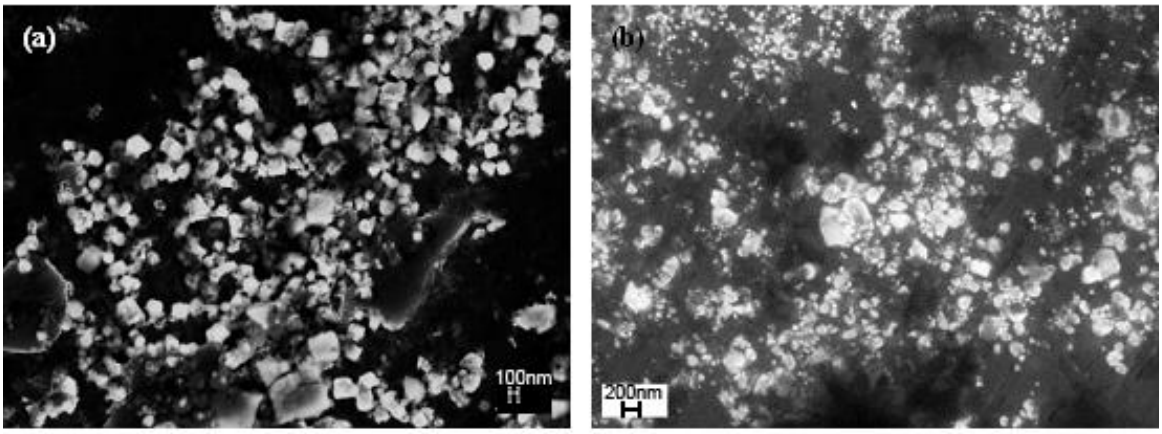

Figure 4.3.1 SEM micrograph showing the morphology of (a) MgO nano particles dropped on a conductive base with Au sprayed on the surface, and (b) endogenous MgO particles collected at 650 ℃ from AZ91D alloy melt by pressurized filtration.

4.3.2. Mg-Al Binary Alloy Grain Refined by MgO Inoculation

The MgO nano particles have been added in Mg-Al binary alloys with various concentrations of aluminium (0.1, 0.3, 1, 3, 9wt%), in order to find out whether the particles can refine aluminium bearing magnesium alloy. As shown in **Figure 4.3.2**, the microstructures of Mg-1wt%Al and Mg-9wt%Al inoculated with 1000ppm MgO nano particles are much finer than those without MgO inoculation. Fully equiaxed grains are observed on both cross and vertical sections of the Mg-1wt%Al and Mg-9wt%Al alloys inoculated with 0.1wt% MgO nano particles.

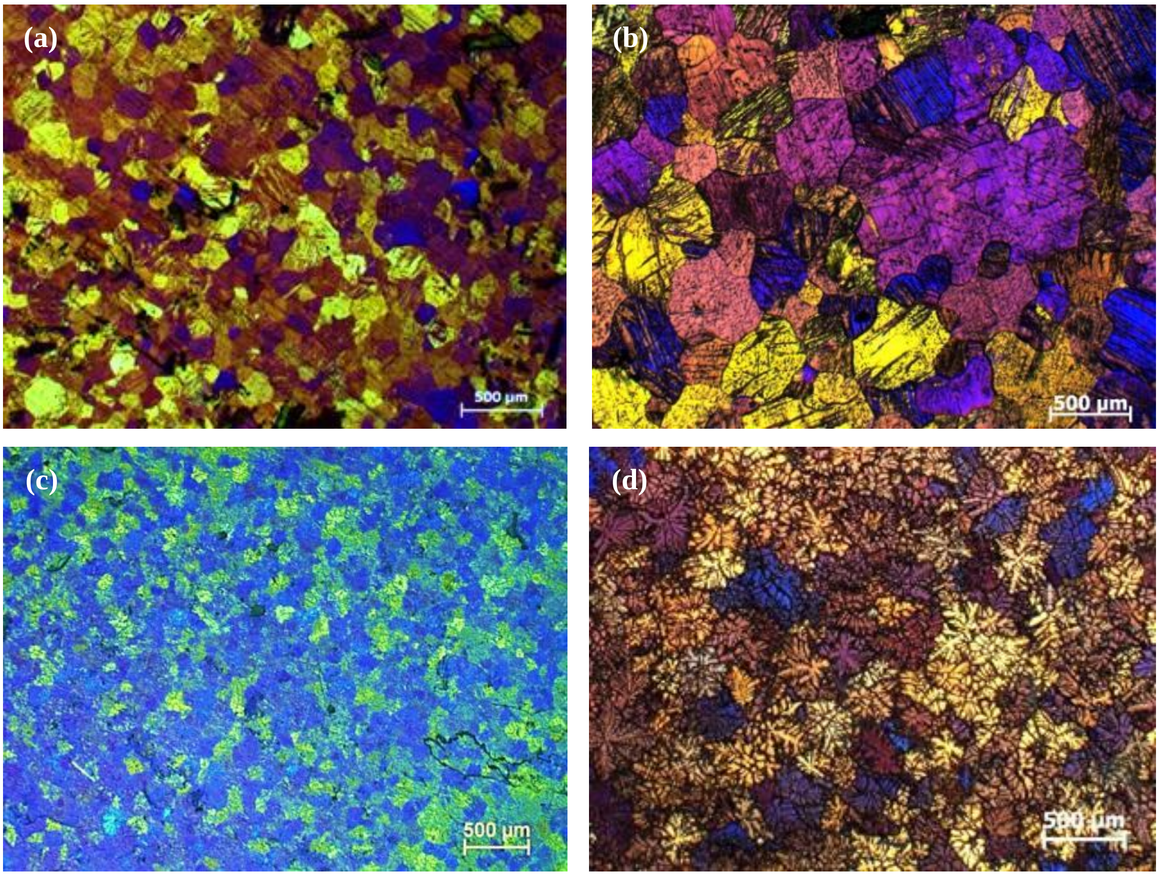

Figure 4.3.2 Microstructures of Mg-Al binary alloy: TP-1 cast at 50 K superheat showing the effect of MgO nano particle inoculation on grain structure: (a) Mg-1wt%Al with 0.1wt% MgO nano particles inoculated, (b) Mg-1wt%Al without MgO particle inoculation, (c) Mg-9wt%Al with 0.1wt% MgO nano particles inoculated, and (d) Mg-9wt%Al without MgO particle inoculation.

Figure 4.3.3 presents the effect of grain refinement achieved by 0.1wt% MgO inoculation on Mg-Al binary alloys with various concentrations of aluminium. According to the results, 0.1wt% MgO nano particles have significantly refined the grain structures in the samples. The grain sizes measured on the samples with MgO inoculation are reduced to a level below 200µm. Therefore, it is proposed that MgO nano inoculant can be used as a grain refinement addition for Mg-Al binary alloys.

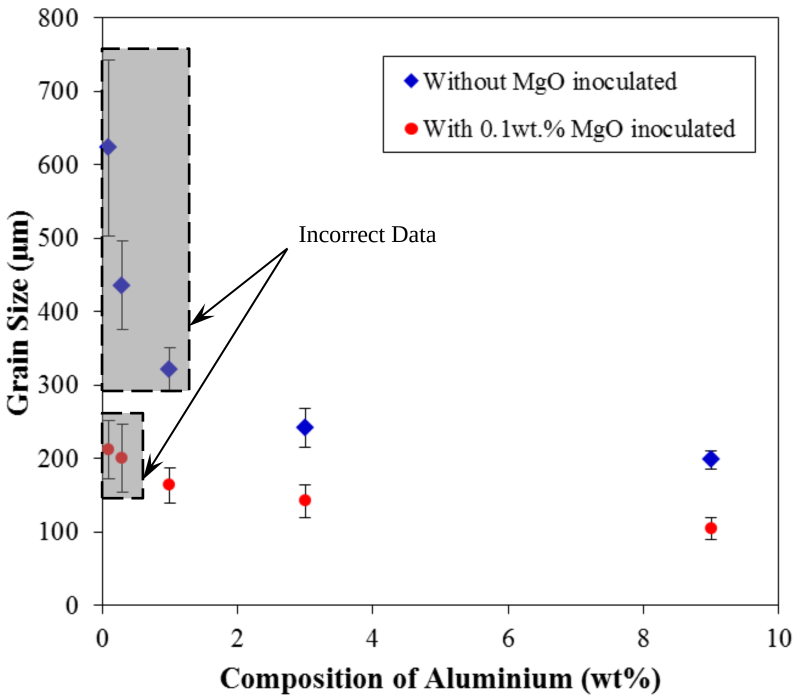

Figure 4.3.3 Grain size of Mg-Al binary alloys TP-1 samples with 50 K superheat as a function of composition of aluminium, showing the effects of MgO nano particle inoculation on grain size. (The data in the boxes are not grain sizes due to the existence of columar structures.)

Although the microstructures of the Mg-Al binary alloys show significant refinement, evidence is still needed to confirm that the added MgO particles are actually in the melt. **Figure 4.3.4** shows the MgO particles collected by the pressurized filtration of the Mg-9wt%Al alloy melt inoculated with 0.1wt% MgO nano particles. As shown in the photograph, the collected MgO particles are typically faceted, cubic with sharp interfaces. The morphology of these particles is consistent with that of the particles in **Figure 4.3.1(a)**. This is very evident that the collected MgO nano particles in **Figure 4.3.4** are the inoculated MgO nano particles and the MgO nano particles actually existed in the Mg-9wt%Al alloy melt before pouring. Therefore, it is concluded that the grain refinement of the microstructures of Mg-Al binary alloys is caused by MgO inoculation.

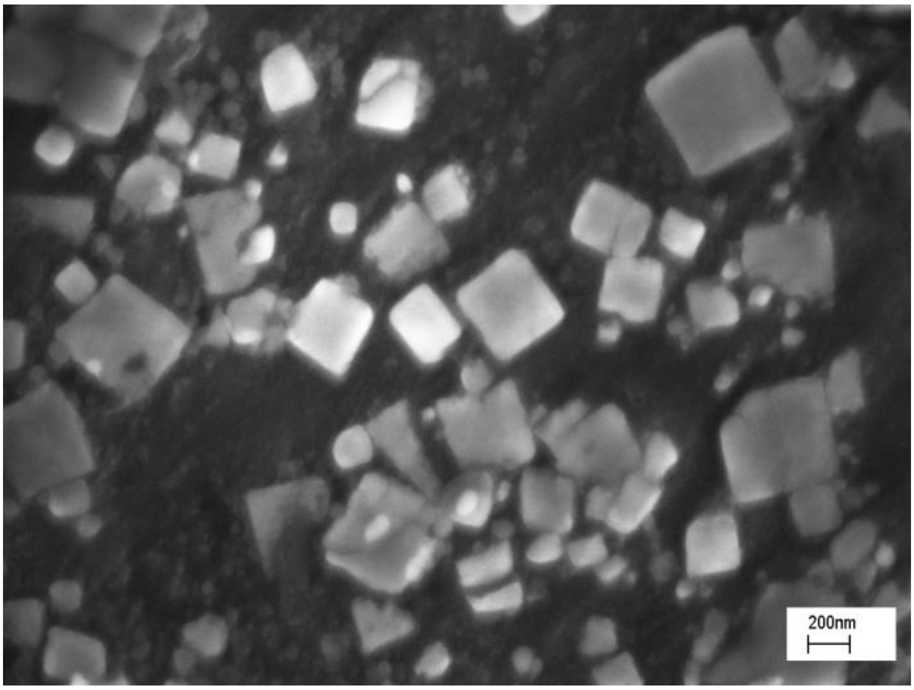

Figure 4.3.4 SEM micrograph showing the morphology of the MgO nano particles collected at 650℃ by the pressurized filtration of the Mg-9wt%Al alloy melt inoculated with 0.1wt% MgO nano particles.

4.3.3. AZ91D Commercial Alloy Grain Refined by MgO Inoculation

According to the results in 4.3.2, the microstructures of Mg-Al binary alloys are significantly refined with 0.1wt% MgO particle inoculation. However, it is still unknown whether the MgO inoculation can be used to refine commercial magnesium alloys. Therefore, MgO nano particles were also added to AZ91D commercial alloy. As shown in **Figure 4.3.5**, the grain structure of the sample with 100ppm MgO inoculation is much finer than the one without. This means that MgO inoculation works well to refine AZ91D commercial alloy. **Figure 4.3.6** shows the grain sizes of AZ91D alloys with various amounts of MgO inoculation. It can be seen that the grain refinement occurs at the level as small as 100ppm in the melt. The raise of MgO inoculation level seems not to increase the refinement effect significantly.

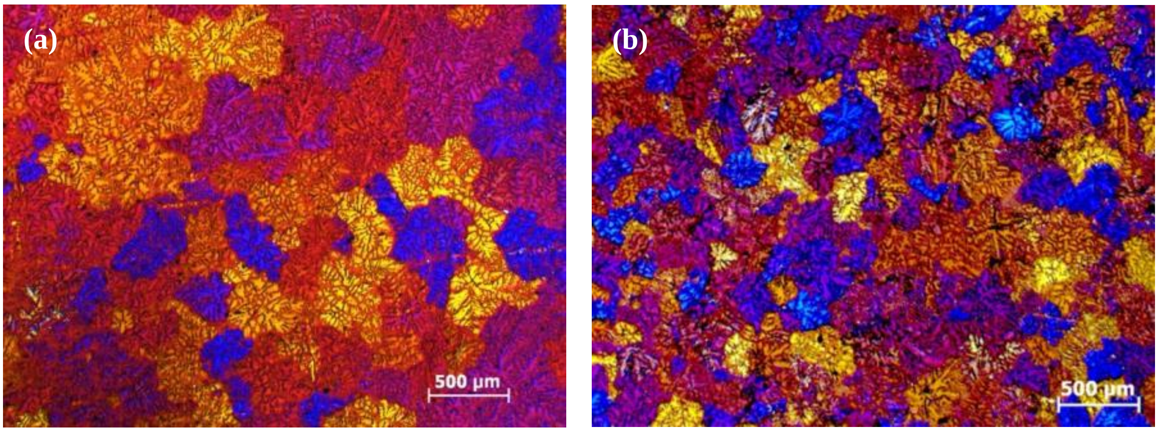

Figure 4.3.5 Microstructures of AZ91D alloy: TP-1 samples cast at 650 ℃ showing the effect of MgO nano particle inoculation on grain structure: (a) without MgO particle inoculation, and (b) with 100ppm MgO nano particle inoculation.

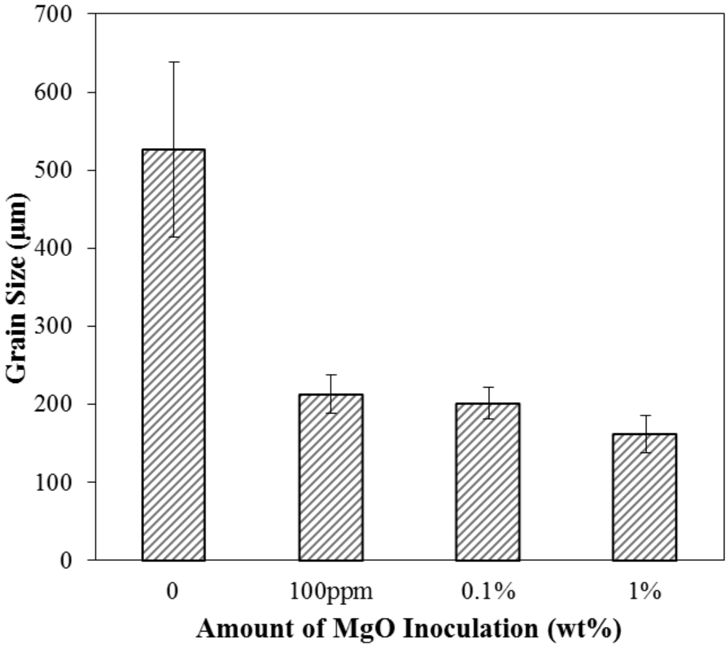

Figure 4.3.6 Grain size of AZ91D alloys with various weight percentage of MgO inoculation, showing the effects of MgO nano particle inoculation on grain size.

Based on the results shown in **Figure 4.3.5** and **4.3.6**, it is suggested that MgO inoculation can refine not only Mg-Al binary alloys but aluminium bearing commercial magnesium alloys such as AZ91. However, the mechanism of the refinement remains unclear. A possible and reasonable explanation is that the added MgO nano particles may act as effective nucleation substrates.

Nevertheless, there hasn't been any report to provide evidence for such an explanation. Since the melt has been stirred for 3 minutes in order to mix the MgO particles into the melt, the other possible explanation is that the stirring process may have some effect on the microstructures. In order to identify the effect of stirring, AZ91D alloy has been stirred for 3 minutes with and without 0.1wt% MgO inoculation. The microstructures of these samples are shown in **Figure 4.3.7**. As shown in the photograph, there are significant differences between the microstructures in **Figures 4.3.7(a)** and **(b)**. The microstructure of the sample with MgO inoculation is much finer than the one without. This indicates that the significant changes in grain sizes of the samples with MgO inoculation are not caused by the stirring process.

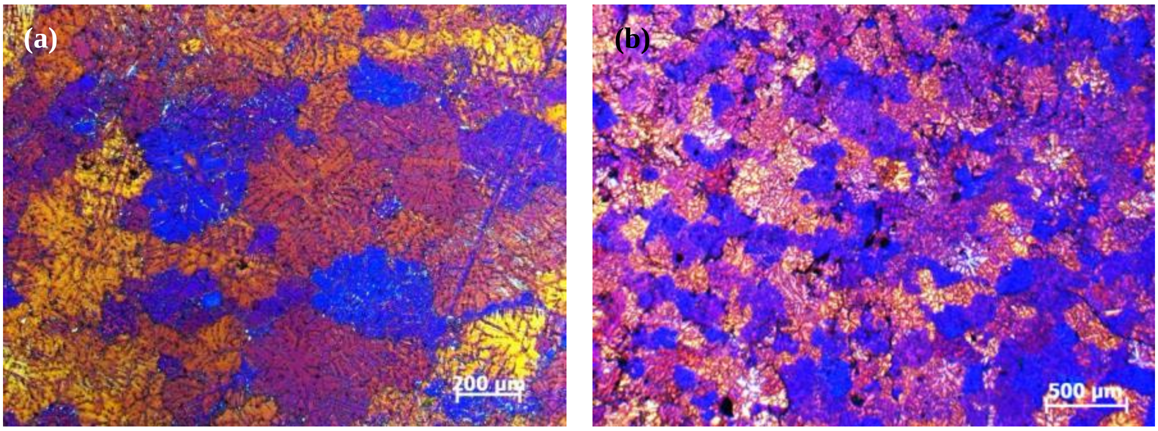

Figure 4.3.7 Microstructures of AZ91D alloy cast at 650 ℃ showing the effect of stirring on grain structure: (a) stirring for 3 minutes without MgO particle inoculation, and (b) stirring for 3 minutes with 0.1wt% MgO particle inoculation.

In order to confirm whether the inoculant MgO particles acted as effective nucleation substrates, the cooling curves for the AZ91D alloy with 100ppm and without MgO inoculation have been measured. These are shown in **Figures 4.3.8** and **4.3.9**. In **Figure 4.3.8**, it is obvious that both curves have the same cooling rates of about 0.22K/s before solidification, and this is consistent with the previous measurement in chapter 4.1. However, the values of undercoolings in the curves are different. For AZ91D alloy with 100ppm MgO inoculation, the measured undercooling is 0.5K. As for the one without MgO inoculation, the undercooling is 1.3K.

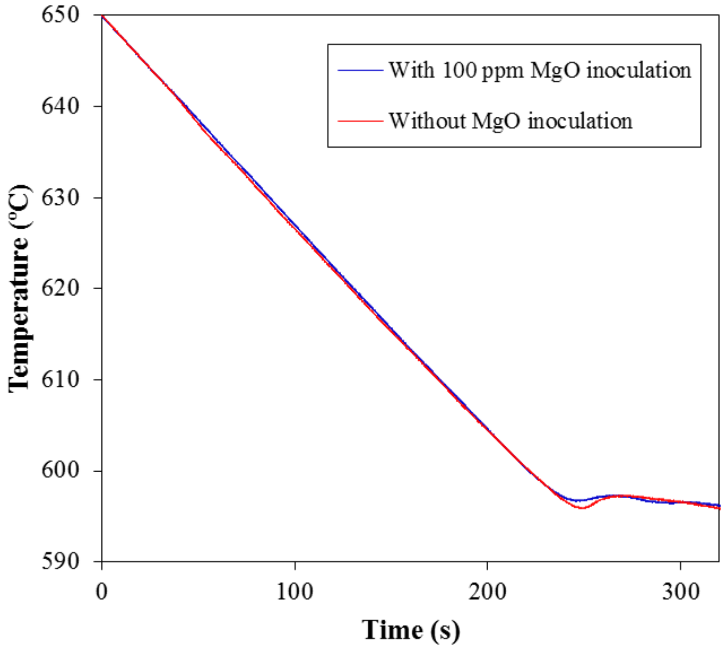

Figure 4.3.8 Measured cooling curves for the AZ91D alloy melt with 100ppm and without MgO inoculation cast at 650 ℃ in cylindrical crucibles covered with 13mm thermal insulation. Both the cooling curves exhibit pronounced recalescence.

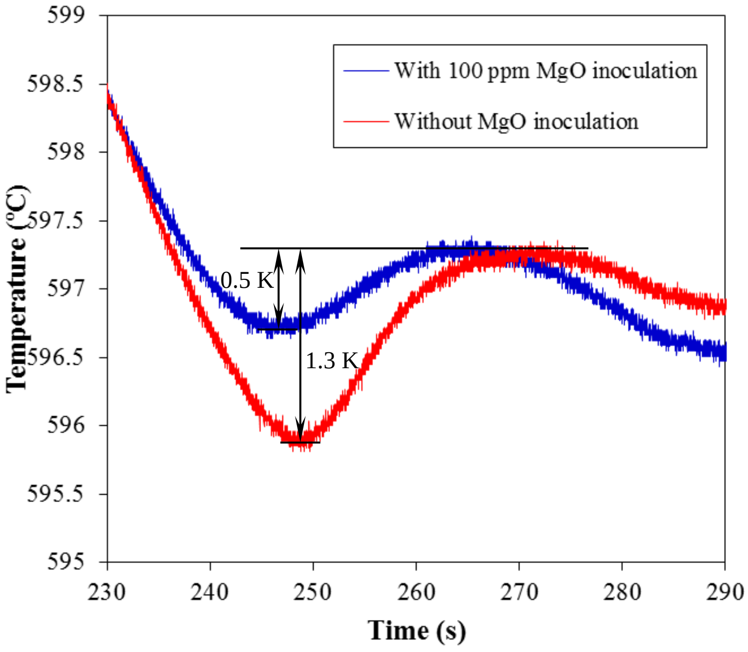

Figure 4.3.9 Portions of measured cooling curves for the AZ91D alloy melt with 100ppm and without MgO inoculation cast at 650 ℃ with 13mm thermal insulation covered the inner cylindrical crucible.

As discussed in the section 4.1.1, smaller undercooling usually means a larger number density of nucleation particles exists in the melt. Based on such an understanding, the alloy with 100ppm MgO inoculation should have more nucleation substrates. The microstructures of the ingots used for cooling curve measurement in **Figure 4.3.10** have further confirmed that the number density of grains for AZ91D with 100ppm MgO inoculation is larger than the one without.

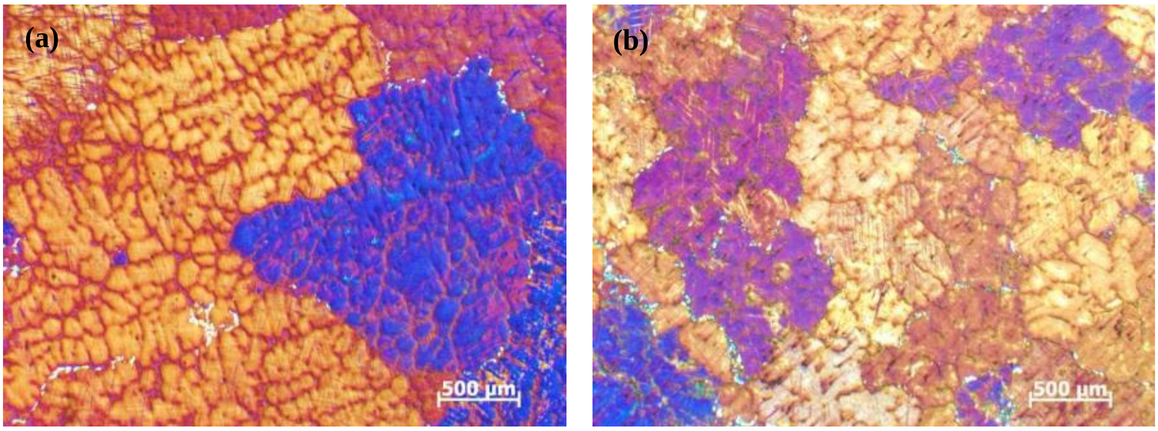

Figure 4.3.10 Microstructures of AZ91D alloy without (a) and with (b) 100 ppm MgO inoculation cast at 650 ℃ in cylindrical crucibles covered with 13 mm thermal insulation. The measured grain sizes are 2.350mm and 1.241mm for samples without and with 100ppm MgO inoculation, respectively.

According to the results shown in **Figure 4.3.8**, **4.3.9**, and **4.3.10**, it can be concluded that there are more nucleation particles in AZ91D with 100 ppm MgO inoculation. The only question here is whether it is the MgO inoculation that caused the increase of the number density of nucleation substrates. In order to answer this question, the added MgO particles need to be, at least, found in the AZ91D melt. **Figure 4.3.11** shows the morphologies of MgO particles collected from AZ91D commercial alloy melt. From the faceted morphology and cubic shapes of the MgO particles it can be confirmed that these particles are the added ones as inoculant. **Figure 4.3.12** is the measured and fitted size distribution of the inoculated MgO particles in the melt. The size distribution of MgO particle inoculants has been well fitted with a log-normal distribution with parameters $d_0 = 0.13\ \mu\text{m}$ and $\sigma = 0.45$. So far, all experimental results have led to the reasonable explanation that the MgO particle additions are the nucleation substrates in AZ91D and they can be used as a grain refiner for aluminium bearing magnesium alloys.

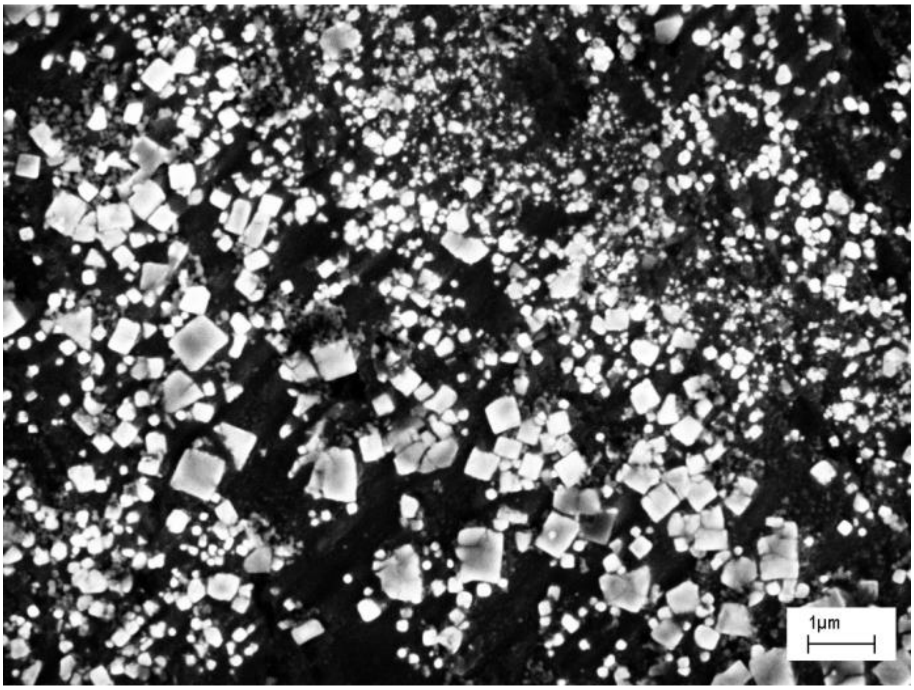

Figure 4.3.11 SEM micrograph showing the morphology of the MgO nano particles collected at 650 ℃ by the pressurized filtration for the melt of AZ91D commercial alloy that was inoculated with 100ppm MgO nano particles.

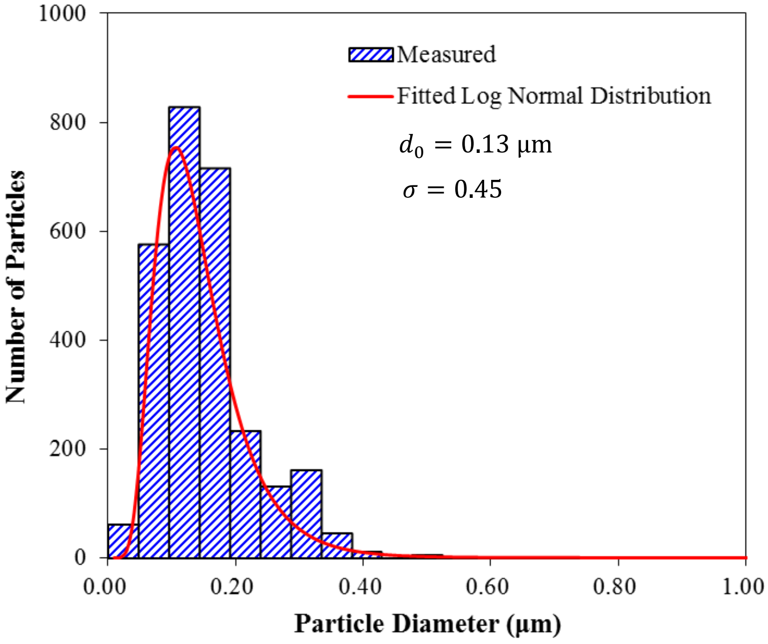

Figure 4.3.12 The measured size distribution of cubic shape MgO particles in the AZ91D alloy melt with 100ppm MgO inoculation by the pressurized filtration. The size distribution of MgO nano particles can be well fitted by a log-normal function with parameters $d_0 = 0.13\mu\text{m}$ and $\sigma = 0.45$.

4.3.4. Master Alloy for Grain Refinement in AZ91D Commercial Alloy

Although the results in section 4.3.2 and 4.3.3 have confirmed that MgO nano particle inoculation can refine aluminium bearing magnesium alloys, the process of inoculation can hardly be applied to foundry practice. There are certain problems that may limit the usage of MgO particle inoculation in foundry practice. The most troubling problem is how to add MgO particles into the magnesium alloy melt. The stirring process that has been used in this experiment is potentially dangerous, especially for large magnesium alloy castings. It may potentially cause a higher level of impurity in the melt since it increases the possibility of oxidation. Also, it will increase the cost for cast ingots. Therefore, an easier and more practical method is required.

Based on the effect of grain refinement of MgO particle inoculation, a new master alloy is developed. It contains 95wt% AZ91D commercial alloy and 5wt% MgO nano particles and was applied as the master alloy to AZ91D castings. **Figure 4.3.13** shows that the faceted morphology of the MgO nano particles in the AZ91D-5wt%MgO master alloy.

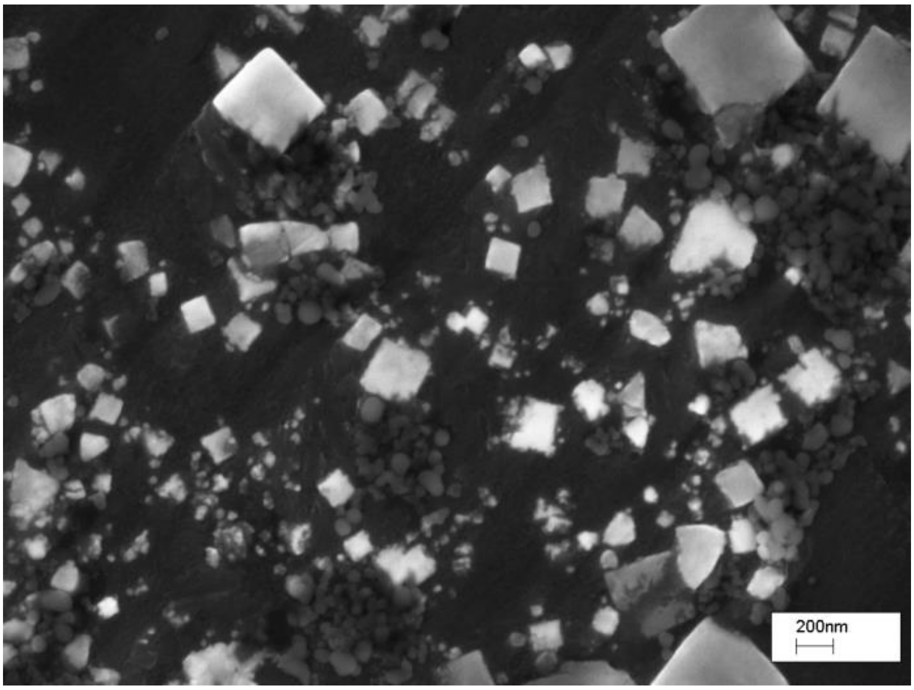

Figure 4.3.13 SEM micrograph of AZ91D-5wt%MgO master alloy, showing the morphology of the MgO nano-size particles in the master alloy.

The only question is whether the microstructures of the castings with the master alloy addition can be significantly refined. **Figure 4.3.14** shows the microstructures of AZ91D alloy cast at 650℃ with 1ppt and 2ppt AZ91D- 5wt%MgO master alloy addition. As it is shown, the grain structures for both samples are refined. However, the grain size for the one with 1ppt master alloy addition appears to be slightly larger.

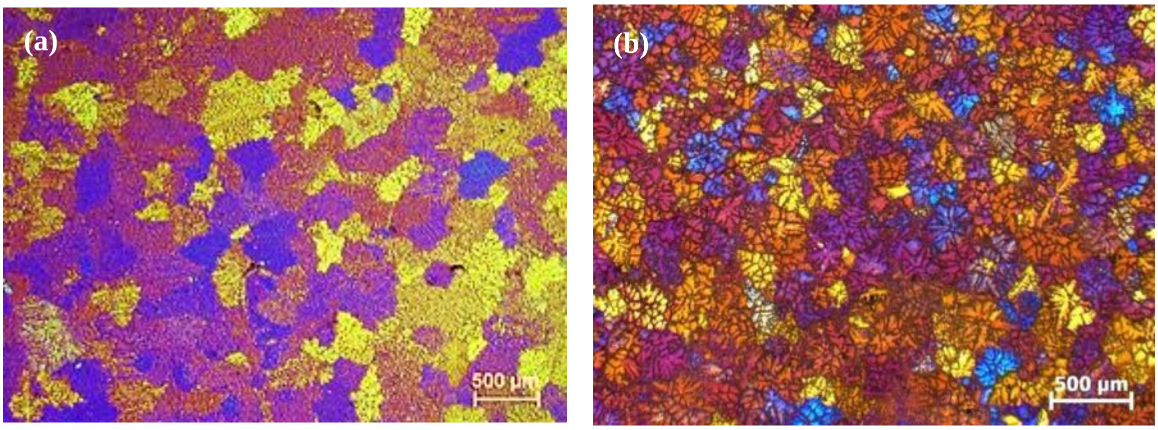

Figure 4.3.14 Microstructures of AZ91D alloy cast at 650℃ showing the refinement effect of AZ91D- 5wt%MgO master alloy on grain structures: (a) with 1 ppt master alloy addition, and (b) with 2ppt master alloy addition.

Based on the results in **Figure 4.3.14**, the addition of the master alloy can refine AZ91D commercial alloy. The next step is to study the relationship between grain sizes and the addition level of master alloy in order to determine the minimum amount that can refine the microstructure of the AZ91D alloy. **Figure 4.3.15** shows the grain size of AZ91D alloys with various amounts of AZ91D-5wt%MgO master alloy addition. The significant grain refinement for AZ91D alloy can be achieved when more than 2 ppt master alloy was added. This means around 100 ppm MgO nano particles are, perhaps, consumed as inoculant in the alloy melt from the addition of master alloy. This result has confirmed the results of AZ91D alloy with various MgO particle inoculation in **Figure 4.3.6**, which indicates that the critical quantity of MgO nano particles is around 100 ppm. Therefore, it is proposed that the AZ91D-5wt%MgO master alloy can be an effective grain refiner for aluminium bearing magnesium alloys.

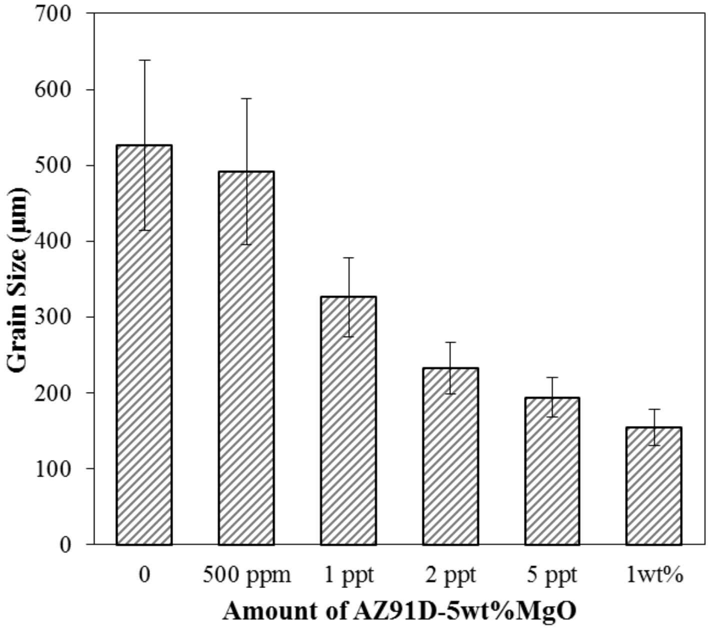

Figure 4.3.15 Grain size of AZ91D alloys with various weight percentage of AZ91D-5wt%MgO master alloy addition, showing the refinement effects on the grain sizes. Note that the amount of addition is the master alloy rather than the MgO particles.

4.3.5. Summary

This experiment aims to develop a grain refinement process for magnesium alloys, especially for aluminium bearing magnesium alloys. It appears that the microstructures of magnesium alloys have been significantly refined after MgO nano particles were added to the alloy melt. The MgO nano particles in the powder are faceted with cubic shapes, which mean that the exposed surface of the MgO nano particles may be {100} plane. This is different from the endogenous MgO particles in the magnesium alloy melt which are terminated with {111} plane. According to the experimental results, the MgO particle inoculation can refine Mg-Al binary alloys that contain various amounts of aluminium as well as AZ91D commercial alloy. The mechanism of the grain refinement is that the MgO particles act as effective nucleation substrates. In order to make MgO inoculation more applicable, an AZ91D-5wt%MgO master alloy was developed. Based on the experimental results, it is suggested that MgO nano particle inoculation or the AZ91D-5wt%MgO master alloy can be an applicable grain refinement additive for aluminium bearing magnesium alloys.

4.4. Melt Quenching of AZ91D with Various Casting Conditions

Superheat of alloy melt has a certain influence on final grain structures as discussed in various publications [18]. It is also known that mould temperature is one of the key factors for die casting processes [72, 91]. In this section, the main objective is to investigate the relationship between casting conditions, such as mould temperatures and pouring temperatures, and the solidification behaviour of magnesium alloys using AZ91D as a reference alloy. The cooling curve measurement is an effective technique to study thermal conditions during solidification. Therefore, it is applied in this experiment to study the thermal environment within the melt and the heat transfer between the melt and the mould. The pouring temperatures and the mould temperatures have been studied as the casting conditions.

4.4.1. Thermal Analysis for Different Casting Conditions

Thermal analysis has been applied to this experiment as the first step to study and understand the solidification behaviour with various casting conditions. In this section, the analysis is based on the cooling of the AZ91D alloy as it is rapidly poured (less than 2 seconds) into a cold mould, as shown in **Figure 4.4.1**.

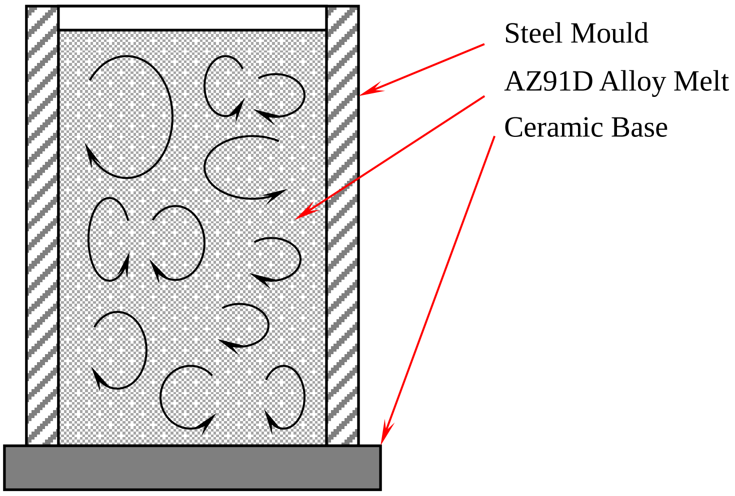

Figure 4.4.1 Schematic illustration of the turbulent fluid flow after AZ91D alloy melt is rapidly poured into a steel mould with a ceramic base.

Because of the turbulent fluid flow during and after pouring, the AZ91D melt can be assumed to have a uniform temperature and because the mould is thin (typically 1-2mm in this experiment) it can also be assumed to have a uniform temperature. Therefore, the heat lost from the metal equals to that gained by the mould subtracting the heat lost by the container to its surroundings, this is given by

$$C_{p1}V_{o1}\mathrm{d}T_1 - A_2 q_2 \mathrm{d}t + C_{p2}V_{o2}\mathrm{d}T_2 = 0 \tag{4.2}$$

where V_{o1} and V_{o2} are the volume, C_{p1} and C_{p2} are the enthalpy per unit volume, and $\mathrm{d}T_1$ and $\mathrm{d}T_2$ are the temperature changes in time $\mathrm{d}t$, of the metal and container respectively. A_2 is the external area of the mould and q_2 is the heat flux per unit area. The initial temperature of the metal is T_{o1} and that of the container is T_{o2}. The heat loss from the container to the environment is relatively small compared to the other two terms. Therefore, equation 4.2 becomes,

$$C_{p1}V_{o1}(T_1 - T_{o1}) + C_{p2}V_{o2}(T_2 - T_{o2}) = 0 \tag{4.3}$$

where T_1 and T_2 are the temperature of the metal and container respectively. According to Hunt and Fan [60], there is a quench effect within several seconds after the melt is rapidly poured into the container. The quench effect will cause the melt and the container to reach a critical heat balance temperature, T_{hb}. Therefore, equation 4.3 becomes,

$$T_{hb} = \frac{C_{p1}V_{o1}T_{o1} + C_{p2}V_{o2}T_{o2}}{C_{p1}V_{o1} + C_{p2}V_{o2}} \tag{4.4}$$

Equation 4.4 stands only when T_{hb} is higher than the liquidus temperature of the melt, T_L. In the case when $T_{hb} < T_L$, solidification will happen before the critical heat balance is reached. Therefore, the heat loss from phase transformation needs to be considered. Since the heat release from phase transformation is much larger than the heat absorbed by the container, T_{hb} should be slightly lower than the liquidus temperature, T_L.

The analysis above is based on the quench effect. The most important assumption for the quench effect is that the rapid pouring causes strong turbulence in the melt, which leads to a critical heat balance temperature of the metal and the container. The assumption is made considering the pouring of the melt will cause strong turbulence within the melt which will increase the heat transfer between the melt and the mould. Based on such an assumption, the pouring temperature and the mould temperature will become relatively important since these two conditions are the major factors that determine the heat balance temperature. **Figure 4.4.2** is the calculated critical heat balance temperature based on the quench effect. In this case, the critical heat balance temperature is controlled by two variables, the pouring temperature of the melt and the preheating temperature for the mould.

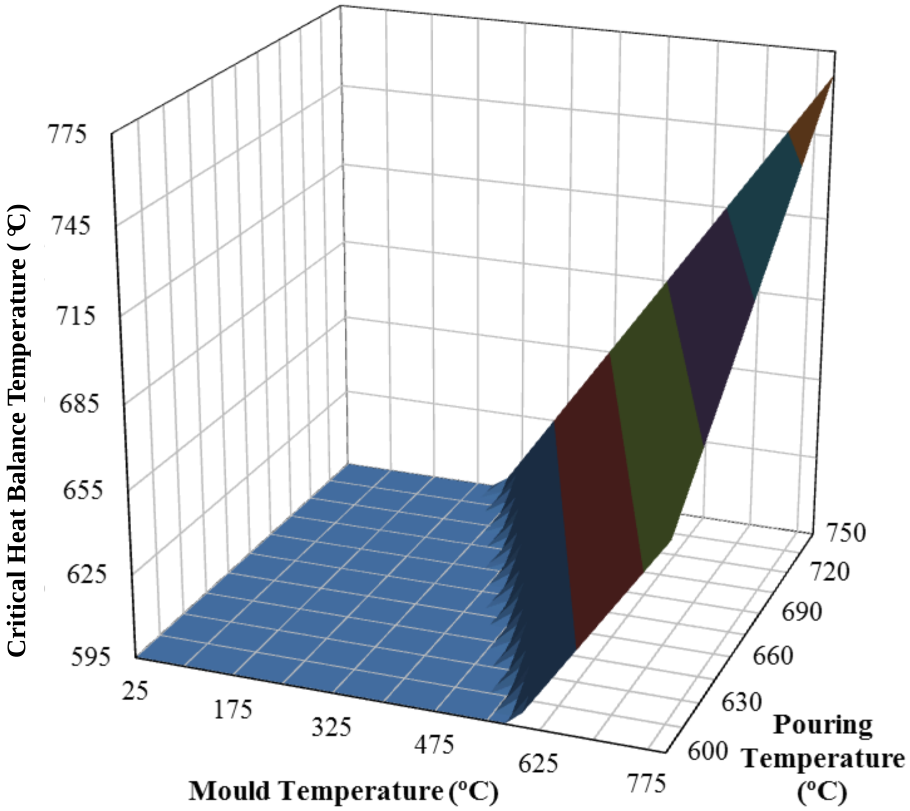

Figure 4.4.2 Calculated results for critical heat balance temperature if heat released from AZ91D alloy melt has been completely absorbed by the steel mould before phase transformation occurs. The calculation is based on the measured value of the container and the melt in this experiment.

As it is shown, the mould temperatures applied are from 25-775 ℃, and the pouring temperatures are varied from 600-750 ℃. The calculation in **Figure 4.4.2** shows that for some pouring temperatures and mould temperatures, the critical heat balance temperatures should be slightly lower than the liquidus temperature of AZ91D alloy. However, there is no experimental evidence to prove that the quench effect or the critical heat balance temperature actually exists. Therefore, the next step is to find experimental evidence to verify the idea of quench effect and the critical heat balance temperature.

4.4.2. Thermal Field after Pouring

According to the analysis in section 4.4.1, the quench effect, if it exists, will lead to a critical heat balance temperature within several seconds after the melt is rapidly poured into the mould. Therefore, if the critical heat balance temperature exists, the thermal field in the mould should be nearly isothermal. In another word, the melt temperatures in the mould should be the same at different locations. Therefore, the cooling curves of AZ91D alloy at various locations in the melt are required. The idea of critical heat balance temperature can be accepted only if the curves everywhere in the melt reach the same temperature at the same time shortly after pouring. In **Figures 4.4.3** and **4.4.4**, both experiments can provide evidence that the critical heat balance temperature occurs within one second after pouring. As it is shown in **Figure 4.4.3**, the four curves vary at first, and then reach the same temperature at the same time. **Figure 4.4.4** shows a similar situation.

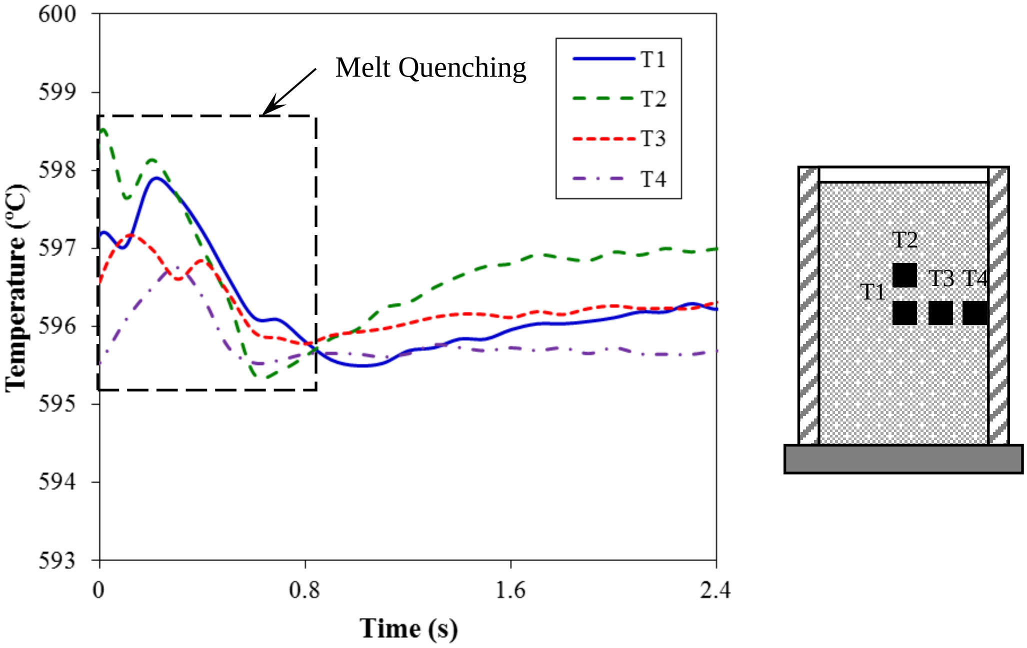

Figure 4.4.3 Measured cooling curves of AZ91D alloy cast at 610 ℃ with the mould temperature of 25 ℃. T1, right in the centre of the mould, both horizontally and vertically. T2, horizontally in the centre of the mould, vertically 1cm above T1. T3,vertically in the centre of the mould, horizontally 1 cm away from the centre. T4, vertically in the centre of the mould, horizontally 2cm away from the centre.

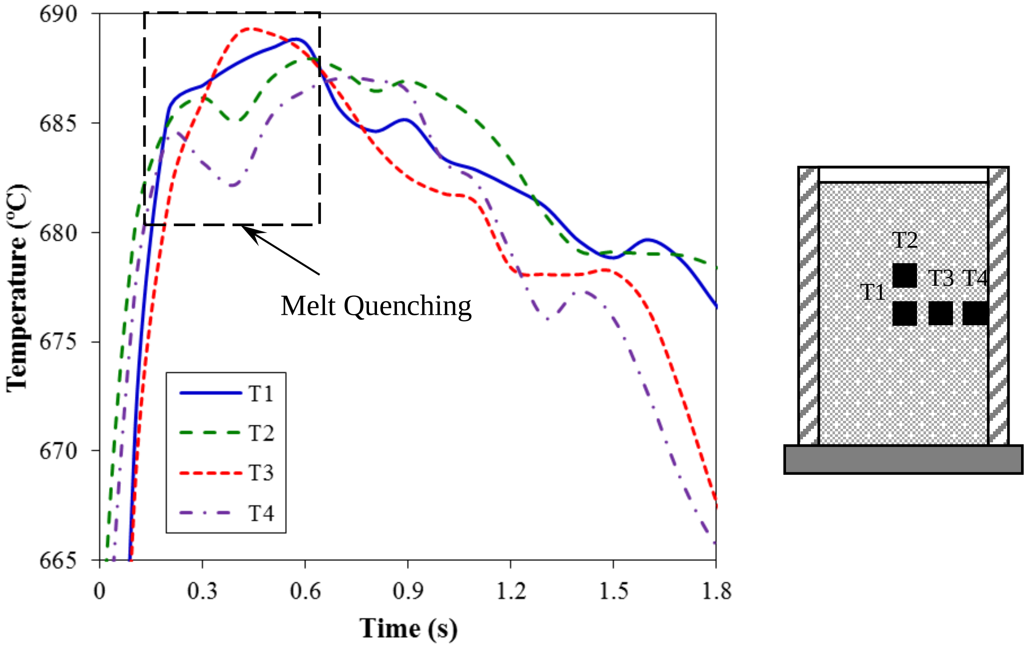

Figure 4.4.4 Measured cooling curves for AZ91D alloy cast at 700 ℃ with the mould temperature of 350 ℃. T1, right in the centre of the mould, both horizontally and vertically. T2, horizontally in the centre of the mould, vertically 1cm above T1. T3,vertically in the centre of the mould, horizontally 1cm away from the centre. T4, vertically in the centre of the mould, horizontally 2cm away from the centre.

The inside diameter of the mould is 52 mm. Therefore, thermocouple T4 is near the inner surface of the mould. If T1 and T4 reach the same temperature, the melt should be almost isothermal. The pouring temperatures and mould temperatures in both experiments are significantly different. However, a critical heat balance temperature is reached shortly after pouring in both cases. Therefore, it is suggested that the idea of the critical heat balance temperature can be accepted. The next question is how this critical heat balance temperature and the isothermal condition occurs. Based on the above understanding, if the melt is poured slowly into the mould, especially when the pouring temperature and the mould temperature are relatively high, an initial temperature gradient will appear in the melt immediately after pouring. Thus, the critical heat balance temperature is caused by the strong turbulence in the melt. As it is known, the turbulent fluid will enhance heat transfer from the melt to the mould.

4.4.3. Cooling Curves of AZ91D Alloy with Various Casting Conditions

According to the analysis in 4.4.1, the critical heat balance temperature can be either above liquidus or slightly below liquidus. This is mainly caused by different pouring temperatures and mould temperatures. In order to prove this idea, cooling curves of AZ91D alloy with various casting conditions are measured. Two different mould temperatures, 25 ℃ and 350 ℃, and five different pouring temperatures, 610 ℃, 630 ℃, 650 ℃, 670 ℃, and 700 ℃ are chosen for the experiment. As the concept of the heat balance temperature has been accepted, the cooling curves were only measured at the centre of the mould, which is the location of thermocoupleT1 in **Figures 4.4.3** and **4.4.4**. The cooling curves of AZ91D alloy with various casting conditions are shown in **Figures 4.4.5**, **4.4.6**, and **4.4.7**. **Figure 4.4.5** is the measured cooling curve and the first derivative for AZ91D alloy melt cast at 700 ℃ with the mould temperature of 350 ℃. **Figure 4.4.6** is the measured cooling curve and the first derivative for AZ91D alloy melt cast at 610 ℃ with the mould temperature of 25 ℃. **Figure 4.4.7** is the measured cooling curve and the first derivative for AZ91D alloy melt cast at 610 ℃ with the mould temperature of 350 ℃.

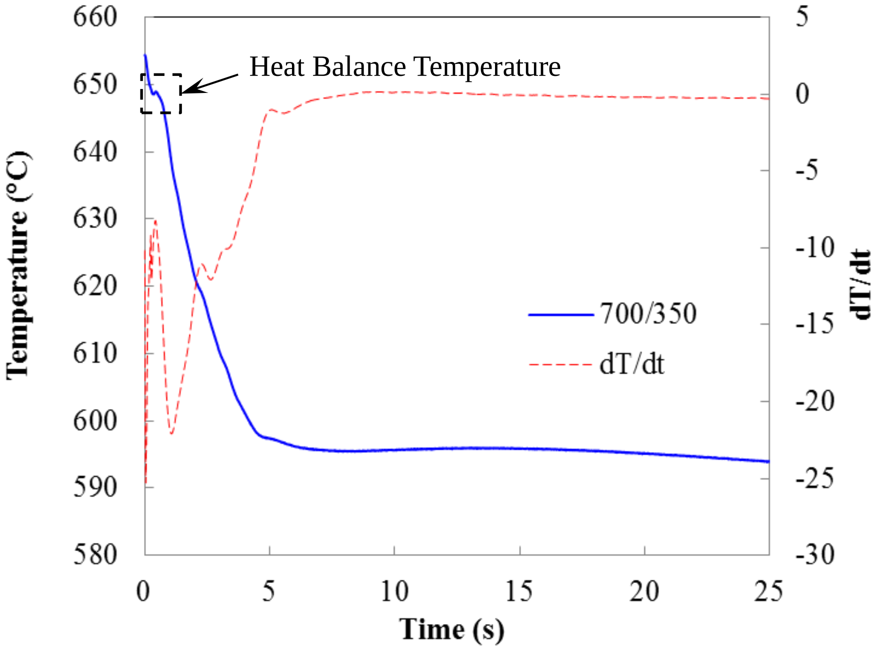

Figure 4.4.5 Measured cooling curve and the first derivative for AZ91D alloy cast at 700 ℃ with the mould temperature of 350 ℃.

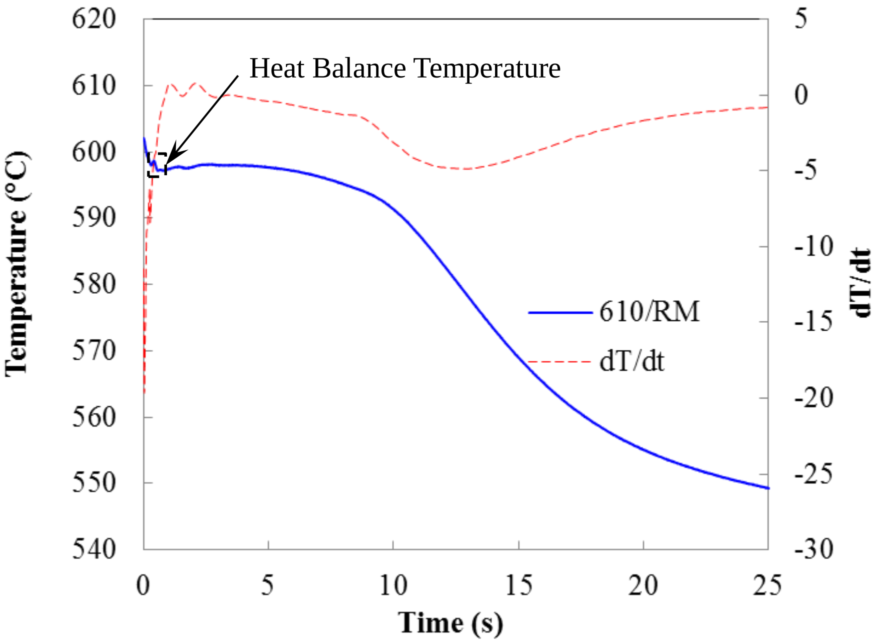

Figure 4.4.6 Measured cooling curve and the first derivative for AZ91D alloy cast at 610 ℃ with the mould temperature of 25 ℃.

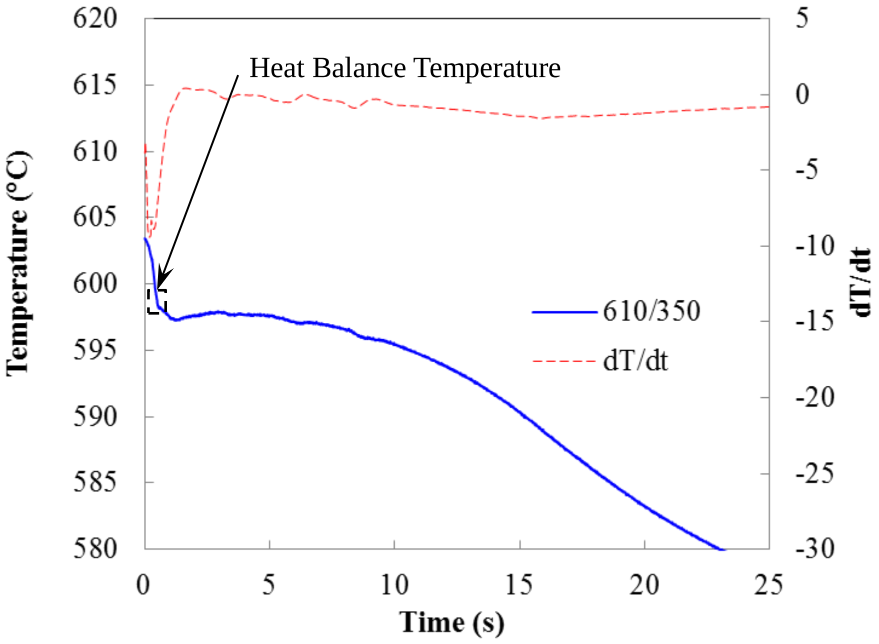

Figure 4.4.7 Measured cooling curve and the first derivative for AZ91D alloy cast at 610 ℃ with the mould temperature of 350 ℃.

In these three measurements, the pouring temperature of the curves in **Figure 4.4.6** and **4.4.7** is 610 ℃, and that of the curve in **Figure 4.4.5** is 700 ℃. The mould temperature of the curves in **Figure 4.4.5** and **4.4.6** is 25 ℃, and that of the curves in **Figure 4.4.7** is 350 ℃. The heat balance temperatures of the curves in **Figure 4.4.5** and **4.4.7** are above liquidus, while that of the curve in **Figure 4.4.6** is below liquidus. Even though the curves in **Figure 4.4.5** and **4.4.6** have the same mould temperature and the curves in **Figure 4.4.6** and **4.4.7** have the same pouring temperature, the critical heat balance temperatures are in different conditions. According to Hunt and Fan [60], it is rather important that whether the critical heat balance temperature is above or below liquidus temperature of the alloy. The solidification behaviour for the two conditions is completely different. As the results in these three figures have shown, pouring temperature and mould temperature don't work alone. They together determine which condition the heat balance temperature will be achieved. Therefore, it can then be concluded that the pouring temperature and the mould temperature are the two most important influential factors for the critical heat balance temperature.

4.4.4. Microstructures of AZ91D Alloy with Various Casting Conditions

The measurement of cooling curves in section 4.4.3 shows that pouring temperature and mould temperature together determine whether the heat balance temperature is above or below liquidus. According to Hunt and Fan [60], solidification will occur from the edge to the centre of the mould if the heat balance temperature is above liquidus. If the heat balance temperature is below liquidus, solidification may occur in the melt everywhere simultaneously. If the heat balance temperature is above liquidus of the melt, shortly afterwards, a temperature gradient will appear in the melt and the melt at the edge will cool down to liquidus temperature first. On the other hand, if the heat balance temperature is slightly below liquidus temperature of the melt, effective nucleation particles will initiate the nucleation and growth all over simultaneously in the melt because of the isothermal condition in the melt. Based on such an understanding, the microstructures of the two conditions should be different. The microstructure of the former condition should be coarser than the latter. Therefore, the microstructures of the cast ingots used for the measurement of cooling curves in section 4.4.3 should also have significant difference.

Figure 4.4.8 and **4.4.9** are the macrostructures and microstructures of AZ91D alloy ingots used for cooling curve measurement both cast at 610 ℃ with 25 ℃ and 350 ℃ mould temperature, respectively. The microstructure for the one with 25 ℃ mould temperature is much finer than the one with 350 ℃. A reasonable explanation is that the difference in microstructures is caused by the different conditions of the heat balance temperature.

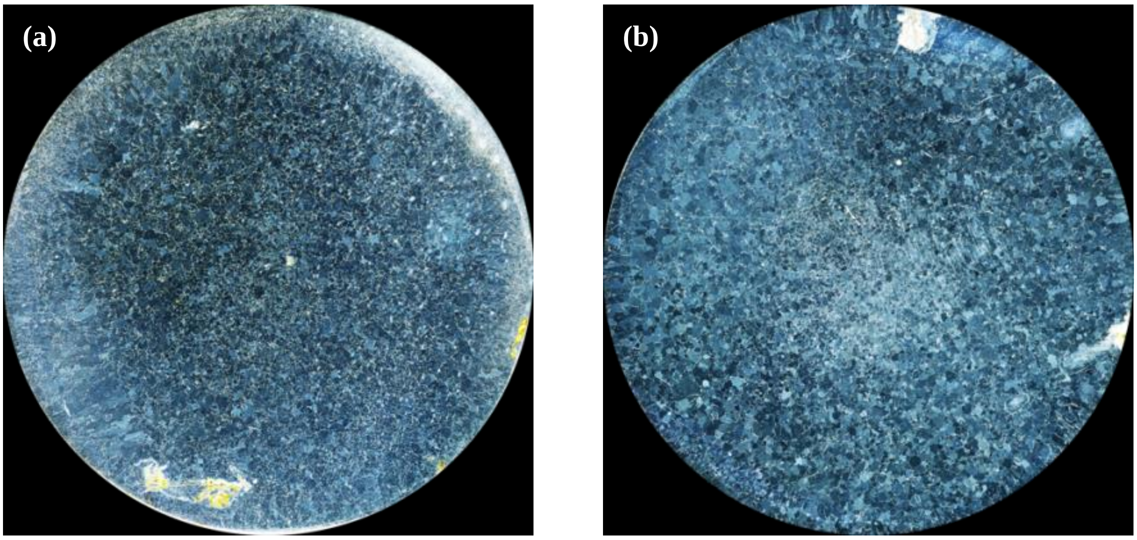

Figure 4.4.8 Micrographs of cross sections of AZ91D alloy ingots used for cooling curve measurement, showing the effect of pouring temperature: (a) cast at 610 ℃ with the mould temperature of 25 ℃; (b) cast at 610 ℃ with the mould temperature of 350 ℃.

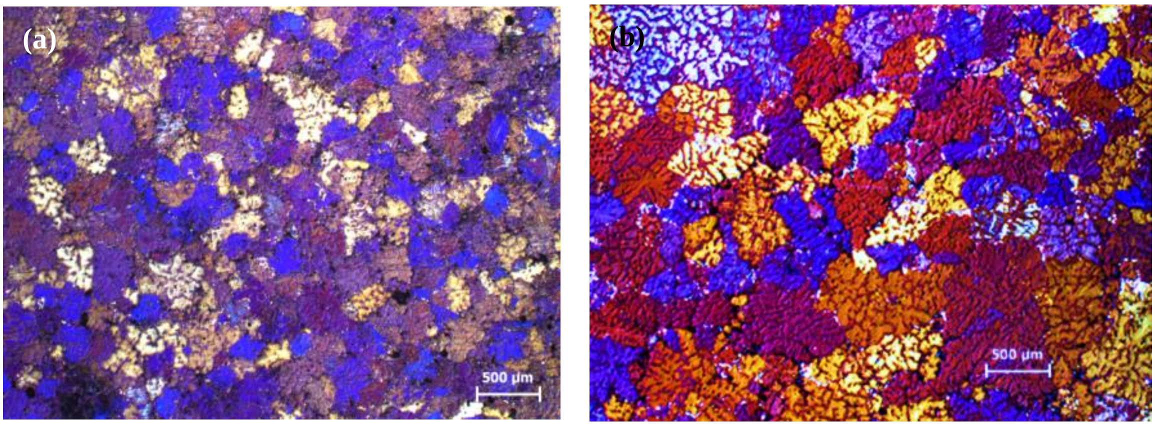

Figure 4.4.9 Microstructures of the cross sections of AZ91D alloy ingots for cooling curve measurement, showing the effect of pouring temperature: (a) cast at 610 ℃ with the mould temperature of 25 ℃; (b) cast at 610 ℃ with the mould temperature of 350 ℃.

4.4.5. Summary

According to Hunt and Fan [60], casting conditions have a large influence on the final grain size. They suggested that a melt quenching effect would occur if the melt was poured rapidly in the casting mould. Theoretically, they explained that the melt quenching effect was caused by the turbulence created after the melt was poured rapidly into the mould which would enhance thermal conductivity and forced the melt and the mould to reach a critical heat balance temperature. The thermal environment in the melt at that time is in an isothermal condition. Although a theoretical explanation has been provided, experimental evidence is still necessary to support the hypothesis. Therefore, the major objective of this experiment is to find whether such melt quenching effect exists or not in practice.

According to four thermocouple measurements shown in **Figures 4.4.3** and **4.4.4**, it is found that the heat balance temperatures actually exist. An equal temperature has been reached by all four thermocouples in approximately 1 second after the melt was poured. Since each of the curves represented the temperature at a different location in the mould, it is believed that the melt is in an isothermal condition. The measurements in **Figures 4.4.5**, **4.4.6**, and **4.4.7** further confirm the existence of the heat balance temperature. They also confirm the idea that pouring temperatures and mould temperatures are the key influential factors that determine whether the heat balance temperature is above or below liquidus of the melt. The macrostructures and microstructures in **Figures 4.4.8** and **4.4.9** show that the heat balance temperature has a certain influence on the grain structures of the cast ingots. It is then concluded that present experiments do support the concept of critical heat balance temperature as suggested by Hunt and Fan [60].

4.5. DC Casting of Magnesium Alloys with Intensive Melt Shearing

Direct chill (DC) casting is one of the technologies to produce billets or slabs of magnesium alloys in the industry. However, the billets or slabs made by the conventional DC casting process often have coarse and non-uniform microstructures, severe chemical segregation, porosity and hot tearing, which not only burden the downstream thermo-mechanical processing but also have a negative influence on the mechanical properties of the final products. In this set of experiments, intensive melt shearing is applied to the DC casting process to produce high quality magnesium DC cast billets. In section 4.5.1, the results of AZ91D magnesium alloy DC casting is presented including the refinement of grain structures and the macrosegregation, and the thermal environment during the newly developed melt conditioned DC (MC-DC). This technique has also been applied to AZ31 magnesium alloy DC casting, and the results are presented in section 4.5.2.

4.5.1. AZ91D DC Casting with Intensive Melt Shearing

Based on the understanding of the high shear mixer, two different effects were expected on the AZ91D alloy melt after intensive shearing is applied to the melt. The first and most desired one is the grain refinement, and the second is the uniformity of microstructure. According to various publications [9-11], grain refinement can potentially decrease shrinkage and hot tearing of AZ91D, and increase uniformity of the microstructure which may, in turn, reduce the tendency for macrosegregation in the castings. **Figure 4.5.1** and **4.5.2** show the macrostructure and the microstructure of the vertical sections of AZ91D DC cast billets with intensive melt shearing. As shown in both figures, there is a clear and narrow transition between very coarse grains and small globular grains. Based on the time record of the experiment, this transition occurs right after the melt shearing device is switched on. Therefore, it is considered that the transition is caused by intensive melt shearing. Before melt shearing started, the microstructure of the AZ91D is formed with coarse grains of dendrite arm branches. The grains are refined significantly with a rosette morphology developed after intensive melt shearing. So it is suggested that intensive melt shearing by the high shear mixer can be an effective process for grain refinement of AZ91D alloy.

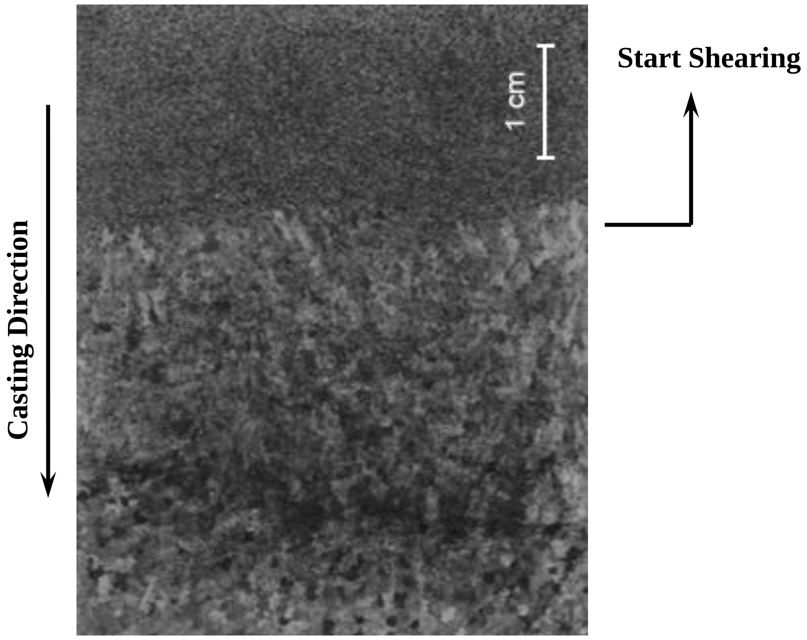

Figure 4.5.1 Macrostructure of the vertical section of AZ91D alloy DC cast billet with intensive melt shearing. The arrows show the casting direction and the location where shearing started.

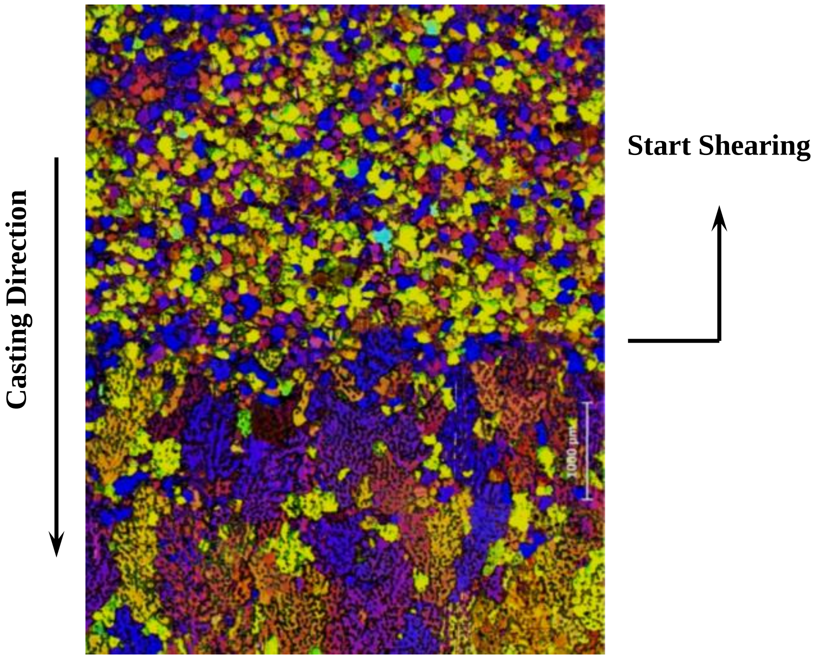

Figure 4.5.2 Microstructure of the vertical sections of AZ91D alloy DC cast billet with intensive melt shearing, showing the transition zone before and after intensive melt shearing.

As discussed above, the second expected effect is structural uniformity. In conventional DC casting of magnesium alloys, macrosegregation is one of the major casting defects. The variation of the concentration of alloying elements throughout the cross section of the billet results in variations of thermal and mechanical properties. **Figure 4.5.3** shows the microstructures of the cross sections of AZ91D magnesium alloy DC cast billets, showing the effect of intensive melt shearing on grain structures. **Figure 4.5.4** presents the relationship between grain size and the distance from billet surfaces with and without shearing. As it is shown in these two figures, the billet without melt shearing has around 200μm difference between the grain sizes from the edge and the centre of the billet without melt shearing. The microstructure throughout the cross section of the billet without melt shearing is suffering from severe macrosegregation. The billet with melt shearing, on the other hand, shows slightly difference in grain sizes from different locations of the cross section. As expected, the microstructure is relatively uniform with melt shearing.

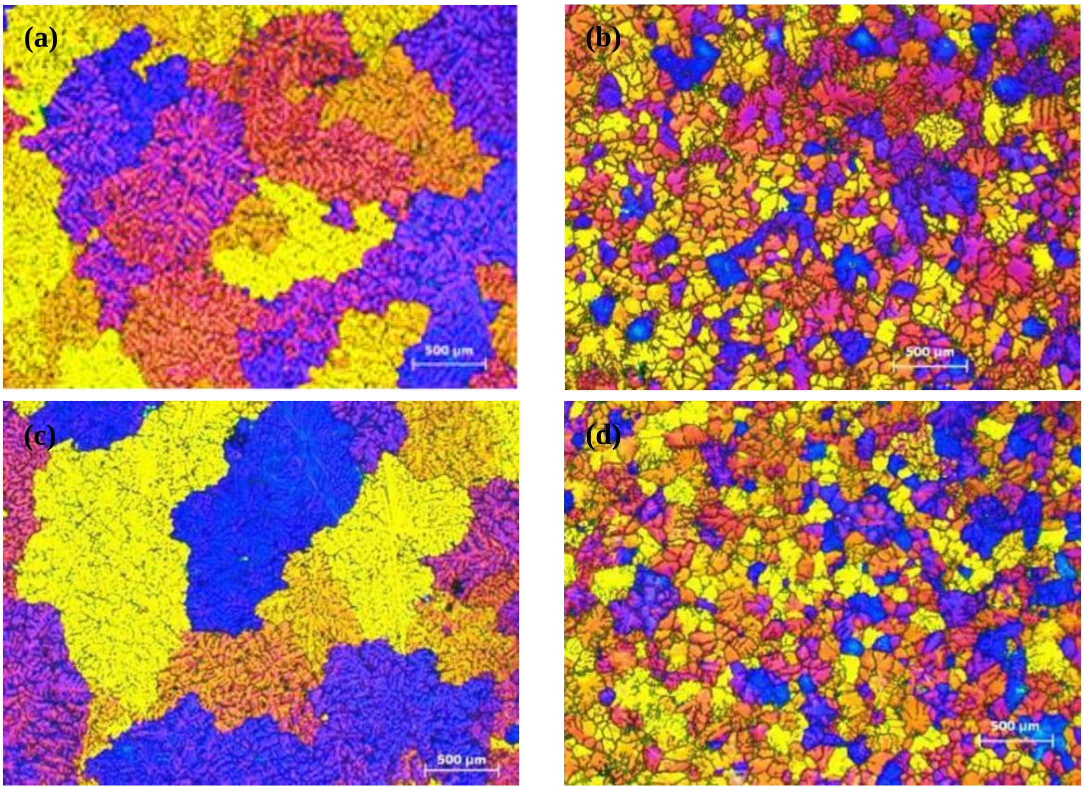

Figure 4.5.3 Microstructures of the cross sections of AZ91D magnesium alloy DC cast billets, showing the effect of melt shearing on grain structures: (a) edge of the billet, without shearing, (b) edge of the billet, with shearing, (c) centre of the billet, without shearing, (d) centre of the billet, with shearing.

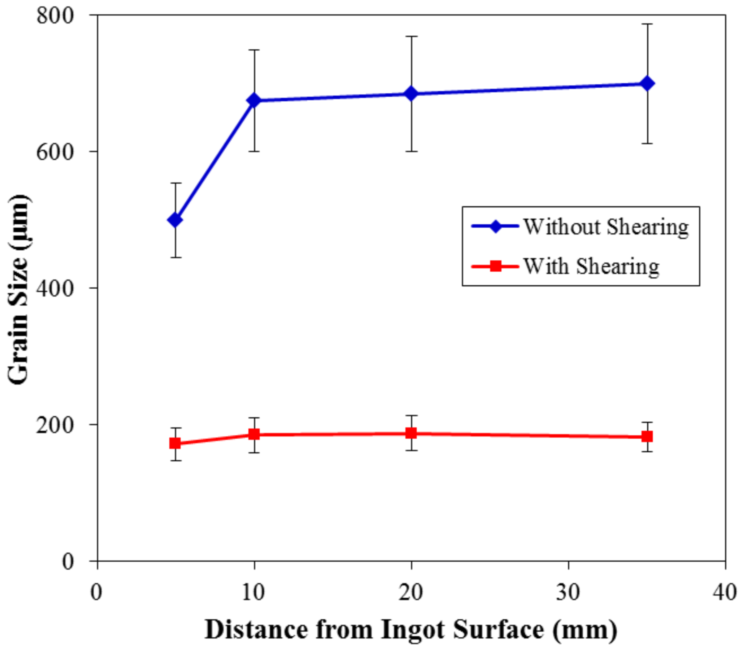

Figure 4.5.4 Grain size as a function of distance from billet surfaces with and without shearing.

According to the results in **Figure 4.5.1**, **4.5.2**, **4.5.3**, and **4.5.4**, intensive melt shearing by the high shear mixer can not only refine the microstructures, but homogenize the microstructure throughout the cross sections of the AZ91D alloy DC cast ingots. However, the mechanism of both effects remains unclear. Based on the understanding of the intensive melt shearing process in section 4.1, the mechanism of grain refinement is because the melt shearing process increases the total number of effective nucleation substrates. As suggested by Fan and his co-workers [32, 38, 115], MgO may have acted as the nucleation substrates for α-Mg because there is a fine orientation relationship at the α-Mg / MgO interface. Experimental results discussed in section 4.1 also suggest that intensive melt shearing can disperse MgO films into individual MgO particles. Therefore, it is suggested that melt shearing by high shear mixer can also increase total number of effective nuclei by dispersing the MgO films in the AZ91D alloy melt during DC casting.

The mechanism of the microstructure homogenization throughout the cross sections is relatively more complicated. According to the results in section 4.4, strong turbulence in the melt can homogenize the thermal field within the melt and force the melt temperatures at different locations to reach a critical heat balance temperature. In this experiment, since intensive melt shearing by the high shear mixer can also cause strong turbulence in the melt continuously, a possible and reasonable explanation for the uniformity of the microstructure is that the thermal field is nearly isothermal after the intensive melt shearing process is applied to the melt. If this explanation is true, the temperature gradient throughout the cross section in the melt should be relatively small. However, there is no experimental evidence to support this hypothesis. In order to study thermal field in the AZ91D alloy melt, the cooling curve measurement was carried out. **Figure 4.5.5** and **4.5.6** are the measured cooling curve and its first derivative for AZ91D alloy melt during DC casting before and after shearing started. The high shear mixer was put in the DC simulator prior to melt pouring, so there would be no chilling effect from the high shear mixer. The thermal couple is 11cm away from the bottom of the melt. As shown in **Figure 4.5.5**, the portion on the left of the dash line is the cooling curve before the melt shearing device was switched on. The temperature of the alloy melt falls less than 10 ℃ in 60s. Therefore, the cooling rate is less than 0.2K/s on average, which can also be seen in **Figure 4.5.6**. The portion on the right of the dash line in **Figure 4.5.5** is the cooling curve after the melt shearing device started to operate. The cooling rate increases tremendously from around 0.2K/s to 8K/s within a very short time period. The reason for the increases in the cooling rate is believed to be homogenizing of the thermal field. The convection forces the melt to reach an isothermal condition. The temperature gradient in the horizontal direction decreases rapidly. This could explain the reason why the microstructure of the billet is uniform after intensive melt shearing. In order to prove this hypothesis of homogenizing the thermal field by intensive melt shearing, cooling curves at different locations in the melt are required. **Figure 4.5.7** shows the measured temperature curves during AZ91D alloy DC casting with melt shearing and four thermal couples at various locations in the melt. As shown here, the dashed line depicts the time when the melt shearing device starts to operate. Before shearing, the largest temperature difference among the four thermocouples is around 40-50 ℃. After shearing started, the differences decrease rapidly and the temperatures reach nearly equilibrium after 20s. This result proves that intensive melt shearing can homogenize the thermal field as it has been suggested above. **Figure 4.5.8** shows the measured temperature curves during AZ91D alloy DC casting without shearing with four thermal couples at various locations in the melt. In comparison of the results, it shows that intensive melt shearing can decrease temperature gradient and homogenizing the temperature field in the melt.

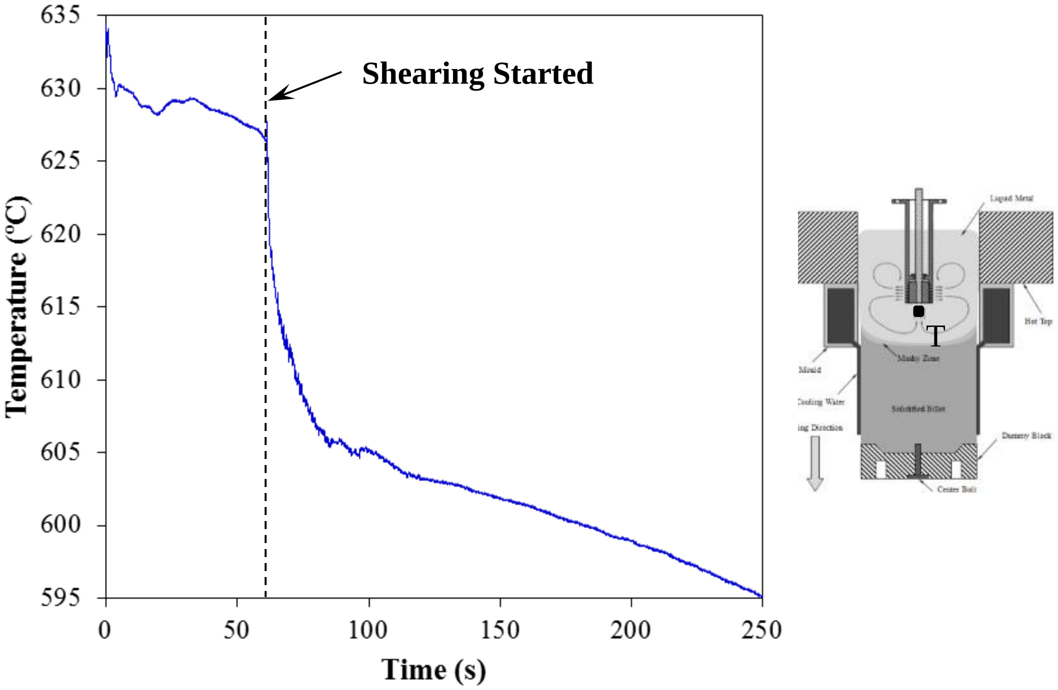

Figure 4.5.5 Measured cooling curve for AZ91D alloy melt cast at 650 ℃ during DC casting before and after shearing started. The thermal couple is 11cm from the bottom of the melt.

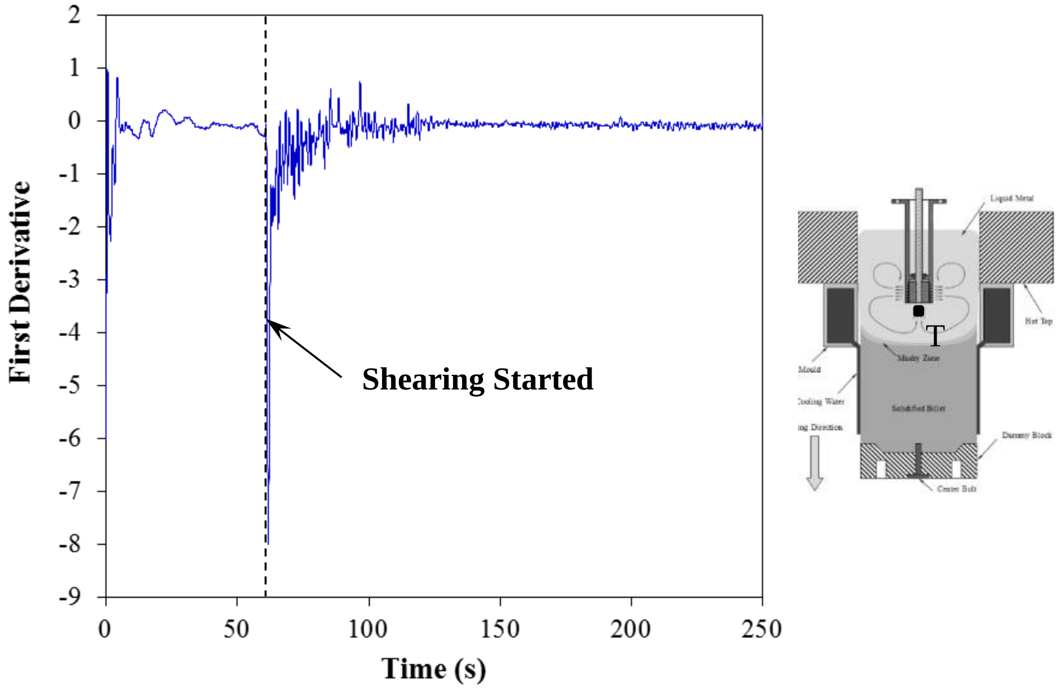

Figure 4.5.6 First derivative of the measured cooling curve for AZ91D alloy melt cast at 650 ℃ during DC casting before and after shearing started. The thermal couple is 11cm from the bottom of the melt.

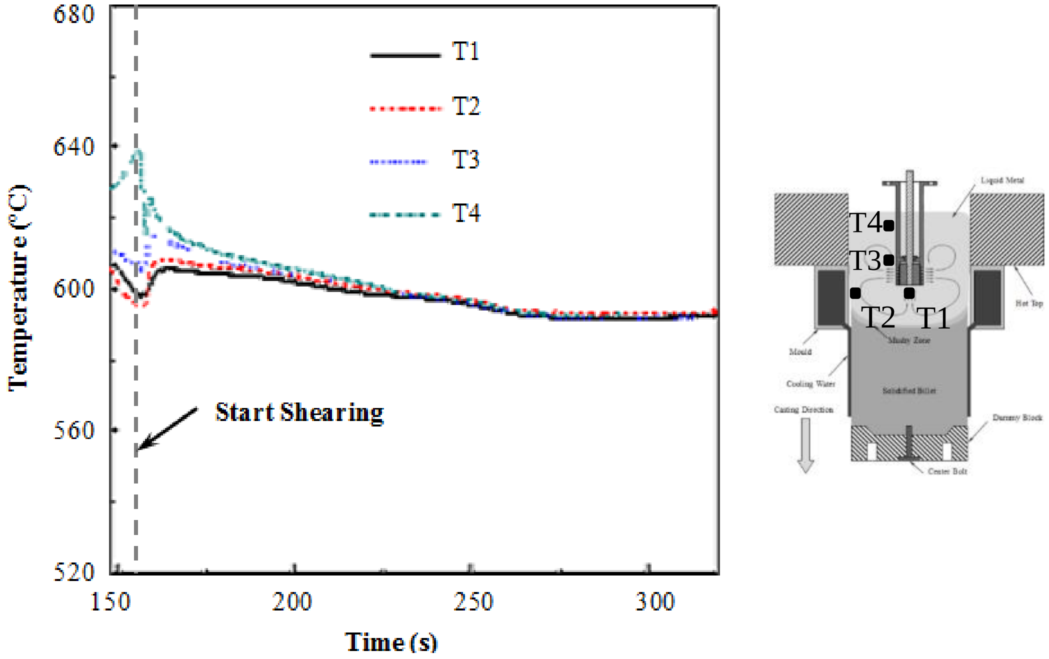

Figure 4.5.7 Measured temperature curves during AZ91D alloy DC casting with shearing cast at 650 ℃. T1, centre, 10mm below the bottom of the high shear unit; T2, edge, 10mm below the bottom of the high shear unit; T3, near to the centre, 30mm above the bottom of the high shear unit; T4, near to the centre, 90mm above the bottom of the high shear unit.

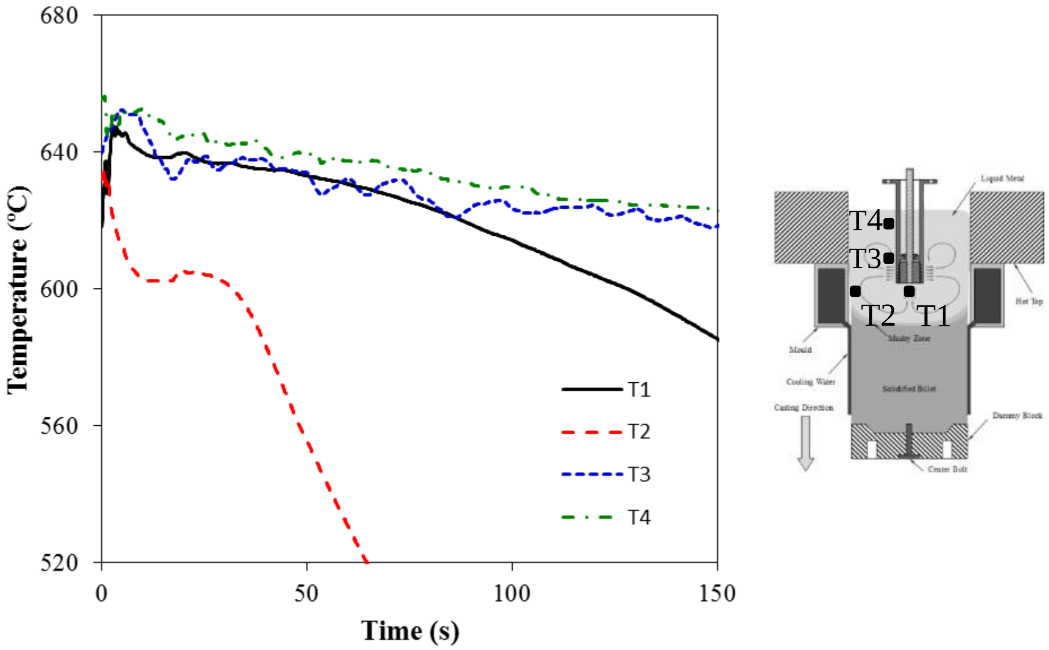

Figure 4.5.8 Measured temperature curves during AZ91D alloy DC casting without shearing cast at 650 ℃. T1, T2, T3, and T4 are of the same location as **Figure 4.5.8**.

4.5.2. AZ31 DC Casting with Intensive Melt Shearing

Based on the results in section 4.5.1, AZ91D alloy DC casting with intensive melt shearing shows significant grain refinement and microstructure homogenization throughout the cross section of ingots. The mechanism of grain refinement is to enhance nucleation by dispersing MgO films in the AZ91D alloy into individual MgO particles and distributed the particles homogenously in the melt. The mechanism of the microstructure homogenization is to homogenize the thermal field and decrease the temperature gradient through the cross section of the melt. Since the intensive melt shearing process is very effective on the AZ91D alloy, the next step is to apply the process to other magnesium alloys. If the effects on the AZ91D alloy DC casting with intensive melt shearing are reproducible in other magnesium alloys, the process can be considered as an effective and applicable process to solve the problems in conventional DC casting of magnesium alloys. **Figure 4.5.9** and **4.5.10** show the microstructures and macrostructures of the vertical sections of AZ31 alloy DC cast billets with and without intensive melt shearing. **Figure 4.5.11** illustrates the cross section microstructures of the AZ31 DC cast billets with and without melt shearing showing the difference between the edge and the centre of the billets.

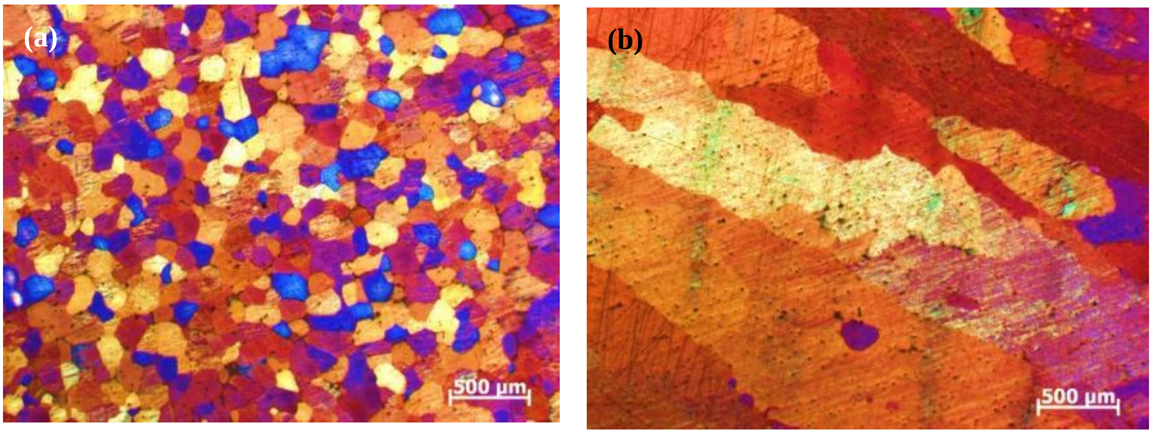

Figure 4.5.9 Microstructures of the vertical sections of the AZ31 alloy DC billets cast at 680 ℃ with (a) and without (b) intensive melt shearing.

As shown in **Figure 4.5.9(a)** and **4.5.10(a)**, the grain structure for the sample with melt shearing is fully equiaxed. The conventional AZ31 DC cast ingots usually has grain structure of fully columnar or columnar mixed with equiaxed grains, as shown in **Figure 4.5.9(b)** and **4.5.10(b)**.

Based on the results shown in these two figures, it is suggested that grain refinement can also be achieved for AZ31 alloy when intensive melt shearing process is applied.

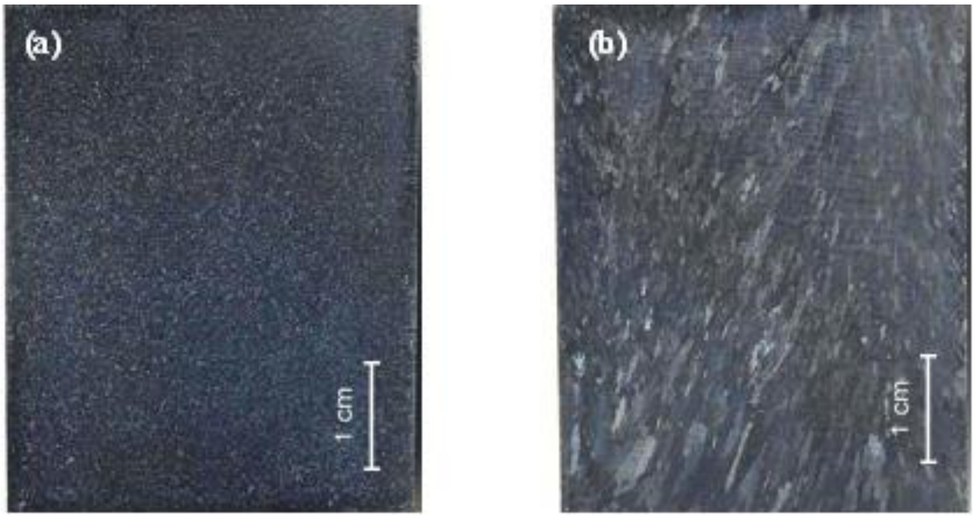

Figure 4.5.10 Macrostructures of the vertical sections of AZ31 alloy DC billets cast at 680 ℃ with (a) and without (b) intensive melt shearing.

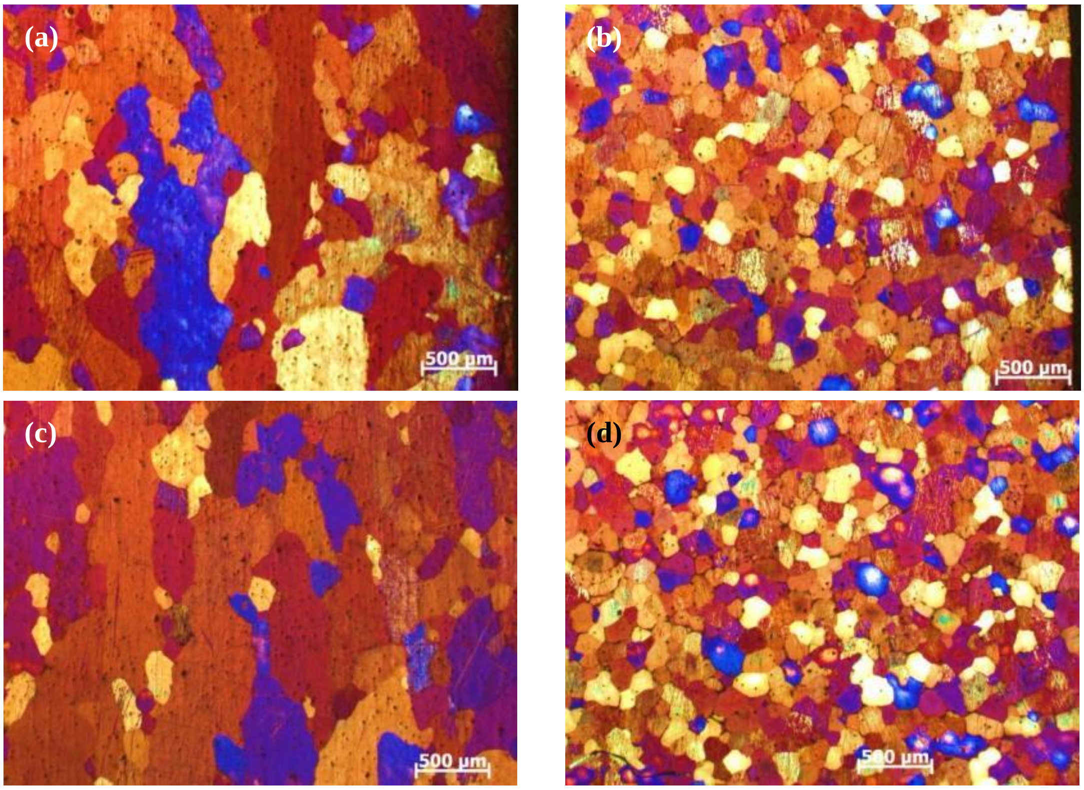

Figure 4.5.11 Microstructures of the cross sections of AZ31 magnesium alloy DC billets cast at 680 ℃ with and without melt shearing, showing the effect of melt shearing on grain structures: (a) edge of the billet, without shearing, (b) edge of the billet, with shearing, (c) centre of the billet, without shearing, (d) centre of the billet, with shearing.

In both **Figure 4.5.11(a)** and **(c)**, some columnar grain structures with various widths are observed in conventional AZ31 DC casting due to the microstructure variation. In **Figure 4.5.11(b)** and **(d)**, the microstructures are equiaxed grains with a slightly difference in sizes throughout the cross sections. Therefore, it is observed that the microstructure throughout the cross sections of the ingots become uniform after intensive shearing is applied to the melt.

4.5.3. Summary

The most important objective of this experiment is to apply the melt conditioning process and previous understanding of solidification behaviour to the industrial application of magnesium alloy DC casting, because the billets or slabs made by the conventional DC casting process often have coarse and non-uniform microstructures, severe chemical segregation, porosity and hot tearing. According to the experimental results, both AZ91D alloy and AZ31 alloy DC cast ingots show significant grain refinement and microstructure uniformity throughout the cross sections after intensive melt shearing is applied. The mechanism of grain refinement is to enhance nucleation by dispersing MgO films in AZ91D into individual MgO particles and distributing the particles homogenously in the melt. The mechanism of microstructure uniformity is the homogenization of the thermal field and the reduction of the temperature gradient through the cross section of the melt. It is then concluded that the melt conditioning process can be applied to magnesium alloy DC casting to improve qualities.

Chapter 5. Discussion

5.1. Grain Refinement of Magnesium Alloys

Zirconium is usually alloyed with aluminium free magnesium alloys to refine the microstructures [11, 13, 18, and 71]. An effective and practical grain refiner has not yet been found for aluminium bearing magnesium alloys [18], such as AZ31 and AZ91D. Kooi et al. [116] and Fan, et al [115] suggested that there are potential orientation relationships at the MgO/α-Mg interface, and the endogenous MgO particles can act as nucleation substrates for aluminium bearing magnesium alloys. Based on such understandings, it is believed that the microstructures of aluminium bearing magnesium alloys can be refined if the number density of MgO particles can be increased significantly.

The experimental results in 4.3 have shown the significant differences between the microstructures of aluminium bearing magnesium alloys with and without the inoculation of MgO nano particles. It is believed that with the inoculation of MgO particles, the microstructure has been significantly refined. However, the mechanism of such a grain refinement remains unclear although it seems likely that the effect is caused by the inoculation of MgO particles. In order to investigate the mechanism of the grain refinement, all possibilities should be taken into consideration.

The possibility of chemical reactions between MgO and solute or impurity elements in the melt and the possibility of decomposition of MgO particles need to be considered. As illustrated in section 4.3, Mg-Al binary alloys have shown significant grain refinement after the MgO nano particles were added as an inoculant. There are only two kinds of elements with the quantity over 0.01wt% in this alloy system. Due to the thermal and kinetic condition in the alloy, it is highly unlikely that the added MgO would react with aluminium. Also, as it is known, the MgO is a ceramic material generally used in fire blocking and its melting point is 3600 ℃. According to the Ellingham diagram [154] of oxides shown in **Figure 5.1**, it is highly unlikely that the MgO would react with the elements or decompose. The SEM micrograph from the experiment also ruled out this possibility since a similarity has been found between the morphologies of the MgO nano particles (**Figure 4.3.1**) and the MgO particles found in the pressurized filtration sample of Mg-9wt%Al alloy inoculated with 0.1wt% MgO (**Figure 4.3.4**).

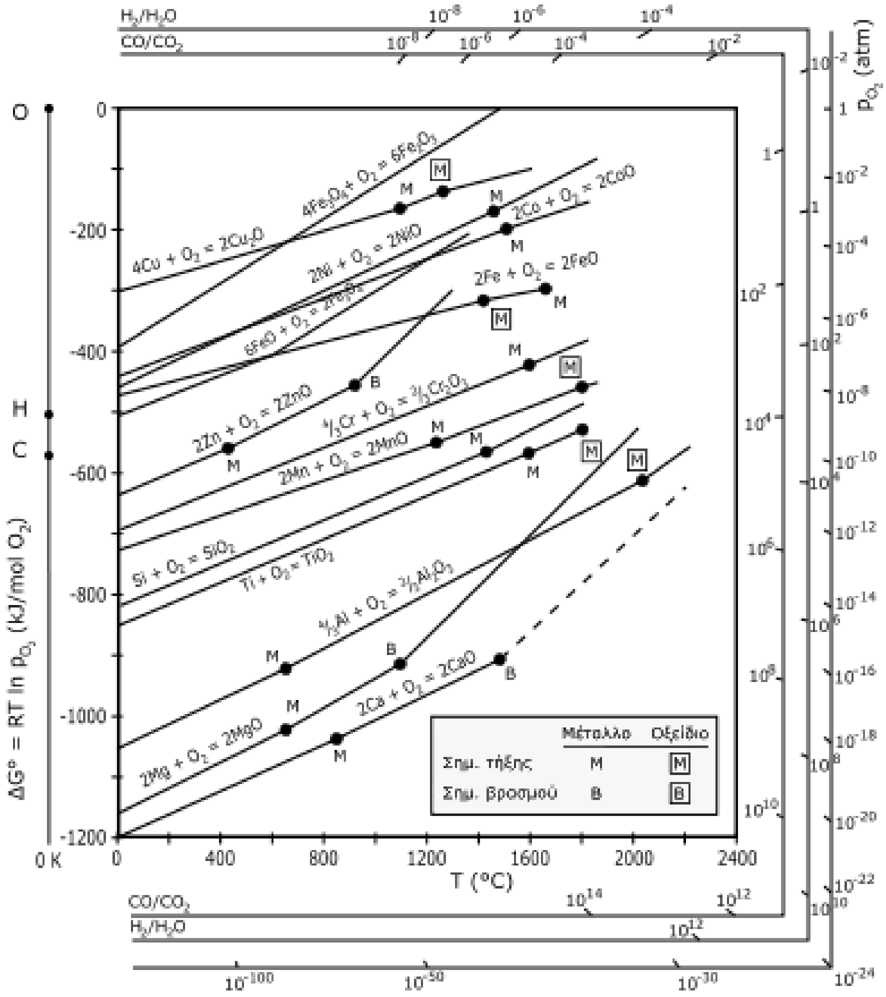

Figure 5.1 Ellingham diagram of oxides [154].

The second possibility is that the technique to add MgO particles in the melt might be the cause of the grain refinement of the magnesium alloys. During the experiments in section 4.3, the stirring process has been applied to the melt in order to add the particles. Thus, it is possible that the grain refinement is achieved by the stirring rather than the inoculated particles. However, a comparison experiment has been done showing that no significant difference has been found in microstructure either with or without the stirring process. It proves that this possibility has also been ruled out.

As discussed above, neither chemical reaction nor inoculation technique has caused the grain refinement. The only possibility left is that the MgO particles must have caused the refinement. Potentially, the MgO particles can refine the microstructure of aluminium bearing magnesium alloys either because they enhance nucleation or because they inhibit grain growth. Therefore, the MgO particles might act either as the nuclei which cause more grains to grow, or as the pinning particles retard the coarsening of the growing grains.

The pinning effect of second-phase particles has been studied by a number of researchers, such as Zener [155] and Hellman and Hillert [156]. Zener [154] is the first one to derive an analytical model of inhibition of grain growth by spherical, monosized, randomly distributed second phase particles. Hellman and Hillert [156] developed a more precise prediction model for the relation between grain size and second phase particles. Their model has been supported by the experimental results from zirconia- and alumina-based ceramic composite. **Table 5.1** shows equations of the models and the calculated results by applying these models to the MgO particles. The calculation is based on the assumption that the MgO particles act as pinning particles distributed randomly in AZ91D alloy. In both equations from the models, $\overline{D}$ is the predicted mean grain size, r_p is the radius of the particles, and f_p is the volume fraction of the particles. Based on simple calculation, the volume fraction of 100ppm MgO particles is 0.005%. The radius of the inoculated MgO particles is around 100-200nm.

Table 5.1 Pinning effect of the inoculated MgO nano particles.

	Zener	**Hellman and Hillert**
Equations	$\frac{\overline{D}}{r_p} = \frac{4}{3f_p}$	$\frac{\overline{D}}{r_p} = \frac{8}{9}{f_p}^{-0.93}$
Predicted Grain Size for AZ91D with 100ppm MgO inoculation (μm)	2637.2007	879.6656

As shown in **Table 5.1**, the predicted grain sizes for AZ91D alloy with 100 ppm MgO inoculation are much larger than the measured grain sizes from the experimental results. This suggests that there would be limited and relatively small influence of the pinning effect on the final grain sizes of the magnesium alloys. In which case, the only possibility remaining is that the MgO particles act as the nucleation substrates and enhance nucleation in aluminium bearing magnesium alloys.

If the MgO particles are the nucleation substrates in aluminium bearing magnesium alloys, there need to be enough particles to nucleate the alloy. The measured linear intercept length is around 200μm for AZ91D alloy with 100ppm MgO inoculation. The number density of grains can be calculated by

$$N_g = \frac{0.5}{\bar{l}^3} \tag{5.1}$$

where N_g is the number density of grains, and $\bar{l}$ is the measured linear intercept length. According to equation 5.1, the number density of grains should be around $10^6/\mathrm{cm}^3$, which is also the minimum required number density of the MgO. The calculated number density of 100ppm MgO particles is in the order of $10^{11}/\mathrm{cm}^3$. This means that the number density of MgO nano particles is more than the minimum required number density.

Based on the above discussion, it seems likely that the MgO particles act as the nucleation substrates and enhance nucleation in aluminium bearing magnesium alloys. However, direct evidence to support the idea is still required. In section 4.3, the cooling curves for AZ91D with and without MgO inoculation have been measured (**Figures 4.3.8** and **4.3.9**). According to the results of the measurement, the cooling rates for both curves are approximately the same. Theoretically, if the AZ91D melts have the same cooling rates, and approximately the same number densities and size distributions of nucleation substrates, the undercoolings should not have significant difference. According to the measurement in section 4.3, the cooling curve for AZ91D with 100ppm MgO inoculation has a much smaller undercooling than the one without MgO inoculation. It is suggested then that the difference in undercoolings in the curves is not caused by systematic errors of the measurement, since the reproducibility of the cooling curve measurement has been proved in section 4.1 (**Figure 4.1.1**). Accordingly, the only possibility is that the reduction of undercooling is related to MgO inoculation.

Figure 5.2 is a schematic illustration of cooling curves of the melts with the same composition and cooling rate but different undercoolings., where T_L is the liquidus, T_R is the recalescence temperature, and T_1 and T_2 are the minimum temperatures for the dash curve and the solid curve, respectively, before recalescence occurs. As the temperature decreases, both curves start to deflect. Before the temperature reaches T_1, the deflection of the dashed curve is more than that of the other. This indicates that at the same temperature before T_1 more heat has been released from the melt with the dash curve through phase transformation. Therefore, either the grains grow faster, or there are more growing grains in the melt with the dash curve. Since the compositions are the same, the growth rate of grains is determined by the undercooling. This means that the growth rate of the grains should be the same at the same temperature.

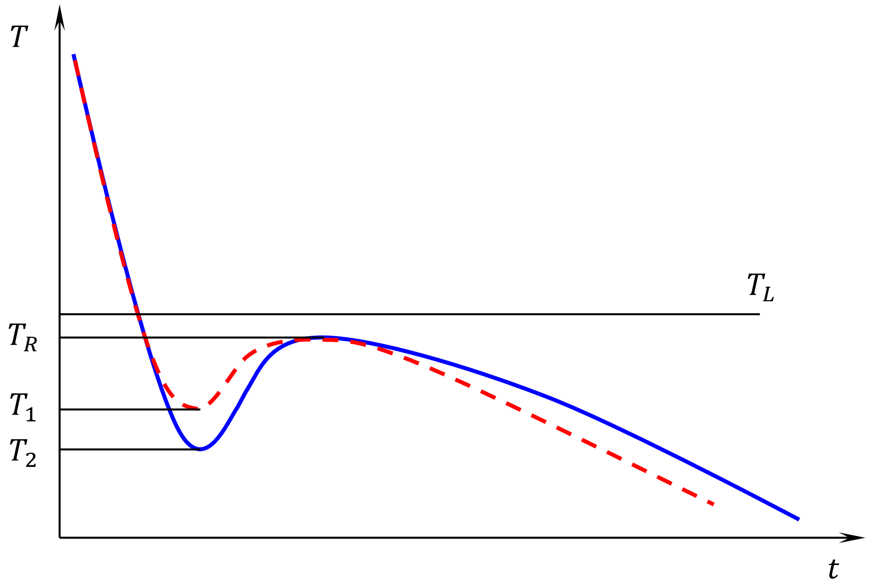

Figure 5.2 Schematic illustration of cooling curves of the melts with the same composition and cooling rate but different undercoolings.

Based on the discussion above, it is proposed that there are more growing grains in the melt with smaller undercooling. More growing grains potentially indicate more nucleant. Accordingly, it is believed that there are more nucleants in AZ91D alloy melt with 100 ppm MgO inoculation than the one without MgO inoculation. A reasonable explanation is that the added MgO particles act as the nucleation substrates and enhance nucleation in aluminium bearing magnesium alloys.

5.1.1. Potency of MgO for Magnesium Alloys

According to the discussion above, the grain refinement achieved by MgO inoculation is likely because the MgO particles act as the nucleation substrates and enhance nucleation in aluminium bearing magnesium alloys. If the explanation is correct, the MgO inoculants should be potent substrates for aluminium bearing magnesium alloys. The interfacial free energy at the nucleating interface is the controlling factor of potency of nucleation substrates in heterogeneous nucleation. However, the interfacial energy can hardly be measured in experiments [27, 28]. The potency of nucleation substrates can then be generally assessed by comparisons of the perfectness of the lattice matching along certain orientations at the solid/substrate interface [33].

If the MgO inoculants are potent substrates for aluminium bearing magnesium alloys, there should be certain orientation relationships at the interface. According to Fan et. al. [115], there is a fixed orientation relationship between the α-Mg and MgO phases along the closely packed directions, $< 1\bar{2}10 > \{0001\}_{\alpha-\mathrm{Mg}}$ and $< 01\bar{1} > \{111\}_{\mathrm{MgO}}$. The calculated misfit according to this OR is 8.01%. Based on the SEM examination, the morphology of the MgO inoculants has cubic faceted shape with straight borders and sharp vertical angles (**Figure 4.3.1**, **4.3.4**, **4.3.11**, and **4.3.15**), which indicates that the exposed surface of the inoculants is {100} plain. Although there is no fine orientation relationship between MgO {100} face and Mg {0001} face that has been suggested by previous publications, it can be observed that the calculated misfit can be even smaller than 8.01% along certain orientations.

Figure 5.3 is a schematic illustration of MgO {100} face and Mg {0001} face. As it is shown, potentially, there are three possible pairs of orientation relationships between MgO {100} face and Mg {0001} face.

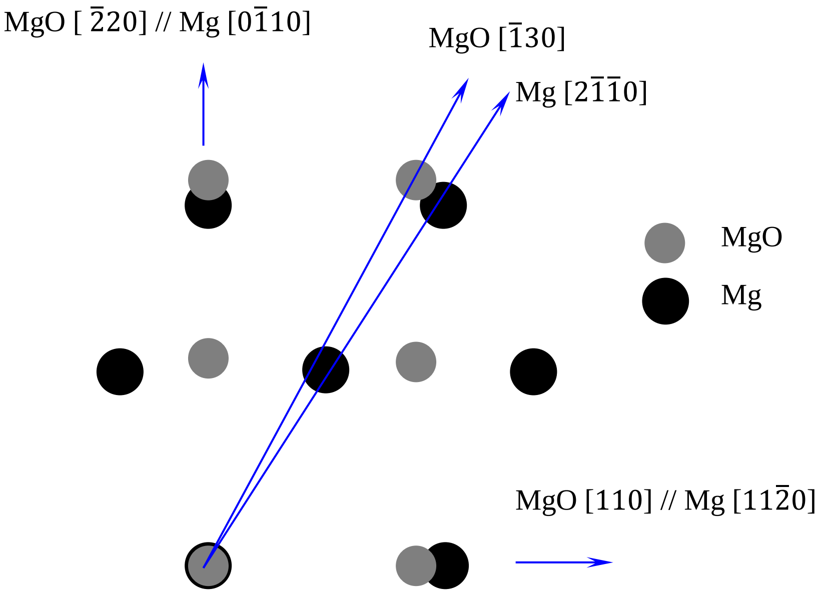

Figure 5.3 Schematic illustration of MgO {100} face and Mg {0001} face.

The calculated misfits for MgO and Mg with various weight percentages of Al are shown in **Table 5.2**. It can be observed that the misfit of $< 2\bar{1}\bar{1}0 > \{0001\}_{\alpha-Mg}$ and $< \bar{1}30 > \{001\}_{MgO}$ is much smaller than the misfit of the $< 1\bar{2}10 > \{0001\}_{\alpha-Mg}$ and $< 01\bar{1} > \{111\}_{MgO}$ with various concentration of aluminium. The misfit of $< 0\bar{1}10 > \{0001\}_{\alpha-Mg}$ and $< \bar{2}20 > \{001\}_{MgO}$ is smaller than that of $< 1\bar{2}10 > \{0001\}_{\alpha-Mg}$ and $< 01\bar{1} > \{111\}_{MgO}$ with low concentration of aluminium. Therefore, it is believed that the {001} face of MgO can be a more potent nucleation substrate for α-Mg than {111} face of MgO.

Table 5.2 Calculation of the three OR misfits between MgO and Mg at 600 ℃.

Al (wt%)	**MgO(111)[$01\bar{1}$] // Mg(0001)[$11\bar{2}0$]**	**MgO(001)[110] // Mg(0001)[$11\bar{2}0$]**	**MgO(001)[$\bar{2}20$] // Mg(0001)[$0\bar{1}10$]**	**MgO(001)[$\bar{1}30$] // Mg(0001)[$2\bar{1}\bar{1}0$]**
0.00	8.01	8.01	5.94	2.40
1.00	7.97	7.97	6.26	2.70
3.00	7.42	7.42	6.58	3.33
9.00	5.46	5.46	7.56	5.24

5.1.2. Efficiency of MgO Inoculation in Magnesium Alloys

The efficiency of nucleation substrates is the number density of effective nucleation substrates per unit volume in heterogeneous nucleation, which is one of the key factors that determine the final grain structure. In classical nucleation theory, the description of efficiency is given by the calculation of nucleation rate. However, it is relatively difficult to provide an accurate quantitative prediction for nucleation rate during solidification. One possible solution for this problem is to use the final grain structure to predict the efficiency of nucleation substrates. Since the effective nucleation substrates will produce final grains, the number density of effective nucleation substrates can, therefore, be approximately considered as the number density of grains.

In section 4.3, the microstructures of AZ91D commercial alloy (**Figure 4.3.6**) with MgO inoculation have been significantly refined compared to the ones without MgO inoculation. The number densities of grains for AZ91D with and without MgO inoculation can be calculated using equation 5.1, and the calculated results are $\sim 10^6/\text{cm}^3$ and $\sim 10^3/\text{cm}^3$, respectively. This indicates that the efficiency of the nucleation substrates is much higher in AZ91D with MgO inoculation.

As calculated in section 5.1, the number density of 100 ppm MgO nano particle inoculation is in the order of $10^{11}/\text{cm}^3$, which is much larger than the number density of grains for AZ91D with MgO inoculation as calculated above. This is because only some of the MgO inoculants can grow freely.

According to Greer et. al. [36, 42, 43], the efficiency of grain refiner could be explained better using the free-growth criterion to describe grain initiation in the isothermal melt, in which a distribution of particle sizes d was assumed. The undercooling required for grain initiation of the individual particle is given by:

$$\Delta T_{fg} = \frac{4\Upsilon_{SL}}{d\Delta S_v} \tag{5.2}$$

where Υ_{SL} is the solid-liquid interfacial energy, ΔS_v is the entropy of fusion per unit volume, and d is the diameter of nucleation substrate. The measured maximum undercooling for AZ91D with 100ppm MgO inoculation is about 0.5℃ before recalescence occurs (**Figure 4.3.8** and **Figure 4.3.9**). According to equation 5.2, if the free growth undercooling is 0.5K, the minimum diameter of nucleation substrates that can grow freely is 1.18μm. This means that any nucleation substrates with a diameter smaller than this critical value cannot grow freely.

The results in **Figure 4.3.12** indicate that the size distribution of the MgO inoculants can be well fitted by a log-normal function with parameters $d_0 = 0.13$ μm and $\sigma = 0.45$. Based on the cumulative size distribution function of MgO inoculants, the probability that the diameter of MgO inoculants is larger than 1.18, is 0.0051%. This means that the number density of MgO inoculants that can grow freely is therefore in the order of $10^6/\mathrm{cm}^3$, which is consistent with the number density of grains for AZ91D with MgO inoculation calculated above.

5.1.3. A Model for Grain Size Prediction by Cooling Curve Analysis

Cooling curve measurement is a typical method usually used for analyzing the thermal field and the phase transformation. Greer et. al. [36, 42, 43] have predicted the undercooling by introducing a given grain refiner with a certain number density and size distribution of the TiB_2 grain refiner. In conventional castings without grain refiner addition, the size distribution of effective nucleation substrates is hard to achieve by typical technologies. The cooling curve, on the other hand, can be measured much easily. This means that it is more convenient to use the cooling curve as the analyzing method for modelling the solidification processes and predicting the final grain structures. In this section, a model based on cooling curve analysis is proposed to predict the number density and size distribution of effective nucleant. As it is known, it is assumed that the number density of an effective nucleant approximately equals the number density of grains. Therefore, the model can predict the grain size using a measured cooling curve.

In a typical cooling curve with pronounced recalescence and relatively slow cooling rate, as shown in **Figure 5.4**, the heat dissipation from the melt per unit time equals the heat absorbed by the environment per unit of time, which is considered as a constant in this model.

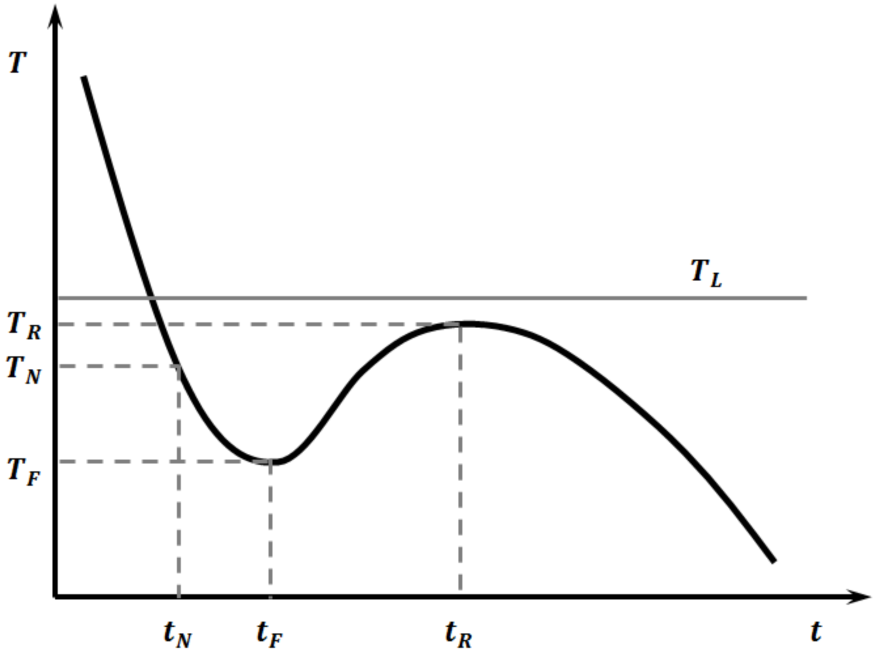

Figure 5.4 Schematic drawing of a typical cooling curve with pronounced recalescence.

Based on such understanding, the heat dissipation from the melt before and after phase transformation occurs should be the same per unit of time. The heat dissipation from the melt before phase transformation occurs can be given by,

$$\frac{\mathrm{d}Q}{\mathrm{d}t} = C_p \cdot \rho \cdot V_m \left.\frac{\mathrm{d}T}{\mathrm{d}t}\right|_{t<t_N} \tag{5.3}$$

where $\mathrm{d}Q/\mathrm{d}t$ is the heat dissipation, C_p is the heat capacity of the melt, ρ is the density of the melt, V_m is volume of the melt, t_N is the time when phase transformation occurs, and $\left.\frac{\mathrm{d}T}{\mathrm{d}t}\right|_{t<t_N}$ is the cooling rate of the melt before t_N.

The heat dissipation from the melt after t_N and before t_F comprises two parts, which are the heat released from the temperature change of the melt and the heat released from the phase transformation of the growing crystal. It is given by,

$$\frac{\mathrm{d}Q}{\mathrm{d}t} = \left(C_p \cdot \rho + \Delta h_f \left. \frac{\mathrm{d}f_s}{\mathrm{d}T} \right|_{T_F \leq T = T_i < T_N} \right) V_m \left. \frac{\mathrm{d}T}{\mathrm{d}t} \right|_{t_N \leq t = t_i < t_F} \tag{5.4}$$

where Δh_f is the latent heat of fusion per unit of volume, f_s is the solid fraction within the melt, T_N is the temperature for phase transformation occurs, T_i and t_i are random temperature and time after phase transformation occurs and before recalescence, and $\left. \frac{\mathrm{d}T}{\mathrm{d}t} \right|_{t_N \leq t = t_i < t_F}$ is the cooling rate at t_i.

The heat dissipation from the melt per unit of time is considered as a constant in this model. From equation 5.3 and 5.4, we have,

$$C_p \cdot \rho \cdot \left. \frac{\mathrm{d}T}{\mathrm{d}t} \right|_{t < t_N} = \left(C_V \cdot \rho + \Delta h_f \left. \frac{\mathrm{d}f_s}{\mathrm{d}T} \right|_{T_F \leq T = T_i < T_N} \right) \left. \frac{\mathrm{d}T}{\mathrm{d}t} \right|_{t_N \leq t = t_i < t_F} \tag{5.5}$$

The change of solid fraction against temperature can be given by,

$$\left. \frac{\mathrm{d}f_s}{\mathrm{d}T} \right|_{T_F \leq T = T_i < T_N} = \frac{1}{V_m} \left. \frac{\mathrm{d}V_s}{\mathrm{d}T} \right|_{T_F \leq T = T_i < T_N} \tag{5.6}$$

where V_s is the volume of the solid phase of the melt.

Since the change of the volume of the solid phase against temperature is caused by the growth of crystal, it can be calculated by the accumulation of each piece of crystal. It is then given by,

$$\left. \frac{\mathrm{d}V_s}{\mathrm{d}T} \right|_{T_F \leq T = T_i < T_N} = \int_{n_N}^{n_i} \frac{\mathrm{d}V_{ij}}{\mathrm{d}T} \mathrm{d}n_j \tag{5.7}$$

where $\mathrm{d}V_{ij}$ is the volume change at t_i of a piece of crystal that starts to grow freely at t_j $(t_N \leq t_j < t_i)$, n_j is the number of effective nucleation substrates which start to grow at t_j, n_N is the number of effective nucleation particles which start to grow at t_N, and n_i is the number of effective nucleation particles which start to grow at t_i.

Since the effective nucleation particles are believed to start free growth gradually with the decrease of temperature, a distribution function can be defined as,

$$P(T) = \mathrm{d}F(T) = \frac{\mathrm{d}n}{V_m \mathrm{d}T} = -\frac{\mathrm{d}n}{V_m \mathrm{d}(\Delta T)} \tag{5.8}$$

where $P(T)$ is the distribution function of numbers of nucleation particles against temperature per unit volume, $F(T)$ is the cumulative distribution function of $P(T)$, and n is the number of effective nucleation particles with undercooling ΔT.

The volume change dV_{ij} can be expressed as,

$$\mathrm{d}V_{ij} = 4\pi R_{ij}^2 \mathrm{d}R_{ij} \tag{5.9}$$

where R_{ij} is the radius at t_i of a piece of crystal which starts to grow at t_j.

The radius change $\mathrm{d}R_{ij}$ is given by

$$\mathrm{d}R_{ij} = v_g \mathrm{d}t \tag{5.10}$$

where v_g is the growth velocity of the crystal. Equation 5.6 therefore becomes,

$$\left.\frac{\mathrm{d}f_s}{\mathrm{d}T}\right|_{T_F \le T = T_i < T_N} = 4\pi \int_{t_N}^{t_i} P(T) R_{ij}^2 v_g dt \tag{5.11}$$

According to Hunt and Lu [157], the growth velocity v_g has a certain relationship with the tip undercooling, given by

$$\Delta T = \left(\frac{v_g}{A}\right)^{(1-a_1)} \tag{5.12}$$

where A is a constant, given by

$$A = \left(\frac{1}{a_0\left(mC_0(k-1)\right)^{a_1}}\right)^{\frac{1}{1-a_1}} \frac{D}{2\Gamma} \tag{5.13}$$

where m is the liquidus slope, C_0 is the alloy composition, k is the equilibrium distribution coefficient, D is the diffusion coefficient, and Γ is the Gibbs-Thomson coefficient. For k varying between 0 and 2, $a_0 = 2.08 - 1.534k + 0.434k^2$, and $a_1 = 0.648 + 0.124k$.

The radius R_{ij} is then given by

$$R_{ij} = \int_{t_j}^{t_i} v_g \mathrm{d}t = A \cdot \int_{t_j}^{t_i} \Delta T^{\frac{1}{1-a_1}} \cdot \mathrm{d}t \tag{5.14}$$

Equation 5.11 then becomes,

$$\left.\frac{\mathrm{d}f_s}{\mathrm{d}T}\right|_{T_F \leq T = T_i < T_N} = 4\pi A^3 \int_{t_N}^{t_i} P(T)\Delta T^{\frac{1}{1-a_1}} \left(\int_{t_j}^{t_i} \Delta T^{\frac{1}{1-a_1}} \cdot \mathrm{d}t\right)^2 dt \tag{5.15}$$

From equation 5.5, we have

$$\left.\frac{\mathrm{d}f_s}{\mathrm{d}T}\right|_{T_F \leq T = T_i < T_N} = \frac{C_p \cdot \rho}{\Delta h_f} \left(\frac{\left.\frac{\mathrm{d}T}{\mathrm{d}t}\right|_{t<t_N}}{\left.\frac{\mathrm{d}T}{\mathrm{d}t}\right|_{t_N \leq t = t_i < t_F}} - 1 \right) \tag{5.16}$$

Equation 5.15 then becomes,

$$\frac{C_p \cdot \rho}{4\pi A^3 \cdot \Delta h_f}\left(\frac{\left.\frac{\mathrm{d}T}{\mathrm{d}t}\right|_{t<t_N}}{\left.\frac{\mathrm{d}T}{\mathrm{d}t}\right|_{t_N \le t = t_i < t_F}} - 1\right) = \int_{t_N}^{t_i} P(T)\Delta T^{\frac{1}{1-a_1}}\left(\int_{t_j}^{t_i} \Delta T^{\frac{1}{1-a_1}} \cdot \mathrm{d}t\right)^2 dt \tag{5.17}$$

From a numerical point of view, a possible solution to calculate phase transformed is to insert $s-1$ points into the time range from t_N to t_F equally, as it is shown in **Figure 5.5**.

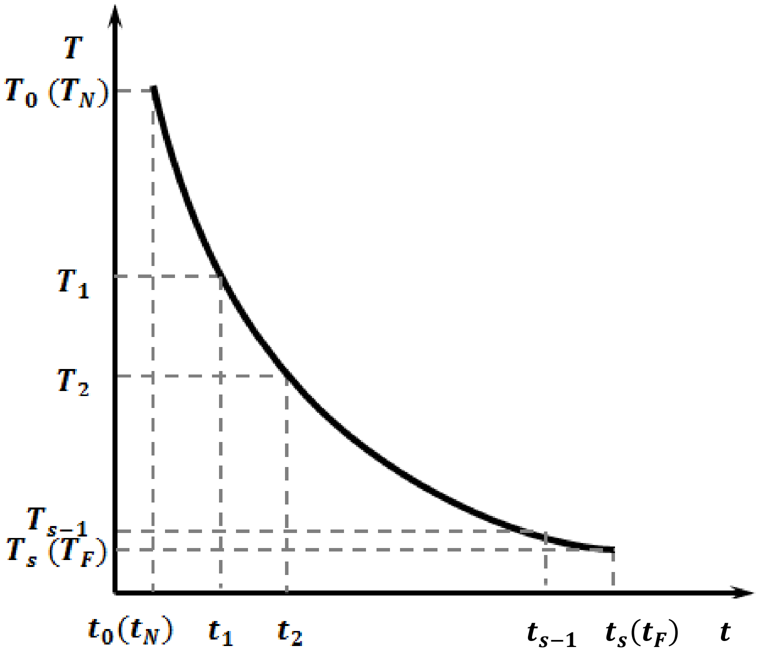

Figure 5.5 Schematic drawing of the numerical solution with $s-1$ points insert into the time range from t_N to t_F.

The radius at the (i)th step of nucleation particles which start to grow at the (j)th step, then, can be given as,

$$R_{ij} = A \cdot \frac{t_F - t_s}{s} \cdot \sum_{p=j}^{i-1} \Delta T_p^{\frac{1}{1-a_1}} \tag{5.18}$$

The change of solid fraction against temperature in 5.15, can be given as,

$$\frac{\Delta f_{s,i}}{\Delta T} = \frac{1}{\Lambda} \cdot \sum_{j=0}^{i-1} \left[P(T_j) \cdot \Delta T_j^{\varepsilon} \cdot \left(\sum_{p=j}^{i-1} \Delta T_p^{\varepsilon} \right)^2 \right] \tag{5.19}$$

where $\Delta f_{s,i}$ is the change of solid fraction between the $(i-1)$th and the (i)th step, ε and Λ are parameters defined as , $\varepsilon = \frac{1}{1-a_1}$ and $\Lambda = \left[4\pi A^3 \cdot \left(\frac{t_F - t_S}{s} \right)^3 \right]^{-1}$.

Therefore, the distribution function $P(T_i)$ becomes,

$$P(T_i) = \Lambda \cdot \Delta T_i^{(-3\varepsilon)} \cdot \frac{\Delta f_{s,i+1}}{\Delta T} - \sum_{j=0}^{i} \left[P(T_j) \cdot \Delta T_j^{\varepsilon} \cdot \left(\sum_{p=j}^{i} \Delta T_p^{\varepsilon} \right)^2 \right] \tag{5.20}$$

where the change of solid fraction against temperature, from equation 5.5, is given by

$$\frac{\Delta f_{s,i+1}}{\Delta T} = \frac{2 \cdot C_p \cdot \rho}{\Delta h_f} \left(\frac{\left.\frac{\mathrm{d}T}{\mathrm{d}t}\right|_{t<t_N}}{\left.\frac{\mathrm{d}T}{\mathrm{d}t}\right|_{t_i+1} + \left.\frac{\mathrm{d}T}{\mathrm{d}t}\right|_{t_i}} - 1 \right) \tag{5.21}$$

Using this model, the numbers of nucleation particles against temperature per unit volume for each temperature point can be calculated through equation 5.20 and 5.21. As a result, the total number of effective nucleation substrates and the grain size can then be predicted. As an application, the cooling curve measurements for AZ91D alloy with and without intensive melt shearing and AZ91D alloy with 100 ppm MgO particle inoculation have been applied to the model. The cooling rates used in the model are provided by the first derivatives of the cooling curves which have been smoothed by average adjacent method. The input parameters are shown in **Table 5.3** and the calculated results of effective nucleation particle number and the predicted grain size are shown in **Table 5.4**.

Table 5.3 Parameters for AZ91D alloy.

Parameters for AZ91D	Symbol	Value	Unit
Density	ρ	1.81×10^3	$\mathrm{kg/m^3}$
Heat Capacity	C_p	1.05×10^3	$\mathrm{J/(kg \cdot K)}$
Liquidus Slope	m	-6.87	$\mathrm{K/wt\%}$
Partition Coefficient	k	0.37	-
Latent Heat	Δh_f	3.73×10^5	$\mathrm{J/kg}$
Diffusion coefficient	D	2.70×10^{-9}	$\mathrm{kg/m^3}$
Gibbs-Thomson coefficient	Γ	1.48×10^{-7}	$\mathrm{kg/m^3}$

Table 5.4 Calculated results for AZ91D alloy.

Grain Size (μm)	without melt shearing	with melt shearing	with MgO inoculation
Calculated	2136	1054	1102
Measured	2005	1210	1241

The predicted number density of effective nucleation substrates and the grain sizes in **Table 5.4** are consistent to the measured grain sizes shown in **Figure 4.1.7** and **4.3.10**. This means that the model can be used to predict grain structures for casting samples with relatively low cooling rates.

5.2. The Role of Solute in Magnesium Alloys

The role of solute in alloys potentially has two kinds of effect on the microstructures. Hunt [55] suggested that composition is one of the key influential factors for columnar equiaxed transition. According to his study, it is more likely to achieve equiaxed grains with higher composition. Previous publications [18, 52, 53] suggested that the final grain sizes of casting samples are determined by the composition. In their model, the growth restriction factor, $Q = mC_0(k-1)$, has an inverse relationship against the grain size d. The relationship is given by,

$$d = a + b/Q \tag{5.22}$$

where a and b are considered as constants related to the efficiency and potency of nucleation particles, respectively.

The experimental results presented in section 4.2 have shown the effect of solute on final grain structures in magnesium alloys. As it is shown in **Figures 4.2.1**, **4.2.2**, **4.2.3**, **4.2.8(a)**, and **4.2.8(c)**, the microstructures of cross sections of Mg-Al or Mg-Zn binary alloys appear to be finer as the composition (Al or Zn) increases. This seems to be consistent with the inverse relationship between Q and grain sizes suggested by various publications. According to the linear intercept measurement results, the fitted values of the parameters a and b in equation 5.22, and the correlation coefficients for the fitting for various casting conditions are shown in **Table 5.5**. The calculated growth restriction factors Q for Mg-Al and Mg-Zn binary alloys are shown in **Table 5.6**. As shown, all correlation coefficients for the linear fittings are larger than 0.95.

Table 5.5 Calculated parameters a and b for various casting conditions.

Casting Conditions	**Mg-Al**			**Mg-Zn**		
	$\boldsymbol{a}$	$\boldsymbol{b}$	**Corr.**	$\boldsymbol{a}$	$\boldsymbol{b}$	**Corr.**
10 ℃ superheat with shearing	62.44	191.22	0.9531	104.09	182.67	0.9777
10 ℃ superheat without shearing	112.47	276.02	0.9693	138.84	387.18	0.9999
30 ℃ superheat without shearing	125.94	359.74	0.9562	161.63	444.53	0.9848
50 ℃ superheat without shearing	205.26	400.13	0.9835	193.77	475.87	0.9872

Table 5.6 Growth restriction factors for Mg-Al and Mg-Zn binary alloys

Q	**0.1wt%**	**0.3wt%**	**1wt%**	**3wt%**	**9wt%**
Mg-Al	0.947	1.813	4.843	13.499	39.468
Mg-Zn	1.046	2.109	5.830	16.460	48.351

As shown in **Figure 4.2.5**, the microstructure of Mg-1wt%Al binary alloy vertical section casting at 658 ℃ without shearing contains both columnar and equiaxed grains. The results from linear intercept measurement might not all be grain sizes, nor columnar widths, but values with no physical significance. The schematic drawing of the microstructure of a TP-1 casting sample shows that the cross section appears to contain equiaxed grains only, even though the microstructure of the TP-1 casting sample is fully columnar grains or contain both equiaxed and columnar grains. Thus, the well fitted linear relationship of grain sizes against $1/Q$ calculated above based on the growth restriction factor model may not exist, and the growth restriction factor model [18, 52, 53] is debatable, at least for Mg-Al and Mg-Zn binary alloys.

Based on Hunt's CET map [55], the conditions for fully equiaxed transition depend on the composition, once the effective nucleation particle number, and the nucleation undercooling is determined. **Figure 5.6** gives an approximate analysis of Mg-Al fully equiaxed transition with five different alloy compositions.

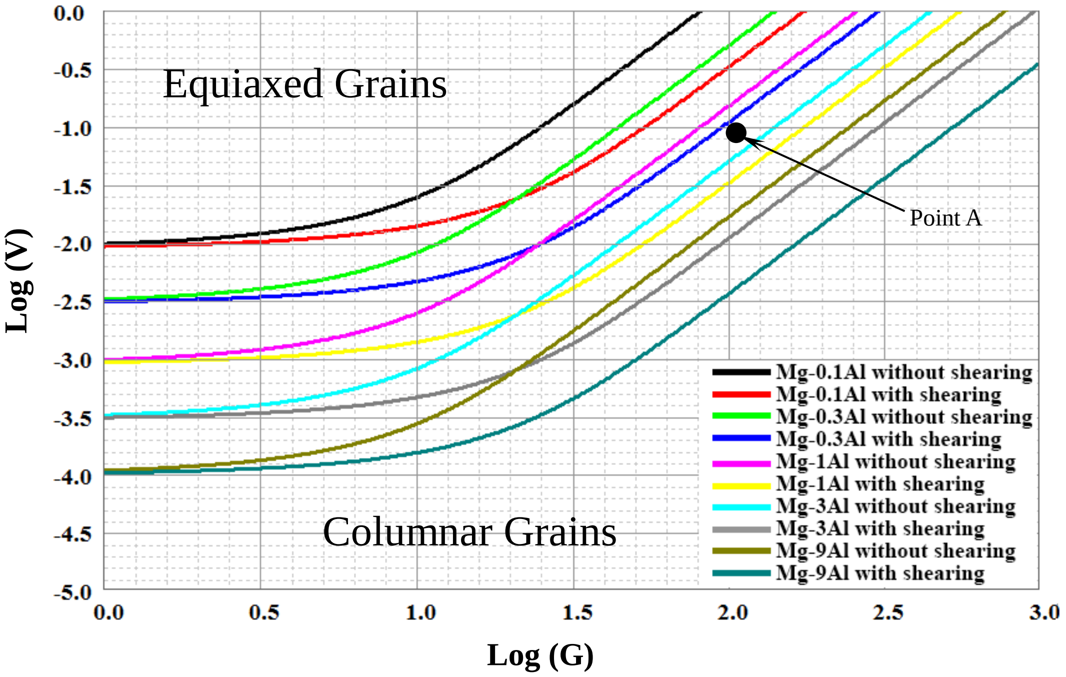

Figure 5.6 Plot of growth velocity $V\,(\mathrm{cm/s})$ against temperature gradient $G\,(\mathrm{K/cm})$ at $N = 10^3/\mathrm{cm}^3$ and $\Delta T_N = 1\mathrm{K}$ without shearing, and $N = 10^6/\mathrm{cm}^3$ and $\Delta T_N = 0.6\mathrm{K}$ with shearing for fully equiaxed transition with five different alloy compositions.

For each line in **Figure 5.6**, the area below the line is the fully columnar zone or the columnar and equiaxed zone, and the area above the line is the fully equiaxed zone for the composition and casting conditions. For the point drops in the fully equiaxed zone, the grain structure, based on Hunt’s CET model [55], can be fully equiaxed. For the point drop in the fully columnar zone or columnar and equiaxed zone, the grain structure contains columnar. For general magnesium TP-1 experiments, the estimation for temperature gradient and growth velocity from geometry and casting time is about 100 K/cm and 0.1 cm/s. As shown in **Figure 5.6**, point A is located below the condition plots for Mg-0.3wt%Al with shearing and Mg-1wt% Al without shearing, and above those for Mg-1wt%Al with shearing and Mg-3wt% Al without shearing. This estimation is consistent with the experimental results shown in **Figure 4.2.6**, and **4.2.7**.

The effect of solute on grain sizes should not consider those values without physical significance. The experimental results of Mg-Al and Mg-Zn binary alloys casting at 10 ℃ superheat with shearing and 10 ℃, 30 ℃, and 50 ℃ superheat without shearing, all show slight differences in grain sizes. These differences are caused by two factors, which are the solute effect, and the number density of the nucleation particles. The difference between Mg-Al and Mg-Zn binary alloys casting at 10 ℃ superheat with and without shearing is considered to be the interference of number density of the nucleation particles. For the experimental results without shearing, the adequacy of nucleation particles remains unclear. For the ones with shearing, since the number density of nucleation particles is large enough, the interference is believed to be ruled out. The differences among grain sizes for Mg-1wt%Al (Zn), Mg-3wt%Al (Zn), and Mg-9wt%Al (Zn) casting at 10 ℃ superheat with shearing indicates that solute composition has affected the grain size since higher compositions result in smaller grain sizes. Nevertheless, the influence is much smaller than suggested in the growth restriction factor model.

5.3. The Role of Solidification Conditions on Magnesium Alloys

A theoretical model developed by Hunt and Fan [60] has suggested that casting conditions such as pouring temperature and mould temperature cause a melt quenching effect when the alloy melt is poured rapidly in the mould and generates strong turbulence. The turbulence in the melt forces the melt to reach an isothermal environment at a critical heat balance temperature. The critical heat balance temperature may potentially result in two different conditions. It is either higher or slightly lower than the liquidus temperature of the melt. If the critical heat balance temperature is higher than the liquidus, a temperature gradient will form in the melt shortly after the heat balance temperature is reached. In such circumstance, temperature of the melt near the mould will reach the liquidus first, and the solidification will start from the edge to the centre of the melt. If the critical heat balance temperature is lower than the liquidus, solidification will occur almost simultaneously at different locations in the melt. Although the model seems to be reasonable, there is no experimental evidence to support it in previous literatures.

In section 4.4, the experimental results for melt quenching effect in AZ91D alloys have been provided. The measured cooling curves at various locations in the melt reach a critical heat balance temperature shown in **Figures 4.4.3** and **4.4.4**. The critical heat balance temperature for **Figure 4.4.3** is below liquidus while the one for **Figure 4.4.4** is above liquidus. Based on these two results, it is observed that the melts have become isothermal and the critical heat balance temperatures have been achieved within one second after the melts have been rapidly poured. The critical heat balance temperature can also be found in **Figures 4.4.5**, **4.4.6**, and **4.4.7**. As shown in these figures, the cooling rates show significant difference before and after the critical heat balance temperature is reached. According to the results, it is proposed that the critical heat balance temperature does exist shortly after the melt is rapidly poured into the mould. It can be seen that from the thermal analysis in section 4.4, the critical heat balance temperature has been mainly determined by the pouring temperature and the mould temperatures. With certain combination of casting conditions, the critical heat balance temperature can be either above liquidus or slightly below liquidus.

According to the above discussion, it can be concluded that the critical heat balance temperature does exist and is caused by the strong turbulence in the melt. Also, the combination of the pouring and the mould temperatures will determine whether the critical heat balance temperature is above or slightly below liquidus temperature. Theoretically, if the critical heat balance temperature is below liquidus, solidification should occur simultaneously at different locations due to the isothermal condition in the melt. Accordingly, the final grain structure is mainly depends on the number density of effective nucleant in the melt. If the critical heat balance temperature is above liquidus, solidification will start from the edge to the centre of the melt. In this circumstance, other parameters such as temperature gradient will have certain influence on the final grain structures.

5.4. Melt Treatment Technique for Magnesium Alloys

5.4.1. Mechanism of Intensive Melt Shearing for Magnesium Alloys

Intensive melt shearing treatment provides fine and uniform microstructures for magnesium alloys. It was proposed in previous discussion that grain refinement is achieved by enhancing heterogeneous nucleation in the magnesium melt with intensive melt shearing. Based on Fan et. al. [38, 115], endogenous MgO particles are suggested as the nucleation substrates for α-Mg since an OR between the α-Mg and MgO phases has been found. The mechanism of the grain refinement effect of intensive melt shearing treatment, therefore, is suggested as dispersing endogenous MgO films into individual particles and distributed them homogeneously in the magnesium alloy melt.

The experimental results in section 4.1 takes AZ91D alloy as an example to investigate the mechanism of grain refinement achieved by intensive melt shearing. The measured cooling curves in **Figures 4.1.2** and **4.1.3** for AZ91D with and without melt shearing show that the melt with shearing have smaller maximum undercooling before recalescence, compared with the one without shearing. Since the cooling rates above liquidus for the two curves are approximately the same, the smaller undercooling for sheared melt must be caused by intensive melt shearing treatment.

As discussed earlier in sections 4.1 and 5.1.3, a typical cooling curve after phase transformation occurs is the equilibrium of the heat released to the environment, the heat released through temperature drop and from the latent heat during phase transformation. Smaller undercooling for sheared melt indicates that at a given temperature before recalescence, the heat released through phase transformation is larger for the sheared melt compared to the non-sheared melt. In which case, more α-Mg phase has transformed in sheared AZ91D alloy melt. Considering that the growth velocity at the given time for sheared melt is smaller based on equation 5.5, the larger latent heat must be caused by larger number of nuclei growing freely. Thus, the number density of effective nucleation substrates in sheared melt must be more than that of the non-sheared melt. The SEM micrographs in **Figures 4.1.9**, **4.1.10** and **4.1.11** have confirmed this explanation. As shown in these micrographs, the endogenous MgO films become individual particles after intensive melt shearing treatment has been applied. The diameters for these individual particles are around 100nm to 1μm and the measured and fitted size distributions of MgO given in **Figure 4.1.12** suggest a log normal distribution of particle numbers against diameters which is consistent to the fitted distribution in the free growth model [36, 42, 43]. Since the MgO particles are loosely packed inside the oxide films, dispersion of such oxide particles can be achieved relatively easily if the shear rate and the shearing time are beyond a critical level [115].

The measured maximum undercoolings for melt with and without shearing are 0.7 ℃ and 1.3 ℃, respectively. According to equation 5.2, the minimum sizes for effective nucleation substrates should be 0.85μm with intensive melt shearing and 0.45μm without intensive melt shearing. The average grain sizes of the solidified samples used for cooling curve measurement are 2005μm for the non-sheared one and 1210μm for the sheared one. According to equation 5.1, the number densities of grains are 0.28mm^{-3} and 0.06mm^{-3} for the ones with and without melt shearing, respectively. The dramatic increase of the number densities of grains can be attributed to the dispersion of MgO films and distribution of MgO particles by intensive melt shearing. In the non-sheared melt, the nucleation of the α-Mg phase first occurs on the largest MgO particle available in the oxide film, and the smaller particles in the same oxide film are made redundant due to the local temperature rise caused by the release of latent heat. Consequently, the residual particles are all engulfed in the growing solid phase. The number of active particles in the non-sheared melt is therefore determined by the number of the oxide films, which can only act as single entities for heterogeneous nucleation.

It can be concluded that intensive melt shearing increases the number density of the active nucleating particles. The mechanism of the grain refinement achieved by intensive melt shearing is primarily from the effective dispersion of the MgO particles in the endogenous oxide films into individual particles and the distribution of the particles homogeneously in the melt.

5.4.2. Application of Intensive Melt Shearing for Magnesium DC Casting

The intensive melt shearing device has been applied to magnesium alloys DC casting to achieve fine and uniform microstructures. The experimental results in 4.5 have shown that for AZ91D and AZ31 commercial alloys, melt shearing treatment can not only refine the microstructure, but also homogenize the thermal field within the melt. The microstructures of AZ91D alloy with and without melt shearing in **Figures 4.5.2** and **4.5.9** have confirmed the grain refinement effect achieved by intensive melt shearing in magnesium alloy DC castings. The microstructures of cross section of AZ91D alloy DC cast billet in **Figures 4.5.1** and **4.5.2** show the transition zone before and after the intensive melt shearing device began to operate. The clear transition zone supports the conclusion that intensive melt shearing treatment can refine the microstructures of magnesium alloys DC castings.

The experimental results shown in **Figures 4.5.3**, **4.5.4**, and **4.5.11** indicate that intensive melt shearing can provide more uniform grain structures. As shown in **Figures 4.5.5** and **4.5.6**, the temperature curve during DC casting of AZ91D with melt shearing shows a sharp decrease in the cooling rate after the melt shearing device starts to operate. It is suggested that this decrease is caused by the homogenization of the thermal field in the melt. The measured temperature curves at various locations in the AZ91D melt with and without intensive melt shearing shown in **Figures 4.5.7** and **4.5.8** can also support the idea.

As suggested in section 5.4.1, the mechanism of this grain refinement effect is that intensive melt shearing disperses the endogenous MgO films into individual MgO particles, which are, in turn, considered to be the effective nucleation substrates. Magnesium alloy melt inevitably contains oxides in forms of particle clusters or films with a non-uniform distribution. Such oxides may act as substrates for nucleation but not effective for grain refinement due to their poor wettability and low number density. Such oxide clusters and films can be dispersed effectively by intensive melt shearing. The melt shearing device can not only disperse oxides but also provides rigorous convection in the melt, which can distribute the individual particles uniformly in the entire melt. Thus, it can be concluded that the intensive melt shearing treatment can provide grain refinement in magnesium alloy DC casting. It is proposed that the mechanism of melt shearing is enhancing heterogeneous nucleation and homogenizing the thermal field in magnesium alloy.

5.5. A Model for the Fully Equiaxed Solidification

Hunt [55] has studied columnar to equiaxed transition and brought out a CET map to explain the mechanism. However, there hasn't been any study on the fully equiaxed solidification with temperature gradient and without CET. In order to fill in the vacancy, an analytical model is presented for the prediction of the advancing velocity of an equiaxed solidification front (ESF). As shown in **Figure 5.7**, there are three different parts for the fully equiaxed solidification in an infinite melt system, which are the solid, the liquid, and the ESF. The EFS in the model is defined as the interval from the nucleation to the impingement of grains. The model considers that the fully equiaxed solidification with temperature gradient advances directionally in the melt system.

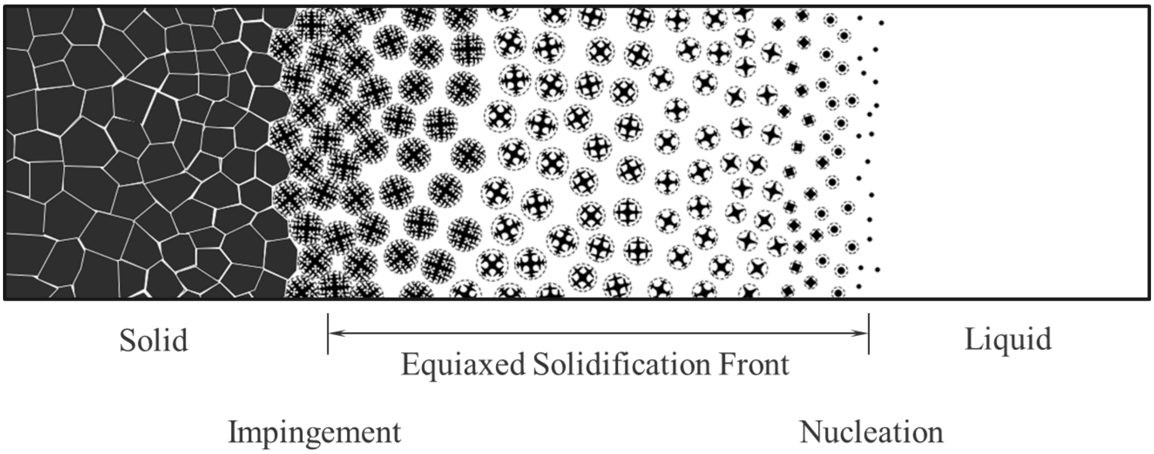

Figure 5.7 Schematic illustration of the fully equiaxed growth and the equiaxed solidification front.

In order to predict the advancing speed of the ESF, some basic assumptions have been made.

- The very first assumption is fully equiaxed solidification in an infinite melt system.
- In order to simplify the model, the nuclei in the melt are considered to be monosized and distributed randomly in the melt.
- The temperature gradient, G, within the melt is assumed to be linear and the latent heat released by solidification wouldn't affect the temperature gradient.

- The diffusion only occurs within the extended sphere, which means the composition in the melt wouldn't change. The well-known concept of extended volume fraction [25] is used, which is shown in **Figure 5.8**.
- According to random close packing theory [158], impingement occurs when the extended volume fraction is 0.63.
- The model considers steady state equiaxed growth which assumes that ESF advances at a constant velocity and the thermal condition ahead of the ESF is independent of time.

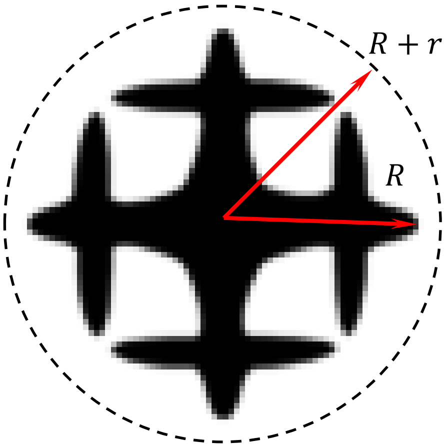

Figure 5.8 Schematic illustrations of the extended volume fraction and the solid fraction of an equiaxed grain.

The extended volume fraction for a single grain, as shown in **Figure 5.8** is the dash sphere with a radius $R+r$. R is the length of the primary dendrite arms from the centre, and r is the radius of the primary dendrite tips. The diffusion of composition, based on previous publications [60], only occurs within the extended volume fraction sphere. Considering that $\mathrm{R} \gg \mathrm{r}$, the extended volume can be given as,

$$\phi_E = \frac{4}{3}\pi R^3 N_e \tag{5.23}$$

where ϕ_E is the extended volume fraction and N_e is the number density of effective nucleation substrates. The relationship between solid fraction f and the extended volume fraction ϕ_E, according to Christian [25], is given by,

$$f = 1 - \mathrm{e}^{-\phi_E} \tag{5.24}$$

According to free growth model [36, 42, 43], the free growth undercooling, ΔT_{fg}, is considered as the nucleation undercooling ΔT_N in this model. As shown in **Figure 5.9**, the forward of *x*-axis is the advancing direction of ESF. x_L is the location where temperature reaches liquidus. x_N and T_N represent the location and temperature where effective nucleation particles start to grow. x_I and T_I depict the location and temperature when impingement between grains takes place. Considering the impingement location moves along with the lapse of time, it takes Δt_I for nucleation particles at x_N in **Figure 5.9** to reach impingement.

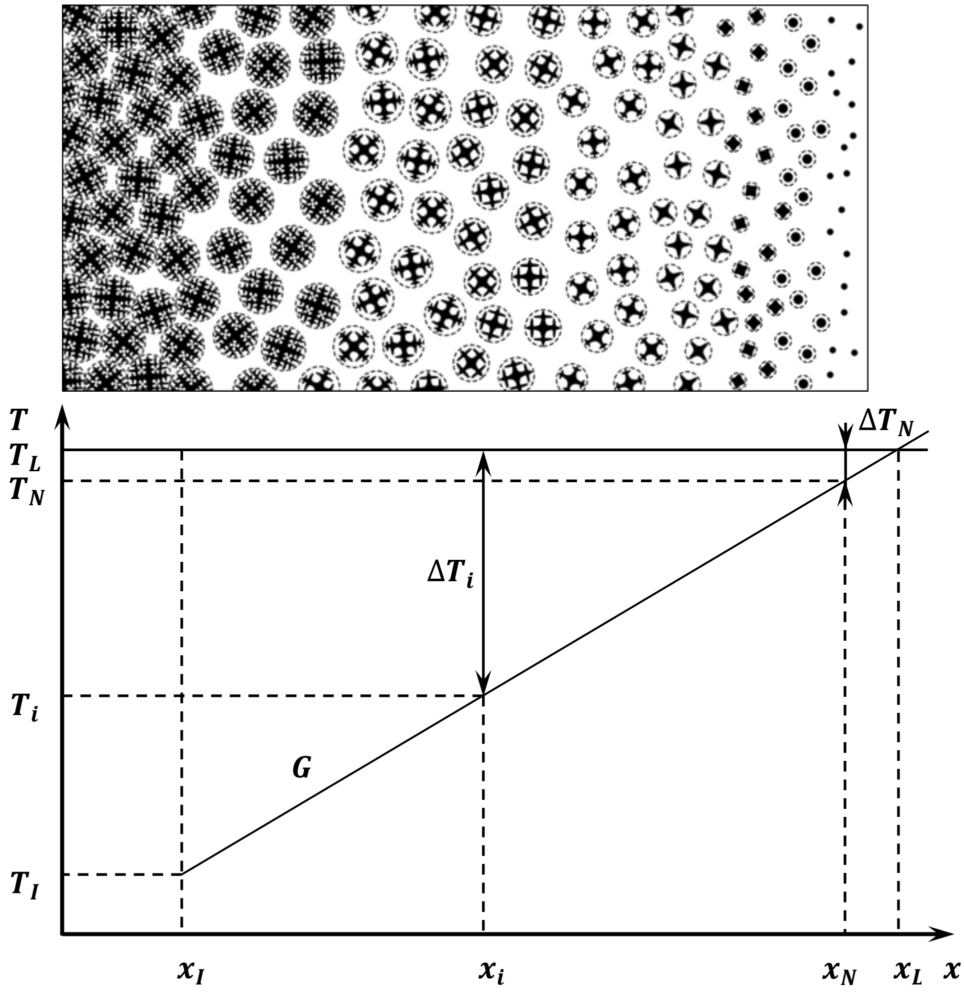

Figure 5.9 Schematic illustration of the equiaxed growth front advance and the thermal field against location in the melt along solidification direction.

The temperature at ESF T_I can be expressed by Sheil equation using the solid fraction, which is given by,

$$f_I = 1 - \left(\frac{T_m - T_I}{T_m - T_L}\right)^{\frac{1}{k-1}} \tag{5.25}$$

where T_m is the melting point for pure metal, T_L is the liquidus of the alloy, and k is the equilibrium distribution coefficient.

From equation 5.24 and 5.25, the undercooling for impingement then becomes,

$$\Delta T_I = \left[\mathrm{e}^{(1-k)\phi_E} - 1\right](-mC_0) \tag{5.26}$$

where m is the liquidus slope, and C_0 is the alloy composition.

The radius of impinged grains is given by

$$R = \int_0^{\Delta t_I} v_g \mathrm{d}t \tag{5.27}$$

According to Hunt and Lu [157], the growth velocity v_g has a certain relationship with the tip undercooling, given by

$$\Delta T = \left(\frac{v_g}{A}\right)^{(1-a_1)} \tag{5.28}$$

where A is a constant, given by

$$A = \left(\frac{1}{a_0\big(mC_0(k-1)\big)^{a_1}}\right)^{\frac{1}{1-a_1}} \frac{D}{2\Gamma} \tag{5.29}$$

where D is the diffusion coefficient, and Γ is the Gibbs-Thomson coefficient. For k varying between 0 and 2, $a_0 = 2.08 - 1.534k + 0.434k^2$, and $a_1 = 0.648 + 0.124k$.

The assumption of steady state growth means that $\frac{\mathrm{d}T}{\mathrm{d}t} = -VG = -\frac{\mathrm{d}(\Delta T)}{\mathrm{d}t}$, where V is the advancing speed of ESF. Equation 5.27 therefore become,

$$R = \frac{1}{V}\int_{\Delta T_N}^{\Delta T_I} \frac{A(\Delta T)^{\frac{1}{1-a_1}}}{G}\,\mathrm{d}\Delta T \tag{5.30}$$

By applying equation 5.23 and 5.26 in equation 5.30, the advancing speed of ESF, V, can be expressed as,

$$V = \frac{\Theta \cdot D \cdot (mC_0)^2}{G \cdot \Gamma} N_e^{\frac{1}{3}}(1 - \xi^{\varepsilon}) \tag{5.31}$$

where ε, ξ, and Θ are defined parameters given in equation 5.32, 5.33, and 5.34.

$$\varepsilon = \frac{2 - a_1}{1 - a_1} \tag{5.32}$$

$$\xi = \frac{\Delta T_N}{\Delta T_I} = \frac{\Delta T_N}{[e^{(1-k)\phi_E} - 1](-mC_0)} \tag{5.33}$$

$$\Theta = \frac{1}{2\varepsilon}\left(\frac{4\pi}{3\phi_E}\right)^{\frac{1}{3}} a_0{}^{(1-\varepsilon)}|1 - k|^{(2-\varepsilon)}\left|e^{(1-k)\phi_E} - 1\right|^{\varepsilon} \tag{5.34}$$

For monosized nucleation particles, the extended volume fraction ϕ_E for impingement is 0.63 based on random close packing theory. This means that ε and Θ are constants only related to the value of k. The advancing speed of ESF can be determined by four major variables: alloy composition, temperature gradient, the number density of the effective nucleating particles, and the nucleation undercooling. In order to examine the variables, parameters of the Mg-Al alloy system have been applied to the model as shown in **Table 5.6**. **Figure 5.10**, **5.11**, **5.12**, and **5.13** show the relationship between the advancing speed of ESF and the four major factors, the alloy composition, the temperature gradient, the number density of the effective nucleating particles, and the nucleation undercooling, respectively.

Table 5.6 Parameters of the Mg-Al alloy system used in the calculations.

Parameter	Definition	Value	Unit
$\boldsymbol{m}$	Liquidus slope	-6.87	$\mathrm{K/wt\%}$
$\boldsymbol{k}$	Equilibrium distribution coefficient	0.37	-
$\boldsymbol{D}$	Diffusion coefficient	2.7×10^{-9}	$\mathrm{m^2 \cdot s^{-1}}$
$\boldsymbol{\Gamma}$	Gibbs-Thomson coefficient	1.35×10^{-7}	$\mathrm{K \cdot m}$
$\boldsymbol{C_0}$	Composition	3	wt%
$\boldsymbol{G}$	Temperature gradient	1000	$\mathrm{K/m}$
$\boldsymbol{N_e}$	Number density of effective nuclei	10^3	$\mathrm{/m^3}$
$\boldsymbol{\Delta T_N}$	Nucleation undercooling	1	K

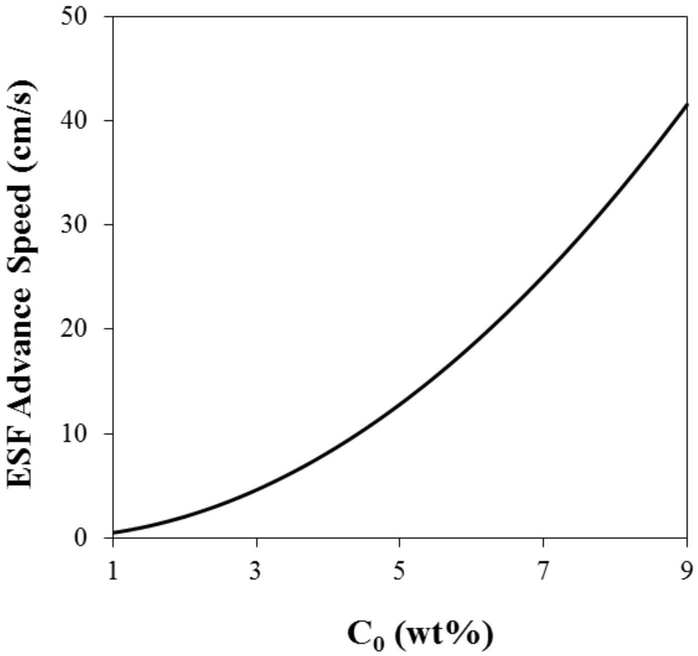

Figure 5.10 Plot of the advancing speed of ESF against the composition C_0 for Mg-Al alloy system, from 1 wt% to 9 wt%.

As shown in **Figure 5.10**, the advancing speed of ESF is increasing with the composition. According to equation 5.26, the impingement undercooling and the distance of ESF increase with the composition linearly. The growth velocity decreases with the increasing of the composition. Since the number density of effective nucleation particles remains unchanged, the decreasing of growth velocity means that it will take more time for the grains to grow before impingement. In this case, it means that both distance and time interval of ESF increase. As discussed, the distance of ESF increases with the composition linearly. The time interval of ESF, on the other hand, increases with the composition, but at a decelerating speed. Therefore, the advancing speed of ESF should increase with the composition which is consistent with the result in **Figure 5.10**.

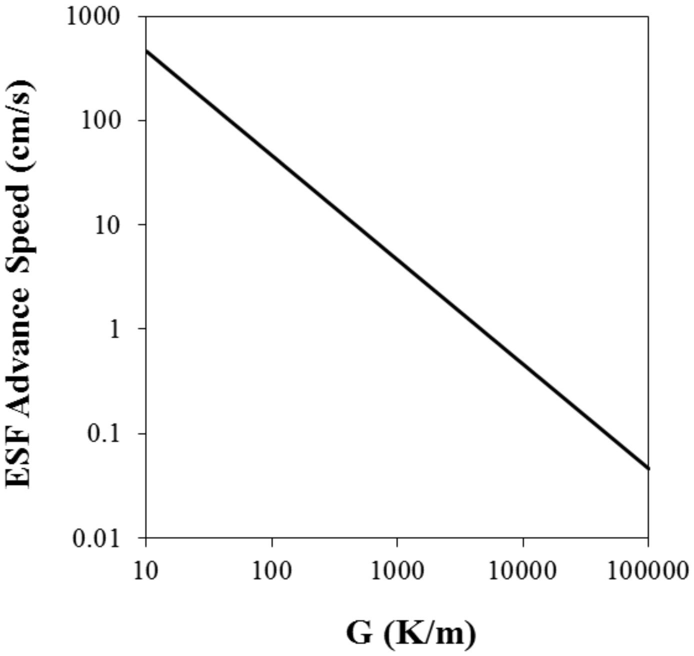

Figure 5.11 Plot of the advancing speed of ESF against the temperature gradient G for Mg-Al alloy system, from 10 $\mathrm{K/m}$ to 10^5 $\mathrm{K/m}$.

In **Figure 5.11**, the advancing speed of ESF is reducing as the temperature gradient increases linearly. According to equation 5.26 and 5.28, the impingement undercooling and the growth velocity is irrelevant to temperature gradient. This means that the time interval of ESF will remain unchanged. The increasing of temperature gradient will decrease the distance of ESF linearly. So the advancing speed of ESF will decreases with the increasing of temperature gradient linearly.

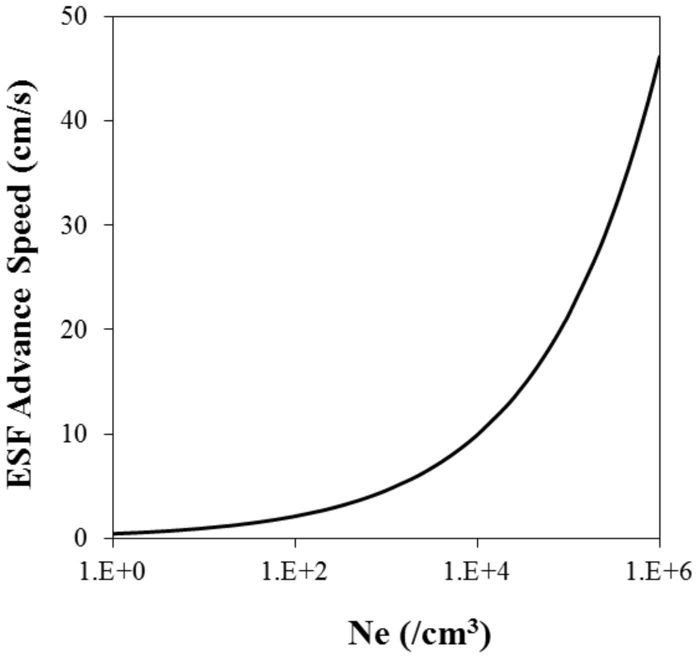

Figure 5.12 Plot of the advancing speed of ESF against the number density of effective nucleation particles N_e from 1 to 10^6.

Figure 5.12 is the plot of the advancing speed of ESF against the number density of effective nucleation particles. As shown, the advancing speed of ESF increases with the number density of effective nucleation particles. When the number density of effective nucleation particles increases, the average size of the final grains will decrease. Since the growth velocity remains unchanged, the growth time before impingement will decrease as the number density of effective nucleation particles increases. Based on this model, the growth time before impingement is the time interval of ESF. Considering that the distance of ESF remains unchanged, the advancing speed of ESF should increase with the number density of effective nucleation particles.

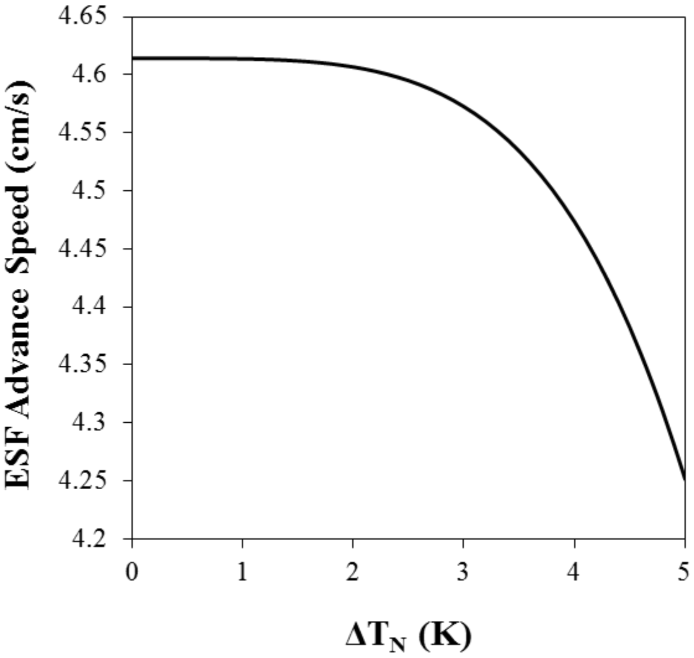

Figure 5.13 Plot of the advancing speed of ESF against the nucleation undercooling ΔT_N from 0 K to 5 K.

As shown in **Figure 5.13**, the nucleation undercooling can also affect the advancing speed of ESF. According to the result, when nucleation undercooling increases, the advancing speed of ESF will decrease. The distance of ESF decreases with the increasing of the nucleation undercooling. The growth velocity remains unchanged. However, since the starting time of growth is delayed, the growth time will slightly increase. This means that the distance of ESF is decreasing and the time interval of ESF is increasing. So the advancing speed of ESF will decrease with the increasing of the nucleation undercooling.

The experimental results from DC casting results of AZ31 and AZ91D alloys are relatively compatible with such calculation. According to the experiment, the pulling speed of the ingots without shearing is 4cm/s. The simulated speed for ESF under the same condition is 8.9cm/s. The measured grain size from experiment is 338μm while the simulated grain size is 600μm. As for AZ31 DC casting with shearing, the pulling speed for experiment is 7.5m/min, and the ESF speed is 12.1cm/s. The grain size from experiment is 80μm while the one from simulation is 53.2μm.

Chapter 6. Conclusions

1. The MgO nano inoculants can refine the microstructure of aluminium bearing magnesium alloy significantly. The potency of MgO nano inoculants is finer than the endogenous MgO films and particles in the magnesium alloy melt. Therefore, it is a practical grain refiner for aluminium bearing magnesium alloys.

2. The solute in the magnesium alloys has limited influence on the microstructures of the cast ingots. The relationship between composition and grain sizes in interpretations from previous studies is debatable. The growth restriction model, therefore, is questionable. The most important role of solute is to determine whether the microstructures of the cast ingots are fully equiaxed, equiaxed and columnar, or fully columnar.

3. Solidification conditions, especially the mould temperature and the pouring temperature, are extremely important influential factors for the microstructures of the magnesium alloy cast ingots. These two factors can determine the critical heat balance temperature after the magnesium melt is rapidly poured into the mould. Due to the strong convection in the melt, the melt quenching effect is believed to exist. The solidification behaviour is influenced by the critical heat balance temperature. If the heat balance temperature is above liquidus, the melt will solidify from the edge to the centre. Otherwise, solidification will happen simultaneously in the entire melt.

4. The mechanism of intensive melt shearing in magnesium alloy castings is believed to be the dispersion of MgO films into individual MgO particles, and the distribution of MgO particles homogeneously in the melt. The microstructures of magnesium alloys have shown significant grain refinement after intensive melt shearing. Therefore, the melt conditioning process can be a potential grain refinement technology for magnesium alloy castings.

5. The conventional DC castings in the magnesium alloy can be improved and optimized by introducing the melt conditioning process. High shear mixer can be an applicable device for

magnesium alloy MC-DC castings. The mechanism of the effect of grain refinement on magnesium alloy MC-DC castings is to enhance nucleation by dispersing MgO films into individual particles and distributing the MgO particles homogeneously in the entire melt. The mechanism of the uniformity of microstructures in magnesium alloy MC-DC castings is to enhance the thermal field by homogenizing the temperature field and reducing the temperature gradient in the melt.

6. A model based on cooling curve analysis is presented to predict the number density and size distribution of effective nucleation substrates. This model is based on the understanding of the free growth model and can be applied to the experiment of cooling curve measurement. The predicted grain sizes of AZ91D alloy without melt shearing, with melt shearing, and with MgO inoculation is compatible to the measured ones, respectively.

7. A model for fully equiaxed solidification is presented. The model considers that the fully equiaxed solidification with temperature gradient advances directionally in the melt system. The equiaxed solidification front (ESF), is defined as the interval from the nucleation to the impingement of the grains. According to the model, the advancing speed of ESF can be influenced by four parameters, which are the alloy composition, the temperature gradient, the number density of the effective nucleating particles, and the nucleation undercooling. The model has been applied to the Mg-Al binary alloy system in order to investigate the relationship between the advancing speed of ESF and the parameters.

Chapter 7. Suggestions for Further Work

In this thesis, the potency and efficiency of nucleation particles have been discussed in order to achieve further understanding of nucleation behaviour in magnesium alloys. The role of solute has been discussed, and the inverse relationship between grain size and growth restriction factor is debatable. A new grain refinement technology of MgO nano particle inoculation or MgO contained master alloy addition is developed. The results show significant grain refinement achieved by MgO inoculation or master alloy addition. The casting conditions have been discussed in detail to provide further understanding of the quenching effect and the critical heat balance temperature after rapid pouring. The melt conditioning technology has then been applied to direct-chill casting of magnesium alloys. The results indicate the mechanism of the melt conditioning process. This study has opened many new directions for further research study. Some of the directions are identified as a direct consequence of the work in this thesis. However, more in-depth understanding is needed for directions in the thesis.

High resolution TEM and 3D-SEM analysis of Mg / MgO interface: The crystallographic orientation relationship between magnesium oxides and the magnesium matrix cannot be identified using conventional scanning electron microscopy or transmission electron microscopy because the sizes of MgO inoculants are too small. In this regard, further high resolution TEM (HRTEM) and 3D-SEM investigation should be performed for samples with MgO inoculants.

Nucleation and cooling curve analysis: Due to the high temperature, atomic scale, and short duration of nucleation in metals and alloys, it is relatively hard to observe nucleation directly in experiments. In order to investigate the efficiency of nucleation substrates, cooling curve analysis has been applied in this thesis because cooling curve is the direct consequence of nucleation and growth of a certain amount of nucleation substrates. As such, it can be used to simulate the number density and the size distribution of nucleation substrates. In order to prove the idea, other experiments with various types of alloys are required rather than simple AZ91D alloys.

Grain growth and composition: Based on the results in this thesis, the inverse relation between the growth restriction factor and the final grain sizes is debatable. The microstructures of the Mg-Al or Mg-Zn binary alloys are more likely to be columnar grains when the composition is relatively low. However, according to empirical understandings, there should be a relationship between composition and grain sizes since the diffused elements should restrict the growth of equiaxed grains. It is therefore expected that a new factor could explain the relationship.

Process development of MC-DC: In the thesis, the high shear mixing device has been applied to conventional DC casting, and the microstructures of the MC-DC cast ingots have been significantly refined. It is believed that the grain refinement of MC-DC on magnesium alloys is caused by the homogenization of thermal field, the dispersion of nucleation substrates, and distribution of those dispersed nucleation substrates. Although the results of MC-DC castings show certain advantages, the mechanism of the nucleation and growth in the MC-DC process remains unclear. For example, it is still unknown whether there is any difference in the sump profile between conventional DC and MC-DC casting. As such, further simulation and analysis of the MC-DC casting is expected.

References

[1] Kainer, K.U. (2003) *Magnesium: Alloys and Technologies*. Wiley-VCH GmbH, Weinheim, 2003.

[2] Avedesian, M.M. and Baker H. (1999) *Magnesium and Magnesium Alloys*. Material Park, OH: ASM International 1999.

[3] Mordike, B.L. and Kainer, K.U. (1998) *Magnesium Alloys and their Applications*. Frankfurt: Weikstoff-Informationsgesellschaft, 1998.

[4] Friedrich, H.E. and Mordike, B.L. (2006) *Magnesium Technology*. Springer-Verlag Berlin Heidelberg 2006.

[5] Hakamada, M., Furuta, T., Chino, Y., and Chen, Y.Q. (2007) Life cycle inventory study on magnsium alloy substitution in vehicles. Energy 2007; 32: 1352-1360.

[6] Polmear, I.J. (1995) *Light Alloys: Metallurgy of the Light Metals, 3rd edition*. J&L Composition Ltd, Filey, North Yorkshire, 1995.

[7] Cantor, B. and O'Reilly K. (2002) Solidification and Casting. Bristol: Institution of Physics Publishing, 2002.

[8] Kurota, K., Mabuchi, M., and Higashi, K. (1999) Review Processing and mechanical properties of fine-grained magnesium alloys. Journal of Materials Science, 1999, 34: 2255-2262.

[9] Yue, T.M., Ha, H.U., and Musson, N.J., (1995) Grain size effects on the mechanical properties of some squeeze cast light alloys. Journal of Materials Science, 1995, 30: 2277-2283.

[10] Dahle, K.A., et al. (2001) Development of the as-cast microstructure in magnesium-aluminium alloys. Journal of Light Metals 2001, 1: 61-72.

[11] Lee, Y.C., Dahle, A.K., and StJohn, D.H. (2000) Grain refinement of magnesium. In Kaplan, H.I., Hryn, J., Clow, B., Magnesium Technology 2000, Nashville, Tennessee, 2000, 211~218.

[12] Emley, E.F. (1966) *Principles of Magnesium Technology*, Pergamon Press, Oxford, United Kingdom, 1966, pp. 126-56.

[13] Cao, P., Qian, M., and StJohn, D.H. (2005) Native grain refinement of magnesium alloys. Scripta Materialia, 2005, 53: 841-844.

[14] Cao, P. and Qian, M. (2005) Discussions on grain refinement of magnesium alloys by carbon

inoculation. Scripta Materialia, 2005, 52: 415-419.

[15] Fu, H.M., et al. (2008) The development of a new grain refiner for magnesium alloys using the edge-to-edge model. Journal of Alloys and Compounds, 2008, 456: 390-394.

[16] Li, Y., et al. (2011) Effects of the grain refiner Mg-Al-C master alloy on the low cycle fatigue life of AZ91D magnesium alloy. Procedia Engineering, 2012, 27: 1808-1816.

[17] Chen, T.J., et al. (2013) Effects of mould temperature and grain refiner amount on microstructure and tensile properties of thixoforged AZ63 magnesium alloy. Journal of Alloys and Compounds, 2013, 556: 167-177.

[18] StJohn, D.H., et al. (2005) Grain refinement of magnesium alloys. Metall and Mater Trans A, 36: 1669-1679.

[19] Becker, D. and Döring, W. (1935) The kinetic treatment of nuclear formation in supersaturated vapors. Annalen der Physik. 1935, Vol. 24, p719-52.

[20] Xu, D. and Johnson, W.L. (2005) Geometric Model for the Critical-Value Problem of Nucleation Phenomena Containing the Size Effect of Nucleating Agent. Physical Review B. 2005, 72:1-4.

[21] Porter, D.A. and Easterling, K.E. (1992) *Phase Transformation in Metals and Alloys, 2nd edition*. T.J. Press Ltd, Cornwall, 1992.

[22] Debenedetti, P.G. (1996) *Metastable Liquids: Concepts and Principles*. Princeton University Press, Princeton, 1996.

[23] Frenkel, J. (1946) *Kinetic Theory of Liquids*. Oxford University Press, Oxford, 1946.

[24] Oxtoby, D.W. (1998) Nucleation of First-Order Phase Transitions. Accounts of Chemical Research. 1998, 31: 91-97.

[25] Christian, J.W. (2002) *The Theory of Transformations in Metals and Alloys*. Pergamon Press, Oxford, 2002.

[26] Bramfitt, B.L. (1970) The Effect of Carbide and Nitride Additions on the Heterogeneous Nucleation Behaviour of Liquid Iron. Metall Trans 1970, 1:1987.

[27] Vonnegut, B. and Turnbull, D. (1952) Nucleation catalysis. Ind. and Eng. Chem. 1952, 44(6):1292-1298.

[28] Cao, X. and Campbell J. (2003) The Nucleation of Fe-Rich Phases on Oxide Films in Al-11.5Si-0.4Mg Cast Alloys. Metall and Mater Trans A, 2003, 34:1409-1420.

[29] Sundquist, B.E. and Mondolfo, L.F. (1961) Orientation Relationships in the Heterogeneous Nucleation of Solid Lead from Liquid Lead. *Trans TMS-AIME*, 1961, 221: 607.

[30] Pound, G.M. (1958) Liquid Metals and Solidification, ASM, 1958, pp87.

[31] Tiller, W.A. and Takahashi, T. (1969) The electrostatic contribution in heterogeneous nucleation theory: Pure liquids. *Acta Met.*, 1969, 17(4): 483-496.

[32] Wang, Y., Fan, Z., Zhou, X. and Thompson, G.E. (2011) Characterisation of magnesium oxide and its interface with α-Mg in Mg-Al-based alloys. *Philosophical Magazine Letters*, 2011, 91(8): 516-529.

[33] Fan, Z. (2012) An Epitaxial Model for Heterogeneous Nucleation on Potent Substrates. *Metallurgical and Materials Transactions*, 2012, 44A: 1409-1418.

[34] Lo, Y.H. (1991) New approach to grow pseudomorphic structures over the critical thickness. *Appl. Phys. Lett.*, 1991, 59:2311-2313.

[35] Huang, F.Y. (2000) Effect of strain transfer on critical thickness for epitaxial layers grown on compliant substrate. *Appl. Phys. Lett.*, 2000, 76(21): 3046-3048

[36] Quest, T.E. and Greer, A.L. (2004) The effect of the size distribution of inoculant particles on as-cast grain size in aluminium alloys. *Acta Mater.* 2004, 52: 3859-3868.

[37] Becker, R. and Döring, W. (1935) Kinetische Behandlung der Keimbildung in übersättigten Dämpfen. Ann. Physik., 1935, 416(8): 719-752.

[38] Men, H., Jiang, B. and Fan, Z. (2010) Mechanisms of grain refinement by intensive shearing of AZ91 alloy melt. *Acta Mater.*, 2010, 58: 6526-6534.

[39] Donnelly, S.E. et al (2002) Ordering in a Fluid Inert Gas Confined by Rat Surfaces, *Science* 2002, 296:507-510.

[40] Turnbull, D. (1953) Theory of Catalysis Of Nucleation By Surface Patches. *Acta Metall.* 1953, 1: 9-14.

[41] Maxwell, I. and Hellawell, A. (1975) A Simple Model for Grain Refinement During Solidification. *Acta Metall.*, 1975, 23: 229-237.

[42] Greer, A.L. et al (2000) Modelling of inoculation of metallic melts: Application to grain refinement of aluminium by Al-Ti-B. *Acta Mater.*, 2000, 48: 2823-2835.

[43] Quest, T.E. and Greer, A.L. (2005) Grain refinement of Al alloys: Mechanisms determining as-cast grain size in directional solidification. *Acta Mater.*, 2005, 53: 4643-4653.

[44] Kurz, W. and Fisher, D.J., (1984) *Fundamental of solidification*. Trans Tech Publications, UK, 1986 (Erstauflage 1984).

[45] Tiller, W.A., Jackson, K.A., Rutter, J.W., and Chalmers, B. (1953) The redistribution of solute atoms during the solidification of metals. *Acta Metall*, 1953, 1(4): 428-437.

[46] Jackson, K.A. (2004) Constitutional supercooling surface roughening. *Journal of Crystal Growth*, 2004, 264: 519-529.

[47] Tarshis, L. A., Walker, J. L., and Rutter, J. W. (1971) Experiments on the solidification structure of alloy castings. *Metall Trans*, 1971, 2(9): 2589-2597.

[48] Kearns, M. A. and Cooper, P. S. (1997) Effects of solutes on grain refinement of selected wrought aluminium alloys. *Mater Sci Technol*, 1997, 13(8): 650-654.

[49] Spittle, J. A. and Sadli, S. (1995) Effect of alloy variables on grain refinement of binary aluminium alloys with Al-Ti-B. *Mater Sci Technol*, 1995, 11(6): 533-537.

[50] Desnain, P., Fautrelle, Y., Meyer, J.L., Riquet, J.P., and Durand, F. (1990) Prediction of equiaxed grain density in multicomponent alloys, stirred electromagnetically. *Acta metall mater*, 1990, 38: 1513-1523.

[51] Hodaj, F. and Durand, F. (1997) Equiaxed grains in multicomponent alloys: Effect of growth rate. *Acta mater*, 1997, 45: 2121-2127.

[52] Easton, M.A. and StJohn, D.H. (2001) A model of grain refinement incorporating alloy constitution and potency of heterogeneous nucleant particles. *Acta Mater*, 2001, 49: 1867-1878.

[53] Easton, M.A. and StJohn, D.H. (2008) Improved prediction of the grain size of aluminum alloys that includes the effect of cooling rate. *Mater. Sci. Eng.*: 2008, 486(A): 8-13.

[54] Spittle, J.A. (2006) Columnar to equiaxed grain transition in as solidified alloys. *International Materials Reviews*, 2006, 51 (4): 247-269.

[55] Hunt, J.D. (1984) Steady State Columnar and Equiaxed Growth of Dendrites and Eutectic. *Mater. Sci. Eng.*, 1984, 65: 75-83.

[56] Tiller, W.A. (1962) Grain size control during ingot solidification - Part II, Columnar-equiaxed Transition, *Trans. Met. Soc. AIME*, 1962, 224: 448.

[57] Lipton, J., Kurz, W., and Heinemann, W. (1983) Modelling Columnar to Equiaxed Transition. *Concast Technol. News*, 1983, 22, 4.

[58] Fredriksson, H. and Olsson, A. (1986) Mechanism of transition from columnar to equiaxed

zone in ingots. *Mater. Sci. Technol.*, 1986, 2(9): 508-516.

[59] Witzke, S., Riquet, J. P., and Durand, F. (1981) Diffusion field ahead of a growing columnar front: Discussion of the columnar-equiaxed transition. *Acta Metall.*, 1981, 29(2): 365-374.

[60] Hunt, J.D. and Fan, Z. (2011) A simple model for the nucleation and growth of equiaxed grains. *John Hunt International Symposium*, Solidification science and technology: Proceedings of the John Hunt international symposium 59-78

[61] Mahapatra, R. B. and Weinberg, F. (1987) The columnar to equiaxed transition in tin-lead alloys. *Metall. Mater. Trans. B*, 1987, 18B: 425-32.

[62] Ziv, I. and Weinberg, F. (1989) The columnar-to-equiaxed transition in Al 3 pct Cu. *Metall. Mater. Trans. B*, 1989, 20B: 731-34.

[63] Gäumann, M., Trivedi, R., and Kurz, W.(1997) Nucleation ahead of the advancing interface in directional solidification, *Mater. Sci. Eng. A*, 1997, 226-228: 763-228.

[64] Wang, C. and Beckermann, C. (1994) Prediction of columnar to equiaxed transition during diffusion-controlled dendritic alloy solidification, *Metall. Mater. Trans. A*, 1994, 25A: 1081-1093.

[65] Martorano, M., Beckermann, C., and Gandin, Ch-A. (2003) A solutal interaction mechanism for the columnar-to-equiaxed transition in alloy solidification, *Metall. Mater. Trans. A*, 2003, 34A: 1657-1674.

[66] Martorano, M. and Biscuola, V. (2009) Predicting the columnar-to-equiaxed transition for a distribution of nucleation undercoolings, *Acta Mater.*, 2006, 57: 607-615.

[67] Wu, M. and Ludwig, A. (2006) A three-phase model for mixed columnar-equiaxed solidification, *Metall. Mater. Trans. A*, 37A: 1613-1631.

[68] Wu, M. and Ludwig, A. (2007) Using a three-phase deterministic model for the columnar-to-equiaxed transition, *Metall. Mater. Trans. A*, 2007, 38A: 1465-1475.

[69] Busk, R.S. (1950) Lattice parameters of magnesium alloys. *J. Metals*, 1950, 2: 1460-1464.

[70] Busk, R.S. (1952) Effect of temperature on the lattice parameters of magnesium alloys. *J. Metals*, 1952, 4: 207-209.

[71] Pearson, W.B. (1958) *A handbook of lattice spacings and structures of metals and alloys*, Pergamon Press, London, 1958.

[72] Greenfield, P. (1972) *Magnesium*, Mills and Boon Limited, London, 1972.

[73] Lyon, R., King, J. F., and Nuttall, F. (1996) in Proceedings of the Third International

Magnesium Conference, G. W. Lorimer ed., Manchester, 1996, p99-108.

[74] Polmear, I.J. (1994) Magnesium alloys and applications. *Mater. Sci. Technol.*, 1994, 10: 1-16.

[75] Baker, H. (1992) *ASM Handbook*, Volume 3, *Alloy Phase Diagrams*. Electronic version.

[76] Willey, L.A. (1973) *Metallography, Structures and Phase Diagrams*, Volume 8, *Metals Handbook,* 8th ed., American Society for Metals, Metals Park, OH 1973.

[77] Czerwinski, F. (2002) The oxidation behaviour of an AZ91D magnesium alloy at high temperatures. *Acta Mater.*, 2002, 50: 2639-2654.

[78] Czerwinski, F. (2004) The early stage oxidation and evaporation of Mg-9%Al-1%Zn alloy. *Corros. Sci.,* 2004, 46: 377-386.

[79] Czerwinski, F. (2004) Factors affecting the oxidation nature of magnesium alloys. *JOM*, 2004, 56(5): 29-31.

[80] Pilling, N.B. and Bedworth, R. E. (1923) The Oxidation of Metals at High Temperatures. *J. Inst. Met*, 1923, 29: 529-591.

[81] You, B.S., Park, W.W., and Chung, I.S. (2000) The effect of calcium addition on the oxidation behaviour in magnesium alloys. *Scripta Mater.*,2000, 42: 1089-1094.

[82] Cahn, R.W., Haasen, P., Kramer, E.J. (1996) *Material Science and Technology*, VCH Verlagsgesellschaft mbH, Weinheim, 1996.

[83] Richetts, N., Cashion, S., and Bailey, R. (2003): in: A. Dahle, Proceedings of the 1st international light metals technology conference 2003, CAST Center Pty Ltd, 2003, p275.

[84] Galovsky, U. and Renger, K. (2003) in: A. Dahle, Proceedings of the 1st international light metals technology conference 2003, CAST Center Pty Ltd, 2003.

[85] Gjestland, H., Westengen, H., and Plahte, S. (1996) in: G.W.Lorimer, Proceedings of the Third Int. Magnesium Conference, Manchester, UK, 1996.

[86] Baker, H. (1992) *ASM Handbook*, Volume 15, *Casting*. Electronic version.

[87] Piwonka, T.S. (1988): in '*Metals Handbook*', Metals Park, OH, *ASM International, 9th edition, volume 15* (1988).

[88] Proffitt H. (1988): in '*Metals Handbook*', Metals Park, OH, *ASM International, 9th edition, volume 15* (1988).

[89] Kenney, M.P., Courtois, J.A., Evans, R.D., Farrior, G.M., Kyonka, C.P., Koch, A.A., and Young, K.P. (1988): in '*Metals Handbook*', Metals Park, OH, *ASM International, 9th edition,*

volume 15 (1988).

[90] Aghion, E. and Eliezer, D. (2004) *Magnesium Alloys*, S. Neaman Inst., Israel, 2004.

[91] Friedrich, H., and Schumann, S. (2000): in Proceedings of 2nd Israeli International Conference on Mg Science and Technology, Dead Sea, Israel.

[92] NADCA: Magnesium Die Casting, North American Die casting Association, USA, 1998.

[93] Hao, H., Maijer, D.M., Wells, M.A., Cockcroft, S.L., Sediako, D., and Hibbins, S. (2004) Development and Validation of a Thermal Model of the Direct Chill Casting of AZ31 Magnesium Billets. *Metall. Mater. Trans. A*, 2004, 35(12): 3843-3854.

[94] P.T. McGlade , (1999) 6th Aus. Asian Pacific Conf. On Aluminum Cast House Technology, Sydeney, Australia, 1999, P.R.Whiteley and J.F. Grandfield.

[95] Eskin, D.G., et. al. (2004) Structure formation and macrosegregation under different process conditions during DC casting. *Mater. Sci. Eng.*: A, 2004, 384: 232-224.

[96] Grandfield, J.F., Eskin, D.G., and Bainbridge, I. (2013) *Direct Chill Casting of Light Alloys*. John Wiley & Sons, Inc. Hoboken, New Jersey, 2013.

[97] Grandfield, J. F., Eskin, D.G., Baker, P.W., and McGlade, P.T. (2013) *Magnesium Direct Chill Casting: A Comparison with Aluminium*. 2013, electronic version.

[98] Hu, K., Phillion, A.B., Maijer, D.M., and Cockcroft, S.L. (2009) Constitutive behaviour of as-cast magnesium alloy Mg-Al3-Zn1 in the semi-solid state. *Scripta Materialia* 2009, 60(6): 427-430.

[99] Mordike, B.L. and Ebert, T. (2001) Magnesium: Properties - applications - potential. *Mater. Sci. Eng.* A, 2001, 302: 37-45.

[100] Michalek J.J., Papalambros P.Y., and Skerlos S.J. (2004) A study of fuel efficiency and emission policy impact on optimal vehicle design decisions. *J. Mech. Des.*, 2004, 126(6): 1062-1070.

[101] Blawert C., Hort N., and Kainer K.V. (2004) Automotive applications of magnesium and its alloys. Trans. Indian Inst. Met., 2004, 57(4):397-408.

[102] Eliezer D., Aghion E., and Froes F.H. (1998) Magnesium science and technology. *Adv Mat Performance*, 1998, 5:201-212.

[103] Medraj M. and Parvez A (2007) Analyse the importance of Magnesium-Aluminium-Strontium alloys for more fuel-efficient automobiles. *Automotive*, 2007, 45-47.

[104] Aghion, E., Bronfin, B., and Eliezer, D. (2001) The role of the magnesium industry in protecting the environment. *Journal of Materials Processing Technology*, 2001, 117(3): 381-385.

[105] Commission of the European Communities (2007), Results of the review of the Community Strategy to reduce CO2 emissions from passenger cars and light-commercial vehicles, {SEC(2007) 60}, {SEC(2007) 61}, COM(2007) 19 final

[106] United Nations (February 2007), Kyoto protocol reference manual on accounting of emissions and assigned amounts

[107] Source: http://www.metalprices.com/

[108] He L. and Li P., (2003) The Developing Technology and Condition of Magnesium Industry. *Foundry Technology*, 2003, 3.

[109] Ke, W., Han, E.H., Han, Y.F., Kainer, K., and Luo, A.A. (2004) in: Magnesium science, technology and applications, ttp Trans Tech publications, Switzerland, 2004, P I.

[110] Tamura Y., Yagi J., Haitani T., Kono N., Tamehiro H., et al. (2003) Observation of Manganese-Bearing Particles in Molten AZ91 Magnesium Alloy by Rapid Solidification. *Mater. Trans.*, 2003, 44(4):552-557.

[111] Byun J.Y., Kwon S.I., Ha H.P., Yoon J.K. (2003) in: *Magnesium alloys and their applications*. Weinheim: Wiley-VCH; 2003.

[112] Kim, Y.M., Yim, C.D., and You, B.S. (2007) Grain refining mechanism in Mg–Al base alloys with carbon addition. *Scripta Mater.*, 2007, 57(8): 691-694.

[113] Cao, P., Qian, M., and StJohn, D.H. (2006) Effect of manganese on grain refinement of Mg–Al based alloys. *Scripta Mater.*, 2006, 54: 1853-1858.

[114] Zhang, M.X., Kelly, P.M., Qian, M., and Taylor, J.A. (2005) Crystallography of grain refinement in Mg-Al based alloys. *Acta Mater*, 2005, 53(11): 3261-3270.

[115] Fan, Z., et al. (2009) Enhanced heterogeneous nucleation in AZ91D alloy by intensive melt shearing. *Acta Mater.*, 2009, 57: 4891-4901.

[116] Kooi, B.J., Palasantzas, G., and JThM De Hosson. (2006) Gas-phase synthesis of magnesium nanoparticles: a high-resolution transmission electron microscopy study. *Appl. Phy. Letts.*, 2006, 89: 16914-1~16914-3.

[117] Qian, M., StJohn, D.H., and Frost, M.T. (2003) in: *Magnesium Alloys and Their Applications*, K.U. Kainer, ed., Wiley-VCH, Wolfsburg, 2003.

[118] Kondic, V. (1968) *Metallurgical Principles of Founding*, Edward Arnold, London, 1968.

[119] Farbenindustrie, I.G. (1931): British Patent GB359,425, 1931.

[120] Farbenindustrie, I.G. (1942): Belgian Patent 444,757, 1942.

[121] Nelson, C.E. (1948) Grain size behaviour in magnesium casting alloys *Trans. AFS*, 1948, 56: 1-23.

[122] Tamura, Y., Haitani, T., Yano, E., Motegi, T., Kono, N., and Sato, E. (2002) Grain refinement of high-purity Mg-Al alloy ingots and influences of minor amounts of iron and manganese on cast grain size. *Mater. Mater. Trans. A*, 2002, 43A(11): 2784-2788.

[123] Motegi, T., Yano, E., Tamura, Y., and Sato, E. (2000) Clarification of Grain Refining Mechanisms of Superheat-Treated Mg-Al-Zn Alloy Castings. *Mater. Sci. Forum*, 2000, 350-351: 191-198.

[124] Boily, S., Blouin M. (2002) : Canadian Patent 2,327,950, 2002.

[125] Nishino, N., Kawahara, H., Shimizu, Y., and Iwahori, H. (2000): in *Magnesium Alloys and Their Applications,* K.U. Kainer, ed., Wiley-VCH, New York, NY, 2000.

[126] Lee, Y.C., Dahle, A.K., and StJohn, D.H. (2000) The role of solute in grain refinement of magnesium: *Metall. Mater. Trans. A*, 2000, 31A: 2895-2905

[127] Fan, Z., Bevis, M., and Ji, S. (2000): British Patent GB2000/003552

[128] Fan, Z., Jiang, B., and Zuo, Y. (2011): British Patent GB2011/051744

[129] Fan, Z., et al. (2009) Melt conditioning by advanced shear technology (MCAST) for refining solidification microstructures. *International Journal of Cast Metals Research*, 22(1-4): 103-107.

[130] Fan, Z., et al. (2009) Shear enhanced heterogeneous nucleation in some Mg- and Al-alloys. International Journal of Cast Metals Research, 22(1-4): 318-322.

[131] Fan, Z., Zuo, Y., and Jiang, B. (2011) A new technology for treating liquid metals with intensive melt shearing. in: Proc. of 5th Light Metals Technology Conf. Germany July 2011.

[132] White J. L. (1990) *Twin Screw Extrusion: Technology and Principles.* Munich: Hanser

[133] Tang, H., Wrobel, L.C., and Fan, Z. (2003) Fluid flow aspects of twin-screw extruder process: numerical simulations of TSE rheomixing. Modelling and Simulation in Materials Science and Engineering, 2003(11): 771-790.

[134] Tang, H., Wrobel, L.C., and Fan, Z. (2003) Numerical evaluation of immiscible metallic

Zn-Pb binary alloys in shear-induced flow, *Mat. Sci. Eng.* A, 2003, 365: 325-329.

[135] Andersen, P.G. (1994) Mixing practices in co-rotating twin-screw extruders Mixing and Compounding of Polymer ed: I. Manas-Zloczower and Z. Tadmor, New York: Hanser, 1994.

[136] Fan, Z., Ji, S., and Liu, G. (2005) Development of the Rheo-Diecasting Process for Mg-Alloys. *Materials Science Forum*, 2005, 488-489: 405-412.

[137] Fan, Z. and Liu, G. (2005) Solidification behaviour of AZ91D alloy under intensive forced convection in the RDC process. *Acta Mater.*, 2005, 53(16): 4345-4357.

[138] Xia, M., et al. (2010) Refinement of Solidification Microstructure by the MCAST Process. *Materials Science Forum*, 2010, 649: 315-323.

[139] Haghayeghi, R., Liu, Y., and Fan, Z. (2008) Melt Conditioned Direct Chill Casting (MC-DC) of Wrought Al-alloys, *Solid State Phenomena*, 2008, 141-143: 403-408.

[140] Bian, Z., Bayandorian, I., Zhang, H.W., and Fan, Z.(2008) Twin Roll Casting and Melt Conditioned Twin-roll Casting of Magnesium, *Solid State Phenomena*, 2008, 141-143: 195-200.

[142] Paul, E.L., Atiemo-Obeng, V., and Kresta, S.M. (2004) *Handbook of Industrial Mixing: Science and Practice*. John Wiley & Sons, Inc. Hoboken, New Jersey, 2004.

[143] Zuo, Y., Jiang, B., and Fan, Z. (2011) Microstructures of DC cast light alloys under the influence of intensive melt shearing. in: Proc. of 5th Light Metal Technology Conf. Germany July 2011.

[144] Zuo, Y.B., Jiang, B., Zhang, Y., and Fan, Z. (2011) Grain refinement of DC cast magnesium alloys with intensive shearing, IOP Conf. Series, *Mater. Sci. and Eng.*, 2011, 27.

[145] Zuo, Y.B., Jiang, B., Zhang, Y., and Fan, Z. (2012) Melt conditioned DC (MC-DC) casting of magnesium alloys. *Magnesium Technology* 2012: 155- 160.

[146] Patel, J.B., Prasada Rao, A.K., Jiang, B., Zuo, Y.B., and Fan, Z. (2012) Melt conditioned direct chill casting (MC-DC) process for production of high quality Mg-Alloy billets. in: 9th International Conference of Magnesium Alloys and their Applications, 2012.

[147] Peng, G.S., Wang, Y., and Fan, Z. (2013) Effect of Intensive Melt Shearing and Zr Content on Grain Refinement of Mg-0.5Ca-xZr Alloys. *Materials Science Forum*, 2013, 765: 336-340.

[148] Xia, M., Prasada Rao, A.K., and Fan, Z., (2013) Solidification Mechanisms in Melt Conditioned Direct Chill (MC-DC) Cast AZ31 Billets. *Materials Science Forum*, 2013, 765: 291-295

[149] Cantor, B. (2003) Heterogeneous nucleation and adsorption. *The Royal Society*, 2003, 361: 409-417.

[150] Girshick, S. L. and Chiu, C. (1990) Kinetic nucleation theory: A new expression for the rate of homogeneous nucleation from an ideal supersaturated vapor. *The Journal of Chemical Physics*, 1990, 93 (2): 1273.

[151] Anisimov, M.P. (2003) Nucleation: Theory and experiment. *Russian Chemical Reviews*, 2003, 72 (7): 591.

[152] Liu, G. (2006) A Study on Twin-Screw Rheo-Diecasting of AZ91D Ma-alloy. Thesis, Brunel University.

[153] Zeiss, Inc. Homepage: http://microscopy.zeiss.com

[154] Ellingham, H. J. T. (1944) Reducibility of oxides and sulfides in metallurgical processes. *J Soc Chem Ind*, 1994, 63: 125-133.

[155] Zener, C. (1948) Grains, Phases, and Interfaces: An Interpretation of Microstructure, *Trans. AIME*, 1948, 175:15-51.

[156] Hellman, P. and Hillert, M. (1975) On the Effect of Second-Phase Particles on Grain Growth, *Scand. J. Met.*, 1975, 4(5): 211-219.

[157] Hunt, J.D. and Lu, S.Z. (1996) Numerical modelling of cellular/dendritic array growth: spacing and structure predictions. *Metall. Mater. Trans. A* 1996, 27:611-623.

[158] Song, C., Wang, P., & Makse, H. A. (2008). A phase diagram for jammed matter. *Nature* 453 (7195): 629-632.